OXYGEN AND HYDROGEN INVESTIGATION OF VOLCANIC ROCKS:

PETROGENESIS TO PALEOCLIMATE

by

ANGELA NICOLE SELIGMAN

A DISSERTATION

Presented to the Department of Geological Sciences
and the Graduate School of the University of Oregon
in partial fulfillment of the requirements
for the degree of
Doctor of Philosophy

June 2016

DISSERTATION APPROVAL PAGE

Student: Angela Nicole Seligman

Title: Oxygen and Hydrogen Investigation of Volcanic Rocks: Petrogenesis to Paleoclimate

This dissertation has been accepted and approved in partial fulfillment of the requirements for the Doctor of Philosophy degree in the Department of Geological Sciences by:

Eugene Humphreys	Chairperson
Ilya Bindeman	Advisor
Paul Wallace	Core Member
Patrick Bartlein	Institutional Representative

and

Scott L. Pratt	Dean of the Graduate School

Original approval signatures are on file with the University of Oregon Graduate School.

Degree awarded June 2016

DISSERTATION ABSTRACT

Angela Nicole Seligman

Doctor of Philosophy

Department of Geological Sciences

June 2016

Title: Oxygen and Hydrogen Investigation of Volcanic Rocks: Petrogenesis to Paleoclimate

Knowledge of the isotopic evolution of volcanic eruptions is essential to volcanologists, geochemists, and paleoclimatologists. I isotopically evaluate the evolution of magmas from their initial formation, to eruption, and then to their alteration during the diffusion of environmental waters into volcanic glass. I focus first on the formation and evolution of large, caldera-forming eruptions from both Gorely volcano in Kamchatka, Russia and 30–40 Ma caldera forming eruptions through Oregon in the United States of America. I utilize oxygen ($\delta^{18}O$), hafnium (εHf), strontium ($^{87}Sr/^{86}Sr$), and neodymium ($^{143}Nd/^{144}Nd$) isotopes to document the creation of caldera-forming eruptions at these eruptive centers through the melting of surrounding crust. I also use U-Pb and $^{40}Ar/^{39}Ar$ to document the timescales of the formation of these large-volume silicic eruptions.

Following eruption, the volcanic glass in tephra and ash can slowly take in environmental water. It is thought that the hydrogen isotopic ratio (δD) of these waters can be used to determine paleoenvironments from the time that the volcanic glass was deposited. The latter portion of my dissertation focuses on the use of hydrogen isotopes of environmentally hydrated volcanic glass to determine

paleoenvironments, and the calibration of the TCEA to analyze oxygen isotopes of hydrated volcanic glass. I first focus on the rate of diffusion of water at ambient temperature to better understand the time frame necessary to hydrate volcanic glass for use as a paleoenvironmental indicator. I also document the hydrogen isotopic ratios that result from the diffusion of water into volcanic glass, which is documented as a decrease in δD with an increase in secondary hydration in all regions worldwide except equatorial. Finally, I focus on the earliest stages of diffusion of water into volcanic glass by analyzing tephra deposits that were collected within days of the 1980 eruptions of Mount St. Helens as well as tephra deposits recently collected in 2015 to identify changes in water concentration and hydrogen isotopic ratios over an ~35 year period.

This dissertation includes both previously published and unpublished co-authored material.

CURRICULUM VITAE

NAME OF AUTHOR: Angela Nicole Seligman

GRADUATE AND UNDERGRADUATE SCHOOLS ATTENDED:

University of Oregon, Eugene
University of Utah, Salt Lake City
Northern Arizona University, Flagstaff

DEGREES AWARDED:

Doctor of Philosophy, Geological Science, 2016, University of Oregon
Master of Science, Geology, 2012, University of Utah
Bachelor of Science, Geology, 2008, Northern Arizona University

AREAS OF SPECIAL INTEREST:

Geochemistry
Volcanology

PROFESSIONAL EXPERIENCE:

Graduate Teaching & Research Fellow, Department of Geological Sciences, University of Oregon, 2011–2016

Geologist, Utah Geological Survey, 2011

Teaching Assistant, Geology & Geophysics, University of Utah, 2009–2011

Geotechnician, Utah Geological Survey, 2010

Lab Manager, Northern Arizona University, 2008

Field Technician, Speedie and Associates, 2008

Seismic Analyst, Washington University in Saint Louis, 2007

GRANTS, AWARDS, AND HONORS:

Good Citizen Award, Department of Geological Sciences, University of Oregon, 2013, 2015

Johnston Grant, Department of Geological Sciences, University of Oregon, 2015

Kleinman Grant for Volcano Research, United States Geological Survey, 2015

On to the Future Award, Geological Society of America, 2014

Smith Scholarship, Department of Geological Sciences, University of Oregon, 2014

Graduate Student Research Grant, Geological Society of America, 2015

Graduate Student Research Grant, Evolving Earth Foundation, 2014

Outstanding Undergraduate Women in Geology Award, Northern Arizona University, 2008

Tom and Rose Bedwell Earth Physics Grant, Northern Arizona University, 2007

PUBLICATIONS:

Seligman, A.N., Bindeman, I.N., Watkins, J.M., Ross, A.M. (under review). Water in volcanic glass: From volcanic degassing to secondary hydration. *Geochimica et Cosmochimica Acta*.

Martin, E., Bindeman, I.N., Palandri, J., **Seligman, A.N.**, Villemant, B. (under review). D/H by TCEA technique in application to volcanic glass as a window into secondary hydration. *Chemical Geology*.

Seligman, A.N., Bindeman, I.N., McClaughry, J., Stern, R.A., Fisher, C. (2014). The earliest low and high $\delta^{18}O$ caldera-forming eruptions of the Yellowstone plume: Implications for the 30–40 Ma Oregon calderas and speculations on plume-triggered delaminations. *Frontiers in Earth Science* **2**, 1–9.

Seligman, A.N., Bindeman, I.N., Jicha, B., Ellis, B., Ponomareva, V., Leonov, V. (2014). Multi-cyclic and isotopically-diverse silicic magma generation in an arc volcano: Gorely eruptive center, Kamchatka, Russia. *Journal of Petrology* **55**, 1561–1594.

ACKNOWLEDGMENTS

I am permanently grateful to the numerous mentors, friends, and family who have supported me through my many years of education. I first need to thank my advisor, Ilya Bindeman, for teaching me so much more than I expected to learn during my five years here. I also need to thank the rest of my dissertation committee (Paul Wallace, Gene Humphreys, and Patrick Bartlein) for their guidance and support, especially towards the end of my PhD. I would also like to thank Mark Reed, who was a member of my comprehensive exam committee and provided a lot of support. In addition to my dissertation committee, I need to give an extra thank you to James Watkins, who coauthored Chapter IV with me. He may not get an official title, but I have personally labeled him as a member of my committee. In addition, I need to thank the VGP group at the University of Oregon, namely Dana Drew, Kristina Walowski, Lucy Walsh, James Rea, Madison Myers, and Dylan Colón. It was immensely helpful to have this group to bounce ideas off of and practice talks to. I know I have excelled more with them by my side. I also need to thank the Geological Sciences office staff. I am slowly realizing that I will never have as productive and efficient an office staff after I leave this department.

My research greatly benefited from the coauthors I had for each of these chapters, especially Brian Jicha, Ben Ellis, and Vera Ponomareva who had to deal with my learning curve while I figured out how to publish my first journal article. My third chapter would not have been possible without the help of Jason McClaughry, who mapped the calderas studied in Chapter III, and helped immensely with my research. I also need to thank Abigail Ross, who helped with

the image processing in Chapter IV. I processed a few of those images, and I know how much time she had to spend working on them. Finally, Chapter V would not have happened without the help of Alexa Van Eaton, who helped me develop the idea for the project. In addition, that project would not have been possible without the help of many researchers at the Cascades Volcano Observatory, including Richard Hoblitt, Larry Mastin, Richard Waitt, John Pallister, and Carl Thornber. I also need to give a special thank you to Gary Nolan. Without his prior research, I would not have gained the idea for the final chapter of my dissertation.

As any lady that has finished graduate school from the geology department at the University of Oregon, I need to thank the Ladies of Riverview (including the honorary Lady of Riverview, Dr. CCD). I could not have made it through these five years without them. Also, I could never write this acknowledgements section without giving a special thank you to Kayak, my little cup of sweet tea, who has spent enough time in my office to earn his own doctorate. When my life got worse, so did his, and he was always there to comfort me with a woo, a wag, and a smile. In addition, I need to give a special thank you to Randy Krogstad, I couldn't have made it through these five years without him. Finally, I need to thank my family, who has always been there to support and encourage me.

This research was supported through a Jack Kleinman Award for Volcano Research from the USGS awarded to Angela Seligman, and grants to Angela Seligman from the University of Oregon, the Evolving Earth Foundation, and the Geological Society of America. This is in addition to NSF grant 1049351 awarded to Ilya Bindeman at the University of Oregon.

For the love of isotopes: Both big and small

TABLE OF CONTENTS

LIST OF FIGURES

Figure Page

Chapter II

Chapter IV

Chapter V

LIST OF TABLES

CHAPTER 1

INTRODUCTION

The geochemistry of volcanic rocks can be incredibly useful for understanding global processes ranging from how large-scale silicic volcanic eruptions are formed, to the use of secondarily hydrated volcanic glass to understand paleoenvironments. Based on the chemical elements that make up volcanic rocks, and the associated isotopic ratios of these elements, researchers can gain a better understanding of whether high silica rhyolites are formed through fractional crystallization (e.g. Gill, 1981; Grove & Kinzler, 1986; Musselwhite et al., 1989; Rogers & Hawkesworth, 1989; Müntener et al., 2001; Grove et al., 2002, 2003) or partial melting of the surrounding crust (e.g. Smith & Leeman, 1987; Atherton & Petford, 1993; Tepper et al., 1993; Rapp & Watson, 1995; Petford & Atherton, 1996; Chappell & White, 2001; Izbekov et al., 2004). Furthermore, if these rocks have taken up meteoric water since their deposition, some researchers have begun to utilize the hydrogen isotopic ratio of those waters to understand paleoenvironments of the region where the rock was deposited (e.g. Friedman et al., 1993; Riciputi et al., 2002; Mulch et al., 2007; Cassel et al., 2014; Canavan et al., 2014). The understanding of both of these processes is important for a wide range of interests from volcanic hazards to global climate change and plate reconstructions, and the details of how and whether these processes can aid in these understandings are detailed here.

In Chapter II, co-authored with Ilya Bindeman, Brian Jicha (University of Wisconsin-Madison), Ben Ellis (ETH Zurich), Vera Ponomareva (The Institute of Volcanology and Seismology in Petropavlovsk-Kamchatsky, Russia), and Vladimir Leonov (The Institute of Volcanology and Seismology in Petropavlovsk-Kamchatsky, Russia), and published in *The Journal of Petrology*, I utilize MELTS and EC-AFC modeling, isotopic ratios ($^{87}Sr/^{86}Sr$, $^{143}Nd/^{144}Nd$, and $\delta^{18}O$), major element compositions, and $^{40}Ar/^{39}Ar$ dating of rocks from Gorely Volcano in Kamchatka, Russia to determine that the large-scale explosive eruptions from Gorely Volcano were formed through partial melting of the underlying basement of the Akhomten Massif, and that Gorely Volcano is a much longer-lived eruptive center than had been previously thought.

In Chapter III, co-authored with Ilya N. Bindeman, Jason McClaughry, Richard A. Stern, and Chris Fisher, and published in *Frontiers in Earth Science*, I utilized isotopic ratios ($\delta^{18}O$ and εHf) and major and trace element geochemistry to determine that the 30–40 Ma calderas across Oregon (Crooked River, Wildcat Mountain, and Tower Mountain) were formed through the influence of the Yellowstone Hotspot. More specifically, based on the prolific low $\delta^{18}O$ eruptions from the Crooked River caldera, I determined that the Crooked River caldera is the oldest known caldera formed from the Yellowstone hotspot. Based on trace element associations and the underlying bedrock, I was able to determine that the other two calderas (Wildcat Mountain and Tower Mountain) were likely formed through small-scale delamination of the underlying crust.

In Chapter IV, co-authored with Ilya N. Bindeman, James M. Watkins, and Abigail M. Ross, and in review in *Geochimica et Cosmochimica Acta*, I utilized a simple water concentration dependent diffusion code to determine (within an order of magnitude) the rate that water diffuses into mafic and felsic volcanic glass at surface temperature. I also determined the trends of hydrogen isotopes that are associated with secondary hydration of volcanic glass (a decrease in δD with increasing hydration for non-equatorial meteoric waters). I also determined the influence that primary magmatic water has on the total δD of water contained within secondarily hydrated volcanic glass. This research is important for understanding the trends associated with secondary hydration of volcanic glass, which are utilized for paleoclimate studies.

In Chapter V, co-authored with Ilya N. Bindeman, Alexa Van Eaton, and Richard Hoblitt, and in preparation for submission to *Geology*, I utilize tephra from the Mount St. Helens eruption that was collected in 1980 to compare to tephra from the same units recently collected in 2015 to understand the earliest stages of secondary hydration after the tephra has been residing on the Earth's surface for 35 years. I utilize D/H ratios and total water concentrations to determine that, although most of the tephra show only average 0.1–0.2 wt.% increases in water concentration, the few samples collected near gas escape pipes, in thicker deposits, show significant signs of secondary hydration, indicating the need for fumarolic activity and elevated heat to significantly hydrate most glasses within a 35 year period. In addition, based on the only moderately depleted δD values of the majority of the tephra, I concluded that the magma of the 1980 summer

eruptions of Mount St. Helens had to have quickly risen from depth, so as to not allow for significant degassing prior to eruption.

In Chapter VI, co-authored with Ilya N. Bindeman, and in preparation for submission to *Geochimica et Cosmochimica Acta*, I develop a new method for oxygen isotope analyses of hydrous volcanic glass using the TCEA at the University of Oregon. This chapter involves the development of new mica standards for oxygen isotope analyses on the TCEA, and involves the use of $\delta^{13}C$ corrections for kinetic fractionations during the analyses. This chapter is based on previous research by Nolan and Bindeman (2013), which proposed that oxygen isotopes might be a more reliable indicator of paleoclimates when studying secondarily hydrated volcanic glass.

In this dissertation, primarily through the use of oxygen and hydrogen isotopes, I am able to understand the full stages of the life of volcanic rocks, all the way from their initial formation to the diffusion of water into the glass structure thousands of years after deposition. This research is beneficial to a wide range of researchers including volcanologists and paleoclimatologists.

CHAPTER II

MULTI-CYCLIC AND ISOTOPICALLY-DIVERSE SILICIC MAGMA GENERATION IN AN ARC VOLCANO: GORELY ERUPTIVE CENTER, KAMCHATKA, RUSSIA

From Seligman, A.N., Bindeman, I.N., Jicha, B., Ponomareva, V., Leonov, V. (2014). Multi-cycly and isotopically diverse silicic magma generation in an arc volcano: Gorely eruptive center, Kamchatka, Russia. *Journal of Petrology* **55**, 1561–1594, doi: 10.1093/petrology/egu034.

INTRODUCTION

Origin of silicic magmas in arc crust

A long-standing question in igneous petrology is how silicic magmas are formed in subduction-related settings and their relation to the formation and recycling of continental crust, as well as its compositional (mafic-silicic) stratification (Rudnick & Fountain, 1995). Mafic magmatism at subduction zones is obviously the initial step to producing more silicic compositions through either fractional crystallization (e.g. Gill, 1981; Grove & Kinzler, 1986; Musselwhite et al., 1989; Rogers & Hawkesworth, 1989; Müntener et al., 2001; Grove et al., 2002, 2003), crustal assimilation (Spera & Bohrson, 2001; Bohrson & Spera, 2001), or partial melting of pre-existing silicic crust (e.g. Smith & Leeman, 1987; Atherton & Petford, 1993; Tepper et al., 1993; Rapp & Watson, 1995; Petford & Atherton, 1996; Chappell & White, 2001; Izbekov et al., 2004b), previously erupted volcanic rocks (Simakin & Bindeman, 2012), or of more mafic crust and cumulates stored in the magma chamber following prior eruptions (e.g. Heath et al., 1998; Dungan & Davidson, 2004). However, these processes likely occur simultaneously, as predicted by heat and mass balance calculations (Annen et al., 2006; Dufek & Burgantz, 2005) and models such as EC-AFC (Spera & Bohrson, 2001; Bohrson & Spera, 2001), and likely include magma-magma and magma-cumulate mixing, which leads to long-term modification, assimilation, storage, and hybridization (MASH;

Hildreth & Moorbath, 1988; Annen et al., 2006), and upward sequestration of silicic components via recycling (e.g. Simakin & Bindeman, 2012). This study provides a detailed look at the processes responsible for the formation of evolved magmas extruded from the Gorely eruptive center of the Kamchatkan volcanic arc (Fig. 1) by using the tools of isotope and trace element geochemistry, and crystallization modeling.

Geological background and overview of the Gorely eruptive history

The Kamchatka Peninsula, located in the NW Pacific (Fig. 1), has some of the most frequent and prolific subduction-related volcanic activity on Earth, including the largest number of calderas relative to the size of the volcanic arc, due to fast convergence (Siebert & Simkin, 2002; Hughes & Mahood, 2008; Bindeman et al., 2010). These volcanoes account for over 16% of global on-land volcanic ejecta, and discharge approximately 240 million tons of material annually (Erlich & Gorshkov, 1979). Most of the current volcanic activity is concentrated in the Eastern Volcanic Belt, which stretches from northern to southern Kamchatka due to subduction of the 80–100 Ma Pacific Plate beneath the Kamchatkan Peninsula at approximately 7–8 cm/yr, and an average slab dip of approximately 55° (Gorbatov et al., 1997; 1999) (Fig. 1). One of these typical caldera-forming volcanoes, Gorely, is located in the southern part of the peninsula in the Eastern Volcanic Belt (Fig. 1).

The Gorely volcanic center has been characterized by a series of explosive and cone-building eruptions throughout its evolution, creating a complex edifice with a currently active summit crater (Fig. 2). Topographically, this eruptive center consists of a large (13 x 12 km) caldera, which encloses the currently active basaltic to andesitic Gorely composite volcano (Fig. 2). Several thick, welded and non-welded tuffs exposed in the vicinity of the present caldera suggest the occurrence of more than one caldera-forming eruption from this center, so that the modern caldera might in fact represent the latest of a suite of nested calderas. The most recent caldera, with an estimated eruptive volume exceeding 100 km^3, based on the caldera size of 12 x 13 km (Selyangin, 2006), is believed to have formed around 38 ka based on dates for a distal tephra deposit

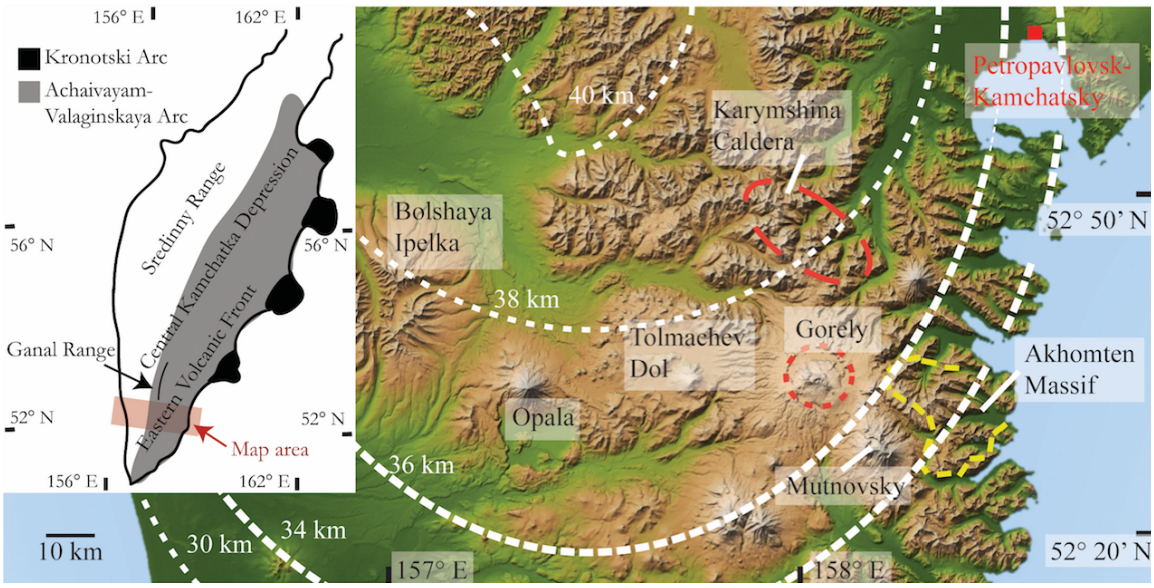

Figure 1. Digital elevation map of south-central Kamchatka showing Gorely volcano and other nearby volcanic centers. Red dashed lines indicate the approximate boundary of the 1.8 Ma Karymshina and 0.3–0.038 Ma Gorely calderas. Outcrops of the 11 Ma Akhomten Granite Massif are outlined in yellow. White dashed lines indicate the thickness of the Kamchatkan crust (from Baboshina et al., 2000). Inset shows the location of the Sredinny Range, the Central Kamchatka Depression, the Eastern Volcanic Front, The Ganal Range, the Kronotski Arc, and the Achaivayam-Valaginskaya Arc for reference (Bindeman et al., 2002 and references therein).

(Braitseva et al., 1995; all the dates for the last ~40 ka are calibrated ^{14}C). Several attempts to determine the age of the youngest welded tuff unit in the area by using $^{40}Ar/^{39}Ar$ geochronology failed due to the predominance of atmospheric Ar. Traditionally, all the welded tuffs around the Gorely caldera (Fig. 2) were assumed to be associated with the most recent caldera-forming eruption (Selyangin & Ponomareva, 1999). A recent dating effort, however, has revealed that some of these welded tuffs may belong to far older mid-Pleistocene (361 ka) eruptions (Bindeman et al., 2010). The youngest welded tuff, in places, is overlain by a dacitic pumice, which may represent the product of the most recent caldera-forming eruption (ca. ~38 ka) and resulting depression of the western part of the caldera (Selyangin & Ponomareva, 1999). Shortly after the cycle of cataclysmic eruptions, a series of smaller eruptions along the caldera rim created basaltic andesite cinder cones and dacite extrusions. The modern intra-caldera volcanic edifice started to form in late Pleistocene times (Selyangin & Ponomareva, 1999) and

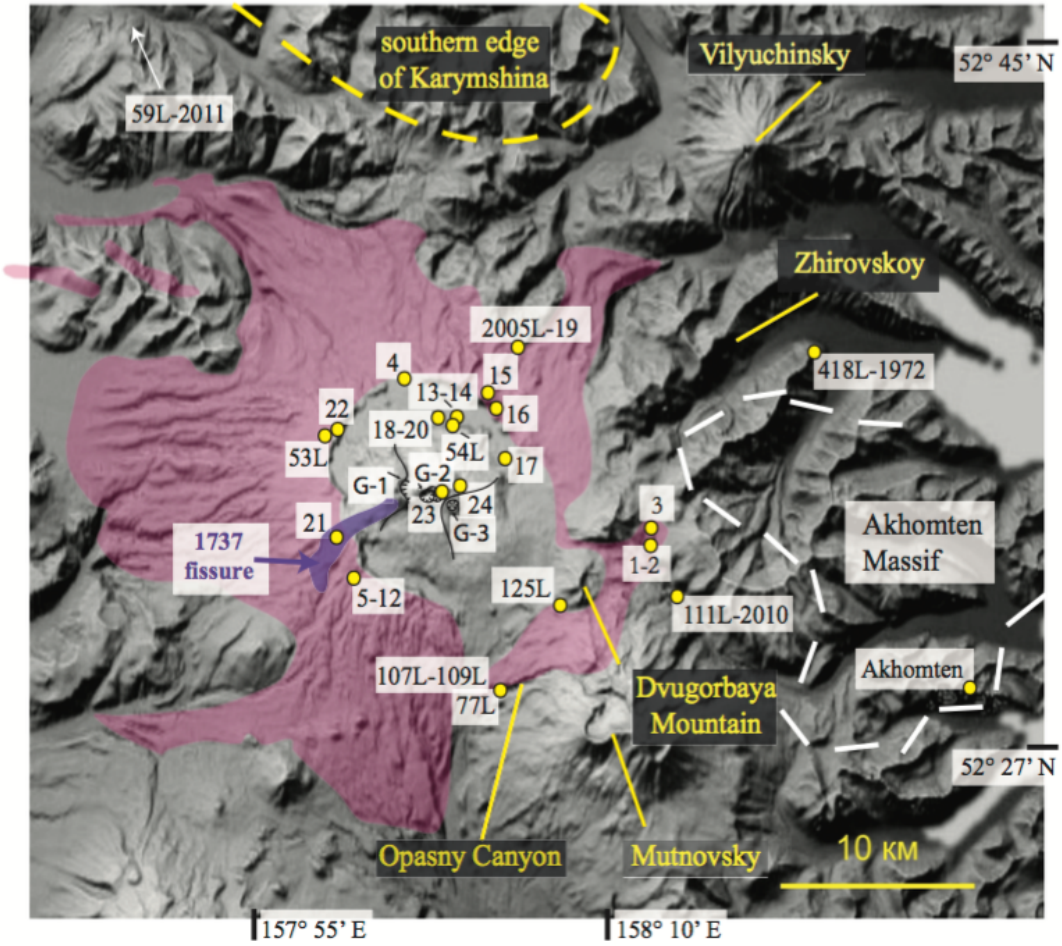

Figure 2. Digital elevation map of Gorely volcano inside a caldera rim (inside the pink region), showing the extent of the ignimbrites and pumice, which are described in this study (shaded in pink), and the location of the studied samples. The sample names have been abbreviated for space (e.g. '11G-3' is written as '3', and '77L-144' is written as '77L'). The locations of Opasny Canyon, Mutnovsky volcano, Zhirovskoy volcano, Dvugorbaya Mountain, and Vilyuchinsky volcano are labeled for reference. White dashed lines denote outcrops of the Akhomten Massif, and yellow dashed lines denote the extent of the southern edge of Karymshina caldera. G-1, G-2, and G-3 are also shown for reference, and stand for Gorely-1, Gorely-2, and Gorely-3 cones, respectively. Note the glacial U-shaped valleys emanating from Gorely.

comprises three merged cones, of which the first two having formed under glaciers (Fig. 2). Gorely 1, the first cone to form, is composed of 14 km^3 of primarily basalt and basaltic andesite. Gorely 2 began to form in the early Holocene at the eastern edge of the

crater of Gorely 1, and is still active today, erupting primarily basalt to basaltic andesite. Gorely 3 is the smallest of the three merged cones (2 km^3) and formed at the southeastern flank of Gorely 2. Gorely 3 is composed primarily of basaltic to andesitic lavas and pyroclastic material. In addition to the summit craters, there are also numerous fissures along the flanks of Gorely, which began developing prior to the Holocene, and continue to erupt episodically today (Selyangin, 2006; Kirsanov & Melekestev, 1991; Selyangin & Ponomareva, 1999; Chashchin, 1999). The youngest lava eruptions occurred along an arcuate fissure in 1737 A.D. (Selyangin, 2006), and intermittent volcanic activity continues today, accompanied by nearly continual release of steam and gas.

Tectonic history and crustal structure of the Eastern Volcanic Front

Previous research on the tectonic history of Kamchatka has provided significant insight into the initiation of volcanic activity in the region, the origin of the approximately 37 km thick crust underlying the Gorely eruptive center, and the origin of the crust of the Eastern Volcanic Front (Lander & Shapiro, 2007; Scholl, 2007; Gordeev et al., 2001; Bindeman et al., 2002; Konstantinovskaya, 2003; Soloviev et al., 2002a, 2002b; Hourigan et al., 2009; Kraus & Scotese, 1993; Balesta, 1991). Prior to ~10 Ma, subduction occurred below the Sredinny Range, 150 km west of the modern volcanic front (Lander & Shapiro, 2007) (Fig. 1). Accretion of the Kronotski arc between 10 and 7 Ma to eastern Kamchatka (Lander & Shapiro, 2007) caused subduction to jump to the east. The Eastern Volcanic Belt, in which the Gorely eruptive center is located, was established around 5 Ma, due to steeper subduction and migration of the trench to the east. Since the Kronotski terrane collided with Kamchatka at an oblique angle, collision began in the south and migrated north through time (Lander & Shapiro, 2007). Specifically, outcrops of the Miocene Akhomten Granite Massif are exposed to the east of Gorely, suggesting that similar crust may extend beneath the volcano (Figs. 1–3). It is also possible that the crust underlying Gorely may include crust from the Achaivayam-Valaginsky Arc which accreted at 45–50 Ma; this is also known as the Olutorsky Arc (Soloviev et al., 2002a, 2002b; Hourigan et al., 2009; Konstantinovskaya, 2003), and is similar to exposures at Ganal Range (e.g. Bindeman et al., 2002), or metamorphosed

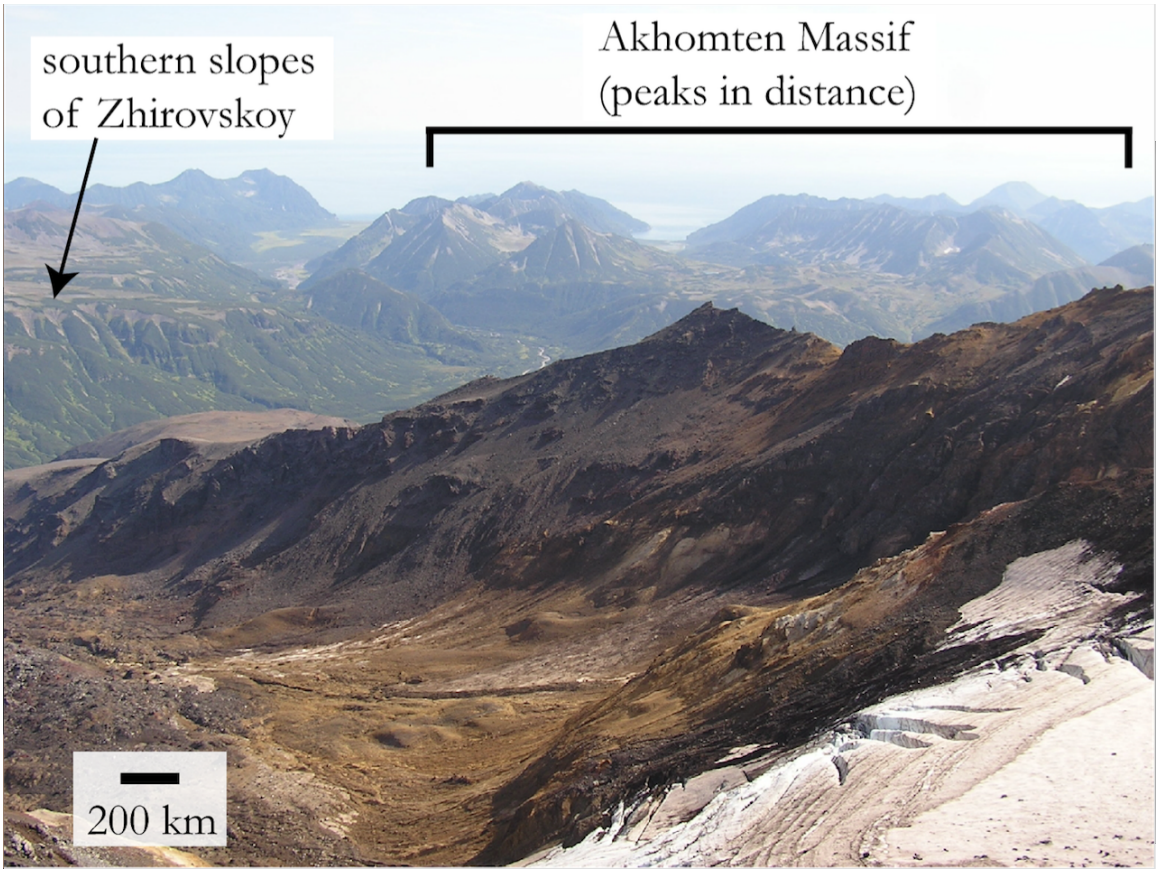

Figure 3. Image looking northeast from Mutnovsky volcano, showing the southern slopes of Zhirovskoy to the north and the Akhomten Massif in the foreground, with jagged, raised peaks.

accretionary sediments trapped in between the Achaivayam-Valaginsky Arc and the Ganal Range (Konstantinovskaya, 2003; Soloviev et al., 2002b) (Fig. 1).

Goals of this study

This study focuses on the processes responsible for the formation of silicic magmas in arc crust at a typical multi-caldera, "long-lived" eruptive center represented by Gorely. In an attempt to determine these processes we use $^{87}Sr/^{86}Sr$, $^{144}Nd/^{143}Nd$, and $\delta^{18}O$ isotopic data in addition to major and trace element compositions, MELTS and EC-AFC modeling, $^{40}Ar/^{39}Ar$ geochronology, pyroxene and plagioclase chemistry, and thin section petrography. Detailed isotopic work allows us to assess the relative roles of fractional

crystallization and crustal assimilation, and to recognize the importance of crustal recycling, even in this setting where the underlying crust is relatively young (Eocene-Quaternary) and petrochemically similar. This situation is typical of many volcanic arcs built on recently accreted terranes. We also address whether isotopically distinct ignimbrites are produced from a large, single, long-lived magma body or multiple smaller magma bodies beneath the Gorely eruptive center, the likely timescales of these processes, and how they relate to glaciations that shaped the area.

METHODS

Samples from this study (Figs. 2, 4, Supplementary Data Figs. A1, A2, Table 1; see Appendix A for Chapter II supplement) include a stratigraphic sequence of tephrochronologically-dated (SD: Fig. A1) Holocene (post-glacial) tephra collected from trenches near road cuts and river drainages, lavas collected from both 'pra-Gorely' ('pra-Gorely' is the term typically used for the older Gorely cone (~0.7 Ma) that was destroyed during a series of caldera-forming eruptions (Selyangin, 2006)) and modern Gorely, and multiple ignimbrites. Ages were determined for tephra units based on stratigraphic order and known ages of regional tephra markers present in the sections (Fig. A1). These marker layers include KO (Kurile lake caldera, ~8.4 ka), KS_2 (Ksudach caldera, ~6.85 ka), KS_1 (Ksudach caldera, ~1.75 ka), OP (Opala, 1.4 ka), and $KSht_3$ (Stübel Cone, Ksudach center AD 1907) (Selyangin & Ponomareva, 1999). Lavas collected for this study were assigned an age based on their known period of eruption (i.e. modern Gorely or pra-Gorely), historical dates, position relative to dated regional tephra, and reflected on the geologic map of Selyangin (2006). One ignimbrite sample was collected near Gorely volcano, four older ignimbrite units were collected from Opasny (Dangerous) Canyon (SD: Fig. A2), and one ignimbrite unit was collected near Dvugorbaya Mountain (Fig. 2; Table 1).

Samples were analyzed for $\delta^{18}O$ at the stable isotope laboratory of the University of Oregon. Individual plagioclase and pyroxene grains, as well as whole-rock fragments

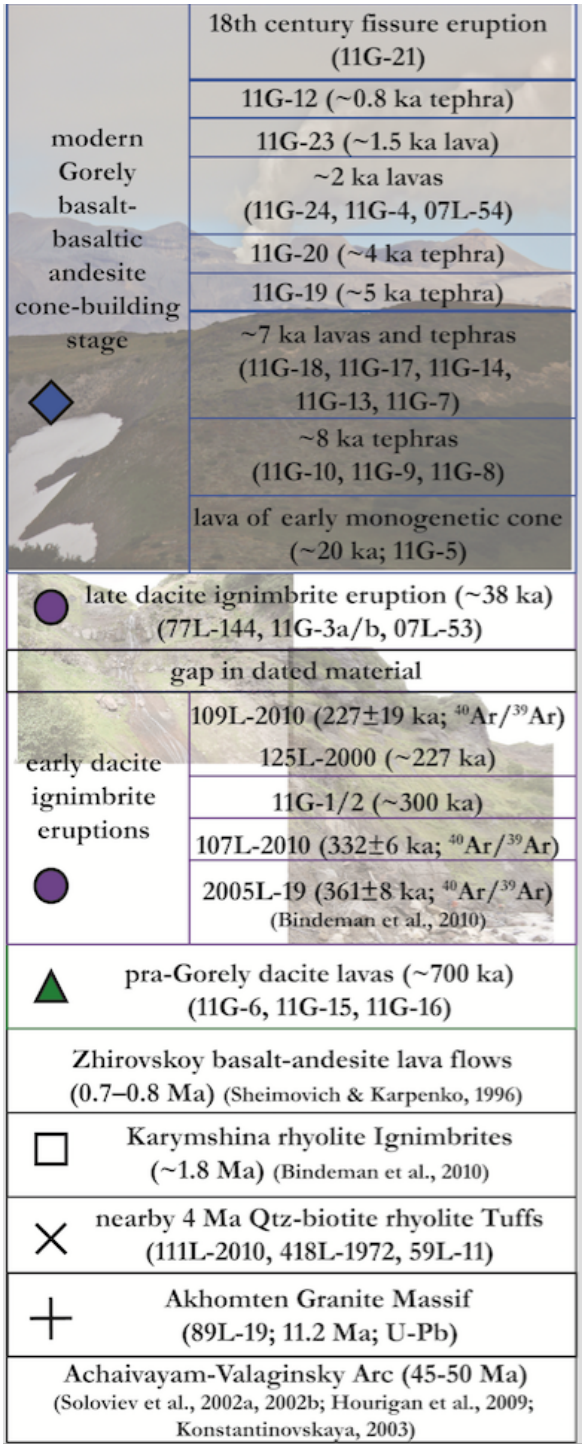

Figure 4. Stratigraphic section illustrating the crust under Gorely volcano. Symbols and colors of each layer, if appropriate, are the same as those used in subsequent figures. Methods used for the ages reported in this section are also listed in Table 1. The image behind the modern Gorely stage shows the current Gorely cone, with steam emanating from the top. The image behind the ignimbrite series shows the sampling location in Opasny Ravine.

Table 1: Method of age determination for Gorely samples

Sample no.	Latitude	Longitude	Rock Type	Age Determination	Age (ka)	2σ
11G-21	N52°32'16"	E157°58'31"	bomb	associated with 18th century fissure eruption	0.261	
11G-12	N52°31'25"	E157°59'07"	tephra	stratigraphic constraints	0.8	
11G-23	N52°33'13"	E158°02'23"	lava	associated with recent cone-building eruptions	1.5	
07L-54	N52°28'19"	E158°05'43"	lava	associated with recent eruption	2	
11G-4	N52°35'37"	E158°00'45"	lava	associated with recent eruption	2	
11G-24	N52°33'29"	E158°03'21"	lava	associated with recent cone-building eruptions	2	
11G-20	N52°35'10"	E158°03'04"	tephra	stratigraphic constraints	4	
11G-19	N52°35'10"	E158°03'04"	tephra	stratigraphic constraints	5	
11G-7	N52°31'25"	E157°59'07"	tephra	stratigraphic constraints	7	
11G-13	N52°35'06"	E158°03'34"	lava	stratigraphic constraints	7	
11G-14	N52°35'06"	E158°03'34"	lava	stratigraphic constraints	7	
11G-17	N52°34'35"	E158°05'16"	lava	stratigraphic constraints	7	
11G-18	N52°35'10"	E158°03'04"	tephra	stratigraphic constraints	7	
11G-8	N52°31'25"	E157°59'07"	tephra	stratigraphic constraints	8	
11G-9	N52°31'25"	E157°59'07"	tephra	stratigraphic constraints	8	
11G-10	N52°31'25"	E157°59'07"	tephra	stratigraphic constraints	8	
11G-5	N52°31'25"	E157°59'07"	lava	associated with early post-caldera monogenetic cone	20	

Table 1 continued

Sample no.	Latitude	Longitude	Rock Type	Age Determination	Age (ka)	2σ
07L-53	N52°34'23"	E157°57'52"	ignimbrite	thin section petrography, $\delta^{18}O$	young ignimbrite series (38 ka)	
11G-3	N52°32'53"	E158°12'04"	pumice	$\delta^{18}O$, sample freshness, lack of burial	young ignimbrite series (38 ka)	
77L-144	N52°28'19"	E158°05'43"	ignimbrite	$^{40}Ar/^{39}Ar$[a]	young ignimbrite series (38 ka)	
109L-2010	N52°28'17"	E158°05'43"	ignimbrite	$^{40}Ar/^{39}Ar$	227	19
125L-2000	N52°30'01"	E158°07'57"	ignimbrite	thin section petrography, $\delta^{18}O$	227	
11G-1	N52°32'19"	E158°12'08"	ignimbrite	thin section petrography, $^{87}Sr/^{86}Sr$	300	
11G-2	N52°32'19"	E158°12'08"	ignimbrite	thin section petrography, $^{87}Sr/^{86}Sr$	300	
108L-2010	N52°28'17"	E158°05'47"	ignimbrite	$^{40}Ar/^{39}Ar$	324	10
107L-2010	N52°28'16"	E158°05'48"	ignimbrite	$^{40}Ar/^{39}Ar$	332	6
2005L-19	N52°37'31"	E158°05'49"	ignimbrite	$^{40}Ar/^{39}Ar$[b]	361	8
11G-6	N52°31'25"	E157°59'07"	lava	pra-Gorely lava[c]	700	
11G-15	N52°35'14"	E158°05'03"	lava	pra-Gorely lava[c]	700	
11G-16	N52°34'59"	E158°05'17"	lava	pra-Gorely lava[c]	700	

[a]the $^{40}Ar/^{39}Ar$ is <100 ka

[b]Bindeman et al. (2010)

[c]pra-Gorely lavas are covered by 362 ka ignimbrites, and are intruded by 500 and 600 ka Karymshina dikes. They are also known to be younger than 800 ka Zhirovskoy deposits.

were picked from each sample using a binocular microscope; with most weights ranging from 1 to 2 mg. Grains were selected from a 0.5 to 1 mm size fraction and grains lacking melt or crystal inclusions were selected preferentially. Samples were analyzed using CO_2-laser fluorination (e.g. Bindeman, 2008) with Gore Mt. Garnet ($\delta^{18}O$ of 5.75‰) as a standard and using BrF_5 reagent. The desired gas was acquired through a series of steps involving multiple LN_2 cryogenic traps that caused the BrF_5 reaction products to be frozen in a mercury diffusion pump as a getter for F_2 gas, leaving pure O_2 as an end result, which was then converted to CO_2 in a small platinum-graphite converter. After

this step, the yield was measured as a means to determine any sample loss, and the CO_2 gas was analyzed on a MAT 253 mass spectrometer for the isotopic ratio of $^{18}O/^{16}O$.

Whole-rock major and trace elements were determined by XRF using standard methods in the GeoAnalytical Lab at Washington State University as described by Johnson et al. (1999). Doubly-fused, low dilution beads were used to determine the ten major elements and a typical suite of trace elements. Analyses were carried using a ThermoARL Advant'XP+sequential X-ray fluorescence spectrometer, with major elements reported as oxide wt. % (anhydrous) and trace elements reported in ppm.

The $^{87}Sr/^{86}Sr$ and $^{143}Nd/^{144}Nd$ isotope compositions of crushed whole-rock powders were determined by Thermal Ionization Mass Spectrometry (TIMS) at New Mexico State University. For these analyses, the freshest fragment of rock without any lithic fragments was picked from each unit, and these fragments were sonicated in water for a minimum of five minutes and dried prior to being ground with a ceramic mortar and pestle. The standard used for the $^{87}Sr/^{86}Sr$ analyses was NBS987 and returned ratios of 0.710271 ± 11 and 0.710294 ± 11. The standard used for $^{143}Nd/^{144}Nd$ was JNdi-1, with ratios of 0.512098 ± 13 and 0.512097 ± 9. None of the ratios were normalized.

$^{40}Ar/^{39}Ar$ dating was undertaken on five ignimbrite units at the University of Wisconsin-Madison Rare Gas Geochronology Laboratory. Groundmass or matrix glass separates weighing ~200 mg were incrementally heated in a resistance furnace following the procedures of Jicha et al. (2012). Argon isotope analyses were made using a MAP 215-50 mass spectrometer with a single Balzers SEM-217 electron multiplier; the isotopic data were reduced using ArArCalc software version 2.5 (http://earthref.org/ArArCALC/). Atmospheric argon was measured 6–10 times prior to and following each incremental heating experiment. Measured $^{40}Ar/^{36}Ar$ ratios of atmospheric argon were normalized to $^{40}Ar/^{36}Ar = 295.5$ (Steiger & Jäger, 1977). The age uncertainties reported in Supplementary Data Table A1 reflect analytical contributions only at the 2σ level and are calculated relative to the 28.201 Ma Fish Canyon sanidine standard (Kuiper et al., 2008); the decay constants used are those of Min et al. (2000).

Pyroxene and plagioclase major element compositions in selected ignimbrite units were determined using a Cameca SX100 electron microprobe at the University of Oregon MicroAnalytical Facility with a beam current of 30 nA, a beam energy of 15 keV, and a beam diameter of 10 μm. The counting time was 10 seconds for Ti and Cr, 20 seconds for K and Mn, 25 seconds for P, 30 seconds for Fe and Ca, 35 seconds for Si, and 40 seconds for Na, Al, and Mg.

RESULTS

Volcanic stratigraphy and dating of the major Gorely ignimbrites

We have expanded the pre-Holocene volcanic history of the Gorely eruptive center by identifying, characterizing, and dating the earliest exposed ignimbrite units found in the vicinity. As the age associations are complex, and based on various dating methods, this information is summarized in Figure 4 and Table 1. In addition to the 361 ka date of Bindeman et al. (2010), we have determined $^{40}Ar/^{39}Ar$ ages for several more ignimbrite units in the area. Three samples produced statistically acceptable plateaus (three or more consecutive steps that contain >60% of the ^{39}Ar released) and have isochrons with trapped $^{40}Ar/^{36}Ar$ ratios that are indistinguishable from the atmospheric $^{40}Ar/^{36}Ar$ ratio of 295.5 (Table 1; Supplementary Data Table A1). For this reason, coupled with the observation that each $^{40}Ar/^{39}Ar$ age is consistent with its stratigraphic position, we consider the plateau ages to give the best estimate of the time elapsed since eruption. $^{40}Ar/^{39}Ar$ dates on welded tuffs from Opasny Canyon (SD: Fig. A2) provide ages of 320–330 ka for the lower two units, ~230 ka for the middle units, and an age of <100 ka for the upper, youngest ignimbrite in this section (77L-144). Two more ignimbrites, which stratigraphically overlie the "<100 ka" ignimbrite have been described near Opasny Canyon, but were not dated in this study. The lower of these units is welded while the upper is a non-welded layer of pumice, which is probably related to the pumice exposed in other directions from the Gorely caldera. The upper three ignimbrite units are not dated and likely fit stratigraphically into the <100–38 ka interval.

Older ignimbrites are partly eroded, covered with younger products, and cannot be mapped individually. Therefore, we have to make assumptions about the age of some samples, which have unclear stratigraphic context (Figure 4; Table 1). Based on similar thin section petrography (higher plagioclase abundance and similar amount of groundmass) and $\delta^{18}O$ to unit 77L-144, unit 07L-53 was assigned a tentative age of 38 ka in accordance with a correlated pumice deposit (Braitseva et al., 1995). Units 11G-1 and 11G-2 (lower and upper portion of the same ignimbrite) in the Falshivaya River failed to produce an $^{40}Ar/^{39}Ar$ age. Despite this, we have assigned it a tentative age of ~300 ka, due to its close association with 2005L-19, based on $^{87}Sr/^{86}Sr$ and thin section petrography. Pumice samples 11G-3a/b were found on the surface, and are grouped with the 38 ka (younger ignimbrite), given the lack of weathering and apparent freshness of the sample, lack of burial by subsequent deposits, and similar $\delta^{18}O$ value to unit 77L-144.

U-Pb zircon geochronology

We attempted to extract zircons from the studied ignimbrites by HF dissolution of bulk rocks, but all were zircon-undersaturated; only one xenocryst was extracted from pumice sample (11G-3a) that yielded Eocene U-Pb ages of 54.7 ± 1.1 (1 s.e.) Ma (core) and 37.5 ± 0.7 (1 s.e.) Ma (rim), suggesting the presence of material underlying the Gorely eruptive center of this age. Rocks of Cretaceous/Eocene age are common in eastern Kamchatka, including the crust of the 45–50 Ma Achaivayam-Valaginsky Arc. The Th/U ratios of this zircon (0.02 for the rim and 0.11 for the core) suggest metamorphic derivation (Rubatto, 2002) and a collision-type origin which we correlate with the Achaivayam-Valaginsky Arc. Furthermore, the Ganal Massif (Fig. 1), which is a portion of the metamorphic basement of the Achaivayam-Valaginsky Arc, contains zircons with ages ranging between 15 and 40 Ma as well as between 55 and 85 Ma, showing two separate metamorphic events. The older age relates to the accretion of the Ganal Massif onto Kamchatka, whilst the younger age reflects the accretion of the eastern Kamchatka Peninsula (Bindeman et al., 2002). These age ranges overlap with both the rim and core of the zircon xenocryst from the Gorely eruptive center.

Zircons from the Akhomten Massif were also dated by the U-Pb method, yielding an age of 11.2 ± 0.08 Ma (1 s.e.). This age slightly predates the established timing of the accretion of the Kronotski arc (10–7 Ma). Furthermore, zircons from three Qtz-Bi bearing ignimbrite units that likely underlie the Gorely eruptive center were dated by the U-Pb method, and all returned ages near 4 Ma (SD: Table A1). These ages are older than those currently known for units erupted from the nearby Zhirovskoy (0.67–0.84 Ma; Shemovich & Karpenko, 1996) and Karymshina (~1.5-2.0 Ma; Bindeman et al., 2010) eruptive centers and, therefore, suggest longer-lived silicic volcanism and magmatism in this region. Compositionally, they are similar to younger Karymshina ignimbrites.

Major element geochemistry of the eruptive products

Newly obtained and compiled analyses of the Gorely eruptive products range from ~52 to 69 wt.% SiO_2 (Table 2), but include only sparse amounts of andesite. This shows a clear bimodal distribution or "Daly Gap" present in the Gorely eruptive products (Figs. 5–6), which will be addressed later in the discussion. Sampling bias is assumed to be minimal due to our range of sample collection, which was not focused on a particular type of sample (e.g. rhyolite versus basalt) and due to our compilation of previously published data from the GEOROC database.

The variation of wt.% SiO_2 versus newly-determined $^{40}Ar/^{39}Ar$ ages, and previously determined ^{14}C Holocene ages (calibrated with the help of Calib 6.0; Selyangin & Ponomareva, 1999) is illustrated in (Fig. 5a). The established stratigraphy demonstrates that following a nearly 700,000 year period of dominantly dacitic ignimbrite eruptions at the Gorely eruptive center, there was a shift in eruptive compositions at 38 ka to predominantly basalt and basaltic andesite (Fig. 5a). This change is illustrated in nearly all the material erupted prior to 38 ka (including the pra-Gorely cone-building stage and the ignimbrite series) being dacitic, whereas the material that forms the modern (younger than 38 ka) Gorely cone is nearly all basalt to basaltic-andesite in composition. Although this is the surficial expression of the Gorely

*Table 2: Major (wt%; normalized to 100%) and trace element (ppm) XRF compositions of Gorely eruptive products and a granite from the Akhomten Massif (*non-normalized total included)*

Sample no.	11G-21	11G-12	11G-23	07L-54	11G-24	11G-4	11G-20	11G-19
Age (Ma)	MG	MG	MG	MG	MG	MG	MG	MG
SiO_2	57.1	53.6	54.7	64.6	56.7	56.2	55.0	52.1
TiO_2	1.13	0.78	1.24	1.02	1.12	1.35	1.16	1.11
Al_2O_3	16.7	17.0	16.8	15.4	16.4	15.4	17.1	18.7
FeO^T	8.10	8.51	9.37	5.50	8.29	9.05	8.26	8.96
MnO	0.16	0.17	0.16	0.13	0.16	0.17	0.16	0.16
MgO	4.00	6.70	4.67	1.59	4.55	4.89	4.79	5.59
CaO	7.05	9.59	7.83	3.95	6.92	6.78	7.95	8.81
Na_2O	3.55	2.64	3.24	4.26	3.54	3.43	3.35	3.16
K_2O	1.88	0.80	1.60	3.19	1.96	2.23	1.73	1.03
P_2O_5	0.38	0.13	0.41	0.36	0.39	0.49	0.41	0.32
*Total	98.90	99.90	98.00	98.90	99.00	99.30	97.60	96.90
Ni	31	34	38	4	42	56	51	56
Cr	53	93	75	5	96	125	117	119
Sc	26	35	28	17	25	27	27	28
V	206	235	241	99	198	231	209	233
Ba	514	240	492	794	539	574	468	328
Rb	36	15	30	64	36	44	32	17
Sr	411	379	432	307	425	366	441	479
Zr	189	75	181	290	197	236	182	120
Y	32	20	34	40	33	39	32	25
Nb	6.3	2.0	6.2	7.9	6.2	7.9	6.2	3.9
Ga	17	17	17	18	18	16	18	18
Cu	69	90	72	13	61	112	98	90
Zn	82	85	90	72	82	94	78	74
Pb	9	6	5	13	9	11	8	5
La	15	5	18	24	17	21	11	13
Ce	41	13	42	52	38	52	33	33
Th	3	1	3	5	3	3	2	2
Nd	25	13	26	31	24	30	25	19
U	2	1	0	3	0	2	2	0

Abbreviations: MG, modern Gorely; PG, pra-Gorely; I, ignimbrite; ages with a specific value are from $^{40}Ar/^{39}Ar$ dating

magmatism, an older, small volume of basalt from previous Gorely eruptions could be buried.

Table 2 continued

Sample no.	11G-7	11G-13	11G-14	11G-17	11G-18	11G-10	11G-8	11G-9
Age (Ma)	MG	MG	MG	MG	MG	MG	MG	MG
SiO_2	54.2	56.5	65.8	56.2	55.1	62.8	52.8	54.0
TiO_2	1.08	1.03	1.02	1.11	1.05	1.15	1.07	1.03
Al_2O_3	18.6	17.6	15.0	16.6	18.1	15.8	18.5	19.2
FeO^T	8.13	7.63	5.20	8.33	8.06	6.22	8.92	8.61
MnO	0.15	0.15	0.13	0.16	0.16	0.15	0.16	0.17
MgO	4.30	4.10	1.42	4.64	4.70	1.94	5.43	3.59
CaO	8.50	7.32	3.41	7.10	7.47	4.55	8.56	8.63
Na_2O	3.41	3.60	4.27	3.53	3.42	4.35	3.15	3.29
K_2O	1.32	1.79	3.43	1.87	1.56	2.66	1.08	1.23
P_2O_5	0.37	0.35	0.36	0.38	0.36	0.33	0.32	0.30
*Total	97.20	99.00	98.10	98.90	97.40	98.00	96.50	96.30
Ni	28	37	4	44	50	4	54	19
Cr	53	80	6	94	99	4	96	47
Sc	26	22	16	25	24	20	26	27
V	212	172	86	192	183	125	218	218
Ba	462	505	834	530	463	730	393	427
Rb	22	32	69	35	27	49	19	23
Sr	550	469	264	444	468	358	511	491
Zr	139	185	311	191	173	262	122	132
Y	25	31	42	33	31	39	24	25
Nb	4.5	5.9	8.4	5.9	5.9	7.8	3.8	5.0
Ga	19	19	17	17	18	17	18	17
Cu	69	36	13	59	84	28	82	68
Zn	76	74	72	81	84	86	82	71
Pb	6	7	15	8	8	12	5	6
La	17	16	22	19	17	21	12	11
Ce	35	39	59	39	35	48	29	26
Th	2	2	6	4	2	4	2	2
Nd	23	25	31	25	23	28	20	17
U	1	0	3	3	1	1	0	0

In addition to analyzing Gorely rocks, we also studied the eruptive products of nearby silicic centers to confirm that our samples are sourced from Gorely volcano, which is possible because of the strong across arc geochemical zonation in Kamchatka (Ponomareva et al., 2007). It is of particular importance to note the differences in chemical composition between the Gorely ignimbrites, which are all similar to one another (e.g., Fig. 7c), and the material erupted from Mutnovsky. This is important

Table 2 continued

Sample no.	11G-5	07L-53	11G-3	77L-144	11G-15	11G-16	11G-6	125L-2000
Age (Ma)	MG	I	I	I	PG	PG	PG	I
SiO_2	52.1	64.7	66.9	63.7	68.2	61.2	65.1	65.8
TiO_2	1.32	1.06	0.80	1.00	0.91	1.44	1.00	1.11
Al_2O_3	17.1	16.4	15.7	16.6	15.1	15.2	16.2	15.5
FeO^T	9.94	4.61	3.98	5.22	3.73	7.70	4.49	4.85
MnO	0.18	0.17	0.11	0.16	0.14	0.19	0.15	0.17
MgO	4.91	1.49	1.25	1.68	0.89	2.01	1.41	1.34
CaO	9.77	3.51	3.08	4.13	2.30	4.58	3.53	3.04
Na_2O	3.31	5.30	4.78	4.96	5.22	4.55	5.19	5.05
K_2O	1.01	2.53	3.20	2.29	3.27	2.52	2.66	2.90
P_2O_5	0.41	0.23	0.23	0.31	0.21	0.59	0.32	0.26
*Total	99.2	98.1	94.8	99.3	98.1	98.5	98.8	98.47
Ni	19	3	5	6	3	4	2	5
Cr	42	7	5	4	3	3	3	5
Sc	36	17	14	18	15	24	16	18
V	320	49	75	96	36	129	51	61
Ba	410	752	767	671	895	727	732	836
Rb	14	43	52	37	59	45	46	51
Sr	604	384	249	362	241	348	342	297
Zr	113	251	295	246	326	258	263	295
Y	27	43	39	41	51	48	43	48
Nb	6	9	10	8	10	9	8	10
Ga	19	18	16	19	18	19	19	18
Cu	104	2	15	18	3	14	3	6
Zn	91	95	63	84	80	106	78	93
Pb	5	11	14	10	15	11	10	13
La	14	23	21	19	28	27	26	27
Ce	29	55	52	47	61	57	52	60
Th	1	3	4	4	4	3	3	4
Nd	22	32	26	27	37	34	32	35
U	0	1	1	2	2	2	1	1

because the ignimbrites collected from Opasny Canyon, which is located near Mutnovsky volcano, were in fact erupted from Gorely (Fig. 2). Gorely magmas are predominantly calc-alkaline in an AFM diagram and follow the boundary between tholeiitic and calc-alkaline series. Figure 7 demonstrates across-arc geochemical changes from the volcanic front (Mutnovsky) to Gorely, and then Opala in the rear arc of the Kamchatkan subduction zone (Fig. 1). This may be due to the increased depth of the subducting slab and decreasing degree of mantle melting (Walker et al., 1995; Ishikawa & Tera, 1997;

Table 2 continued

Sample no.	109L-2010	11G-1	11G-2	108L-2010	107L-2010	2005L-19	89L-9[c]
Age (Ma)	0.227	I	I	0.324	0.332	0.361[a]	11.2[b]
SiO_2	63.3	68.1	67.1	62.1	66.2	65.6	74.3
TiO_2	1.10	0.93	0.99	1.21	0.91	0.94	0.30
Al_2O_3	16.6	15.3	15.7	16.6	16.2	16.2	13.3
FeO^T	5.49	3.86	4.11	5.81	4.14	4.21	2.09
MnO	0.18	0.13	0.12	0.19	0.15	0.16	0.60
MgO	1.67	0.78	0.80	1.81	0.88	1.26	0.04
CaO	3.97	2.21	2.39	4.47	2.93	3.24	1.72
Na_2O	4.87	5.20	4.94	4.99	5.35	5.36	4.48
K_2O	2.41	3.27	3.57	2.23	2.93	2.69	3.15
P_2O_5	0.40	0.21	0.24	0.52	0.26	0.27	0.06
*Total	97.4	98.1	98.1	100	98.9	99.5	99.99
Ni	4	6	6	3	4	0	1
Cr	3	5	4	4	4	2	9
Sc	19	16	17	21	17	17	7
V	70	40	47	89	46	45	41
Ba	597	902	874	679	795	783	1061
Rb	38	56	64	34	57	47	109
Sr	348	242	265	432	323	348	156
Zr	223	326	313	222	275	270	172
Y	45	55	48	43	47	48	22
Nb	8	10	11	8	9	8	4
Ga	19	17	18	19	19	18	13
Cu	8	12	13	10	6	4	12
Zn	97	82	83	105	87	81	33
Pb	9	16	14	12	14	10	13
La	21	28	26	21	24	23	15
Ce	48	67	66	54	58	55	28
Th	3	4	5	4	4	3	9
Nd	30	39	36	34	37	33	7
U	0	1	2	0	1	1	3

[a]Data from Bindeman et al. (2010)

[b]U-Pb age

[c]89L-9 is a fine-grained granodiorite of the Akhomten Massif

Taylor & Nesbitt, 1998; Churikova et al., 2001; Hochstaedter et al., 2001). Mutnovsky magmas in the volcanic front are more depleted in K_2O relative to Gorely (Fig. 7c), whereas Opala magmas from the back-arc have similar K_2O contents to Gorely; Karymshina magmas have a wider range in K_2O. Gorely dacites have slightly elevated

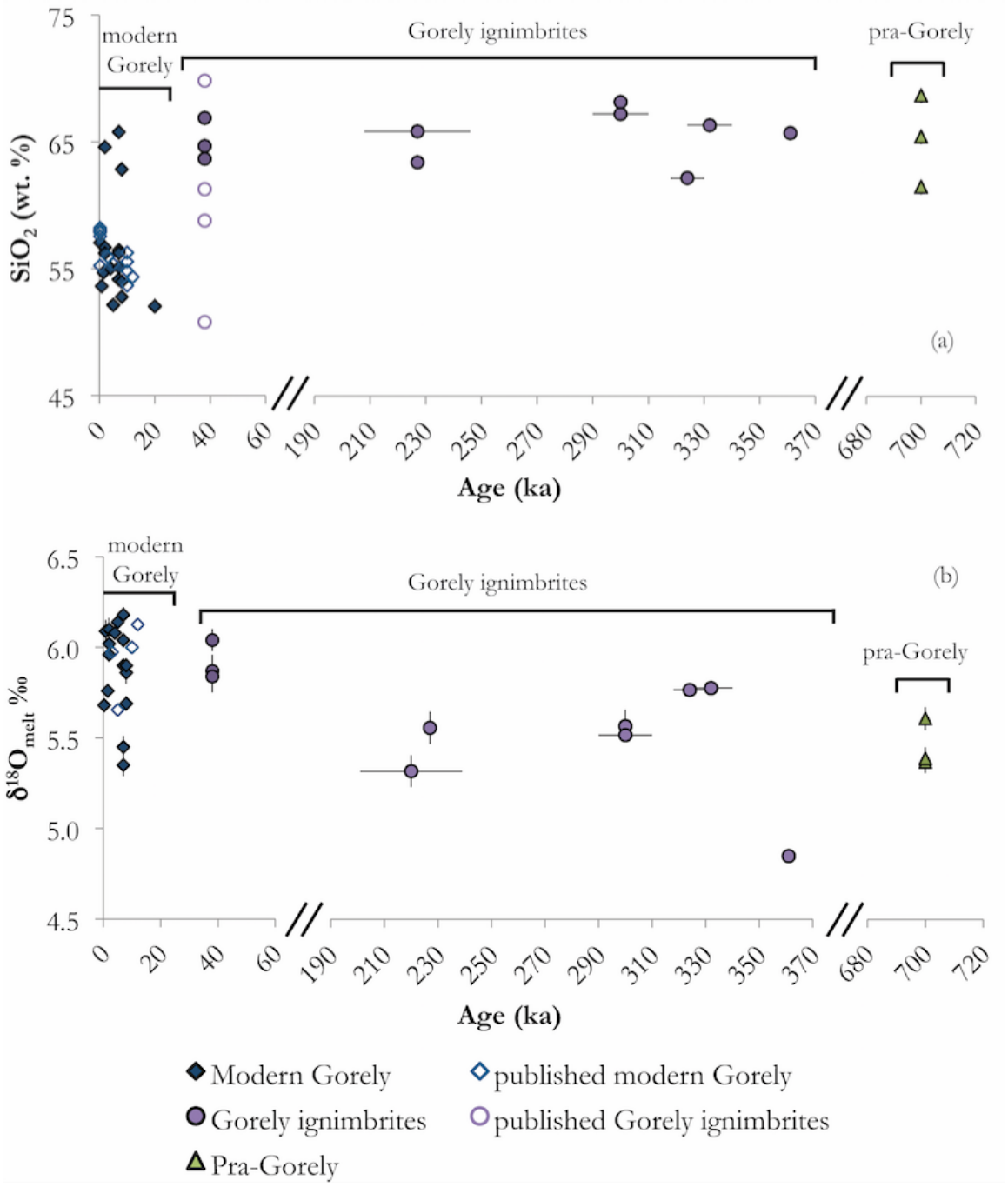

Figure 5. Temporal evolution trends for Gorely magmas. a) Age vs. SiO_2 wt.% (±2σ). b) Age vs. $\delta^{18}O_{melt}$ (±1 st. err.). Four dated ignimbrites are shown (109L-2010 (227 ka), 108L-2010 (324 ka), 107L-2010 (332 ka), 2005L-19 (361 ka)). All other ages are based on stratigraphic order or associations with other units (Table 1). Published Gorely ignimbrite data (SiO_2) are from Duggen et al. (2007), and the age for ignimbrite 2005L-19 (361 ka) is from Bindeman et al. (2010). Note the break in time between pra-Gorely and the early ignimbrite series, and between the old and young ignimbrites.

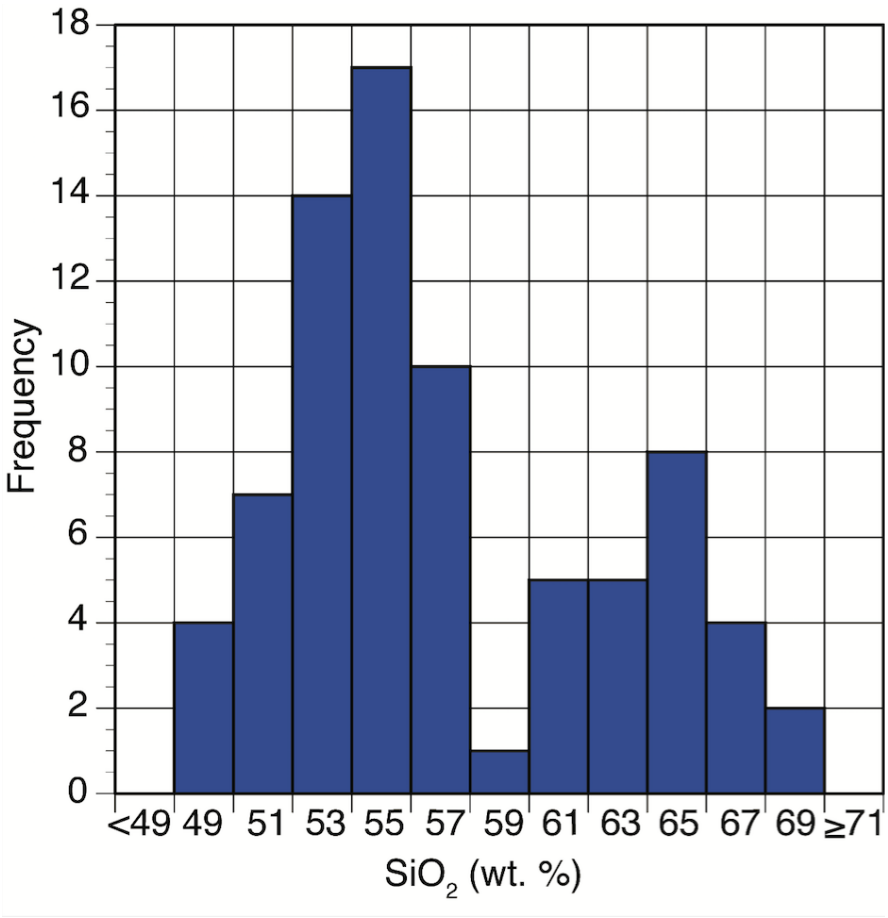

Figure 6. Histogram of SiO_2 (wt. %) for all Gorely units, including data from the literature (including the GEOROC database (http://georoc.mpch-mainz.gwdg.de/georoc/)). Each bin is labeled with the lower SiO_2 wt.% value, and spans 2 wt.% SiO_2. The histogram shows the bimodality of the rock compositions from Gorely volcano, displaying a clear Daly Gap. Data are from this work and: Chashchin et al. (2011); Duggen et al. (2007); Kepezhinskas et al. (1997); Pineau et al. (1999); Ishikawa et al. (2001); Popolitov & Volynets (1981).

Na_2O concentrations relative to Mutnovsky, Opala, and Karymshina products (Fig. 7b), whereas more mafic materials from these eruptive centers generally have the same Na_2O concentration. In contrast, Gorely magmas have CaO concentrations that are lower than Mutnovsky, Opala, and Karymshina (Fig. 7a). In terms of P_2O_5 wt.%, nearly all the Gorely magmas have a higher P_2O_5 concentration (peaking at ~60 wt.% SiO_2) than material erupted from Opala, Mutnovsky, and Karymshina volcanoes (Fig. 7d). Additional major element variation diagrams are included in Supplementary Data Fig. A3.

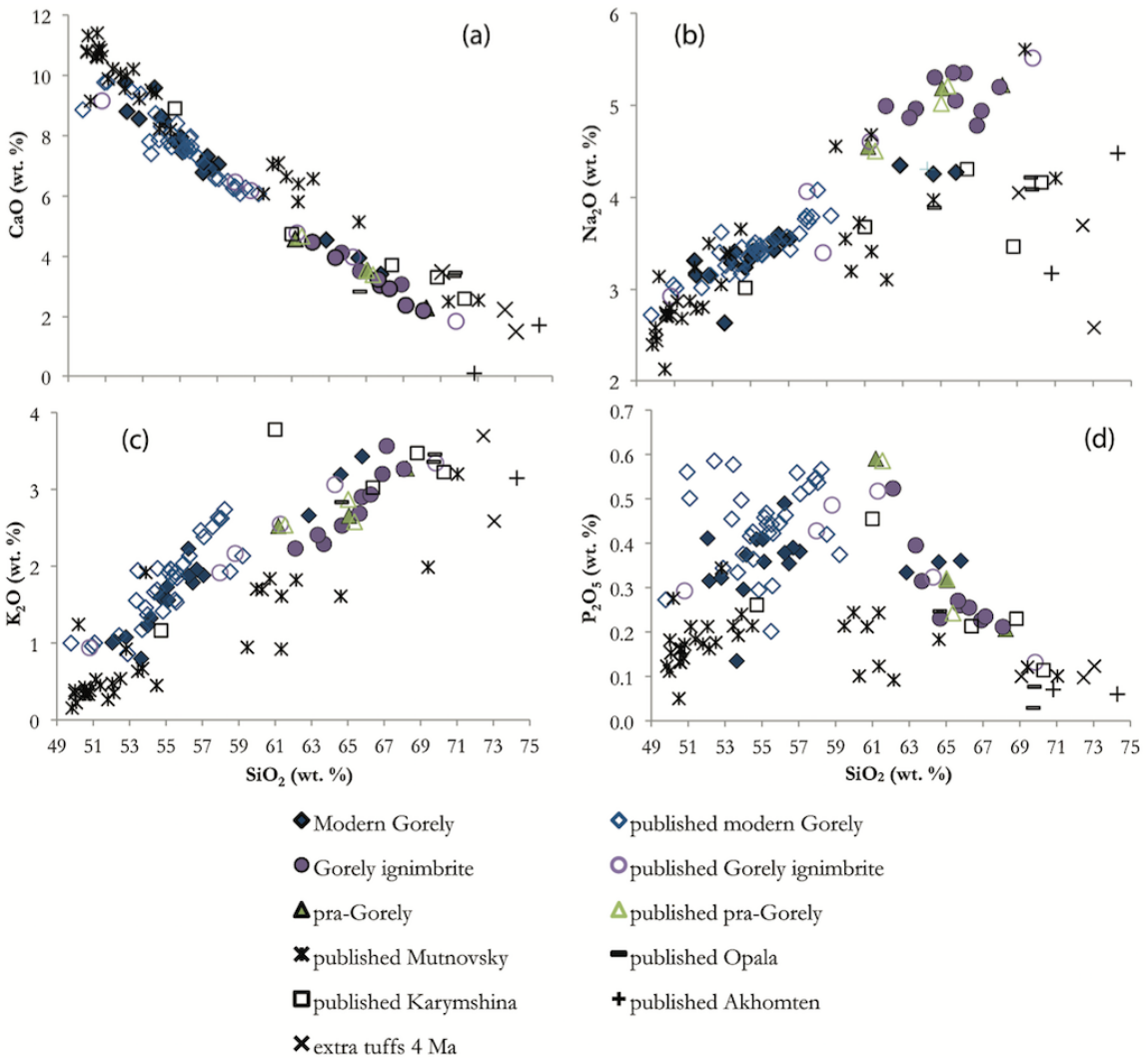

Figure 7. Major element compositional variations that distinguish Gorely magmas from nearby volcanic centers (Mutnovsky, Opala, Karymshina, and nearby 4 Ma tuffs – see Figs. 1–2). Gorely data are from this study and those listed in the caption to Fig. 5. Karymshina data are from Shipley (2011); Mutnovsky data are from Duggen et al. (2007); Bindeman et al. (2004); Kepezhinskas et al. (1997); Hochstaedter et al. (1996); Pineau et al. (1999); Poplitov & Volynets (1991); Opala data are from Bindeman et al. (2004).

Petrography of the erupted products

The petrography of fourteen representative Gorely units: eight ignimbrites and six lavas is summarized in Table 3.

Table 3: Thin section petrography of the Gorely eruptive products[a]

Sample no.	77L-144	11G-2	107L-2010	07L-53	11G-21	11G-14	11G-6
Rock Type	ignimbrite	ignimbrite	ignimbrite	ignimbrite	bomb	lava	lava
plagioclase	9%	7%	5%	11%	5%	6%	2%
opx	5%	5%	2%	3%	3%	4%	3%
cpx	2%	5%	1%	7%	5%	7%	2%
glass	25%	20%	30%	10%	0%	0%	0%
vesicles	12%	10%	5%	5%	40%	2%	0%
groundmass	58%	62%	61%	66%	85%	81%	89%
olivine	0%	0%	0%	0%	2%	0%	0%
amphibole	0%	0%	0%	0%	0%	0%	1%
magnetite	1%	1%	1%	3%	0%	2%	3%
mineral abundance	17%	18%	9%	24%	15%	19%	11%
crystals in clusters	3%	5%	1%	5%	3%	7%	5%
approximate grain size (mm)	1–2	0.5–2	0.5–2	1–2	0.5–2	0.5–2	1–2
mafic enclaves	yes	yes	yes	yes	no	yes	no
plagioclase zoning	N/R	R	N/R	N/R	N/R	N/R	N/R
sieve texture*	X		X		X		

[a]mineral abundances were determined by taking all the minerals of each type in the field of view (i.e. plagioclase, opx, cpx) and visually clustering them into a corner of the field of view and approximating the percent of the field of view that mineral covers. This was done at least 15 times for each thin section, and the percentage for each mineral was averaged for that unit.

*'X' signifies a greater amount of the texture and includes both plagioclase and pyroxene minerals, 'N' = normal zoning, 'R' = reverse zoning

'opx' = orthopyroxene, 'cpx' = clinopyroxene

Ignimbrites

Phenocrysts in all units include plagioclase + orthopyroxene + clinopyroxene + magnetite ± apatite. Plagioclase abundance in the ignimbrite units ranges from 5–11 %, while pyroxene ranges from 3–10 % (both are ~0.5–6 mm in length). Groundmass, glass, and vesicle abundance ranges from 58–81 %, 5–30 %, and 1–20 % respectively. Ignimbrite units typically have a groundmass that is variable on a thin section scale: with both devitrified and glassy varieties, colors ranging from gray to black, and some clasts containing abundant plagioclase microlites (Supplementary Data: Fig. A4). Many ignimbrites contain sieve-textured plagioclase and pyroxene grains, indicating resorption, with unit 125L-2010 having the largest proportion of euhedral grains. The youngest and oldest ignimbrite units do not differ markedly in terms of their petrography. Six of the

Table 3 continued

Sample no.	109L-2010	108L-2010	07L-54	11G-13	11G-24	2005L-19	125L-2000
Rock Type	ignimbrite	ignimbrite	lava	lava	lava	ignimbrite	ignimbrite
plagioclase	5%	4%	7%	17%	7%	6%	5%
opx	2%	2%	3%	5%	3%	3%	4%
cpx	1%	1%	7%	5%	4%	5%	3%
glass	10%	10%	0%	0%	0%	5%	5%
vesicles	1%	20%	0%	60%	35%	10%	1%
groundmass	80%	81%	80%	70%	82%	80%	81%
olivine	0%	0%	0%	3%	4%	0%	0%
amphibole	0%	0%	0%	0%	0%	0%	0%
magnetite	2%	2%	3%	0%	0%	1%	2%
mineral abundance	10%	9%	20%	30%	18%	15%	14%
crystals in clusters	0%	0%	5%	1%	1%	3%	25%
approximate grain size (mm)	0.5–1	0.5–2	0.5–2	0.5	0.5–2	0.5–2	0.5–4
mafic enclaves	significant amount	significant amount	no	no	no	yes	yes
plagioclase zoning	N/R	N/R	N/R	R	N/R	N/R	N/R
sieve texture*	trace	X		X	X	X	

*'X' signifies a greater amount of the texture and includes both plagioclase and pyroxene minerals, 'N' = normal zoning, 'R' = reverse zoning
'opx' = orthopyroxene, 'cpx' = clinopyroxene

eight ignimbrites contain glomeroporphyritic aggregates of plagioclase, clinopyroxene, and orthopyroxene. The minerals in these clusters are not elongated and, therefore, do not indicate crystal compaction prior to eruption. The volume of glomeroporphyritic aggregates ranges from 1–25 % (SD: Fig. A5). The degree of resorption of crystals in glomerocrysts is variable, with the most resorption in unit 07L-53, whereas units 125L-2000 and 11G-2 contain many large crystal clusters without much resorption.

All ignimbrites contain small mafic enclaves (SD: Fig. A6), ranging in size from ~1 mm up to ~1 cm in diameter, with most being around 2 mm. The enclaves are oval in shape (Fig. SD: A6), with a groundmass of plagioclase microlites. The plagioclase and pyroxene phenocrysts within the enclaves are predominantly euhedral, although in unit 77L-144 they are mostly resorbed.

Lavas

All lava units contain the same phenocryst assemblage of plagioclase + clinopyroxene + orthopyroxene + magnetite ± apatite, of which 1–7 % is contained in glomeroporphyritic aggregates. Unlike the ignimbrite units, some of the lava units also contain olivine (modern Gorely: 11G-13, 11G-21, 11G-24) and amphibole (pra-Gorely: 11G-6) phenocrysts. The abundance of plagioclase and pyroxene ranges from 2–17 % and 5–11 % respectively, ranging in size from ~0.5–3 mm in length. In comparison to the ignimbrites, the lavas have slightly larger amounts of plagioclase, although the range in pyroxene abundance is similar between the two. Groundmass and vesicle abundances range from 70–89 % and 0–60 % respectively, with no units containing pristine glass (Table 3). The groundmass varies from abundant plagioclase microlites to devitrified glass. Some units show evidence of resorption in their phenocrysts, with 11G-21, 11G-24, and 11G-13 (all modern Gorely units) showing the most resorption.

All the units contain crystal clusters (1–7 %) of plagioclase, clinopyroxene, and orthopyroxene. The degree of resorption in the glomerocrysts varies from unit to unit. Only one lava (11G-14; modern Gorely) contains mafic enclaves (~2 mm wide and 3–4 mm long) in a groundmass of plagioclase microlites and rare plagioclase and pyroxene crystals (~0.5–2 mm).

Trace element variations

Trace elements show separate trends between the andesites-dacites and the basalts-basaltic andesites in terms of K_2O, Rb, Ba, and Sr concentrations at constant SiO_2 (Fig. 8–9). Although the relative incompatibility and subsequent concentration of K_2O, Rb, and Ba will vary based on the crystalizing assemblage, offsets of this magnitude cannot be produced from closed-system fractional crystallization. The entire ignimbrite series falls on the same trends, signifying a common parental melt or source rock under Gorely for all the ignimbrites in this study. Figure 9 shows the trace element trends with respect to Zr. Zirconium should be a highly incompatible element in the zircon-undersaturated Gorely magmas. Although the trends are less clear in Figure 9, the offset is still obvious

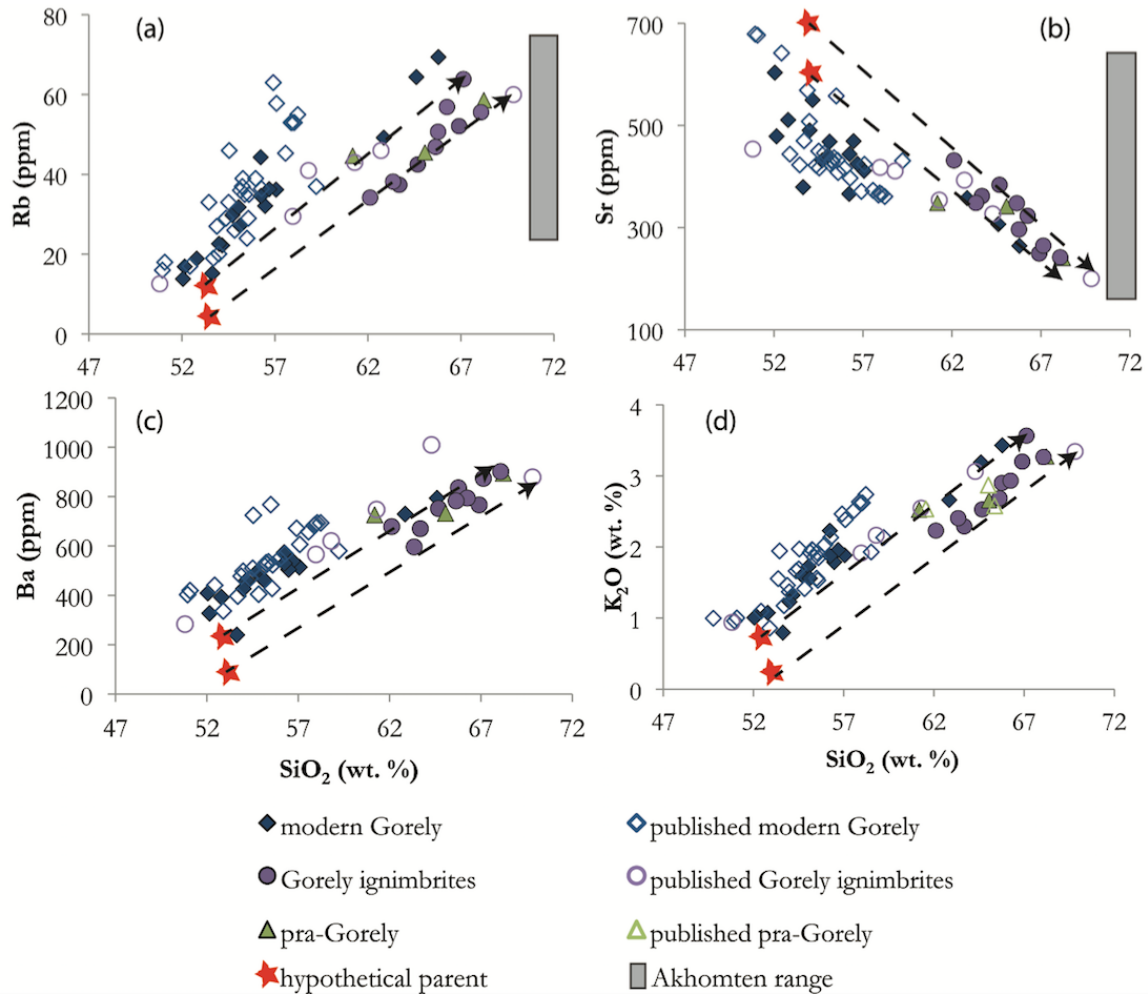

Figure 8. Harker variation diagrams showing two separate trends for basic (49–59 wt.% SiO_2) and silicic (62–69 wt.% SiO_2) sub-groups of rocks. If fractional crystallization were the only process occurring, K_2O, Rb, Ba, and Sr should all follow smooth and continuous trends, which is not shown here. Dashed arrows indicate possible fractionation trends from a hypothetical parent (indicated by yellow star) that is different from the parent of the basalt-basaltic andesites. Error bars denote 2σ, but are smaller than the symbol size. Data for Gorely are from this study and those listed in the Figure 5 caption. Data for the range in the Akhomten Massif compositions are from this study and Vinogradov (1995).

in the Rb and Ba plots. Overall, these elemental trends clearly illustrate that fractional crystallization of basalt at one or multiple depths (see below) is incapable of explaining the extended magmatic series of Gorely to produce the dacites.

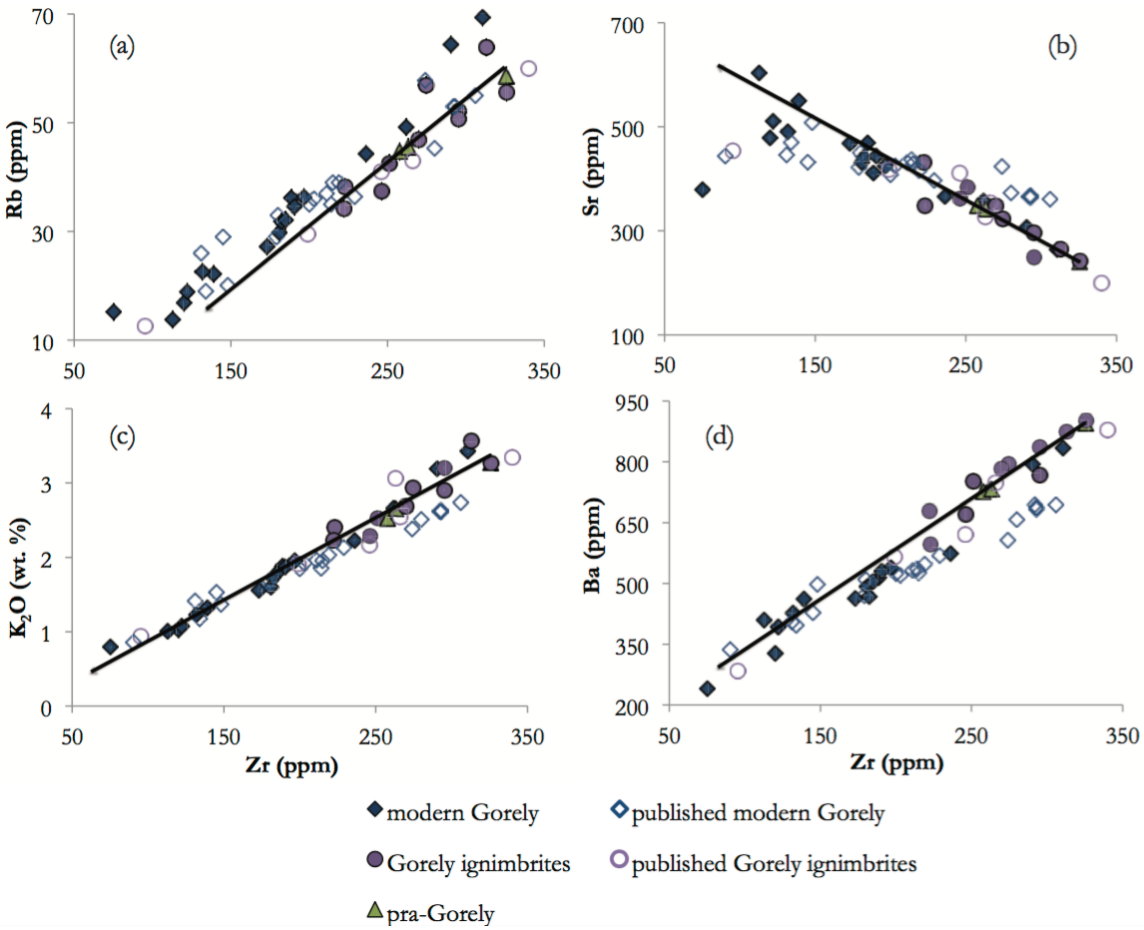

Figure 9. Similar variation diagrams to Figure 8, but with Zr on the x-axis, which is an incompatible trace element in the zircon undersaturated Gorely magmas. The black arrow on each graph is a linear trend for the Gorely dacites, which points back to a possible initial source if a consistent fractionating trend is occurring. The trend is not as clear as is shown in Figure 7, but Rb and Ba still show a clear offset from the Gorely basalts. Error bars denote 2σ, but are smaller than the symbol size. Data are from this study and: Duggeen et al. (2007); Kepezhinskas et al. (1997); Ishikawa et al. (2001).

Pyroxene and plagioclase chemistry

Gorely ignimbrites contain both clinopyroxene and orthopyroxene, both of which are largely unzoned (Table 4; Supplementary Data Fig. A7). Pyroxene chemistry does not appear to vary consistently between grains and those that are contained within aggregates. The presence of xenocrysts in the orthopyroxenes from 11G-2 is suggested by the larger variation, although there is no significant variability between the cores and rims of these pyroxene grains. Plagioclase in the Gorely ignimbrites ranges from An_{35}–

Table 4: Pyroxene mineral chemistry

	Notes	cpx/opx	n analyses	SiO_2	TiO_2	Al_2O_3	FeO*	MnO	MgO	CaO	Na_2O	K_2O	Cr_2O_3	P_2O_5
109L-2010	s.c	opx	2	53.0	0.24	0.50	18.4	1.57	23.9	1.50	0.07	0.01	0.01	0.00
	s.c	opx	2	53.5	0.3	0.6	17.3	1.0	24.9	1.8	0.0	0.0	0.0	0.0
	s.c	cpx	2	51.2	0.7	2.6	8.4	0.3	15.5	21.8	0.4	0.0	0.0	0.1
	s.c	cpx	2	51.3	0.6	1.6	9.8	0.9	14.6	21.5	0.4	0.0	0.0	0.1
	s.c	cpx	2	51.7	0.6	1.8	9.1	0.6	15.3	20.4	0.4	0.0	0.0	0.1
125L-2000	s.c	opx	2	53.1	0.3	0.3	17.5	1.4	24.4	1.6	0.0	0.0	0.0	0.0
	s.c	opx	2	53.0	0.3	0.7	17.5	1.4	23.7	1.7	0.0	0.0	0.0	0.0
	s.c	opx	2	53.0	0.4	0.8	18.0	1.4	24.3	1.6	0.0	0.0	0.0	0.0
	s.c	opx	2	53.3	0.3	0.8	18.0	1.3	24.4	1.7	0.0	0.0	0.0	0.0
	s.c	cpx	2	51.9	0.5	1.4	8.6	0.8	15.0	21.8	0.4	0.0	0.0	0.1
77L-144	s.c	opx	2	53.4	0.3	0.7	18.0	1.6	24.5	1.4	0.0	0.0	0.0	0.0
	agg. 1	opx	2	53.0	0.5	1.5	16.6	0.9	25.1	2.0	0.0	0.0	0.0	0.0
	agg. 2	opx	2	53.4	0.3	0.6	18.2	1.5	24.3	1.4	0.0	0.0	0.0	0.0
	s.c	opx	2	53.6	0.2	0.5	18.0	1.0	24.4	1.4	0.0	0.0	0.0	0.0
11G-2	s.c	opx	2	53.4	0.3	1.0	17.4	0.9	24.9	1.8	0.0	0.0	0.0	0.0
	agg. 1	opx	2	51.9	0.5	0.9	22.1	0.9	21.0	2.1	0.0	0.0	0.0	0.0
	s.c	cpx	2	52.3	0.5	1.4	9.2	0.8	15.5	20.3	0.4	0.0	0.0	0.1
	agg. 1	cpx	2	52.1	0.6	1.4	9.2	0.8	15.0	20.9	0.4	0.0	0.0	0.1
108L-2010	m.e.	opx	2	53.2	0.2	0.8	18.1	1.3	24.0	1.5	0.0	0.0	0.0	0.0
	s.c	cpx	2	52.0	0.5	1.4	10.6	0.9	14.2	20.1	0.4	0.0	0.0	0.1
	s.c	cpx	2	51.3	0.7	2.4	8.9	0.4	15.5	20.1	0.3	0.0	0.0	0.1
107L-2010	s.c	opx	2	53.9	0.3	0.7	16.6	1.4	25.6	1.4	0.0	0.0	0.0	0.0
	s.c	opx	2	54.2	0.3	0.7	16.5	1.4	25.9	1.4	0.0	0.0	0.0	0.0
	s.c	opx	2	53.4	0.3	0.9	16.8	1.6	25.1	1.5	0.0	0.0	0.0	0.0
	s.c	cpx	2	52.1	0.4	1.3	10.4	0.9	14.5	20.1	0.3	0.0	0.0	0.1

*s.c.=single crystal; agg.=aggregate; m.e.=mafic enclave; opx=orthopyroxene; cpx=clinopyroxene

An_{48}. One plagioclase aggregate was analyzed, and is towards the higher end of An content for Gorely ignimbrites (Table 5).

Isotopic variations

$\delta^{18}O$ values of co-existing plagioclase and pyroxene grains as well as groundmass samples were determined for all units, and these were used to calculate the melt $\delta^{18}O$ values (Table 6). $\delta^{18}O_{plag}$ values range from 4.53–6.18 ‰, and the $\delta^{18}O_{melt}$ values from 4.85–6.41 ‰ (Table 6). This is a fairly wide range for any single arc volcano, with values ranging from normal $\delta^{18}O$ (between ~5.5–6.5 ‰), which could be produced by fractional crystallization of a mantle-derived basalt, to distinctly low-$\delta^{18}O$ (<5.7 ‰), which requires assimilation of moderate amounts of low $\delta^{18}O$ hydrothermally altered material. The low $\delta^{18}O$ values characterize both silicic and mafic units. These units are spaced somewhat randomly throughout the evolution of the Gorely eruptive center, with two being from the "pra-Gorely" stage ~0.7 Ma (11G-6 and 11G-16), two erupting during the early ignimbrite eruptions at 0.361 and 0.220 Ma (2005 L-19 and 125L-2010 respectively), and the last two being from the modern Gorely stage (11G-17 and 11G-18).

These $\delta^{18}O$ variations through time are shown in Figure 5b, where there is a small range in $\delta^{18}O_{melt}$ during the pra-Gorely stage of cone-building (the cone present prior to the earliest known caldera-forming eruptions). The range in $\delta^{18}O_{melt}$ (4.85–5.78 ‰) is then at its largest in the early ignimbrite series of eruptions, while also containing the lowest $\delta^{18}O_{melt}$ value (4.85 ‰). The range then decreases significantly (with only normal $\delta^{18}O_{melt}$ values) during the younger ignimbrite series at 38 ka (Fig. 5b). The modern Gorely series of eruptions (younger than 38 ka) shows an increase in $\delta^{18}O_{melt}$ range (5.38–6.22 ‰).

The $^{87}Sr/^{86}Sr$ and $^{143}Nd/^{144}Nd$ compositions of major ignimbrites from the Gorely eruptive center display a range from 0.70328–0.70351 and from 0.51303–0.51309 respectively (Table 6). These ranges are higher ($^{87}Sr/^{86}Sr$) and lower ($^{143}Nd/^{144}Nd$) than average Kamchatkan mantle values (0.70275 and 0.51310, respectively) as reported by

Table 5: Plagioclase mineral chemistry

	Notes	An Content	SiO_2	TiO_2	Al_2O_3	FeO	MnO	MgO	CaO	Na_2O	K_2O	P_2O_5
109L-2010		42.2	57.1	0.07	26.9	0.49	0.00	0.05	8.02	7.05	0.32	0.03
125L-2000		43.4	57.6	0.05	26.7	0.49	0.00	0.05	8.50	6.92	0.44	0.02
77L-144		47.8	55.5	0.05	26.8	0.59	0.01	0.06	10.2	6.92	0.30	0.02
11G-2	aggregate	47.7	56.7	0.05	27.6	0.61	0.02	0.06	9.45	6.75	0.35	0.04
108L-2010		35.3	59.1	0.00	25.3	0.43	0.00	0.04	7.42	8.02	0.48	0.03
107L-2010		40.2	57.0	0.06	25.0	0.42	0.00	0.05	8.60	6.74	0.34	0.03

Duggen et al. (2007) based on hypothetical isotopic endmember estimates. These instead trend towards a crustal endmember, and overlap with other silicic rocks from the area (notably Akhomten and Karymshina; see discussion below) (Fig. 1).

Thermometry and barometry results

The $\delta^{18}O$ values of coexisting plagioclase and pyroxene were used to determine the magmatic temperature based on isotopic fractionation between $\delta^{18}O_{plag}$ and $\delta^{18}O_{pyx}$ using Chiba et al. (1989) A-factors (Fig. 10, Table 6). We used the known $\delta^{18}O$ of each mineral, and the measured anorthite content of the plagioclase, as A-factors change ~0.1 % per 10 % change in anorthite. Uncertainties for this method are based on the analytical error of the $\delta^{18}O$ analysis (2σ up to 0.15 ‰), the chosen anorthite content (discussed below), and the A-factor needed to determine the temperature of a given plagioclase-pyroxene fractionation (standard error of 0.09 from Chiba et al., 1989). The $\delta^{18}O$ analyses were conducted on multiple whole crystals, with weights ranging from 1–2 mg, and are therefore representative of the average for a batch of crystals. Pyroxenes do not exhibit significant compositional zoning, while plagioclase shows both normal and reverse zoning, with a variation of ~10 An units for all the ignimbrites analyzed.

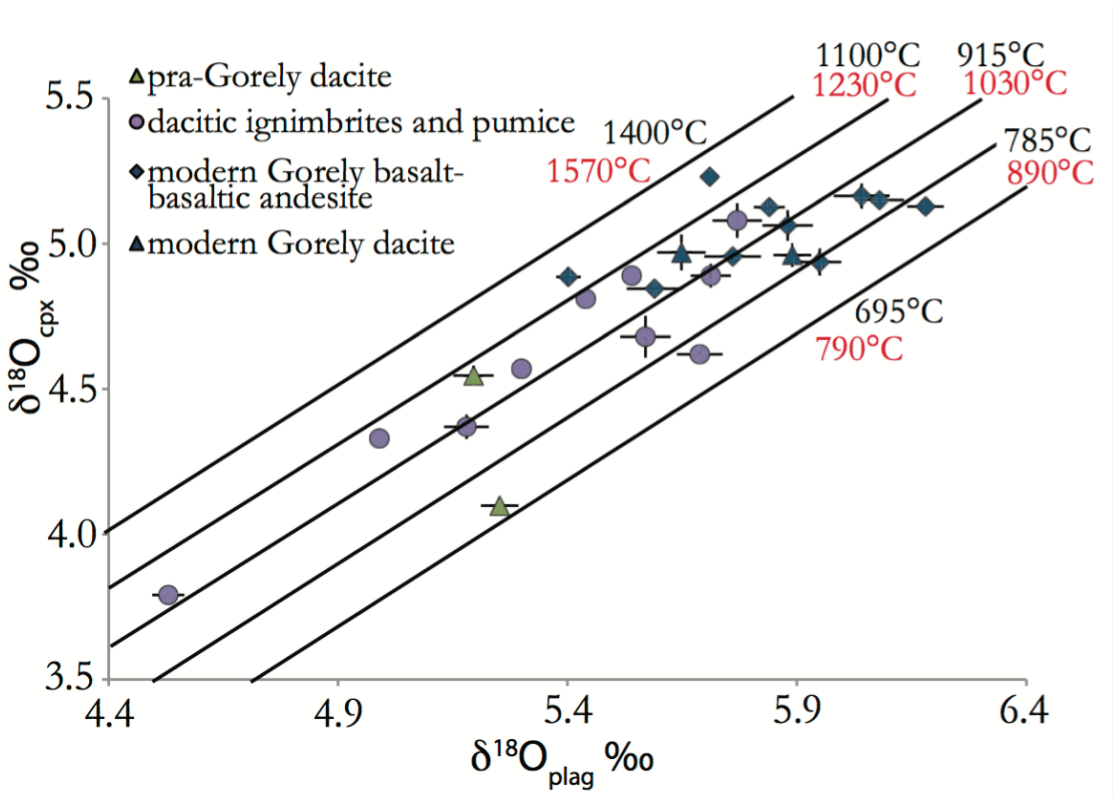

Figure 10. Variation of $\delta^{18}O_{plag}$ vs. $\delta^{18}O_{cpx}$ for the Gorely magmatic rocks (±2σ). Shown are $\Delta^{18}O_{plag\text{-}cpx}$ isotopic temperature ranges for basalts from modern Gorely (black) and dacites from both the ignimbrites and pra-Gorely (red), based on the isotope fractionation thermometer of Chiba et al. (1989), and using An_{43} (dacites) and An_{65} (basalts). Contours are calculated by holding the temperature and An content constant in the Chiba et al. (1989) thermometer and varying the $\Delta^{18}O_{plag\text{-}cpx}$; see text for discussion.

Temperatures were determined for modern Gorely basalt to basaltic andesite using an An_{65} plagioclase composition, which is the average An composition observed by Tolstykh et al. (2012) for basalt to basaltic andesites from the Gorely eruptive center. Temperatures for the dacites (pra-Gorely lavas and ignimbrites) were determined using An_{43}, based on the average An composition of plagioclase in the dacitic ignimbrites analyzed from this study, which is similar to that documented by Tolstykh et al. (2012). If the dacitic An content is decreased from An_{43} to An_{35} (the lowest An content determined here), this will cause an average increase in temperature of 44 °C, and if An_{48} is used (the highest An content found in this study) the temperature will decrease by an average of 26 °C. If the An content was increased by 10 to An_{75} or decreased by 10 to An_{55} for the

Table 6: Sr-Nd-O isotope compositions and thermometry results of Gorely eruptive products. $\delta^{18}O$ values are per mil deviations from VSMOW

Sample no.	$\delta^{18}O_{plag}$	2σ	$\delta^{18}O_{cpx}$	2σ	$\delta^{18}O_{gm}$	2σ	$\delta^{18}O_{melt}$ Plag[b]	s.e.
07L-53	5.57	0.10	4.68	0.08			6.41	0.09
07L-54	5.73	0.11					6.02	0.09
107L-2010	5.44	0.02	4.81	0.11			5.78	0.09
108L-2010	5.54	0.11	4.89	0.11			5.77	0.09
109L-2010	5.30	0.11	4.57	0.12			5.56	0.09
11G-1	5.18	0.07	4.37	0.05			5.57	0.06
11G-10	5.65	0.11	4.97	0.12			5.90	0.06
11G-12	6.09	0.13					6.09	0.06
11G-13	5.84	0.07	5.13	0.04			5.91	0.04
11G-14	5.89	0.08	4.96	0.08			6.22	0.04
11G-15	5.25	0.08	4.10	0.06			5.64	0.06
11G-16	5.20	0.09	4.55	0.07			5.40	0.06
11G-17	5.40	0.05	4.89	0.06			5.47	0.06
11G-18	5.71	0.02	5.23	0.05			5.38	0.06
11G-19	6.18	0.08	5.13	0.06			6.14	0.04
11G-2	5.19	0.09					5.55	0.06
11G-20	6.08	0.11	5.15	0.06			6.12	0.04
11G-21	5.59	0.12	4.85	0.05			5.68	0.04
11G-23	5.76	0.12	4.96	0.05			5.79	0.04
11G-24	5.88	0.11	5.06	0.11			5.96	0.40
11G-3a[a]	5.71	0.16	4.89	0.07			6.07	0.06
11G-3b[a]	5.69	0.12	4.62	0.06			6.04	0.06
11G-4	6.04	0.12	5.16	0.09			6.11	0.06
11G-5					5.9	0.10		
11G-6	5.10	0.02					5.41	0.06
11G-7	6.07	0.10					6.08	0.04
11G-8	5.71	0.11					5.69	0.04
11G-9	5.95	0.09	4.94	0.09			5.96	0.04
125L-2000	4.99	0.09	4.33	0.08			5.32	0.09
2005L-19	4.53	0.10	3.79	0.06			4.85	0.09
77L-144	5.77	0.08	5.08	0.09			5.84	0.09

[a]11G-3a and 11G-3b are two pumice clasts from the same eruption

[b]$\delta^{18}O_{melt}$ values were calculated from the pyroxene and plagioclase phenocryst $\delta^{18}O$ values based on known fractionation factors between the mineral and melt at known SiO_2 concentrations (Bindeman et al., 2004)

Table 6 continued

Sample no.	$\delta^{18}O_{melt}$ CPX[b]	s.e.	$\Delta^{18}O_{pyx\text{-}plag}$ temperature (°C)	$^{87}Sr/^{86}Sr$	2σ	$^{143}Nd/^{144}Nd$	2σ
07L-53	5.9	0.10	980				
107L-2010	6.13	0.10	1190	0.70328	0.00001	0.513046	0.00001
108L-2010	5.96	0.09	1190				
109L-2010	5.71	0.10	1100[c]	0.70332	0.00001	0.513074	0.00001
11G-1	5.80	0.10	1020[d]	0.70351	0.00001	0.513025	0.00001
11G-10	6.83	0.06	1150				
11G-13	5.85	0.06	1010				
11G-14	6.25	0.07	930				
11G-15	5.54	0.07	820				
11G-16	5.56	0.06	1130				
11G-17	5.60	0.06	1200				
11G-18	5.87	0.06	1250				
11G-19	5.59	0.07	760				
11G-20	5.79	0.06	820				
11G-21	5.61	0.06	975				
11G-23	5.57	0.07	910				
11G-24	5.80	0.06	900				
11G-3a[a]	6.25	0.06	1020				
11G-3b[a]	5.98	0.07	870				
11G-4	5.87	0.06	890				
11G-9	5.51	0.07	780				
125L-2000	5.62	0.10	1150				
2005L-19	5.07	0.07	1050	0.70343	0.00001	0.513093	0.00002
77L-144	6.24	0.10	1130	0.70335	0.00001	0.513035	0.00001

[a]11G-3a and 11G-3b are two pumice clasts from the same eruption

[b]$\delta^{18}O_{melt}$ values were calculated from the pyroxene and plagioclase phenocryst $\delta^{18}O$ values based on known fractionation factors between the mineral and melt at known SiO_2 concentrations (Bindeman et al., 2004)

[c]109L-2010 reported a 2-pyx (Putirka, 2008) temperature of 926 °C ± 5.2 (1 s.d.) based on 2 analyses

[d]11G-1 reported a 2-pyx (Putirka, 2008) temperature of 891 °C ± 8.0 (1 s.d.) based on 12 analyses

basalt to basaltic andesite samples, the temperature would decrease by an average of 59 °C or increase by an average of 58 °C, respectively.

Our $\delta^{18}O$ data nicely demonstrate that both plagioclase and pyroxene record a 1.7 ‰ range in $\delta^{18}O$ values at magmatic temperatures (Fig. 10), illustrating diverse $\delta^{18}O$ magma compositions. Using realistic An % and plagioclase-pyroxene A-factors, temperatures range from ~1230–780 °C, and we observe no particular distinction in temperature between magmas of diverse composition, nor age. The ignimbrites plot in a

magmatic range of temperatures from 1230–890°C, although the higher of these isotopic temperatures are unusually high for dacites (Fig. 10, Table 6).

We also used the two-pyroxene thermobarometer of Putirka (2008), which provides temperature and pressure uncertainties of ±56 °C and ±3.7 kbar respectively (Table 6). Pyroxene chemistry was determined on five ignimbrite units, but coexisting pyroxenes (orthopyroxene and clinopyroxene) were only found in four of them (Table 4). Unit 109L-2010 provided two temperatures that met the equilibrium requirement of a K_D (based on Fe-Mg exchange) between 0.95 and 1.23. The average temperature for 109L-2010 is 926 °C (±5 °C 1 st. dev.) at an average pressure of 5 kbar (±0.8). 107L-2010 yielded 11 temperature estimates, which average 891 °C (±8) at a pressure 6 kbar (±1.1). Both temperatures determined by pyroxene thermometry are over 100 °C lower than those determined by $\Delta^{18}O_{plag\text{-}pyx}$ (Table 6), which can be explained by disequilibrium between pyroxene and plagioclase grains.

DISCUSSION

Closed system fractional crystallization using MELTS

Shallow differentiation

MELTS (Ghiorso et al., 1995; Asimow & Ghiorso, 1998) modeling was conducted in an attempt to obtain the liquid line of descent for the Gorely magmas, and to test if it is possible to generate dacites through fractional crystallization of basalt (Figs. 11–12; Supplementary Data Table A3). A realistic water concentration for the parental basalt of ~1 wt.% was used, which provided the best fit. The starting composition chosen was based on a Gorely basalt from Duggen et al. (2007) (Supplementary Data Table A3). The major element composition was varied within reasonable limits (within ~10 %) until a best possible fit to the dacitic composition was found. MELTS modeling shows that only at shallow conditions (1 kbar, NNO oxygen fugacity) is a Gorely basalt broadly capable of producing the Gorely dacites, which requires 60–75 % fractionation and constitutes ~25–40 % of the original magma (Fig. 11). Even though our two-pyroxene data suggest

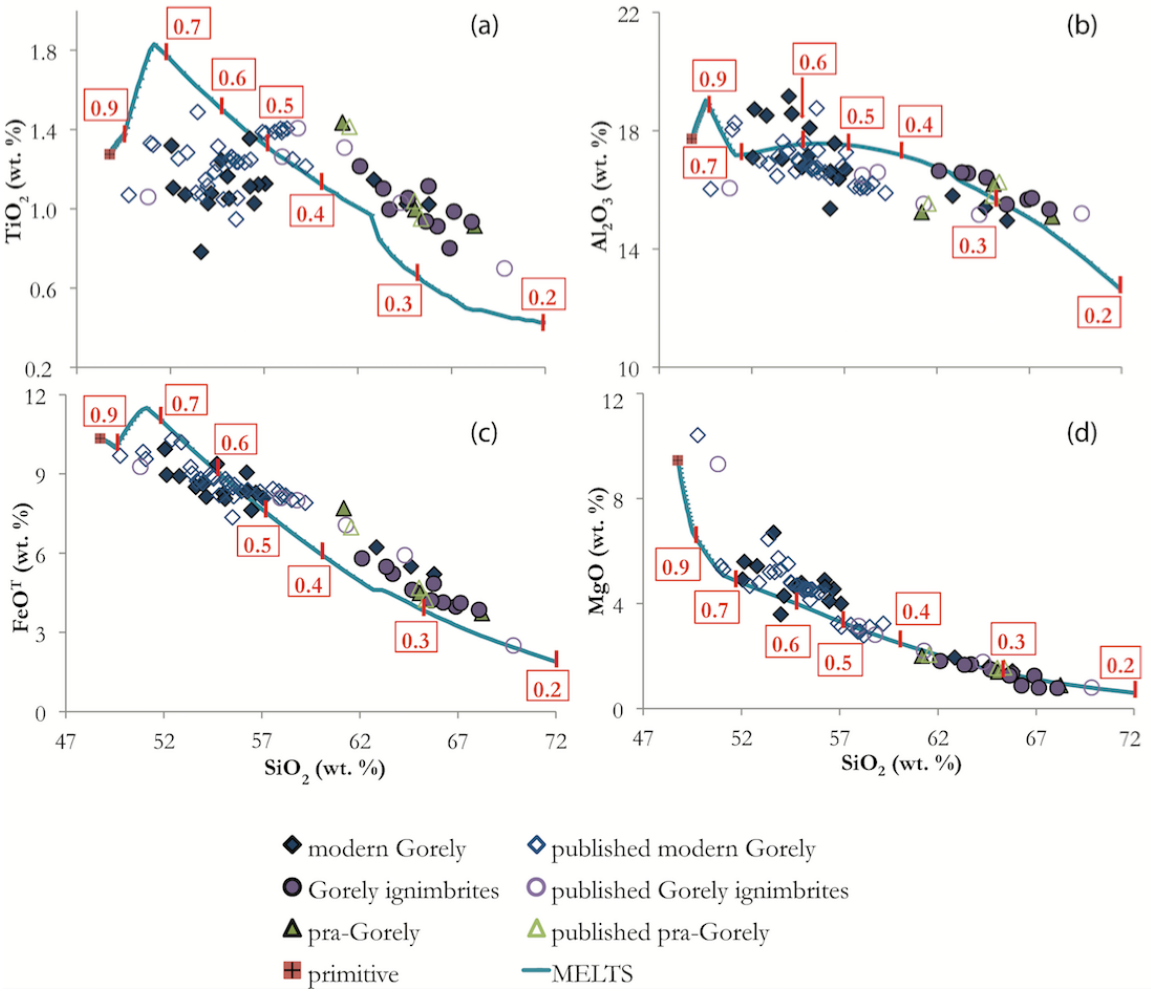

Figure 11 (continued on next page). Major element MELTS modeling of Gorely basaltic magmas to produce dacitic compositions through fractional crystallization. MELTS parameters are: 1 kbar pressure, NNO oxygen fugacity, and a liquidus temperature of ~1240 °C. The MELTS trends overlap with the evolved compositions reasonably well for most major oxides, except for offsets in TiO_2, P_2O_5, CaO, and the alkalis; see text for discussion. MELTS modeling at higher pressure (including two-stage modeling from 5–1 kbar) or lower oxygen fugacities does not fit the data (see Fig. 12). Data sources are listed in the Figure 5 caption.

differentiation at higher pressure, modeling at 5–6 kbar gave significantly different trends to that displayed by the Gorely magmas for most major elements (Fig. 12). Varying the oxygen fugacity to QFM and QFM+2 generated a slightly better fit to the data for some elements, but caused the trend to be very different for others (Fig. 12). Based on the best-fit conditions, MELTS yields a liquidus temperature of ~1240 °C. However, even though a 'best-run' MELTS model, the model trends do not fit the Gorely data perfectly for

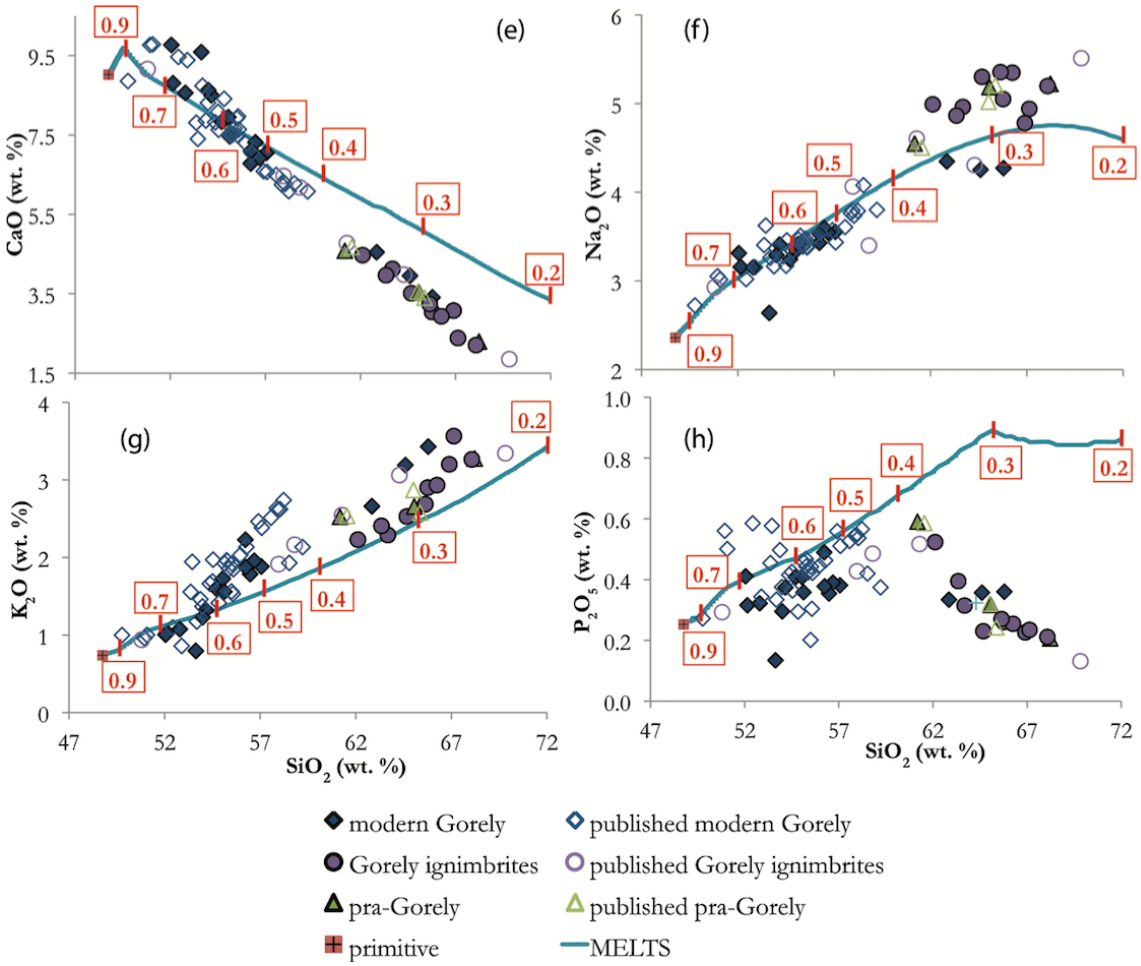

TiO_2, P_2O_5, CaO, or the alkalis. These discrepancies could be due to the fact that the pressure, H_2O concentration, and oxidation state are still unknown for the Gorely magmas, which would cause the timing for multiple mineral-saturation (i.e. apatite, plagioclase, Fe-Ti oxides) to be incorrect. Another possible reason for these discrepancies could be that the calibration of apatite crystallization and plagioclase composition in MELTS is not yet sufficient. Although this is true, these variables were all modified throughout different MELTS runs until the best possible fit was achieved, and we still think MELTS modeling was beneficial to this study.

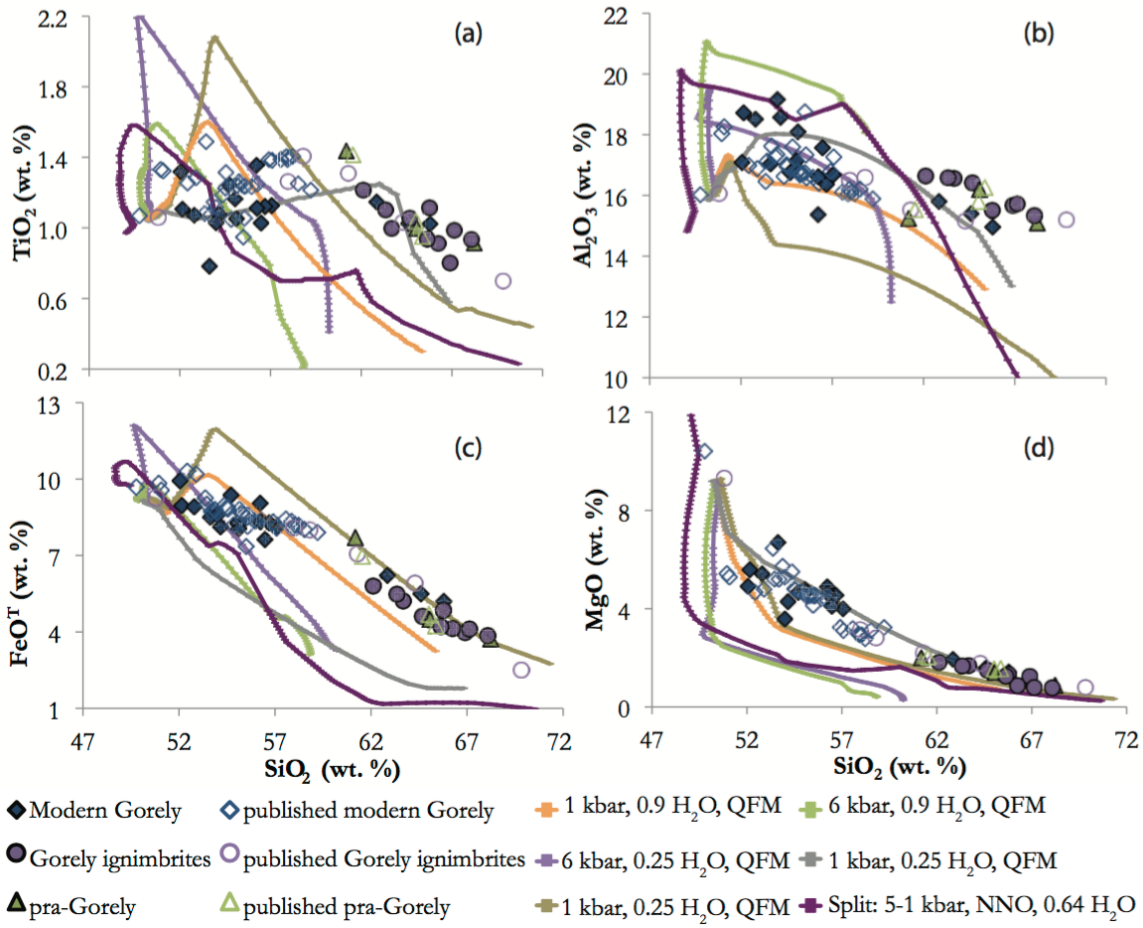

Figure 12 (continued on next page). MELTS modeling at varying pressure, melt water content, and oxygen fugacity. The split run was done at 5 kbar for the basalts, and then switched to 1 kbar at 55 wt.% SiO_2. These runs clearly show that crystallization at higher pressure, or lower oxygen fugacity or water content cannot produce the evolved Gorely compositions.

Deep differentiation

Shallow differentiation has been partially challenged by Gavrilenko & Ozerov (2010), who suggest a two-stage differentiation model for the Gorely magmas, similar to that proposed by Annen et al. (2006), in which there is an early state of high-pressure differentiation at 6–8 kbar, and a second stage of differentiation at 1–1.5 kbar. Therefore, we also attempted a two-stage differentiation model using MELTS, but the trend still did not fit our data (Fig. 12). For all elements, the fits worsen due to early crystallization of pyroxene at higher pressure. This causes an early, strong, decrease in MgO and CaO,

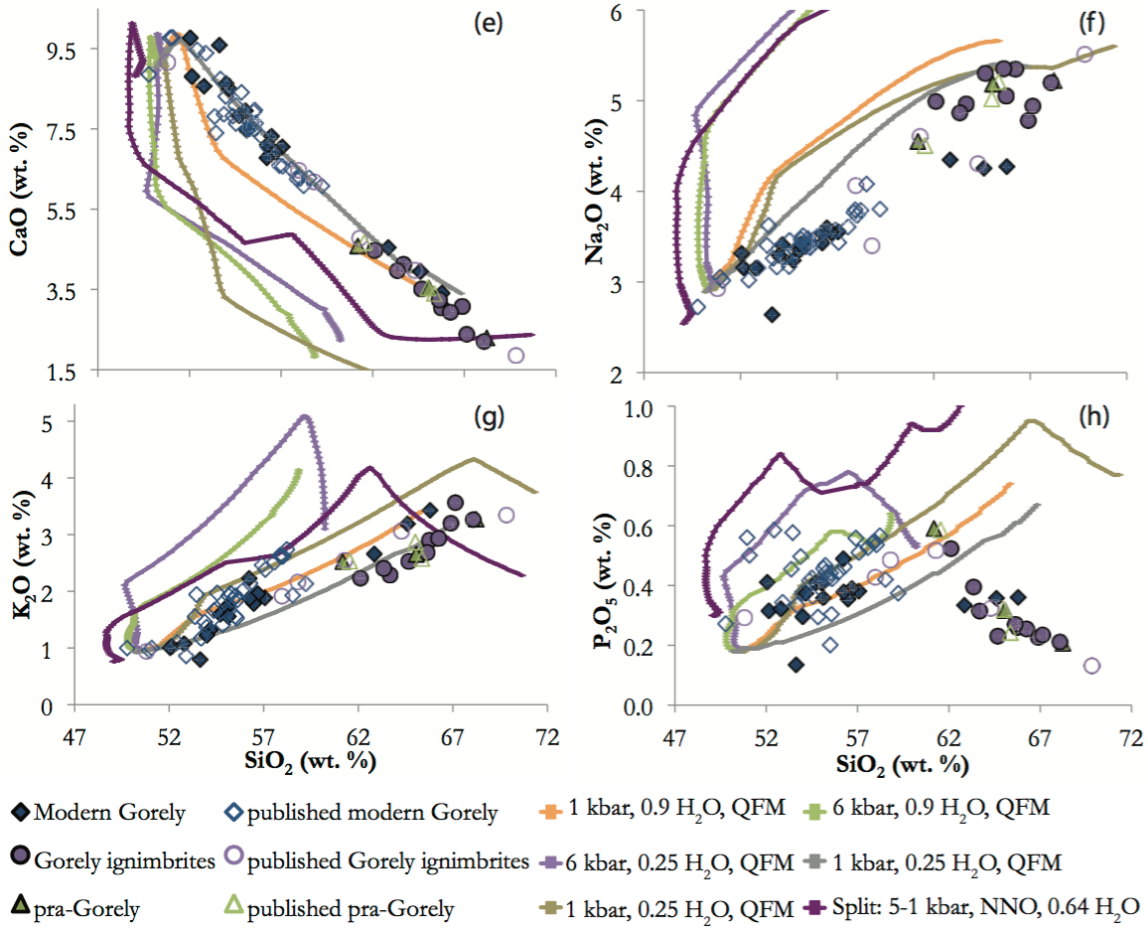

which does not follow the Gorely trend. In addition, it causes all other elements to increase steeply at low SiO_2 for the Gorely magmas. This causes any differentiation at depth (including the two-stage differentiation) not to overlap with either the mafic or evolved Gorely magmas, even when H_2O content and oxidation state are varied (Fig. 12). These results do not preclude minor refills of deep, differentiated magma, which may contain some pyroxene, but they do show that the primary chemical makeup of the magma was achieved at shallow depths, which is supported by our $\delta^{18}O$ results (see below).

Daly Gap, low $\delta^{18}O$ magmas, and the relative roles of fractional crystallization and crustal melting

MELTS modeling suggests that it is compositionally difficult, but possible to produce the evolved compositions of the ignimbrite units by 60–75 % fractional crystallization of large quantities of basalt. Another indication of the need for a process besides just fractional crystallization to produce these dacites is the clear preponderance of silicic rocks and the bimodality of volcanism at the Gorely eruptive center, which represents an unmistakable Daly Gap (Fig. 6). It is important to note that this trend is not likely due to a sampling bias, since we included all data on Gorely magmas from the GEOROC database. The origin of the Daly Gap (Daly, 1925; Chayes, 1963) in volcanic suites has been debated for decades. The Daly Gap may reflect derivation of the magmas from multiple chemically distinct reservoirs (e.g. mantle, crustal, or residual mushes), or through the physics of crystal retention following fractional crystallization (Chayes, 1963; Brophy, 1991; Grove et al., 1997; Marsh, 1981; Thompson et al., 2002; Czuppon et al., 2012; Dufek & Bachmann, 2010), or it may be a natural side effect of fractional crystallization, since magmas of intermediate composition may actually be formed through 'mingling and mixing' (Reubi & Blundy, 2009). More recently, Dufek & Bachmann (2010) suggested mechanical ways to produce a Daly Gap through retention of crystal mushes of intermediate composition, which suggests that the 'missing' andesites may still be located at greater depths. These authors suggested that liquid-crystal separation occurs most efficiently at crystallinities of ~50–70 volume percent (the 'extraction window'). This range encompasses the 60–75 % crystallization needed to form the Gorely dacites (according to MELTS modeling). Deering et al. (2011; 2012) use such an 'extraction window' to show that compositional offsets, which we also observe, can be produced through a change in the depth of differentiation or a change in oxygen fugacity, and a subsequent change in the liquid line of descent, without the need for crustal assimilation. Furthermore, Melekhova et al. (2013) suggest that magmas with high H_2O concentrations (and lower temperatures) are more likely to produce a Daly Gap via amphibole influence on SiO_2, and thus strictly through fractional crystallization; this may pertain to the Gorely magmas, since a few units contain amphibole, although most are amphibole-undersaturated. This is similar to the work of Grove & Donnelly-Nolan

(1986), who suggested that differentiation over a large compositional range, but over a small temperature range might aid in the formation of a Daly Gap. However, although the Daly Gap noted in the Gorely data may in theory be produced by arbitrary choices of polybaric liquid lines of descent, variations in intensive parameters (oxygen fugacity, H_2O concentration), the presence of amphibole, and mechanics of extraction, the trace element trends described above, and the isotopic diversity, which we observe in the Gorely ignimbrites requires diverse sources and processes.

One line of evidence against strictly isobaric fractional crystallization is the separate trends shown in the Harker diagrams for K_2O, Rb, Ba, and Sr (Figs. 8–9). This offset must be due to one of three processes: 1) crystallization of the basalts at a different depth than the dacites; 2) the 'extraction window' processes described by Dufek & Bachmann (2010); or 3) assimilation of crustal rocks that are lower in K_2O, Ba and Rb and enriched in Sr. Deering et al. (2011) show that offsets in Rb and K_2O can be produced through fractional crystallization using the 'extraction window' of crystal mushes proposed by Dufek & Bachmann (2010), along with variations in differentiation depth. Although this method may work for Deering et al. (2011), their data do not show the isotopic variations that our data show, and differentiation of the Gorely basalts at a higher pressure in the presence of amphibole is only capable of producing dacites with lower Rb concentrations. This is not possible for Ba or K_2O, and the trend is opposite for Sr. This is because bulk partition coefficients of a cumulate assemblage changing from amphibole-free to amphibole-bearing when fractionating from basalt (50% pyroxene, 50% plagioclase) to dacite (30% amphibole, 35% plagioclase, 35% pyroxene) are not greater than 1. For amphibole in dacite, partition coefficients (D's) are 0.28 (Ba), 0.18 (Rb), 0.081 (K), and 0.6 (Sr), while plagioclase D's in dacite are 0.3 (Ba), 0.24 (Rb), 0.1 (K), and 4.4 (Sr). D's for plagioclase in basalt are 0.2 (K), 0.067 (Rb), 0.7 (Ba), and 3.08 (Sr). A realistic D of Sr in clinopyroxene is ~0.11, and nearly 0.0 for Rb, K, and Ba (Ewart & Griffen,1994; Nagasawa & Schnetzler, 1971; Bindeman et al., 1998; Onuma et al., 1968). Furthermore, the similar slopes for the basalt-basaltic andesites and andesite-dacites on the Harker diagrams suggest that the bulk partition coefficients were either the same or similar. An increase in compatibility of these elements (e.g. Rb in a hypothetical amphibole-rich dacite) would cause a change in slope (making it more shallow, but

continuous), but would not create a jump similar to what we see (Figs. 8-9). Therefore, this method of melt extraction is not capable of producing the offset trends that we see in our data, and a different method must be occurring.

The strongest argument against a single evolving magmatic series, or a single evolving crystal mush, is that based on the isotopic heterogeneity. The low $\delta^{18}O$ and $^{143}Nd/^{144}Nd$ values, and high $^{87}Sr/^{86}Sr$ determined in this study suggest the involvement of a variety of crustal assimilants. The oxygen isotope data suggest periodic melting and assimilation of hydrothermally altered, low $\delta^{18}O$ material into the Gorely magmatic system. Although crustal melting and differentiation have likely occurred at different depths for some basalts or dacites, shallow crustal assimilation must be a near-ubiquitous, pre-eruptive process in order to imprint and preserve this low $\delta^{18}O$ signature in some eruptive products. This is shown in the six units erupted from Gorely that have a $\delta^{18}O_{melt}$ below the MORB value of 5.7 ± 0.2 ‰ (Table 6; Fig. 5b).

Other magmas, including most of the Holocene basalts and basaltic andesites from the modern Gorely stratocone are normal in $\delta^{18}O$ (>5.7 ‰), and their $\delta^{18}O$ variations may be explained by 10–50 % fractional crystallization of $\delta^{18}O$ mantle-derived basalt (Fig. 11). However, even normal $\delta^{18}O$ values do not necessarily preclude assimilation of normal $\delta^{18}O$ hydrothermally altered materials, which could still alter the magma's major element composition. Hydrothermal alteration by ~14 ‰ meteoric water at low to moderate temperature, with $\Delta^{18}O_{rock\text{-}water}$ of 15–17 ‰, leads to a nil isotopic effect. This same nil effect is also characteristic for hot, but isotopically shifted meteoric waters that have interacted and equilibrated with enough rocks upstream. This would cause the $\delta^{18}O$ of the water to have already shifted to higher values, which would cause the water to have no effect on the $\delta^{18}O$ of the rocks it interacted with later (i.e., the normal $\delta^{18}O$ rocks of Gorely). Six dacite units, including two ignimbrites (11G-1/2, 108L-2010), have normal $\delta^{18}O$ values >5.7 ‰. Although the major element compositions could be crudely explained by 60–75 % fractional crystallization, the trace element compositional offsets prevent this, as is explained above. In addition, the higher $^{87}Sr/^{86}Sr$ and lower $^{144}Nd/^{143}Nd$ and $\delta^{18}O$ values for the remaining dacitic ignimbrites, lavas, and

tephras, and their variation with time, is consistent with periodic shallow assimilation of hydrothermally altered crust, which we explore in the following sections.

Potential crustal contributions to Gorely magmas

Since the currently oldest known ignimbrite of 361 ka (2005L-19) erupted from the Gorely magmatic system has the lowest $\delta^{18}O$ value, the system could have assimilated older surrounding crust (basement) that was already hydrothermally altered. Sources of underlying material that might affect the composition of the Gorely magmas include the Late Miocene Akhomten Granite Massif, ~2–1.5 Ma rhyolitic ignimbrites extruded (or remaining) from the nearby Karymshina caldera, the nearby 4 Ma ignimbrites from this study, and silicic material from neighboring stratovolcanoes or their subvolcanic plumbing systems: Opala, Karymshina, Zhirovskoy, and Mutnovsky (Figs. 1, 7, 13). However, it is important to note that there could be earlier, now buried, unknown Gorely ignimbrite eruptions prior to 2005L-19 (Figs. 1–2, Bindeman et al., 2010). These could have experienced hydrothermal alteration during pra-Gorely magmatism, and were later assimilated back into the magmatic system through a series of caldera collapses; thereby lowering the $\delta^{18}O$ of the magma that was later erupted (as unit 2005L-19). This is similar to the interpretation proposed for low $\delta^{18}O$ Yellowstone magmas (Bindeman et al., 2001). We use $^{87}Sr/^{86}Sr$ and $^{143}Nd/^{144}Nd$ ratios, $\delta^{18}O$ values, as well as major and trace element concentrations to identify possible sources for crustal contributions to the Gorely magmas.

The strontium and neodymium isotopic compositions of Karymshina magmas are similar to those of the Gorely eruptive center, and could produce the desired ratios through assimilation (high $^{87}Sr/^{86}Sr$, low $^{143}Nd/^{144}Nd$); however, $\delta^{18}O_{melt}$ values for the Karymshina magmas are exclusively higher than the $\delta^{18}O_{melt}$ values of the Gorely magmas, suggesting that buried Karymshina rocks must have undergone high-temperature hydrothermal alteration, and lost Rb, Ba, and K_2O, if they were to contribute to Gorely magmatism (Fig. 13).

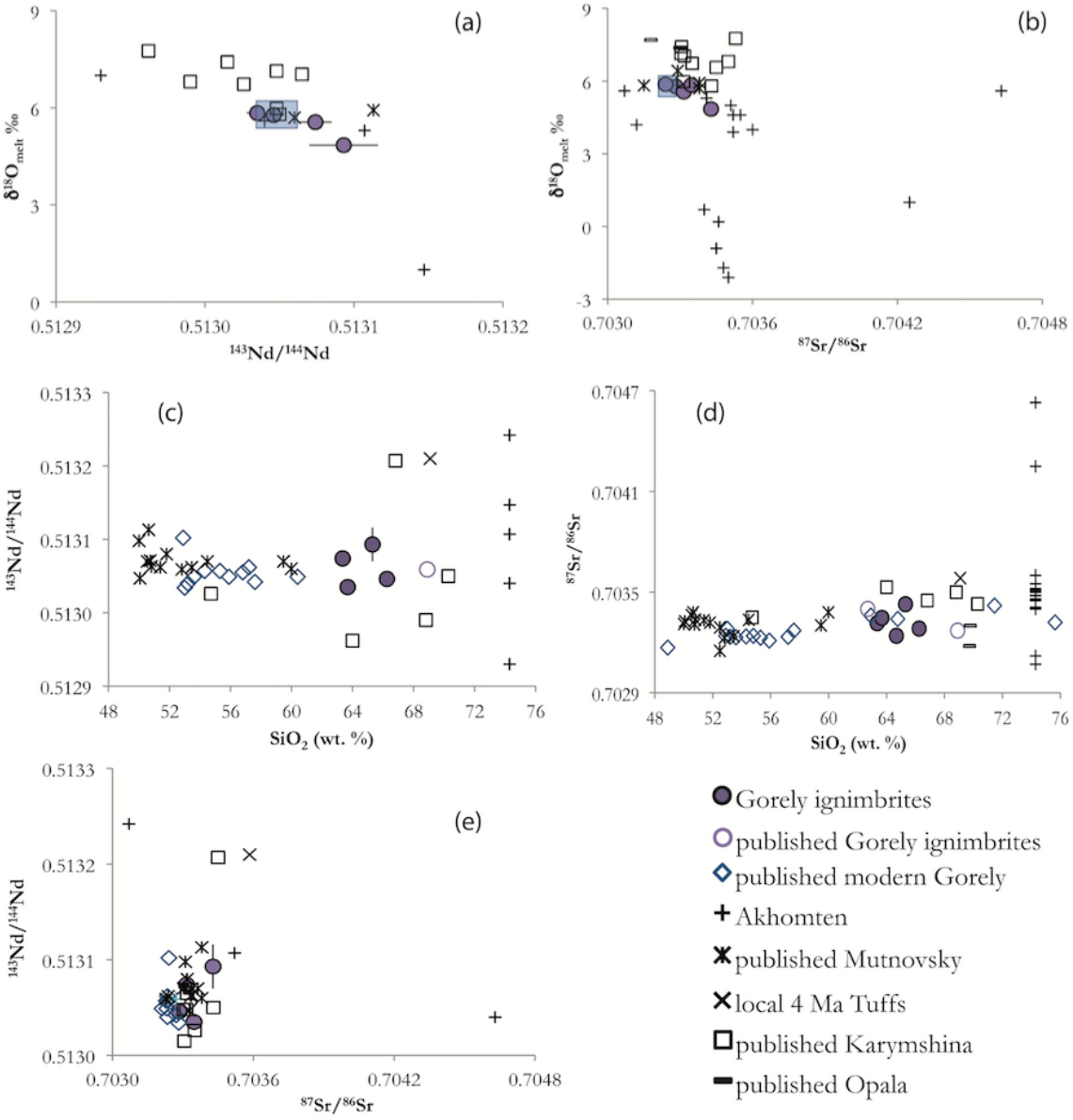

Figure 13 (continued on next page). Sr-Nd-O isotope variations in Gorely silicic compositions compared with modern Gorely lavas and tephra, and silicic rocks from neighboring centers: Akhomten Massif, Opala volcano, Karymshina volcano, 4 Ma tuffs, and Mutnovsky volcano (Figs. 1–2). The range for modern Gorely lavas and tephra is shown as a blue box in the $\delta^{18}O_{melt}$ plots using $\delta^{18}O_{melt}$ calculated in this study and $^{87}Sr/^{86}Sr$ and $^{143}Nd/^{144}Nd$ data from Duggen et al. (2007)). (f–g) temporal $^{87}Sr/^{86}Sr$ and $^{143}Nd/^{144}Nd$ of the Gorely ignimbrites. Gorely data from the literature are listed in the Figure 5 caption in addition to Hedge & Gorshkov (1977) and Shipley (2011); data for Karymshina, Mutnovsky, and Opala are listed in the Figure 6 caption; Akhomten Massif $\delta^{18}O$ data are from Vinogradov (1995); $\delta^{18}O$ values from the Akhomten Massif are whole rock values, and $\delta^{18}O$ values from Mutnovsky volcano are for glass. All other data are calculated melt compositions from $\delta^{18}O$ analyses on phenocrysts from this study (Table 6).

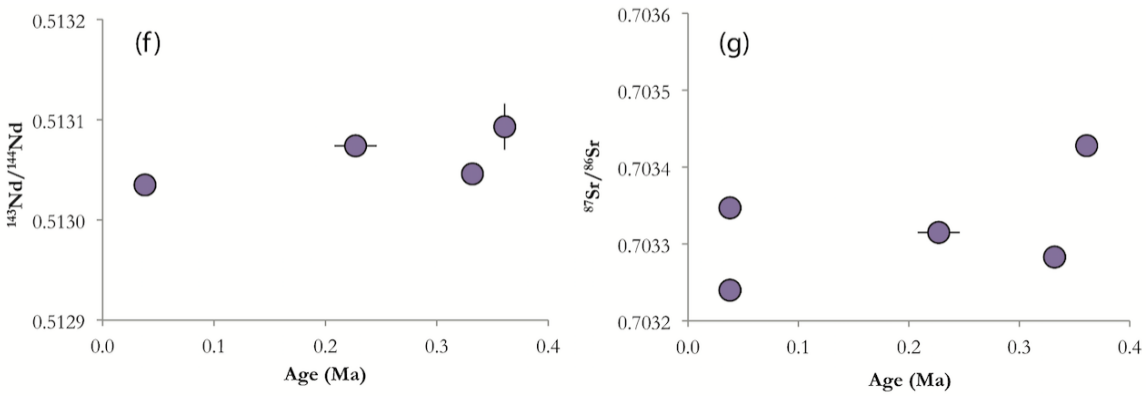

Although Mutnovsky $^{87}Sr/^{86}Sr$ and $^{143}Nd/^{144}Nd$ values are appropriate for assimilation into the Gorely magmas (Fig. 13), and the lower K_2O content of the Mutnovsky magmas could produce the offset in K_2O of the Gorely dacites (Fig. 7), the Mutnovsky magmas are universally normal in $\delta^{18}O$ (basalts and andesites) (Bindeman et al., 2004). Furthermore, as evidenced by Duggen et al. (2007) using double-spike Pb isotope techniques, even though Mutnovsky is only ~10 km away from the Gorely eruptive center (Fig. 1), the Mutnovsky magmas do not contaminate the Gorely magmas. Earlier 300–100 ka low $\delta^{18}O$ dacitic ignimbrites from Gorely, including those exposed in the Opasny Ravine are thus derived from Gorely and not Mutnovsky, and did not assimilate Mutnovsky material during their production. In addition, Opala, which is ~58 km west of Gorely, is unlikely to share a magma plumbing system, due to its high $\delta^{18}O$ signature (Bindeman et al., 2004). Moreover, the isotopic data from this study show that the $^{143}Nd/^{144}Nd$ of the 4 Ma tuffs is too high to produce the low $^{143}Nd/^{144}Nd$ of the Gorely magmas. Zhirovskoy, a nearby, eroded volcano, is characterized by basalts to basaltic andesites and is not yet isotopically characterized.

The Akhomten Granite Massif of Miocene age, proximal to Gorely (Figs. 1–2), has yielded a whole rock Rb-Sr isochron of 12.5 ± 0.8 Ma (Vinogradov, 1995), which is largely confirmed by a U-Pb zircon crystallization age of 11.2 ± 0.08 (1 s.e.) from this study (Supplementary Data: Table A1). This massif is characterized by a wide range of $^{87}Sr/^{86}Sr$ and $^{143}Nd/^{144}Nd$ (0.70307– 0.70463 and 0.51293–0.513242 respectively), and importantly, has low and variable Rb, and high and variable Sr contents (Vinogradov,

1995), largely reflecting a diverse crustal source. Most importantly, the massif is characterized by a wide range of $\delta^{18}O$ values, with many rocks exhibiting low $\delta^{18}O$ values (Fig. 13), all of which overlap with, or are lower than, Gorely isotopic values. It is not known whether the Akhomten Massif developed low $\delta^{18}O$ values upon its emplacement, or whether Quaternary volcanic activity has been imprinted on it. Given the age of the Akhomten Massif, it is likely associated with the timing of collision of the Kronotski block with Kamchatka between 10 and 5 Ma (Lander & Shapiro, 2007), suggesting the Akhomten Massif may be sourced from the Kronotski block. The xenocrystic zircon which we found (37.5 ± 0.7 (1 s.e.) Ma rim (likely metamorphic due to a low Th/U ratio) and 54.7 ± 1.1 (1 s.e.) Ma core) suggests that the assimilated source rocks might have included the older basement of the Achaivayam-Valaginsky Arc, which forms much of the basement under eastern Kamchatka and was accreted between 45 and 50 Ma. The Akhomten Massif may underlie Gorely (Fig. 1) and thus may have been assimilated by the Gorely dacites, giving them their isotopic diversity and low $\delta^{18}O$ signature (Fig. 13). Similar conclusions for diverse $\delta^{18}O$ assimilants were made by Weismaier et al., (2012) for Teide in the Canary Islands. We thus used Akhomten as the most-likely end-member in Energy-Constrained Assimilation-Fractional Crystallization (EC-AFC) modeling.

EC-AFC as a means to determine the source for assimilation

EC-AFC (Spera & Bohrson, 2001; Bohrson & Spera, 2001) was used to determine if, chemically and isotopically, the overlying country rocks, or the Akhomten Massif in particular, could be a plausible source for assimilation by the Gorely magmas. We found that the Akhomten Massif is the most probable source (Fig. 14; Supplementary Data: Fig. A8). For the thermal set-up and equilibration parameters we used the liquidus temperature determined by MELTS modeling discussed earlier (1240 °C) and an initial temperature of the assimilant of 500 °C, which is appropriate for the middle crust or preheated upper crust. Lower temperatures did not achieve the assimilation needed in terms of the isotopic ratios ($\delta^{18}O$, $^{87}Sr/^{86}Sr$, and $^{143}Nd/^{144}Nd$) to produce the dacitic

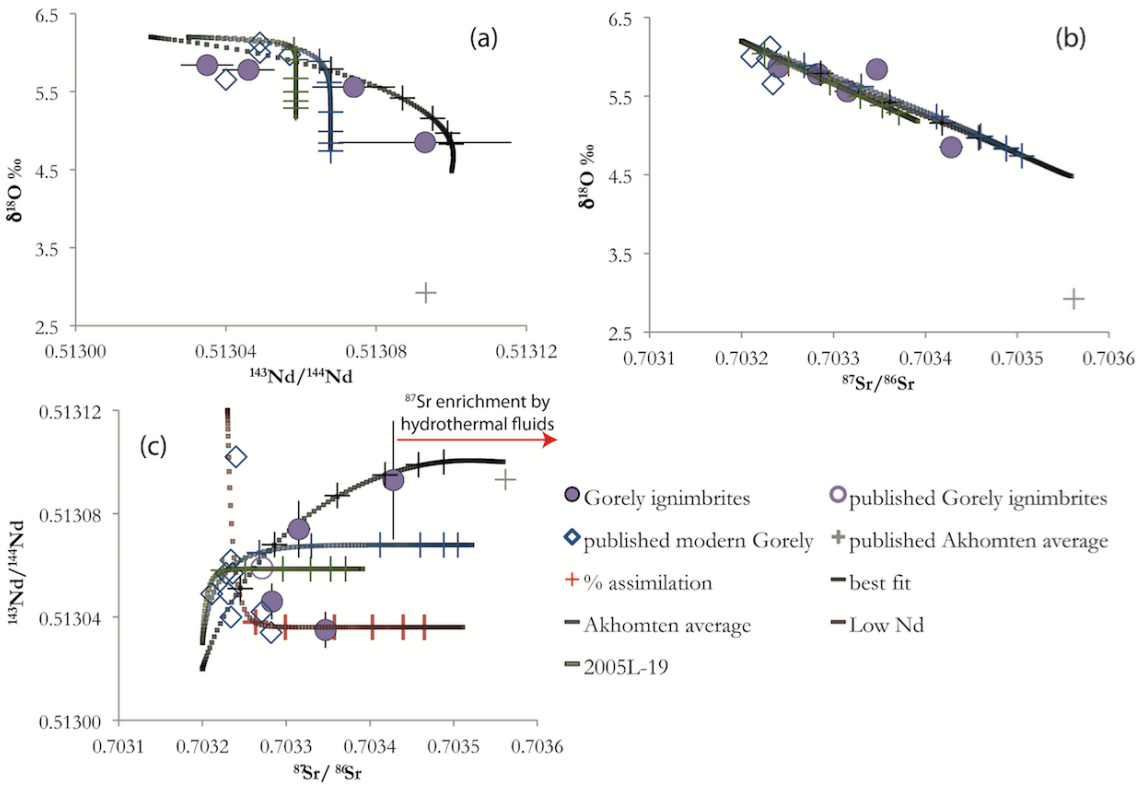

Figure 14. EC-AFC modeling of Gorely magmas to fit the Sr-Nd-O isotopic compositions of the ignimbrites. Four separate models are shown (best fit, average Akhomten, 2005L-19, and initial low $^{143}Nd/^{144}Nd$ (Low Nd)). The plus signs are color coordinated with each separate model run and represent the % assimilation (5, 10, 20, 30, 40, and 50). Gorely literature data are from Duggen et al. (2007) and Kepezhinskas et al. (1997), and Akhomten data are from Vinogradov (1995).

composition of the ignimbrite. This implies the need for a previously heated system prior to the initiation of assimilation, with an equilibration temperature of ~1000 °C. We left all other values the same as those suggested by Bohrson & Spera (2001) for the 'standard, nonlinear, upper-crustal case'. Modeling was based on the Sr, Nd, and O isotope, and Sr and Nd compositions of the mafic and dacitic Gorely magmas and the Akhomten Massif (Supplementary Data: Tables A4–A7).

We ran four separate models to quantify the degree of assimilation: 1) the assimilation of the average Akhomten Massif; 2) the assimilation of the first erupted Gorely ignimbrite (2005L-19; 361 ka); 3) a low $^{143}Nd/^{144}Nd$ assimilant; and 4) reverse modeling to determine the isotopic end-member by using the best fit of isotopic ratios

and concentrations to achieve the ignimbrite compositions. We only used recharge in the best fit run and kept the recharge composition the same as that of the initial magma (Sr and Nd concentrations, as well as Sr, Nd, and O isotopic ratios similar to those of Gorely basalts). Details for these runs are listed in Supplementary Data Tables A4–A7.

The best-fit model is the only one that achieved a high enough $^{143}Nd/^{144}Nd$ for the ignimbrite compositions. This clearly demonstrates that a higher $^{143}Nd/^{144}Nd$ ratio is needed than that of the first known ignimbrite erupted (2005L-19), or of the average Akhomten Massif, but not necessarily higher than what is seen in the Akhomten Massif. This is in contrast to the $^{87}Sr/^{86}Sr$, which was easily achieved by all model runs. In terms of $\delta^{18}O$, all runs achieved a reasonable $\delta^{18}O$ for the ignimbrites using the realistic (and low, 3–4‰) range of $\delta^{18}O$ in Akhomten. Given the large isotopic heterogeneity of the Akhomten Massif (standard deviations of 2.81, 0.000378, and 0.0001169 and values ranging from 1.0 to 7.0 ‰, 0.70307 to 0.70463, and 0.512930 to 0.513242 for $\delta^{18}O$, $^{87}Sr/^{86}Sr$, and $^{143}Nd/^{144}Nd$, respectively) this is not surprising.

One curious result of this modeling is the need for rather high $^{87}Sr/^{86}Sr$ in relation to the high (not low) $^{143}Nd/^{144}Nd$ of the assimilant to produce the Gorely ignimbrites. The high $^{87}Sr/^{86}Sr$ and variable nature of the average Akhomten Massif makes this a possible assimilant to form the Gorely ignimbrites. Therefore, we ran a fourth model in which a Gorely basalt had a higher initial $^{143}Nd/^{144}Nd$, and assimilated a lower $^{143}Nd/^{144}Nd$ portion of the Akhomten Massif. This allowed the model to run through one of the ignimbrite samples (77L-144), and near another (107L-2010), showing that it is possible that not all ignimbrite units were formed through a single-path assimilation process, which could be made possible through: 1) the variable nature of the Akhomten Massif; and 2) preferential addition of radiogenic Sr through hydrothermal alteration.

Hydrothermal fluids emanating near the Gorely volcanic center (from Zhirovskoy, Mutnovsky, and Opala) have $^{87}Sr/^{86}Sr$ ranging from 0.70349–0.70429 (Vinogradov & Vakin, 1983), which are all higher than the highest $^{87}Sr/^{86}Sr$ observed at Gorely (0.70343). Through hydrothermal circulation, these high $^{87}Sr/^{86}Sr$ values may be the source of the two high $^{143}Nd/^{144}Nd$, high $^{87}Sr/^{86}Sr$ ignimbrites (2005-L19 and 109L-

2010), which could have retained excess Sr, with a higher $^{87}Sr/^{86}Sr$ ratio, leached from the Cretaceous crust. This would likely be caused by precipitation of alunite (e.g. John et al., 2008), which is a strontium-rich mineral commonly found in hydrothermal systems. Assimilation of this type of material could explain the high Sr (348 ppm) and high $^{87}Sr/^{86}Sr$ we see in these two Gorely ignimbrites. A negative correlation of $^{87}Sr/^{86}Sr$ and $\delta^{18}O$ for silicic rocks across Kamchatka (Bindeman et al., 2004) supports this interpretation (Fig. 13).

According to the EC-AFC modeling conducted here, approximately 15 % assimilation is needed to produce 109L-2010 (dacite ignimbrite), and approximately 30 % assimilation to produce 2005-L19 (dacite ignimbrite). These numbers would change if the parameters in the EC-AFC model were altered, such as if the liquidus temperature or initial temperature of the assimilant were decreased. Therefore, other components, such as recharge would likely need to be added to achieve this amount of assimilation.

Although trace elements were not included in the EC-AFC modeling, we nevertheless show that portions of the Akhomten Massif have the Rb and Sr concentrations needed to produce the offsets observed in the Gorely magmas (Fig. 8–9). This is shown in the large range in Rb and Sr concentrations throughout the Massif, many of which are lower in Rb and elevated in Sr (Vinogradov, 1995).

Temporal evolution of Gorely magmatism: Evidence through petrography and isotopes

The large range in the isotopic signatures of the Gorely magmas described above provides strong evidence for assimilation of a crustal source (the Akhomten Massif) that could imprint its $^{87}Sr/^{86}Sr$, $^{144}Nd/^{143}Nd$, and $\delta^{18}O$ values through the combined effects of assimilation-fractional crystallization and hydrothermal alteration, but also has the ability to repeatedly produce the petrochemically and mineralogically similar dacitic compositions observed through the early evolution the Gorely eruptive center (Figs. 5, 13).

The decrease in isotopic diversity of the Gorely magmas with decreasing age and the increasing predominance of normal $\delta^{18}O$ values may indicate that after tens to hundreds of thousands years of "waxing", the magmatic plumbing system under Gorely became less prone to assimilation (Fig. 5). Alternatively, the magma plumbing system may now tap more "normal" or by now laterally averaged crustal sources with normal $\delta^{18}O$, and less diverse Sr and Nd isotopic values, due to the low $\delta^{18}O$ protolith being exhausted. In addition, the presence of mafic enclaves in thin sections (Table 3) and hand samples of all of these ignimbrites suggests mafic injections into the magma system at a time near the eruption, not allowing the necessary time to thoroughly mix and equilibrate this mafic material into the magmatic system prior to eruption. As was earlier documented by Sparks & Marshall (1986), and again in Izbekov et al. (2004a), the ability of magmas to thoroughly mix and re-equilibrate after a mafic injection depends primarily on the viscosity and density of the magma subsequent to thermal equilibration, followed by mechanical disintegration (mingling). As was detailed by Izbekov et al. (2004a), the presence of mafic enclaves suggests that mafic recharge was rare, due to the need for a larger temperature and viscosity difference between the pre-existing magma and the mafic intrusion to form quenched blobs. In addition, the small degree of resorption in some of the phenocrysts contained within the mafic enclaves suggests a relatively small amount of time between mafic recharge and eruption, leaving little time for the recharge to equilibrate with the pre-existing magma.

The earliest known eruptions from Gorely include the formation of the pra-Gorely cone (~0.7 Ma). These eruptions include two low $\delta^{18}O_{melt}$ units (Fig. 5), which suggests that there must be either earlier erupted ignimbrites, which are currently buried and not sampled, or the production of the pra-Gorely magmas must have included assimilation of hydrothermally altered surrounding crust, such as the Akhomten Massif.

Following the formation of the pra-Gorely eruptives, there was an extended period of ignimbrite-forming eruptions (~360–38 ka). All but two of the ignimbrite units (108L-2010 and 109L-2010) contain glomeroporphyritic crystal aggregates (Plag+Pyx±Mt), and these two units also contain the largest amount of mafic enclaves, with little resorption of the phenocrysts of the mafic enclaves; this suggests that mafic

magma injection may have triggered convection and stirred the cumulate layers near the walls and base of the magma chamber, and that the eruption occurred within a short period of time following a mafic injection (e.g. Bergantz & Breidenthal, 2001; Izbekov et al., 2004a). We speculate that the high $\delta^{18}O$ temperatures that we observe (Fig. 10), which are higher than the MELTS determined equilibration temperatures and the two-pyroxene temperatures, may indicate that some crystals represent "protocrysts", i.e. they formed early in an evolving (hotter and deeper (5–6 kbar)) magma chamber, similar to what was noted in Tollan et al. (2012), or "xenocrysts", i.e. they were sourced from a different parent and were entrained in the 1 kbar Gorely magma system. This is documented by the abundant evidence of mixing (mafic enclaves, crystal aggregates, and sieve textures), and also by the two units (109L-2010 and 11G-2), which yielded pyroxene temperatures of 926 and 891 °C, respectively, which are over 100 °C lower than those indicated by the O isotope fractionation thermometer (1050 and 1020 °C respectively) (Table 6). As these crystals are also compositionally zoned (plagioclase have complex, normal, and reverse zoning (Table 3)), and at times show sieve textures, this interpretation suggests that these crystals have not had time to equilibrate in terms of their $\delta^{18}O$ composition prior to their entrainment in a colder and more differentiated magma product, since oxygen has a slower diffusion rate than Fe and Mg in pyroxene, and we know the pyroxenes have not been fully equilibrated (e.g. Bindeman, 2008). The final ignimbrite known to erupt before the ~38 ka eruptions, 125L-2000, is also the ignimbrite with the highest percentage of crystals contained within crystal clusters (25 %), suggesting that it may have erupted left over crystal clusters from previous eruptions that remained along the walls of the magma reservoir, or that it erupted smaller pockets of left over crystal mush, prior to a period of possible quiescence at the Gorely eruptive center (Table 3).

The next phase of ignimbrite-forming eruptions occurred between 100 ka and 38 ka. None of these units erupted low $\delta^{18}O$ material. Mafic enclaves and crystal clusters were observed in thin section, suggesting a similar process of eruption triggering to the earlier ignimbrites (Table 3). Similar to the pra-Gorely temperatures, the late ignimbrite eruptions show a range of both normal and high temperatures as indicated by isotopic

fractionation, although none of these units produced a reliable equilibrium temperature from the two-pyroxene thermometer. This again suggests that some crystals were entrained without enough time for equilibration (Fig. 10).

The post-38 ka cone-building phase continues through to the present day. At least two small volume Holocene (~7 ka) units have produced low $\delta^{18}O_{melt}$ values (11G-17 and 11G-18), which likely represent sampling of lingering small pockets of low $\delta^{18}O_{melt}$ under Gorely. This post-38 ka, cone-building period of eruptions also shows a drop in SiO_2 wt.% from previous eruptions (Fig. 5a), illustrating a less evolved phase even than that of the pra-Gorely period.

In summary, magmatism is temporally diverse in $\delta^{18}O$, $^{87}Sr/^{86}Sr$, $^{144}Nd/^{143}Nd$ (Fig. 5b, 12f, 12g) and composition. This is consistent with a model whereby each magma chamber is nearly entirely emptied of melt following every ignimbrite eruption, as any significant amount of melt remaining in the chamber would not allow for such large changes in strontium and neodymium isotope composition through time. The batch of melt that produced subsequent eruptions must have had a maximum residence time of 10^3–10^5 years, based on the time spans between ignimbrite-forming eruptions, evolving through processes including fractional crystallization and assimilation of either older country rocks or hydrothermally altered crustal material (the Akhomten Massif) as observed elsewhere (e.g. Druitt et al., 2012).

Foundering of the lower crust as a source of early silicic volcanism?

It has been proposed that the "ignimbrite flare-up" in the western United States was a consequence of the delamination of the sub-horizontal Farallon slab beneath the western U.S.A. following accretion of the Siletzia Terrane (Christiansen & Yeats, 1992; Humphreys, 1995). Likewise, in Kamchatka there was a much younger episode of accretion (the Kronotski Arc) between 10 and 7 Ma (Lander & Shapiro, 2007), and an earlier episode (45–40 Ma) of accretion of the Achaivayam-Valaginsky Arc (Soloviev et al., 2002a, 2002b; Hourigan et al., 2009; Konstantinovskaya, 2003). Both of these events would have contributed to thickening of the crust beneath Kamchatka. Since Akhomten

(an upper- to mid-crustal granite) is only ~11 Ma, delamination of the lower thickened crust under eastern Kamchatka would help to explain its rapid uplift and rugged topography (Fig. 3).

Block foundering and associated heating of the lower crust may help to explain the silicic explosive volcanism in southern and eastern Kamchatka (Bindeman et al., 2010), as well as the elevated Nb concentrations of the Gorely magmas (average of 2.6 ± 0.57 (1 s.d.) normalized to N-MORB) relative to typical subduction-related magmas (average of 1.46 ± 0.63) and OIB (20.6) (Table 2; Fig. 15) (Turner et al., 2007; Kersting & Arculus, 1994; Dorendorf et al., 2000; Churikova et al., 2001; Ishikawa et al., 2001; Tatsumi et al., 1995; Ariskin et al., 1995; Volynets et al., 2000; Sun & McDonough, 1989). More specifically, Figure 15b shows Gorely basalts (rear arc) in comparison to Mutnovsky (volcanic front) and Klyuchevskoy (Central Kamchatka Depression) basalts, in addition to basalts from Sunda, New Zealand, the New Hebrides, Java, and New Britain. Since the Central Kamchatka Depression magmas originate partially as a consequence of back-arc spreading, these provide a good comparison to magmas that are not fully sourced through subduction. As is shown in Figure 15b, the Gorely basalts have compositions in between those of OIB and other subduction-related mafic magmas around the world. Foundering of the lower crust could result in decompression melting of deeper, less depleted mantle and thus magmas with more OIB-like compositions. In addition to the elevated Th relative to LREE observed by Duggen et al. (2007), we also observe high Nb, Zr, Ce, and P (Fig. 15b), which we suggest shows a smaller contribution of subduction fluids to the Gorely magmas, relative to volcanoes closer to the volcanic front, such as Mutnovsky. Based on elevated olivine Ni and Mn concentrations, Gavrilenko et al. (in press), propose that the Gorely basalts originate mostly from a pyroxenitic source (rather than a peridotitic source). This would be consistent with our model if Gorely magmatism had a component of sinking and melting of a delaminated basaltic root (e.g. the reverse diapir of Elkins Tanton & Hager, 2000). Therefore, we propose that Gorely magmas still carry a recognizable but subtle delamination component.

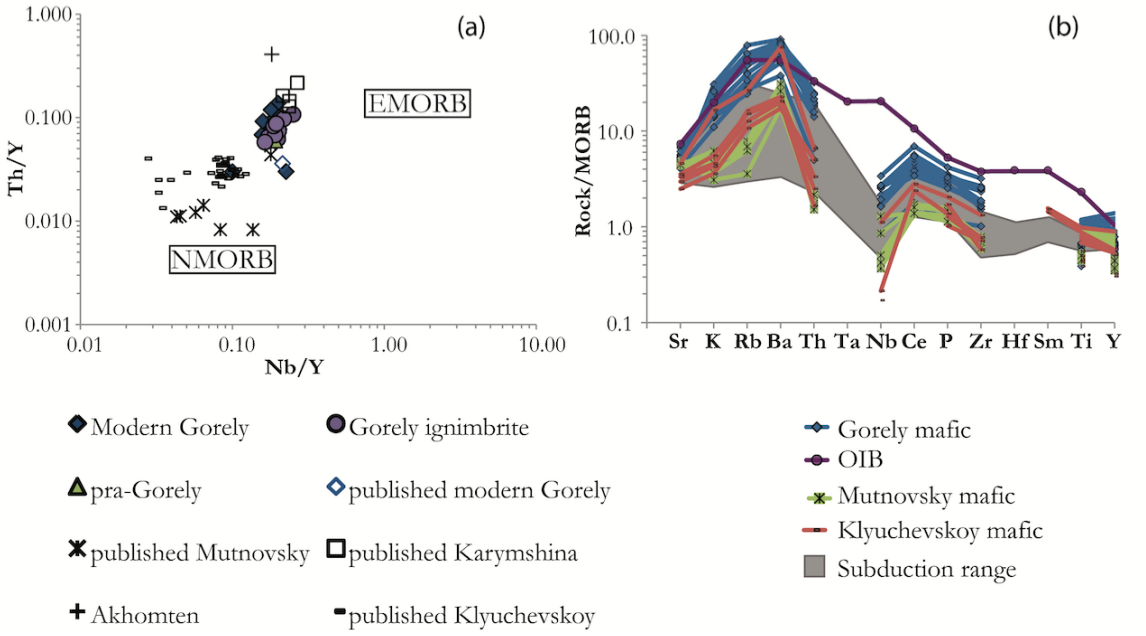

Figure 15. Trace element tectonic discrimination diagrams for Gorely. (a) Th/Y vs Nb/Y plot, showing that Gorely basaltic magmas have higher Nb and Th concentrations than mafic magma from Klyuchevskoy (Central Kamchatka Depression) and Mutnovsky (Volcanic Front). (b) MORB-normalized trace element variation diagram illustrating that the Gorely basalts have a geochemical signature between OIB and subduction-related Kamchatkan volcanoes. The gray field 'Subduction range' is from the Basaltic Volcanism Study Project (1981) and includes data from Sunda (tholeiitic and calc-alkaline basalt), New Zealand (high-Al basalt), the New Hebrides (high-K basalt), Java (high-Al basalt), and New Britain. Data here clearly show that Gorely rocks typically have a geochemical signature that is more enriched than typical island arc compositions and, therefore, have compositions between subduction and OIB magmas. Published Kamchatkan data include Duggen et al. (2007); Kepezhinskas et al. (1997); Turner et al. (2007); Kersting & Arculus (1994); Dorendorf et al. (2000); Churikova et al. (2001); Ishikawa et al. (2001); Tatsumi et al. (1995); Ozerov et al. (1995); Volynets et al. (2000). OIB and N-MORB data is from Sun & McDonough (1989).

Glacial advances as a source for low-$\delta^{18}O$ magmas, and sporadic volcanic activity

As is shown in Figure 16, the earliest ignimbrite-forming eruptions at Gorely, as well as the more recent ignimbrite eruptions at ~38 ka, occur during glacial periods. Other recent ignimbrite eruptions in Kamchatka, from Odnoboky (from the Karymsky center), Ksudach, Uzon-Shorokoye, and Khangar (from the Sredinny Range) also erupted during maximal (75 %) glacial periods (Fig. 16; Bindeman et al., 2010). We include glacial

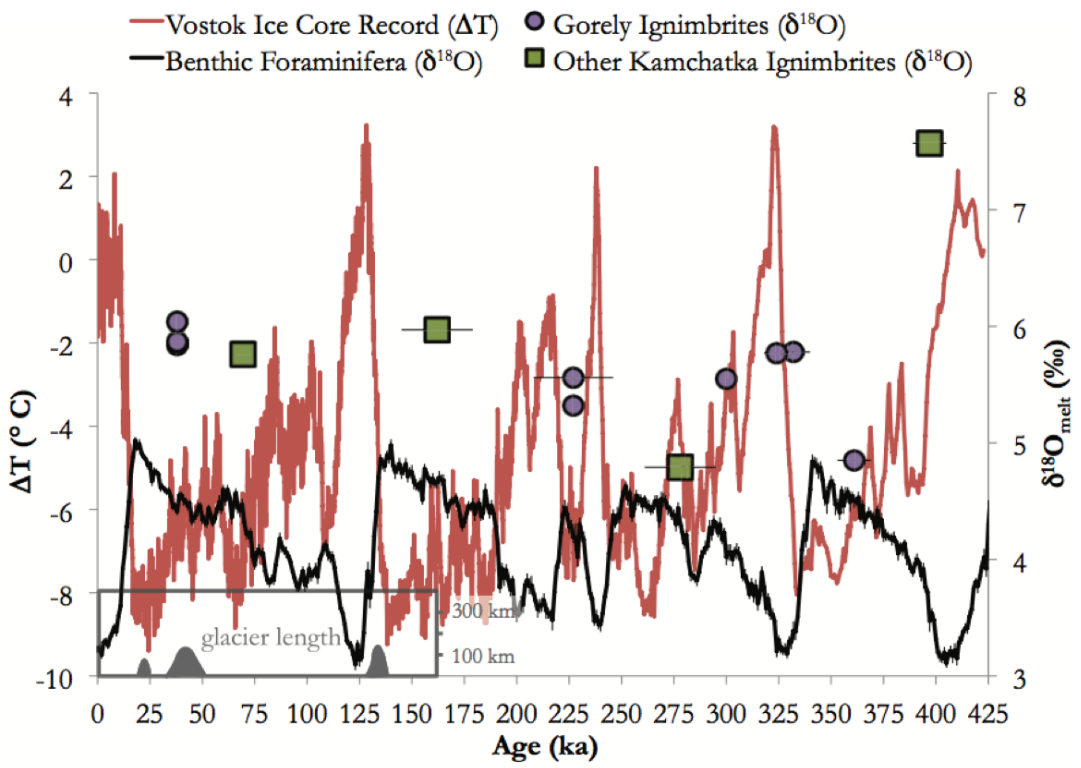

Figure 16. Correlations between ages of newly dated, large ignimbrite-forming eruptions from Gorely volcano and global glacial cycles using the Vostok ice core and benthic foraminifera climate proxies. Glacial length of the Kamchatka Peninsula (Barr & Clark, 2012) is also plotted in the lower left hand corner of the graph and represents the maximum length of the Kamchatkan glaciers during a specific time, which are sometimes offset from the global record. Notice that frequent ignimbrite eruptions (some with low $\delta^{18}O$ values) occur during maximal glacial conditions (high benthic foraminifera $\delta^{18}O$ and low Vostok ice ΔT), which is explained by frequent glacial erosion of the surface of the volcano, leading to decompression of the shallow (1 kbar, Fig. 10) magma chamber (e.g. Geyer & Bindeman, 2011). Gorely data with age error bars are $^{40}Ar/^{39}Ar$ dated, and those without are correlated ages. Data from other Kamchatka ignimbrites include eruptions from Odnoboky, Ksudach, Uzon-Shorokoye, and Khangar (data from Bindeman et al., 2010). Benthic foraminifera data are from Lisiecki & Raymo (2005); Vostok ice core data are from Jouzel et al. (1987; 1993; 1996), and Petit et al. (1999).

length data (based on the moraine record) from Barr & Clark (2012) for Kamchatka in Figure 16, because they propose that glacial cycles in Kamchatka are offset from the average global glacial cycles. Even when using their data, which suggests fewer periods of glaciation in Kamchatka, our 38 ka ignimbrite eruptions still fall within a period of maximum glaciation. Even though this is counter-intuitive to research that shows an

increase in volcanism during shifts from glaciation to deglaciation (Tuffen, 2010), increases in volcanism during glacial periods have been shown to occur in Kamchatka, likely due to glacial bulldozing effects, and intrastadial sector collapses (Geyer & Bindeman, 2011). Additionally, we suggest that subglacial hydrothermal weakening (e.g. Merle et al., 2010) could have further aided in the frequent upper Pleistocene ignimbrite-forming eruptions at Gorely. The abundant low $\delta^{18}O$ silicic volcanism in Kamchatka, and Gorely in particular, serves as further confirmation of greater depletion of the magmas by lower $\delta^{18}O$ glacial meltwaters in Kamchatka as compared to North America or the Andes (Folkes et al., 2013).

Repeated intracaldera glaciations in Gorely would allow for a low $\delta^{18}O$ hydrothermal circulation system, which would create a sufficient supply of low $\delta^{18}O$ rocks for assimilation into the Gorely magma system. At the same time, the surface action of glaciers could have created conditions for frequent ignimbrite eruptions from short-lived, variably $\delta^{18}O$ fingerprinted, ephemeral magma chambers (e.g. Geyer and Bindeman, 2011).

CONCLUSIONS

This study demonstrates considerable complexity in the evolution of a single, periodically glaciated, arc volcano. We have established a model of silicic magma generation at the Gorely eruptive center that involves periods of magmatic and hydrothermal activity spanning two of the most recent glacial cycles. Large-volume, isotopically distinct silicic magma can be generated incrementally at relatively shallow depths between more subdued phases of cone-building activity, which is possibly enhanced through small-scale crustal foundering. Shallow depths of crustal assimilation and silicic magma generation are demonstrated in this study through two primary means: 1) MELTS modeling was not able to accurately reproduce the geochemical trends of the Gorely dacites, and could not even produce the trends of the Gorely basalts at pressures of 5 kbar; 2) The compositional gaps and isotopic variations are best explained by assimilation of the 11 Ma Akhomten Massif crust; and 3) There is a limit to the depth of production of low $\delta^{18}O$ magmas

(Bindeman et al., 2007). The production of large-volume, isotopically distinct, silicic magma occurs through a combination of fractional crystallization, assimilation of older and variably altered country rocks, and entrainment of cumulate crystal clusters. These silicic magma chambers are likely to empty nearly completely in ignimbrite eruptions after 10^3–10^5 years of assembly, based on the frequency of ignimbrite eruptions and the significant changes in isotopic composition. Furthermore, this study emphasizes the importance of analyzing these "long-lived" volcanic centers with multiple geochemical tools, including geochronology, isotopes, major and trace element chemistry, mineral chemistry, and petrographic analysis, to determine their eruptive history. The use of just one of these tools would not reveal this long and detailed history of crustal foundering, crustal melting, crystal settling, mafic input, and eruption during alternating glaciations. We acknowledge the need for further work to establish a high-precision eruptive history for the entire Gorely volcanic center, which will better constrain the time needed to form these ignimbrites.

BRIDGE

In this chapter (Chapter II), I used a range of isotopic ratios ($^{87}Sr/^{86}Sr$, $^{143}Nd/^{144}Nd$, $\delta^{18}O$), major element compositions, and MELTS and EC-AFC modeling of rocks from the Gorely eruptive center to document the process of partial melting of the surrounding crust to form the more explosive volcanic eruptions formed from Gorely volcano. I also documented, through the use of $^{40}Ar/^{39}Ar$ dating, that the Gorely eruptive center is a longer-lived volcanic center than was previously thought.

In the following chapter (Chapter III), I will again utilize isotopic ratios ($\delta^{18}O$ and εHf) to understand explosive volcanic activity. This time, though I will be focusing on even more explosive volcanic eruptions, which span across Oregon and have no known magmatic source. Using isotopic ratios, trace element concentrations, and the surrounding geology, I will begin to document how these large-scale explosive eruptions were formed.

CHAPTER III

THE EARLIEST LOW AND HIGH $\delta^{18}O$ CALDERA-FORMING ERUPTIONS OF THE YELLOWSTONE PLUME: IMPLICATIONS FOR THE 30–40 Ma OREGON CALDERAS AND SPECULATIONS ON PLUME-TRIGGERED DELAMINATIONS

From Seligman, A.N., Bindeman, I.N., McClaughry, J., Stern, R.A., Fisher, C. (2014). The earliest low and high $\delta^{18}O$ caldera-forming eruptions of the Yellowstone plume: Implications for the 30–40 Ma Oregon calderas and speculations on plume-triggered delaminations. *Frontiers in Earth Science* **2**, 1–9, doi: 10.3389/feart.2014.00034.

INTRODUCTION

Trace element and isotopic data of magmatic rocks have long been used to relate magma petrogenesis to geotectonic settings (e.g. Jicha et al., 2009; Auer et al., 2008; Seligman et al., 2014). We use these methods to investigate three large 30–40 Ma calderas in eastern Oregon that were recently identified and have an unknown geotectonic origin (McClaughry et al., 2009b) (Figure 1). Despite nearly 40 m.y. of erosion, these calderas preserve volcano-tectonic depressions with respective rings of hydrothermally altered post-caldera rhyolite intrusions, thick intracaldera tuffs, and central resurgent and ring-fracture rhyolite domes. The rocks that form these three paleontologically important calderas were originally mapped as part of the John Day and Clarno formations, signifying a correlation and likely source. These three eastern Oregon calderas are all located near the Klamath-Blue Mountain gravity-anomaly lineament (Figure 1), which marks the boundary between the Blue Mountains Province and the accreted Siletzia terrane, and were all erupted through the Paleozoic Blue Mountains Province (Figure 1). Limestone is locally present in the accreted terranes underlying the calderas and is present as xenoliths in multiple tuffs. Other calderas and caldera-forming tuffs that we studied for comparison belong to the volcanic front of the ancestral Cascades.

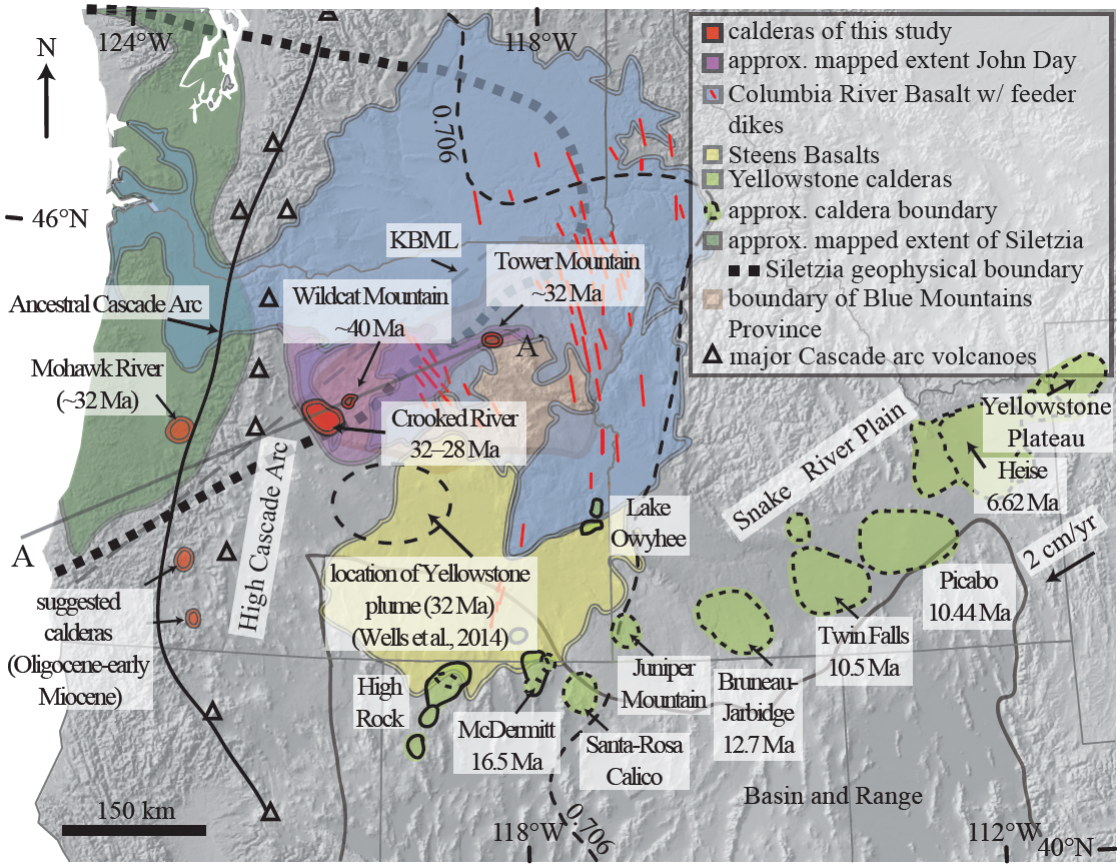

Figure 1. Map showing the location of the newly identified Crooked River, Wildcat Mountain, Tower Mountain, and Mohawk River calderas (McClaughry et al., 2009a; 2009b; 2010; age for Tower Mountain caldera is from Martin Streck, personal communication) in relation to other key features of the Pacific Northwest. Location of the 32 Ma Yellowstone plume derived from G-Plates (Wells et al., 2014; Seton et al., 2012; see the supplementary material (Appendix B) for the map features and ages). Accounting for rotation of Oregon (Wells et al., 1998) causes the locations of the Crooked River caldera and the reconstructed Yellowstone plume to coincide, as shown in the supplementary material. A-A' transect is shown in cross section in Figure 7.

Around 50 Ma, subduction of the nearly horizontal Farallon slab was halted by accretion of the Large Igneous Province known as Siletzia (56–49 Ma) from western Oregon to southwestern British Columbia (Atwater and Stock, 1998; Wells et al., 2014). Accretion caused 1) dismemberment of the subducting Farallon slab, 2) subduction to migrate westward and reinitiate along the western margin of Siletzia, and 3) stagnation of the nearly horizontal limb of the Farallon slab beneath Oregon, where geophysical data suggest the slab remnant is presently lodged (Gao et al., 2011; Darold and Humphreys, 2013). Previous work by Duncan (1982) and Wells et al. (1984) suggested that the long-

lived Yellowstone plume powered magmatism responsible for development of the Siletzia Large Igneous Province oceanward from the Pacific Northwest coast. However, the proposed scenario results in an unusually large ~30 m.y. gap in recognized Yellowstone plume-related eruptions between 56–49 Ma Siletzia magmatism (Wells et al., 2014) and eruption of the Columbia River basalts at ~17 Ma in eastern Oregon and coeval calderas in northern Nevada (Coble and Mahood, 2012; Ferns and McClaughry, 2013).

Renewed Cascadia subduction and related arc magmatism built a north-south Cascade volcanic front, initiating in southern Washington and northern Oregon, with the first ancestral Cascade volcanoes and calderas appearing around 42 Ma (du Bray and John, 2011). East of the ancestral Eocene-Oligocene Cascade arc, voluminous 30–40 Ma ash-flow tuffs associated with large caldera forming eruptions were deposited as part of the Clarno and John Day formations. However, the causative tectonic and magmatic origins of these calderas and their correspondent ash-flow tuffs remain enigmatic (McClaughry et al., 2009b).

The present study aims at determining how the voluminous silicic magmas in these newly identified calderas were formed, assuming that each site of abundant silicic magmatism requires large quantities of basaltic heat and mass fluxes from the mantle. Herein, we define processes that may foster genesis of large-scale, within-plate volcanism. In particular, we explore whether the Yellowstone plume could have been somehow responsible for the genesis of these large-volume centers of volcanism, and if so, how it can be reconciled with the ongoing subduction of the Farallon slab under North America. We use major and trace element geochemistry, new U-Pb geochronologic data, and in situ O and Hf isotopic investigations of zircons for three recently identified calderas, whose rocks are part of the John Day and Clarno formations (Figure 1) (McClaughry et al., 2009b): Crooked River, Tower Mountain, and Wildcat Mountain. We then compare their isotopic and trace element characteristics with those of contemporaneous calderas known to be part of the Cascade arc: the large 25-km diameter Mohawk River caldera (McClaughry et al., 2010) and several other regionally abundant

40–25 Ma tuff layers (Figure 1), known to be part of the ancestral Cascade arc. Our trace element and isotopic data thus place constraints on crustal and mantle processes that previously have been investigated from a geodynamic and geophysical perspective.

MATERIAL AND METHODS

In this study we apply single crystal and in situ methods for determining the primary magmatic values for these rocks, primarily from the Crooked River caldera, that have been heavily altered. Intense hydrothermal alteration has caused many of the minerals, such as feldspar, to break down to clays, and for most of the quartz to be secondarily reprecipitated. Any quartz or feldspar analyzed from the Crooked River caldera was pretreated in HF to remove any outer rind of alteration and checked for melt inclusions to be sure these are primary minerals. Furthermore, when reducing the data, we trust the lowest feldspar and quartz $\delta^{18}O$ values, since higher values are typically indicative of secondary effects due to the higher $\Delta^{18}O_{min\text{-}H2O}$ values. In addition, we primarily focus on analyses of alteration-resistant zircon when studying rocks from the Crooked River caldera. $\delta^{18}O$ compositions of 1–2 mg of quartz, plagioclase, pyroxene, olivine, amphibole, and bulk zircon phenocrysts were determined by laser-fluorination in the stable isotope laboratory at the University of Oregon (e.g., Bindeman, 2008). $\delta^{18}O$ compositions of cores and rims of mounted and imaged zircon crystals were further refined in their $\delta^{18}O$ values by targeting cores and rims in situ using the Cameca 1280 ion microprobe at the University of Alberta (±0.16‰ 2σ). The Lu-Hf isotopic composition of zircon was then determined for some of these same spots at Washington State University's Radiogenic Isotope and Geochronology Lab (±0.8–2.0 εHf) (Fisher et al., 2014). Individual zircon cores and rims were then analyzed for ^{238}U-^{206}Pb ages using the CAMECA ims 1270 ion microprobe at UCLA. Analytical techniques are described in detail in the supplementary material (see Appendix B). Selected XRF data were obtained at Pomona College and others at Washington State University (published), and basalt and basaltic andesite samples were analyzed for trace elements by ICP-MS at the Solid Earth Geochemistry Lab at Harvard to determine the geochemical signature of the source magmas.

RESULTS

Petrography and geochemistry of rocks associated with the large Oregon calderas

The Mohawk River caldera currently has two units associated with it (the Tuff of Mohawk River and the basalt of Mt. Tom). The location of the Mohawk River caldera, within the ancestral Cascade volcanic arc domain, implies a subduction-related petrogenesis (Figure 1). Furthermore, the presence of abundant (10–20 %) phenocrysts in the tuff of Mohawk River and its calc-alkaline geochemistry (low Nb and Zr), which are also characteristics of other major coeval tuffs of the ancestral Cascade arc that we studied (du Bray and John, 2011), suggest a subduction-type source and derivation by fractionation of a cool and wet basaltic magma (Figures 1, 2B; see Appendix B for all Chapter III supplements). Other studied tuffs (Dexter, Fox Hollow, and Bond Creek) have similar mineralogical characteristics.

Rocks analyzed from the Tower Mountain and Wildcat Mountain calderas include their major caldera forming tuffs (the tuff of Steins Pillar from the Wildcat Mountain caldera and the tuff of Dale from the Tower Mountain caldera), as well as pre- and post-caldera domes and lavas that range continuously from basalt to rhyolite. Rocks associated with these calderas include hydrous minerals (amphibole ± biotite). The presence of hydrous minerals and the continuous range in magma compositions is similar to many rocks found in subduction-type settings. However, their locations far behind the already well-defined ancestral Cascade arc (du Bray and John, 2011) indicate that their genesis is not subduction related. The rhyolites of the Tower Mountain and Wildcat Mountain calderas have Nb+Y abundances that overlap with those of the high and ancestral Cascade rhyolites (Figure 2B). In contrast, the correlated basalts have high field strength element (HFSE) abundances and Nb/Yb and Th/Yb ratios that are elevated relative to N-MORB (Figure 2A and supplementary material) and the modern (e.g. Mazama) and ancestral Cascades (Bacon 1989; Bacon et al., 1997; du Bray and John, 2011). These relations are consistent with a deep, undepleted, sublithospheric mantle origin (Pearce and Pete, 1995).

In contrast, rocks associated with the Crooked River caldera are nearly aphyric, containing sparse quartz and feldspar, compositionally bimodal (basalt and rhyolite), and

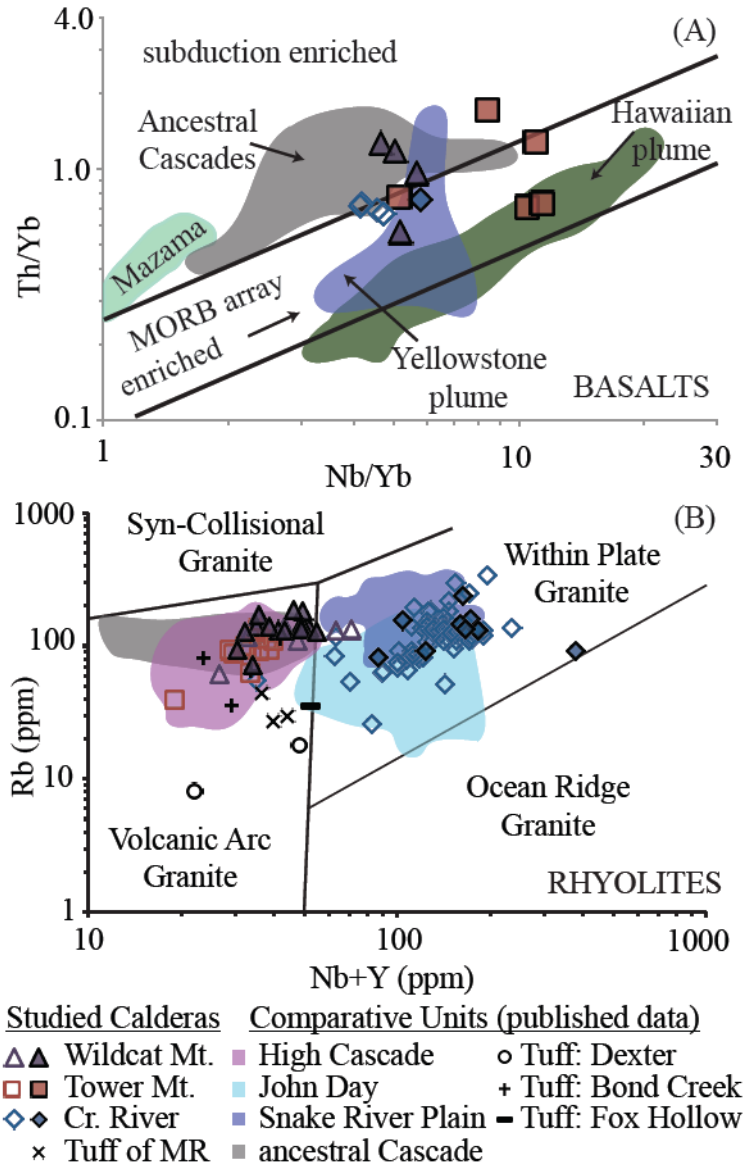

Figure 2. Trace element data for rocks from the studied calderas and other nearby Cenozoic volcanic rocks (see the supplementary material). A) Discrimination diagram showing trace element ratios for pre- and post- caldera basalts associated with the three eastern Oregon calderas; data field boundaries from Pearce and Peate (1995). All of the basalts have elevated Nb/Yb and Th/Yb relative to N-MORB. For caldera data, closed symbols are from this study and open symbols represent compiled published data from multiple sources (see supplementary data in Appendix B for references). B) Trace element discrimination diagram of Pearce et al. (1984) shows the relative abundances of Rb versus Nb+Y in rocks from the four studied calderas versus those of other nearby Cenozoic volcanic rocks, including specific tuffs of the ancestral Cascades (Dexter, Bond Creek, and Fox Hollow). The distinct overlap in the compositions of the Snake River Plain rocks of the Yellowstone hotspot track and those of the Crooked River rhyolites suggests similar petrogenetic histories.

do not contain hydrous minerals. These characteristics are consistent with a dry, high temperature, crystal poor magma. Rocks analyzed from the Crooked River caldera include multiple caldera-forming tuffs, ring-fracture rhyolites, and basaltic lavas. These types of rocks are similar to many rhyolites of the Yellowstone-Snake River Plain (Nash et al., 2006; Christiansen and McCurry, 2008; McCurry and Rodgers, 2009; Watts et al., 2011). The Crooked River and correlative John Day Formation rhyolites also have distinctly elevated Nb+Y concentrations (Figure 2B). Similar to the basalts of the Tower Mountain and Wildcat Mountain calderas, the basalts associated with the Crooked River eruptive center also have elevated HFSE and Nb/Yb and Th/Yb ratios relative to N-MORB (Figure 2A and supplementary material). These data are again consistent with a deep, undepleted, sublithospheric mantle origin (Pearce and Pete, 1995).

U-Pb dating of zircons and eruptive histories of the Oregon calderas

In an attempt to better constrain the eruptive order of the calderas, we determined U-Pb ages of zircons from three units of the Crooked River caldera. Although the ages of these three units correlate with known stratigraphic positions, their errors are unusually large, and we therefore report two possible ages for each unit. For all other units, we rely on previously determined $^{40}Ar/^{39}Ar$, K/Ar, and U-Pb ages as well as stratigraphic constraints.

$\delta^{18}O$ and εHf_i compositions: A case for crustal remelting

$\delta^{18}O$ and εHf_i compositions of zircon in the rhyolites of the four calderas were used as proxies for magmatic values and thus help distinguish magmatic processes that contributed to the petrogenesis of each of the four studied calderas. εHf_i in the individual zircons (+5.2 to +12.6) is lower than that of depleted mantle, as expected of young magma sourced from nondepleted mantle. There is an overall similarity of relatively high εHf_i value across the four calderas located west of the $^{87}Sr/^{86}Sr = 0.706$ line. The lowest εHf_i values (+5.2, +5.3) are from a single zircon in the tuff of Dale from the Tower Mountain caldera (+5.2, +5.3), which suggests the influence of an older (lower εHf_i) crustal source such as pre-Mesozoic sedimentary deposits of North America (Figure 6).

Measured $\delta^{18}O_{zircon}$ values are both lower and higher than normal mantle $\delta^{18}O_{zircon}$ values (+5.0–5.6 ‰; Valley et al., 2005). Magmas that crystallize $\delta^{18}O_{zircon}$ >5.6 ‰ generally necessitate assimilation of high $\delta^{18}O$ rocks (e.g. older supracrustal rocks), which is seen in rocks erupted from the Crooked River, Tower Mountain, and Wildcat Mountain calderas, whereas $\delta^{18}O_{zircon}$ <5.0 ‰ typically requires assimilation of material that was previously hydrothermally altered by low $\delta^{18}O$ meteoric water (Crooked River caldera – see below for further details) (e.g., Watts et al., 2011). $\delta^{18}O$ of zircons and quartz from the Mohawk River caldera in the ancestral Cascades arc of western Oregon (Figure 1) have εHf_i that ranges from +8.6–+12.4, and normal to moderately low $\delta^{18}O_{zircon}$ (~+5.0 ‰), which are in equilibrium with quartz ($\delta^{18}O$ = +6.9–+7.7 ‰). These normal $\delta^{18}O$ values are similar to other major coeval tuffs studied here from the ancestral Cascades (Figures 3–5), and also from arc rocks worldwide (Johnson et al., 2009; Bindeman et al., 2010). Conversely, rocks of the Wildcat Mountain and Tower Mountain calderas have elevated (+6.2–+7.9 ‰) zircon $\delta^{18}O$ values that are in equilibrium with other analyzed phenocrysts (plagioclase, quartz, and a few amphiboles) and subsequently show true magmatic isotopic fractionations (Figures 3–4). High $\delta^{18}O$ values require melting of high $\delta^{18}O$ rocks, such as supracrustal sediments and limestone, present in the surrounding Paleozoic Blue Mountains Province and xenoliths in most tuffs, which we determined to have a carbonate $\delta^{18}O$ value of +24.7‰. Alternatively, high $\delta^{18}O$ values could be coming from the underlying Siletzia terrane pillow lavas and high $\delta^{18}O$ sediments on top of Siletzia.

Zircons (cores and rims) in nine rhyolite units associated with the Crooked River caldera have a mixture of homogenous low and high $\delta^{18}O$ values, and heterogeneous $\delta^{18}O$ values within each sample (Figure 5). Only zircon and scarce quartz and feldspar phenocrysts preserve magmatic $\delta^{18}O$ values, because nearly all phenocrysts in the Crooked River rocks are altered. These low $\delta^{18}O$ units (+1.8–+4.5 ‰) include the major caldera-forming tuff of Smith Rock ($\delta^{18}O_{zircon}$ = +2.6 ‰; ~29 Ma), the tuff of Eagle Rock ($\delta^{18}O_{zircon}$ = +4.4 ‰; 29.7 Ma), and four ring fracture rhyolites ($\delta^{18}O_{zircon}$ = +2.3, +2.4, +2.4, +4.5). In addition, using laser fluorination we obtained a bulk zircon value of +4.2 ‰ for the 28.65 Ma Picture Gorge Ignimbrite of the John Day Formation (Figure 5). The

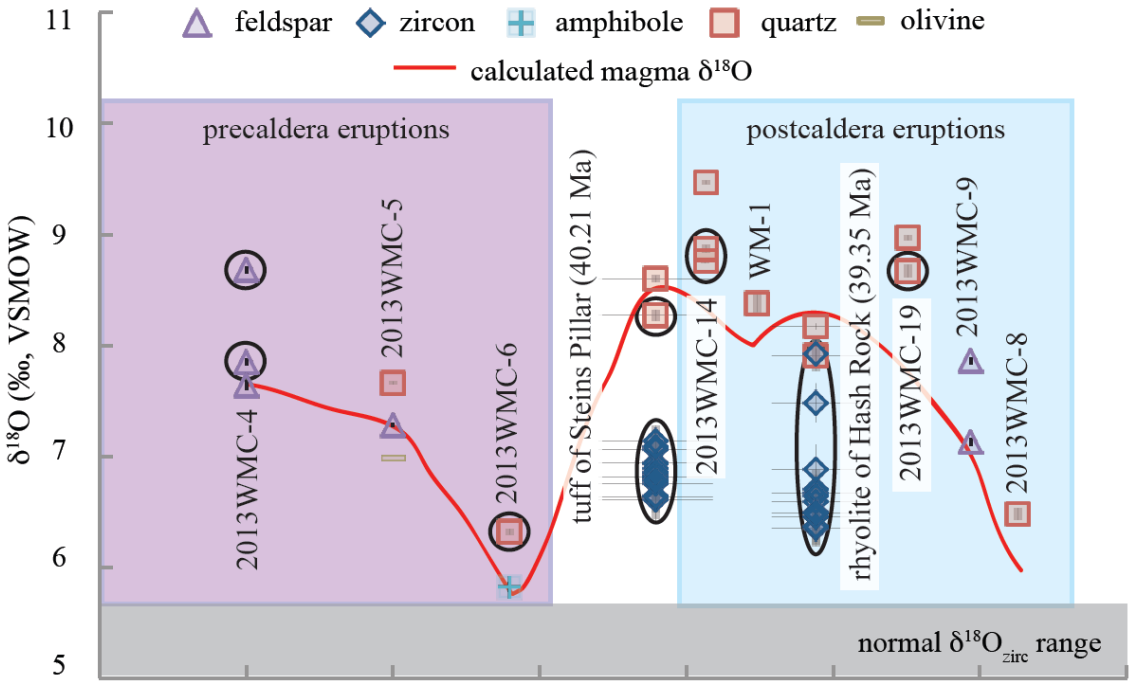

Figure 3. $\delta^{18}O$ vs. age for zircon, feldspar, quartz, olivine, and amphibole for rocks associated with the Wildcat Mountain caldera (references for ages are listed in the supplementary material in Appendix B). The vertical and horizontal bars through the symbols are 2σ error for the age (if applicable) and $\delta^{18}O$ analysis, respectively. A circle around the analysis indicates single grain analysis. The units analyzed are split into pre- and post-caldera subsets due to the lack of known relative ages for all units except two. The calculated magma $\delta^{18}O$ curve is based on the fractionation between average zircon (1.8 ‰), quartz (-1 ‰), or feldspar (~0 ‰) and the magma. The normal $\delta^{18}O_{zircon}$ range (5.0–5.6 ‰) is from Valley et al. (2005).

low $\delta^{18}O_{zircon}$ value suggests it was likely sourced from the Crooked River caldera. These low $\delta^{18}O_{zircon}$ values of successive caldera-forming ignimbrites and post-caldera lavas indicate that Crooked River is a voluminous low $\delta^{18}O$ province. The earlier erupted tuffs, however, have high $\delta^{18}O$ values: Antelope Creek ($\delta^{18}O_{zircon}$ +7.4–+8.8 ‰; ~29.6 Ma) and the Tuff of Rodman Spring ($\delta^{18}O_{quartz}$ +9.1–+10.7 ‰; 32.5 Ma), while post-Picture Gorge ignimbrite eruptions exhibit heterogeneous $\delta^{18}O_{zircon}$ populations: tuff of Barnes Butte (+2.3–+8.7 ‰; 28.3 Ma), and the ring-fracture rhyolite of Ochoco Reservoir (+2.0–9.0 ‰; 27.54 Ma). Large-scale remelting of previously erupted, initially high $\delta^{18}O$ tuffs and lavas, which were hydrothermally altered is required to produce so many low $\delta^{18}O$ units. These processes are similar to those that are considered responsible for low $\delta^{18}O$

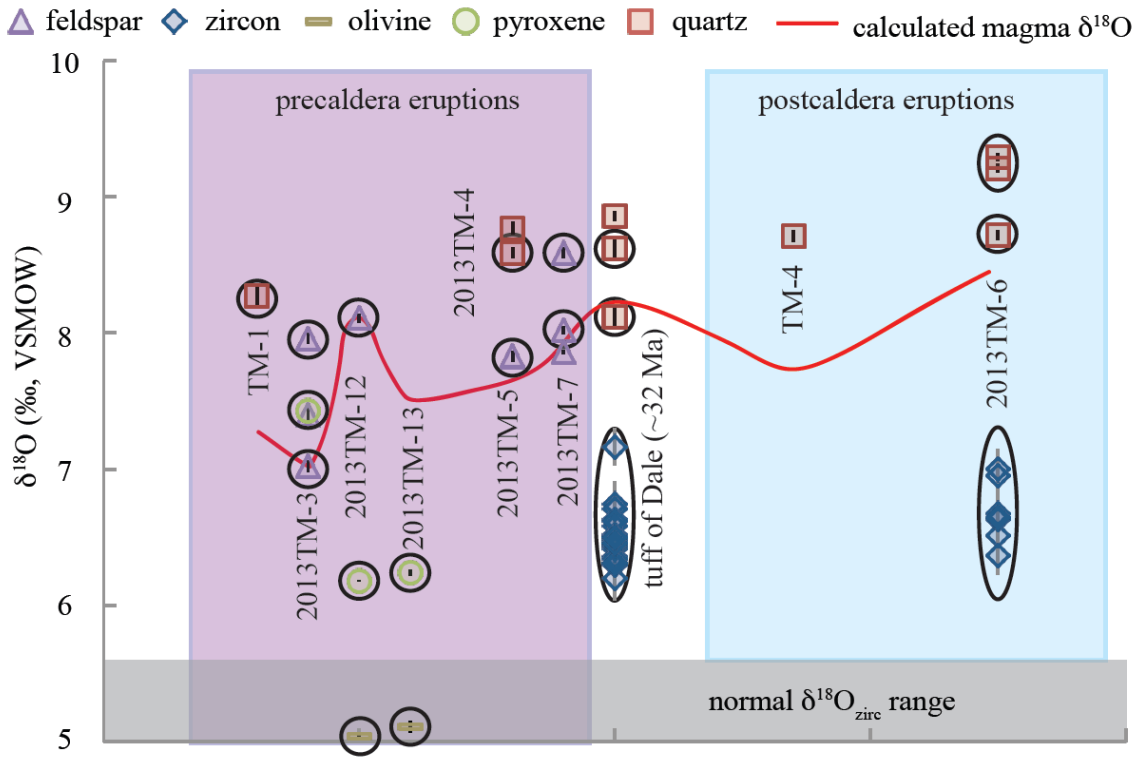

Figure 4. $\delta^{18}O$ vs. age for zircon, feldspar, quartz, olivine, and pyroxene for rocks associated with the Tower Mountain caldera. The age for the tuff of Dale is based on personal communication by Martin Streck. See Figure 3 for other symbols and explanations.

magmatism associated with the vast majority of the Yellowstone-Snake River Plain calderas (e.g. Bindeman and Simakin, 2014) (Figure 1).

The $\delta^{18}O$ values in all three central and eastern Oregon calderas signify large degrees of crustal melting of both high $\delta^{18}O$ basement and low $\delta^{18}O$ hydrothermally altered rocks. Since the zircons were extracted from rhyolites that were formed through crustal melting, the lower than depleted mantle εHf_i values also indicate influence of basement rocks that originated from sublithospheric mantle. The similarity of the εHf_i values across the three calderas therefore signifies a similar source, such as the surrounding Paleozoic Blue Mountains Province (Figure 6). Therefore, the difference in $\delta^{18}O$ values between the Wildcat and Tower Mountain calderas and the Crooked River caldera is not due to the difference in what is being melted, but is due to the degree of hydrothermal alteration. In other words, the elevated $\delta^{18}O$ values of the Wildcat

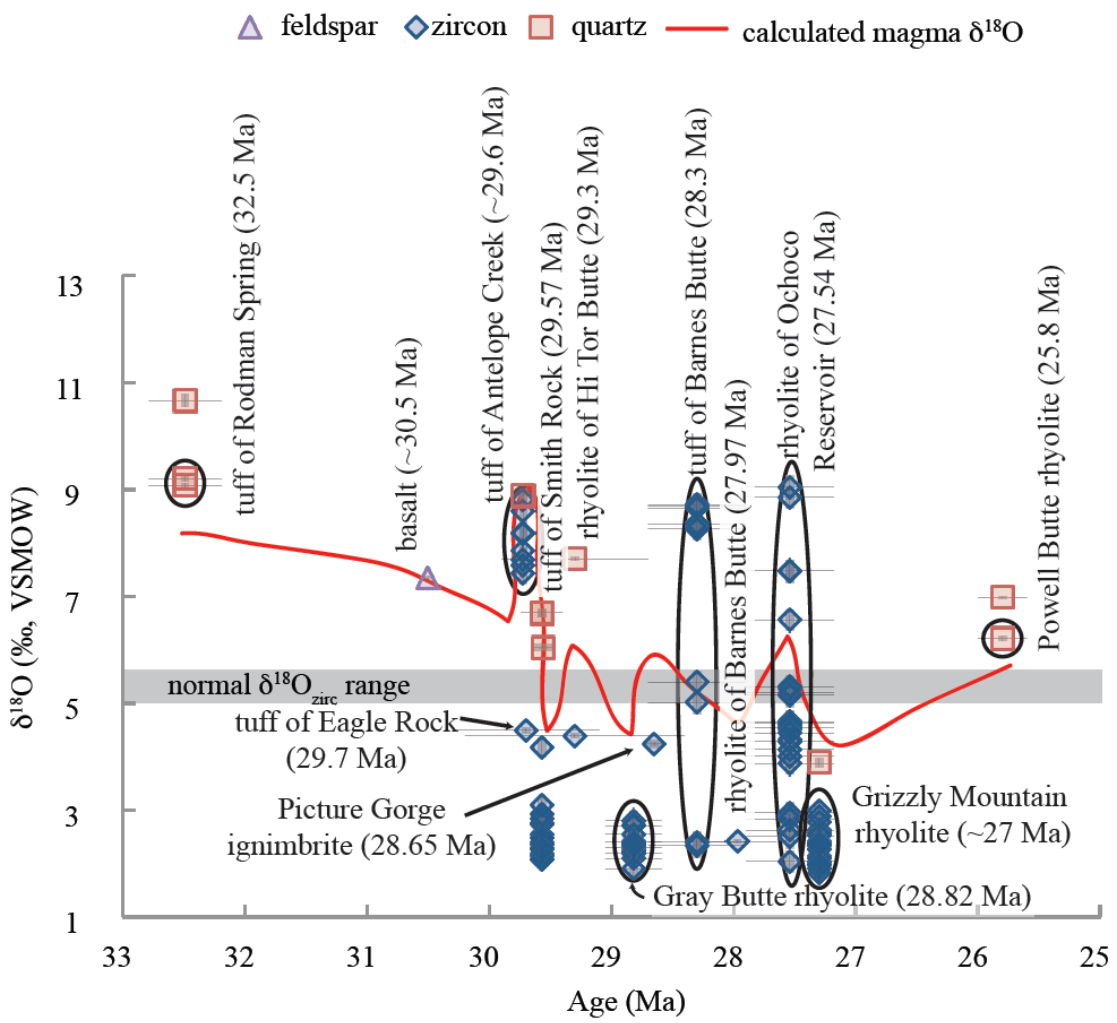

Figure 5. $\delta^{18}O$ vs. age for zircon, feldspar, and quartz associated with the Crooked River caldera. Ages are from this work and previous studies (listed in the supplementary material). The low $\delta^{18}O_{zircon}$ values of the Crooked River caldera are contrasted by the high $\delta^{18}O_{zircon}$ values of the Tower Mountain (Figure 4) and Wildcat Mountain (Figure 3) calderas. See Figure 3 for other symbols and explanations.

Mountain and Tower Mountain calderas define regional high $\delta^{18}O$ levels, from which the low $\delta^{18}O$ Crooked River magmas were derived after hydrothermal alteration.

DISCUSSION

Low $\delta^{18}O$ rhyolites associated with the Yellowstone hotspot

Eruptive centers associated with the Yellowstone plume have produced some of the world's most voluminous low $\delta^{18}O$ magmas. Low $\delta^{18}O$ magmas are associated with

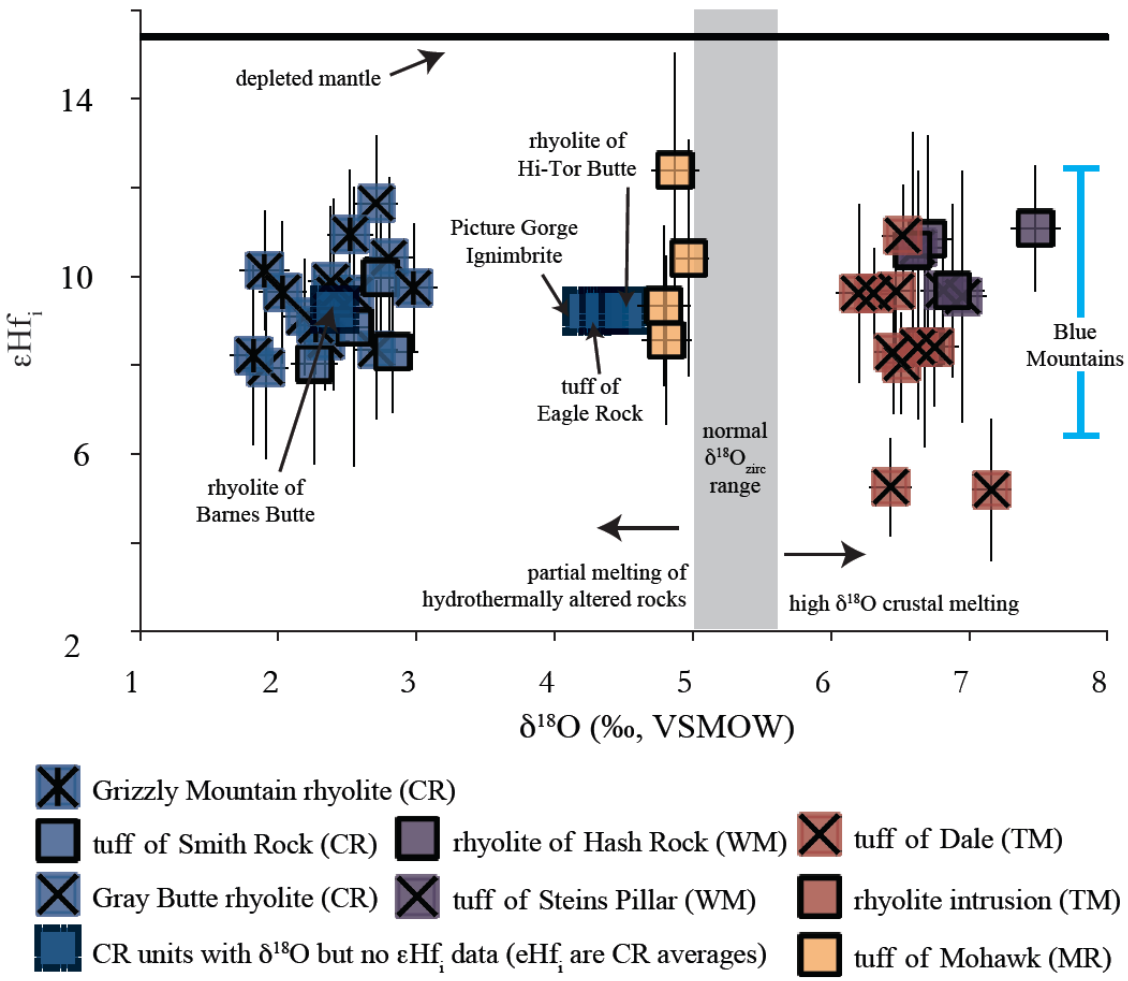

Figure 6. $\delta^{18}O$ vs. εHf_i data for samples of the studied calderas. εHf_i values for the Picture Gorge Ignimbrite, the rhyolite of Hi-Tor Butte, the Tuff of Barnes Buttes, and the Tuff of Eagle Rock are average values for the Crooked River caldera, since they were analyzed for $\delta^{18}O$ and not εHf, and are symbolized by a blue square with a dashed border. εHf_i depleted mantle value is from Nowell et al. (1998). The range in εHf_i values of zircons from the Blue Mountains Province is from Schwartz et al. (2011).

nearly all currently identified Yellowstone-plume related calderas, which have an aggregated low $\delta^{18}O$ eruption volume >10,000 km^3 (Boroughs et al., 2005; Cathey et al., 2011; Watts et al., 2011; Drew et al., 2013). Although plume magmas do not initially have lighter oxygen isotopic ratios, their larger heat source makes it possible, and more likely, to foster widespread hydrothermal circulation, alteration, and subsequent remelting that yields low $\delta^{18}O$ magmas (e.g. Bindeman and Simakin, 2014), which could be possible at eruptive centers such as Crooked River, as is further argued below. We

therefore use low $\delta^{18}O$ values in voluminous tuffs as an indicator of a need for an exceptionally large heat source to achieve repeated shallow crustal remelting.

Calderas of Oregon as geodynamic indicators

The location of the central-eastern Oregon calderas to the east of the ancestral Cascade volcanic arc, which was already developed prior to formation of these calderas (du Bray and John, 2011) (Figure 1), suggests these magmas are related to a within-plate tectonic process. Another significant trend involving their location is represented by their location along the suture between the Siletzia terrane and the terranes underlying the Blue Mountains Province (Figure 1). If these calderas were associated with flat slab subduction, a wider swath of ancestral Cascade arc volcanoes across Oregon should be (but is not) present. Instead, the ancestral Cascades reside to the west of the high Cascades (du Bray and John, 2011), which are still located to the west of the three eastern Oregon volcanoes of this study (Figure 1). If these magmas were formed through back-arc spreading, then an arc-parallel or rift-parallel arrangement of volcanic vents is expected, which is seen in back arc volcanism such as Kamchatka (Münker et al., 2004) or in rifting environments such as eastern Africa (Chorowicz, 2005). If these calderas were a northwestern extension of the 'ignimbrite flare-up' of the Great Basin of the southwest United States (Coney, 1978) one would expect to see a time transgressive series of eruptions due to the proposed 'peeling off' of the underlying Farallon slab from the base of the North American crust (Humphreys, 1995), which is also not observed (Figure 1). This hypothesis is also contrasted by seismic imaging by Gao et al. (2011) and Darold and Humphreys (2013) who imaged the Farallon slab beneath this region of Oregon, signifying that there has been no wholesale peeling off of the Farallon slab in this area. Therefore, a different tectonic process is needed, which incorporates the location of these calderas to the east of the ancestral Cascades arc and along the suture between the Siletzia terrane and the terranes underlying the Blue Mountains, which is likely a region of geodynamic instability (Gorcyzk et al., 2012).

A case for Yellowstone plume assisted delamination and the earliest appearance of caldera-forming volcanism of the Yellowstone plume

Recent work by Wells et al. (2014) shows that the Yellowstone plume was under central Oregon by ~35 Ma, and more specifically under the Crooked River caldera 32–28 Ma (see movie in supplementary material). Therefore, based on the location of the Yellowstone plume, and the location and geochemistry of the two ~30 Ma eastern Oregon calderas, we propose that their magmas are formed through interactions between the Yellowstone plume and delamination of the overlying crust near a region of geodynamic instability. The older 40 Ma Wildcat Mountain caldera likely has a different instability-based origin, which will be discussed below.

Current regional geodynamic models document complex interactions between the subducting Farallon slab and the Yellowstone plume (e.g. Johnston and Thorkelson, 2000; Murphy et al., 2003; Obrebski et al., 2010; Liu and Stegman, 2012). Models suggest that the plume could have five different options for how it interacted with the crust: 1) migrating through a gap in the Farallon slab; 2) migrating around the subducting slab, perhaps in bifurcating fashion; 3) melting through the slab; 4) ponding under the slab but allowing decompression basaltic partial melts to penetrate through it; or finally 5) ponding under the slab and causing the slab to buoyantly rise and restrict volcanism on top. The Yellowstone plume could have used any of the first four of these scenarios to migrate east of the Farallon slab following the formation of the Siletzia terrane.

In terms of plume-assisted delamination, numerical modeling by Burov et al. (2007) suggests that Rayleigh-Taylor instabilities of the lower crust occur within a few million years of the arrival of a plume at the base of the lithosphere. Camp and Hanan (2008) utilize plume-assisted delamination to explain the formation of the Columbia River Basalts. Plume-assisted delamination proceeds with: 1) creating cracks in the overlying crust through dikes and sills and 2) lowering the density and viscosity (10^{20} Pa•s; Steinberger and O'Connell, 1998) of the underlying mantle, which may in turn accelerate Stoke's sinking velocity, giving it sufficient time for devolatilization-melting of the surrounding mantle. Furthermore, non-plume-assisted delamination can still occur

within ~5 m.y. based on numerical modeling, depending on the density of the lower crust and the viscosity of the mantle (e.g. Elkins-Tanton and Hager, 2000; Elkins-Tanton, 2005). Non-plume-assisted delamination may explain the magma formation of the 40 Ma Wildcat Mountain caldera.

More specifically, we propose that the magmas of the Tower Mountain and Wildcat Mountain calderas were produced through delamination and devolatilization of portions of the underlying terranes of the Blue Mountains (Figure 7). Delamination was likely caused through one of two processes. The first possibility is that the docking of the Siletzia terrane between 51 and 49 Ma could have resulted in instabilities at its boundary with the Blue Mountains Province. Localized instabilites could have caused the first episode of delamination, producing the magmas of the Wildcat Mountain caldera, which formed ~40 Ma. The delamination event that formed the magmas of the Tower Mountain caldera, which erupted ~8 m.y. later, was likely caused by plume-assisted delamination, based on the longer period of time between the docking of the Siletzia terrane and the eastern migration of the Yellowstone plume. These hypotheses are supported by our new geochemical data. The mantle lithosphere beneath eastern Oregon was previously hydrated and modified by tens of millions of years of flat subduction prior to accretion of the Siletzia terrane (Atwater and Stock, 1998). If a portion of the terranes underlying the Blue Mountains were delaminated underneath the Wildcat Mountain and Tower Mountain calderas, previous hydration and modification would allow for subsequent devolatilization following delamination. Delamination would further allow magma to be produced from a deeper, non-depleted region of the mantle, as is supported by the trace elemental signature of basalts studied in this region (Figure 2A). Delamination also allows the magmas to be produced from a cooler, wetter mantle, subsequently producing phenocrystic rocks that are rich in hydrous minerals, which is characteristic of the rocks erupted from the Wildcat and Tower Mountain calderas.

In contrast, we propose that the Crooked River magmas are sourced directly from the Yellowstone plume. The formation of these magmas may also involve delamination, but this time of the Siletzia terrane, due to the close proximity between Crooked River and the suture between the Siletzia terrane and the Blue Mountains Province (Figure 1).

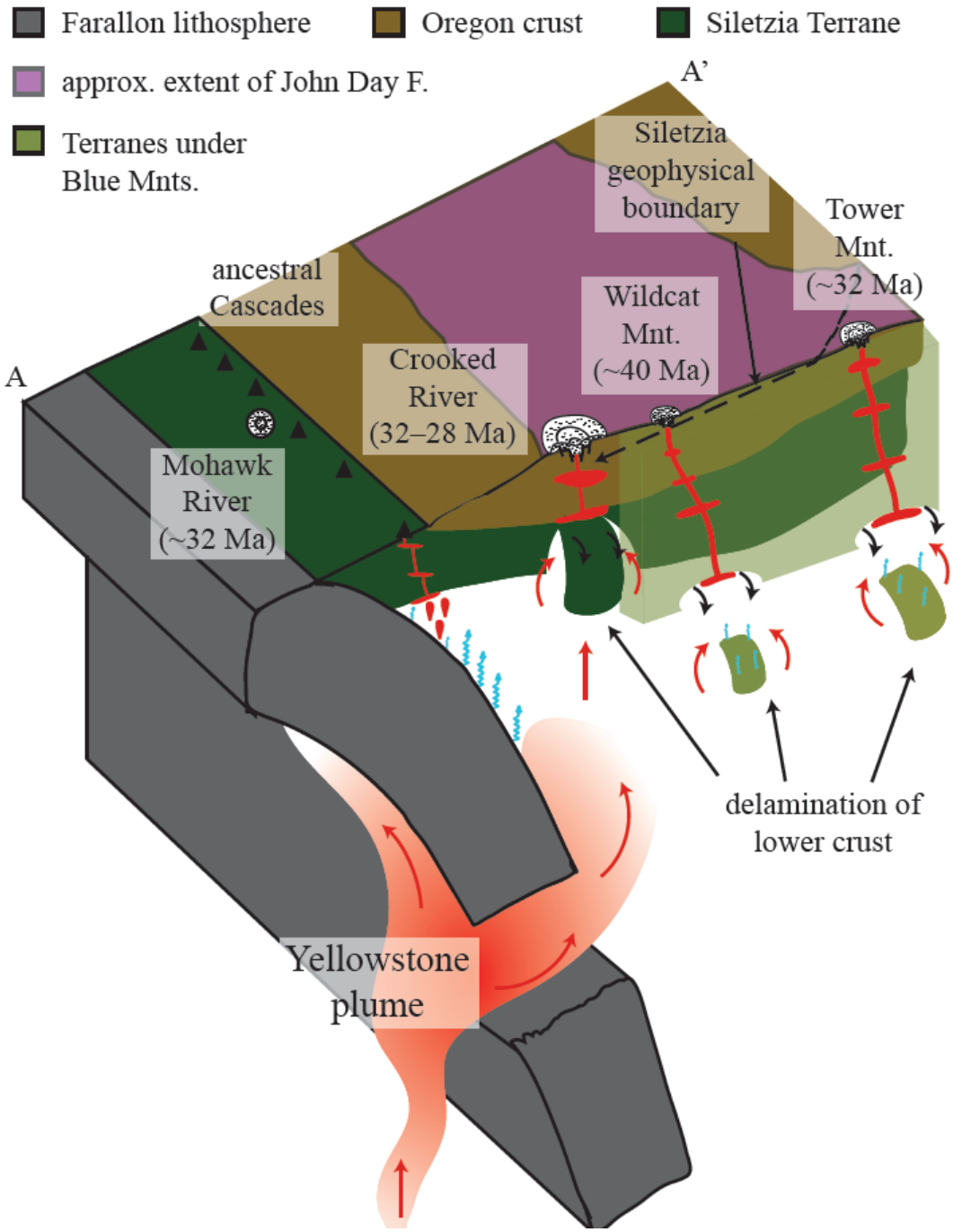

Figure 7. Schematic diagram illustrating the magmatic/tectonic setting that prevailed during formation of the four newly identified calderas. Small-scale delamination, devolatilization, and hydrous mantle melting of delaminated terranes underlying the Blue Mountains along the suture with the Siletzia terrane results in the magmas erupted from the Tower Mountain and Wildcat Mountain calderas. The largest episode of delamination (of the Siletzia terrane) produced the magmas of the Crooked River (super) caldera, aided by encroachment of Yellowstone plume. The location and compositional characteristics of the Mohawk River caldera (Figures 1–2) are consistent with subduction-related arc magmatism. The location of the A-A' transect is shown in map view in Figure 1.

Evidence for the Yellowstone plume producing magmas of the Crooked River caldera include: 1) geodynamic reconstructions using G-Plates by Wells et al. (2014) placing the Yellowstone plume under the Crooked River caldera from 32–28 Ma, which is the period of major and repeated silicic ignimbrite eruptions there (Figure 1; movie in supplementary material); 2) The nearly aphyric, "hot and dry" nature of rocks and mineral assemblages associated with the Crooked River caldera, similar to other eruptions of the Yellowstone plume (Nash et al., 2006; Christiansen and McCurry, 2008; McCurry and Rodgers, 2009; Watts et al., 2011), signifies the need for a large heat source; 3) The enriched-MORB geochemical signature of the basalts, signifying the need for a non-depleted mantle source, similar to the Yellowstone plume (Figure 2A); 4) The bimodal basalt-rhyolite character; and finally 5) The low $\delta^{18}O$ oxygen isotopic signature of multiple major Crooked River ignimbrites and post-caldera lavas, and zircon $\delta^{18}O$ diversity in some later units, similar to nearly all such magmas in the Yellowstone hotspot track. This amplifies the need for remelting and recycling of previously erupted and hydrothermally-altered ignimbrites being incorporated in the eruptive material and thus requires a large heat source under the eruptive center (e.g. Bindeman and Simakin, 2014). Hence, we propose that the Crooked River caldera represents the oldest low $\delta^{18}O$ province of the Yellowstone plume. Although not directly related to geotectonics, it is the recycled, low $\delta^{18}O$ nature of Crooked River ignimbrites and post-caldera lavas that provides the most compelling evidence for the earliest caldera-forming eruptions of the Yellowstone plume at ~32 Ma.

BRIDGE

In this chapter (Chapter III), I used isotopic ratios ($\delta^{18}O$ and εHf) in addition to trace element concentrations to document the formation of large-scale explosive volcanism across Oregon from 30–40 Ma. Utilzing the unusually low $\delta^{18}O$ values of the zircons from the Crooked River caldera, I was able to determine that the large Crooked River caldera is sourced from the Yellowstone plume. In addition, based on the location of the Tower Mountain and Wildcat Mountain calderas, in a region of geologic instability, and the trace element concentrations of the basalts, it appears that the magmas forming these calderas were sourced through small-scale delamination of the underlying crust.

To futher understand the source of these calderas, I became interested in the use of secondarily hydrated volcanic glass. However, little was known about the process of secondary hydration of volcanic glass, which is used to determine paleoelevations of regions. This is what is detailed in the next chapter (Chapter IV). In the following chapter, I will utilize suites of tephra from around the world to document the rate of secondary hydration, and the hydrogen isotopic ratios that are associated with the process of secondary hydration. In addition, I will document the effect that the residual primary magmatic water has on the total δD of the water extracted from secondarily hydrated volcanic glass, and the need for a primary magmatic water correction when using hydrated volcanic glass to understand paleoelevations.

CHAPTER IV

WATER IN VOLCANIC GLASS: FROM VOLCANIC DEGASSING TO SECONDARY HYDRATION

In review at Geochimica et Cosmochimica Acta as co-authored material with Ilya N. Bindeman, James M. Watkins, and Abigail M. Ross. I conducted the majority of this work, with advising by Ilya Bindeman. I drafted all the figures and the writing is mine, with assistance by Ilya Bindeman and James Watkins. James Watkins and I constructed the model in Matlab together that is utilized in this chapter. Abigail Ross is an undergraduate student that I advised, and she assisted with some of the image processing that was used in this chapter to understand the relative surface areas of the tephra.

INTRODUCTION

Volcanic glass is widely used for paleoclimate studies due to its uptake of meteoric water following deposition (Friedman et al., 1993b). This process is also known as secondary hydration or 'rehydration'. The presence of environmental waters in volcanic glass has been used as a tracer of the δD of local precipitation at the time of deposition (e.g. Riciputi et al., 2002; Mulch et al., 2007; Cassel et al., 2014; Canavan et al., 2014), and the extent of hydration by meteoric waters has been used to estimate the age of obsidian artifacts (e.g. Friedman et al. 1966; Anovitz et al., 2004). However, volcanic glass can be deposited with unknown quantities of primary magmatic water, which varies as a consequence of magmatic degassing processes (Newman et al., 1988; Dobson et al., 1989; Castro et al., 2014). Both magmatic and meteoric water can have distinct δD values (e.g. DeGroat-Nelson et al., 2001; Tuffen et al., 2010), depending on the δD value of the meteoric water that is diffusing into the glass, the degree of volcanic degassing that has occurred, and the original δD of the parental undegassed magma (Figs. 1–2). Therefore, these two types of water can obscure each other in δD-H_2O space when they are both present in volcanic glass, even though they could both provide useful information if the properties of one can be known or constrained. Furthermore, the general understanding of

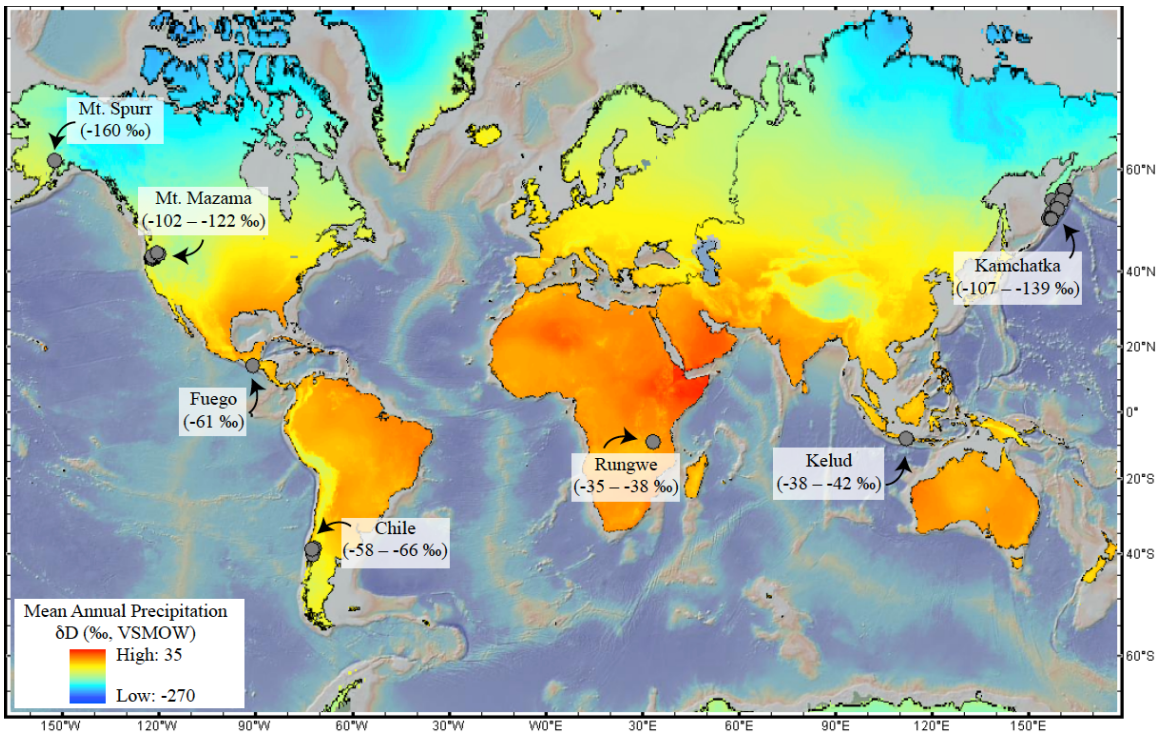

Figure 1. Sample locations along with local δD of precipitation range in ‰ plotted on a world map with an overlay of δD values (‰) of current precipitation (Bowen and Revenaugh, 2003; Bowen, 2015). The map was created using GeoMapApp as the underlying base map (the Global Multi-Resolution Topography (GMRT) synthesis). GPS coordinates and local δD (‰) of precipitation values for sample locations can be found in Table 1.

the process of secondary hydration is minimal, and it is still not well understood how long it takes for mafic and felsic glass to become secondarily hydrated at surface temperature and pressure.

Secondary hydration of volcanic glass

Rehydration of degassed (primarily water-free) silicate glass is a complex process of interface kinetics, water in-diffusion, and possibly minor re-speciation of hydrogen between dissolved molecular water and hydroxyl groups (e.g. Zhang, 1999; Anovitz et al., 2008; Nolan and Bindeman, 2013). The proposed models for rehydration range from a simple linear increase to a square root of time dependence (e.g. Friedman et al., 1966;

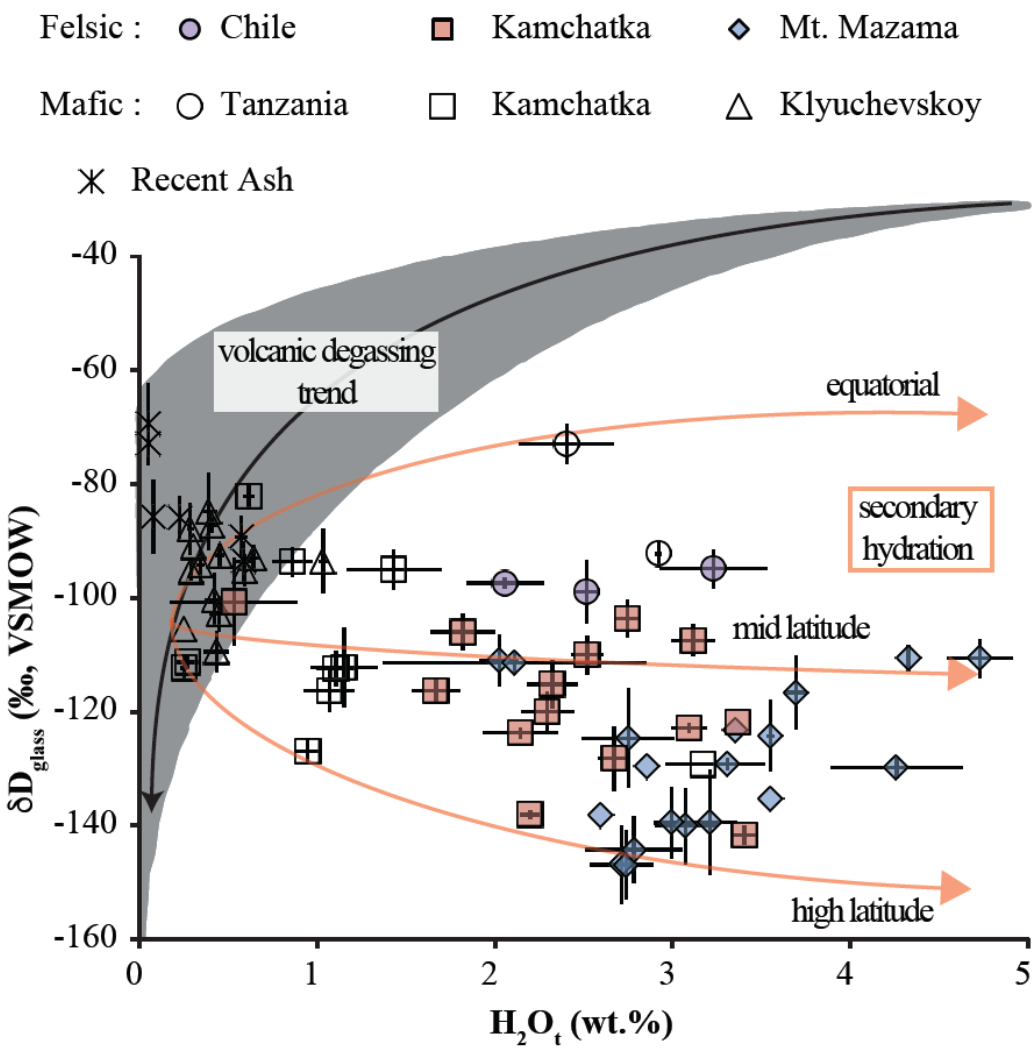

Figure 2. δD_{glass} in relation to the total water concentration of water extracted from the glass (±1σ). Two separate trends are shown: 1) The relationship between the δD (‰) and H_2O_t (wt.%) of volcanic degassing from Newman et al. (1988) and Castro et al. (2014) showing a decrease in δD (‰) with a decrease in total water concentration in the glass. The volcanic degassing trend illustrates the wide range in δD values for magmatic waters worldwide, with a trend towards heavier δD values at higher water concentrations; and 2) The relationship between the δD (‰) and H_2O_t (wt.%) of secondary hydration, which generally shows a decrease in δD (‰) with an increase in total water concentration in the glass. Although these trends are opposite one another, there is an overlap in δD (‰) values at water concentrations below ~1 wt.% H_2O_t between volcanic degassing and secondary hydration of volcanic glass. Otherwise, above ~1 wt.% H_2O_t, δD (‰) values below ~ -70 ‰ signify secondary hydration for non-tropical samples, while heavier δD (‰) values signify volcanic degassing and the presence of mostly primary magmatic water. This is based on the typical lower δD (‰) of precipitation in comparison to the δD (‰) of magmatic water. Local δD of precipitation for the locations where our glass samples were collected range between -35 and -160 ‰ (Fig. 1).

Nolan and Bindeman, 2013 and references therein). Since the diffusion coefficients of water in glass are a strong function of water concentration (Zhang and Behrens, 2000), hydration proceeds with a 'hydration front' that is possible to observe under a microscope (Ross and Smith, 1955; Friedman et al., 1966) and has therefore been used as a chronometer for dating. Riciputi et al. (2002) used microscopic observations and SIMS depth profiling of ancient obsidian artifacts of known age to quantify the distance of the hydration front 'X' into volcanic glass and determined that this distance (X) is proportional to the sum of linear and square root terms evaluated at time (t) (e.g. Friedman et al. 1966; Anovitz et al., 2004):

$$X \sim at + b\sqrt{Dt} \quad (1)$$

where a and b are coefficients that depend on glass composition and climate, and D is a concentration dependent diffusion coefficient.

Secondary hydration of rhyolitic glass at ambient temperature and pressure is thought to occur first through the exchange of hydrogen and deuterium ions with water soluble ions such as Na^+, K^+, and Ca^{2+} and then by the absorption of H_2O_{mol} (molecular H_2O) (Jezek and Noble, 1978; Cerling et al., 1985; Oelkers, 2001; Rébiscoul et al., 2007; Valle et al., 2010). In contrast, alteration of basaltic glass leads to the formation of water-rich (20–30 wt.% H_2O_t) palagonite on the outer rind of the glass (Stroncik and Schmincke, 2002; Crovisier et al., 2003; Parruzot et al., 2015). Although the hydration of mafic and felsic glass is different in some ways, previous work by Crovisier et al. (2003), Cailleteau et al. (2008), and Valle et al. (2010) showed that during the process of secondary hydration of both mafic and felsic volcanic glass, a thin (nanometers to micrometers, depending on time) layer of maximally (4–5 wt.% H_2O_t) hydrated glass, or 'gel layer', is formed on the surface of the glass. Increased densification, which leads to the closure of pores, causes the gel layer to serve as a protective film, which decreases the rate of further hydration of the glass interior. The formation of a gel layer is essential for studies involving nuclear waste disposal, but a decrease, instead of a termination, in the rate of alteration can still be problematic for paleoenvironmental research that utilizes

hydrogen isotopes, as was demonstrated by Anovitz et al. (2009) and Nolan and Bindeman (2013).

Hydrogen isotopes in secondarily hydrated volcanic glass

Friedman et al. (1966, 1993b) first proposed that hydrogen isotopes in secondarily hydrated ash and pumice could be used as a tool to monitor the D/H of the original hydrating water. Friedman et al. (1993a) showed that water uptake during rehydration results in an approximately -29 – -31 ‰ offset between felsic glass and water due to kinetic fractionation and the faster diffusion of hydrogen relative to deuterium. Their experiments led to a semi-empirical fractionation factor of $\alpha_{glass\text{-}water} = 0.9668 \pm 0.0005$ ($10^3 \ln\alpha_{glass\text{-}water}$ of -34). Subsequent research (e.g. Shane and Ingraham, 2002; Mulch et al., 2008; Cassel et al., 2014; Dettinger and Quade, 2015) has demonstrated that this empirically derived fractionation factor does not vary significantly across different surface level climatic conditions.

Recent studies have attempted to determine the reliability of the use of hydrogen isotopes as a paleoenvironmental indicator. Anovitz et al. (2009) used polished obsidian surfaces and isotopically labeled vapors to show that during secondary hydration at high temperature (150 °C), primary magmatic water dissolved in volcanic glass exchanges isotopically with the secondary water that diffuses into the glass. That is, any hydrogen already dissolved in the glass is not strongly bound to the aluminosilicate matrix and is able to exchange and/or undergo further diffusion into the glass. Subsequently, Nolan and Bindeman (2013) used long-term (3 years) time series experiments at 70, 40, and 20 °C with natural ash from the already secondarily hydrated 7.7 ka Mt. Mazama eruption to show that hydrogen isotopes equilibrate with surrounding deuterated waters on a timescale of years for 70 °C and 40 °C experiments. While hydrogen isotopes were able to readily exchange between ash and surrounding waters, the total water concentration and the $\delta^{18}O$ of the extracted water in the Nolan and Bindeman (2013) experiments remained relatively constant and identical to the original water. These studies by Anovitz

et al. (2009) and Nolan and Bindeman (2013) indicate that once ash becomes secondarily hydrated, its hydrogen isotopic ratio may be subject to change.

Primary versus secondary waters in volcanic glass

When relating D/H and H_2O_t (total water including molecular and hydroxyl groups) in secondarily hydrated tephra to ambient meteoric water, it is important to be able to estimate the residual amounts of (isotopically distinct) primary magmatic water (Fig. 2). Thus, an inherent difficulty exists in determining quantities of residual magmatic water left in volcanic glass, the environmentally-added water, and how to distinguish between these two during analysis. Furthermore, the potential exchange of hydrogen isotopes between the infiltrating secondary waters and the original primary magmatic waters, as well as the changing D/H of secondary waters through time, could further complicate environmental signals.

It is thought that the major difference between magmatic and environmental water is that, at low H_2O_t concentrations, magmatic water is predominantly in the form of dissolved OH^-, whereas environmental water is predominantly H_2O_{mol} (e.g. Newman et al., 1986; Silver et al., 1990; Giachetti et al., 2015). This is due to the higher energy, or temperature, needed for $H_2O_{mol} + O^{2-} = 2OH^-$ respeciation to form SiOH bonds rather than hydrogen bonds that are formed during the addition of H_2O_{mol}. Investigation of water speciation and distinguishing between different water types during progressive degassing creates potential opportunities to distinguish between magmatic and meteoric water (Fig. 3). Giachetti et al. (2015) used the TGA (Thermogravimetric Analysis) technique and compiled data for known water concentrations of 0.0005–22.5 ka intermediate to felsic volcanic glass ranging from approximately 0–4 wt.% H_2O_t to model the rate of secondary hydration of intermediate–felsic volcanic glass. They concluded that, at surface temperatures, intermediate to felsic volcanic glass has a rehydration diffusivity of approximately 10^{-23} m^2s^{-1} (± approximately one order of magnitude). These authors also numerically modeled TGA outputs to gain further insight into the process of secondary hydration through attempting to distinguish the difference in magmatic and

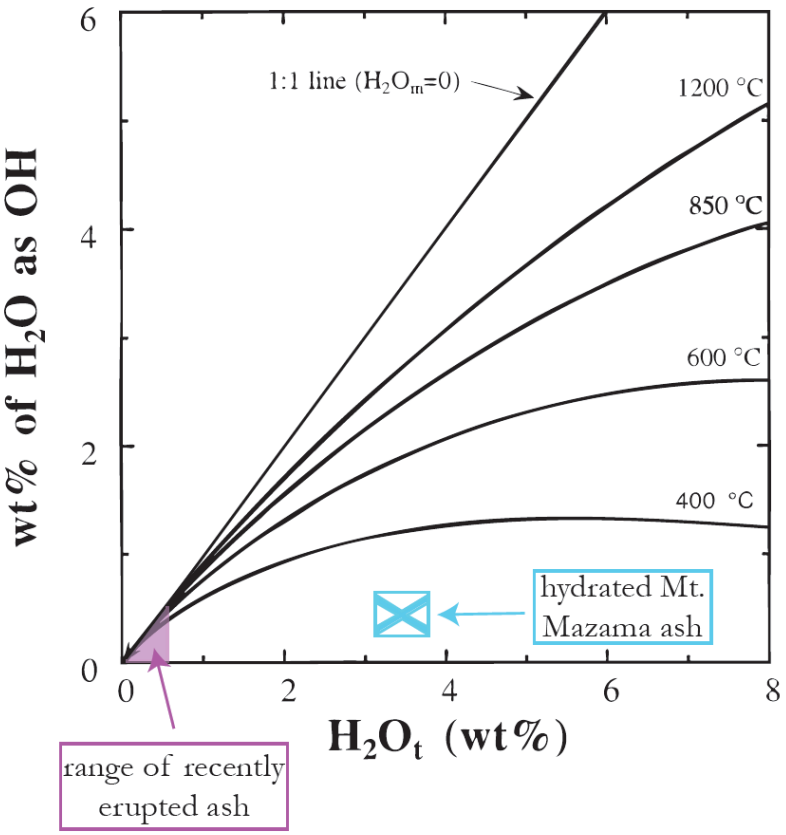

Figure 3. Relative quantities of H_2O_t and OH^- as modified from Ihinger et al. (1999), illustrating the larger quantities of OH^- relative to total H_2O_{mol} as temperature increases. We include potential ranges of recently erupted ash, which are from this study. We also include the location of secondarily hydrated Mt. Mazama ash from Nolan and Bindeman (2013), illustrating the low OH^- concentration relative to the concentration of H_2O_{mol} for low temperature hydration.

meteoric water in volcanic glass. As with any step heating technique, the assumption is that secondary water (H_2O_{mol}) is released at lower temperatures, while the more strongly bound primary magmatic water (OH^-) is released at higher temperatures. They showed that the 1060 CE Glass Mountain rhyolitic pumices from California contain only small amounts (0.2–0.5 wt.%) of residual primary magmatic water, and had 1–2 wt.% meteoric water. In addition, TGA coupled with FTIR (Fourier Transform Infrared) spectroscopy and D/H determination of hydrous Mt. Mazama ash was used by Nolan and Bindeman (2013) to understand proper heating temperatures to remove the most loosely bound adsorbed water on the glass, and at what temperatures the most tightly bound, possibly

magmatic water, is released. These authors observed a progressive increase in OH^-/H_2O_{mol} in the glass during successive heating and dehydration steps, which potentially documented the release of secondary meteoric water as H_2O_{mol} with low δD values. Importantly, the δD value of this progressively extracted water did not vary significantly below 600 °C. High OH^-/H_2O_{mol} and higher δD values were observed within the final 0.5 wt.% H_2O_t at the end of step heating (above 600 °C), which is interpreted to be primary magmatic water.

Collectively, these studies demonstrate that it is possible to obtain an estimate of the proportion of primary and secondary water in volcanic glass. It is not currently practical to conduct experiments for measuring the hydration rate of glass at room temperature due to the very slow rates of secondary hydration (1–10 μm/1000 years; Friedman et al., 1966; this study, see below). Below we attempt to further the understanding of secondary hydration at surface temperatures through the use of hydrogen isotopes, total water concentration, and relative vesicularities by using a natural experiment involving tephra of known ages.

Goals of the present study

Given the gaps in our understanding of the secondary hydration process, our research questions include:

1) What is the rate of secondary hydration for mafic and felsic volcanic glass?

2) What causes the difference in hydration rates between mafic and felsic glass?

3) How do the isotopes of hydrogen (D/H) behave during secondary hydration?

4) What effect does the D/H of the residual primary magmatic water have on the D/H of the total water during analyses of volcanic glass?

5) Is the fractionation between meteoric water and water-in-glass the same for mafic and felsic glasses?

To answer these questions, we use a series of natural volcanic tephra layers of known age across different climates to provide insight into the secondary hydration process in terms of the rates of secondary hydration and its isotopic signature (Table 1, Fig. 1). These volcanic tephra layers from around the world cover a large range of δD_{met} (δD of meteoric water) that also range in age, chemical composition, water concentration (H_2O_t, wt.%) and δD (‰). By utilizing volcanic ash and tephra, we gain a wider range of data than would be possible through the use of obsidian artifacts, and are able to compare our data to previously determined hydration rates of obsidians (Riciputi et al., 2002; Eerkens et al., 2008). In addition, we focus on six tephra units ranging from basalt to rhyolite that have different porosities, which we measure, to constrain the influence of vesicularity and composition on the secondary hydration process. Using this information, we then create simplified hydration models utilizing our water concentration and age data to estimate the diffusivities for secondary hydration of felsic and mafic glass.

METHODS

Samples

We use basaltic andesite scoria collected by us from Klyuchevskoy volcano in Kamchatka, Russia, with ages ranging from 0.05–7.3 ka. This volcanic scoria was used specifically due to the similar basaltic andesite composition of all samples collected from the same trench across an approximately 7000 year time span (Ponomareva et al., 2007; Auer et al., 2009; Ponomareva et al., 2013). Other mafic samples from Kamchatka include: the 3.5 and 7.2 ka eruptions of Avachinsky volcano, the 7.5 ka eruption of Kizimen, the 0.05, 1.0, 1.5, and 2.8 ka eruptions of Shiveluch volcano, and the voluminous pyroclastic products from the 7.6 ka caldera-forming eruption of Kurile Lake (Braitseva et al., 1997; Ponomareva et al., 2004; Kyle et al., 2011). We also analyzed mafic samples from Tanzania that include the 2.0 and 4.0 ka eruptions of Rungwe (Fontijn et al., 2010) (Tables 1–2; Fig. 1).

Felsic tephra samples were collected from Kamchatka, Chile, and the United States (Tables 1–2; Fig. 1). The Kamchatka units include: the 7.9 ka eruption of

Table 1
Location, age, and local precipitation δD (‰, VSMOW) of glass samples

Sample Name	Volcano	Age (ka)	Location N	Location E	Elevation (m)	Current local δD (‰) of precipitation
99163/9	Avachinsky	3.500	53.32	158.91	826	-124
99201/1	Avachinsky	7.150	53.25	159.04	369	-117
VF-74-200	Fuego	0.040	14.50[a]	-90.90[a]	2579	-69
VF-74-45	Fuego	0.040	14.50[a]	-90.90[a]	2579	-69
808 KAR 4	Karymsky	7.900	54.03	159.18	294	-120
Margomulyo-1p	Kelud	0.001	-7.93	112.24	617	-42
Campling-4p	Kelud	0.001	-7.97	112.18	329	-38
98032/4	Khangar	7.000	54.95	157.50	935	-134
80013/4	Kizimen	7.500	54.88	160.37	376	-124
KLV5-1	Klyuchevksoy	0.050	56.14	160.80	922	-136
KLV5-10	Klyuchevksoy	3.100	56.14	160.80	922	-136
KLV5-11	Klyuchevksoy	3.200	56.14	160.80	922	-136
KLV5-12	Klyuchevksoy	3.400	56.14	160.80	922	-136
KLV5-13	Klyuchevksoy	3.600	56.14	160.80	922	-136
KLV5-15	Klyuchevksoy	4.700	56.14	160.80	922	-136
KLV5-18a	Klyuchevksoy	5.700	56.14	160.80	922	-136
KLV5-22	Klyuchevksoy	7.300	56.14	160.80	922	-136
KLV5-3	Klyuchevksoy	1.000	56.14	160.80	922	-136
KLV5-5	Klyuchevksoy	1.600	56.14	160.80	922	-136
KLV5-6	Klyuchevksoy	2.300	56.14	160.80	922	-136
KLV5-7	Klyuchevksoy	2.600	56.14	160.80	922	-136
KLV5-8	Klyuchevksoy	2.700	56.14	160.80	922	-136
KLV5-9	Klyuchevksoy	2.800	56.14	160.80	922	-136
8880/5	Ksudach	1.800	51.87[a]	157.53[a]	318	-112
8889/2	Ksudach	6.400	51.87[a]	157.53[a]	318	-112
97KAM-03a	Kurile Lake	7.600	51.50	156.53	19.2	-107

Table 1 continued

Sample Name	Volcano	Age (ka)	Location N	Location E	Elevation (m)	Current local δD (‰) of precipitation
97KAM11	Kurile Lake	7.600	51.50	156.53	19.2	-107
97KAM29AL	Kurile Lake	7.600	51.38	157.27	73.2	-107
97KAM29DL	Kurile Lake	7.600	51.38	157.27	73.2	-107
97KAM29HW	Kurile Lake	7.600	51.38	157.27	73.2	-107
97KAM32D1	Kurile Lake	7.600	51.36	157.27	60.7	-107
97KAM-21CG	Kurile Lake	7.600	51.50	157.02	364	-112
97KAM-29AB	Kurile Lake	7.600	51.38	157.27	73.2	-107
97KAM29DB	Kurile Lake	7.600	51.38	157.27	73.2	-107
CLD205J	Llaima	10.00	-38.762	-71.6248	782	-62
2013MM-1	Mt. Mazama	7.700	43.92	-121.34	1366	-106
2013MM-10	Mt. Mazama	7.700	43.54	-121.95	1466	-107
2013MM-11	Mt. Mazama	7.700	43.48	-121.90	1419	-106
2013MM-12	Mt. Mazama	7.700	43.45	-121.87	1449	-106
2013MM-13	Mt. Mazama	7.700	43.38	-121.80	1434	-106
2013MM-14	Mt. Mazama	7.700	43.18	-121.79	1447	-106
2013MM-15	Mt. Mazama	7.700	43.09	-122.21	1650	-108
2013MM-16	Mt. Mazama	7.700	43.05	-122.35	1193	-102
2013MM-18	Mt. Mazama	7.700	43.14	-122.01	1887	-112
2013MM-2	Mt. Mazama	7.700	43.41	-121.22	1410	-106
2013MM-3	Mt. Mazama	7.700	43.43	-121.28	1433	-106
2013MM-4	Mt. Mazama	7.700	43.46	-121.39	1436	-106
2013MM-5	Mt. Mazama	7.700	43.52	-121.46	1327	-105
2013MM-6	Mt. Mazama	7.700	43.60	-121.50	1301	-105
2013MM-7	Mt. Mazama	7.700	43.59	-121.57	1310	-105
2013MM-8	Mt. Mazama	7.700	43.47	-121.70	1362	-105
2013MM-9	Mt. Mazama	7.700	43.56	-121.96	1479	-107
2014MM-1	Mt. Mazama	7.700	44.10	-119.99	1426	-108

Table 1 continued

Sample Name	Volcano	Age (ka)	Location N	Location E	Elevation (m)	Current local δD (‰) of precipitation
Mazama-WMC	Mt. Mazama	7.700	44.43	-120.60	1201	-105
42-Cordova	Mt. Spurr	0.022	61.3[a]	-152.30[a]	2795	-160
57-Ashton	Mt. Spurr	0.022	61.3[a]	-152.30[a]	2795	-160
98-10	Opala	0.300	52.55[a]	157.39[a]	823	-122
98-33/2	Opala	3.500	52.43	157.33	172	-112
98KAM2.3	Optr	4.600	52.63	157.48	385	-116
98KAM2.4	Optr	1.500	52.63	157.48	385	-116
CLD155A	Puyehue-Cordon Caulle	4.500	-40.25	-72.22	178	-58
KF149B	Rungwe	4.000	-9.05	33.63	2035	-38
KF155D	Rungwe	2.000	-9.08	33.57	1856	-35
96025/4	Shiveluch	1.000	56.57	161.51	372	-129
97044/1	Shiveluch	0.050	56.65	161.46	1028	-139
97049/2	Shiveluch	1.450	56.65	161.46	1028	-139
97051/2	Shiveluch	2.800	56.65	161.46	1028	-139
CLD064B	Sollipulli	3.000	-39.07	-72.52	979	-66

[a]approximate sample location

Table 2

δD (‰, VSMOW) (pre and post magmatic correction) and wt.% H_2O_t of water extracted from glass for each sample

Sample Name	Volcano	Age (ka)	composition	δD (‰)	s.d.	H_2O_t (wt.%)	s.d.	δD (‰) magmatic corrected
99163/9	Avachinsky	3.500	basaltic andesite	-112	2.2	0.2	0.02	NA
99201/1	Avachinsky	7.150	andesite	-95	3.5	1.4	0.26	-113
VF-74-200	Fuego	0.040	basalt	-86	3.7	0.2	0.01	NA
VF-74-45	Fuego	0.040	basalt	-86	6.4	0.1	0.01	NA
808 KAR 4	Karymsky	7.900	dacite	-141	1.6	3.4	0.07	-149
Margomulyo-1p	Kelud	0.001	basaltic andesite	-69	7.1	0.0	0.01	NA
Campling-4p	Kelud	0.001	basaltic andesite	-73	1.6	0.0	0.01	NA
98032/4	Khangar	7.000	dacite	-138	0.7	2.2	0.05	-150
80013/4	Kizimen	7.500	andesite	-129	0.2	3.2	0.21	-137
KLV5-1	Klyuchevksoy	0.050	basaltic andesite	-88	4.5	0.3	0.02	NA
KLV5-10	Klyuchevksoy	3.100	basaltic andesite	-95	2.8	0.6	0.01	-146
KLV5-11	Klyuchevksoy	3.200	basaltic andesite	-109	3.7	0.4	0.07	-179
KLV5-12	Klyuchevksoy	3.400	basaltic andesite	-100	4.7	0.4	0.05	-173
KLV5-13	Klyuchevksoy	3.600	basaltic andesite	-105	0.0	0.2	0.00	NA
KLV5-15	Klyuchevksoy	4.700	basalt	-93	5.6	1.0	0.02	-123
KLV5-18a	Klyuchevksoy	5.700	basaltic andesite	-92	1.9	0.4	0.02	-160
KLV5-22	Klyuchevksoy	7.300	basaltic andesite	-93	2.2	0.6	0.03	-140
KLV5-3	Klyuchevksoy	1.000	basaltic andesite	-85	6.8	0.4	0.04	NA
KLV5-5	Klyuchevksoy	1.600	basaltic andesite	-87	1.4	0.4	0.03	-162
KLV5-6	Klyuchevksoy	2.300	basaltic andesite	-95	1.7	0.3	0.01	NA
KLV5-7	Klyuchevksoy	2.600	basaltic andesite	-103	3.0	0.4	0.06	-170
KLV5-8	Klyuchevksoy	2.700	basaltic andesite	-91	0.0	0.3	0.00	NA
KLV5-9	Klyuchevksoy	2.800	basaltic andesite	-94	3.1	0.3	0.02	NA
8880/5	Ksudach	1.800	dacite	-122	0.0	3.4	0.00	-129
8889/2	Ksudach	6.400	dacite	-116	2.0	1.7	0.13	-132
97KAM-03a	Kurile Lake	7.600	rhyolite	-107	2.7	3.1	0.12	-116
97KAM11	Kurile Lake	7.600	rhyolite	-110	3.3	2.5	0.09	-120

Table 2 continued

Sample Name	Volcano	Age (ka)	composition	δD (‰)	s.d.	H_2O_t (wt.%)	s.d.	δD (‰) magmatic corrected
97KAM29AL	Kurile Lake	7.600	rhyolite	-115	4.2	2.3	0.14	-126
97KAM29DL	Kurile Lake	7.600	rhyolite	-120	3.4	2.3	0.15	-131
97KAM29HW	Kurile Lake	7.600	dacite	-128	5.6	2.7	0.09	-138
97KAM32D1	Kurile Lake	7.600	dacite	-123	0.9	3.1	0.10	-131
97KAM-21CG	Kurile Lake	7.600	andesite	-112	3.1	1.1	0.10	-138
97KAM-29AB	Kurile Lake	7.600	basaltic andesite	-111	1.1	0.3	0.06	NA
97KAM29DB	Kurile Lake	7.600	basalt	-93	2.6	0.9	0.11	-124
CLD205J	Llaima	10.00	dacite	-99	5.5	2.5	0.06	-109
2013MM-1	Mt. Mazama	7.700	rhyolite	-140	6.7	3.1	0.17	-149
2013MM-10	Mt. Mazama	7.700	rhyolite	-110	2.2	4.3	0.01	-117
2013MM-11	Mt. Mazama	7.700	rhyolite	-124	8.7	2.7	0.26	-134
2013MM-12	Mt. Mazama	7.700	rhyolite	-124	6.2	3.5	0.02	-132
2013MM-13	Mt. Mazama	7.700	rhyolite	-129	0.0	2.8	0.00	-139
2013MM-14	Mt. Mazama	7.700	rhyolite	-139	6.3	3.0	0.09	-148
2013MM-15	Mt. Mazama	7.700	rhyolite	-130	1.7	4.2	0.37	-136
2013MM-16	Mt. Mazama	7.700	rhyolite	-111	4.5	2.0	0.11	-124
2013MM-18	Mt. Mazama	7.700	rhyolite	-111	2.0	2.1	0.74	-124
2013MM-2	Mt. Mazama	7.700	rhyolite	-135	0.0	3.5	0.00	-142
2013MM-3	Mt. Mazama	7.700	rhyolite	-147	6.8	2.7	0.18	-156
2013MM-4	Mt. Mazama	7.700	rhyolite	-147	6.0	2.7	0.15	-156
2013MM-5	Mt. Mazama	7.700	rhyolite	-144	5.9	2.8	0.27	-154
2013MM-6	Mt. Mazama	7.700	rhyolite	-139	9.2	3.2	0.15	-147
2013MM-7	Mt. Mazama	7.700	rhyolite	-129	1.1	3.3	0.21	-137
2013MM-8	Mt. Mazama	7.700	rhyolite	-123	0.0	3.3	0.00	-131
2013MM-9	Mt. Mazama	7.700	rhyolite	-116	6.4	3.7	0.05	-124
2014MM-1	Mt. Mazama	7.700	rhyolite	-110	3.4	4.7	0.18	-116
Mazama-WMC	Mt. Mazama	7.700	rhyolite	-138	0.0	2.6	0.00	-148
42-Cordova	Mt. Spurr	0.022	andesite	-89	3.6	0.6	0.03	NA

Table 2 continued

Sample Name	Volcano	Age (ka)	composition	δD (‰)	s.d.	H_2O_t (wt.%)	s.d.	δD (‰) magmatic corrected
57-Ashton	Mt. Spurr	0.022	andesite	-93	3.5	0.6	0.05	NA
98-10	Opala	0.300	rhyolite	-100	7.7	0.5	0.35	-151
98-33/2	Opala	3.500	dacite	-106	3.1	1.8	0.18	-120
98KAM2.3	Optr	4.600	dacite	-123	1.0	2.1	0.21	-136
98KAM2.4	Optr	1.500	rhyolite	-103	3.4	2.7	0.07	-113
CLD155A	Puyehue-Cordon Caulle	4.500	dacite	-95	3.4	3.2	0.30	-103
KF149B	Rungwe	4.000	andesite	-92	5.8	2.9	0.91	-101
KF155D	Rungwe	2.000	andesite	-73	2.4	2.4	0.22	-84
96025/4	Shiveluch	1.000	andesite	-116	3.6	1.1	0.14	-141
97044/1	Shiveluch	0.050	andesite	-82	2.2	0.6	0.03	NA
97049/2	Shiveluch	1.450	basaltic andesite	-127	2.0	0.9	0.08	-155
97051/2	Shiveluch	2.800	andesite	-112	6.9	1.1	0.19	-135
CLD064B	Sollipulli	3.000	dacite	-97	0.9	2.0	0.22	-110

Karymsky volcano, the 1.8 and 6.4 ka eruptions of Ksudach volcano, the 7.6 ka eruption of Kurile Lake, the 0.3 and 3.5 ka eruptions of Opala volcano, the 7.0 ka eruption of Khangar volcano, and the 1.5 and 4.6 ka Optr eruptions (Braitseva et al., 1997). Chilean units are from the: 10 ka Llaima, 3.0 ka Sollipulli, and 4.5 ka Puyehue-Cordon Caulle eruptions (Fontijn et al., 2014). We also collected multiple samples throughout Oregon from the 7.7 ka Mt. Mazama eruption that formed Crater Lake.

All samples analyzed in this study are ≤ 10,000 years old. Based on their relatively young, post-glacial Holocene ages, we assume that they are hydrated with meteoric water that has approximately similar δD to current precipitation. Therefore, all samples should be young enough that the δD (‰) of the meteoric water hydrating them should not be significantly changing on a millennial timescale (e.g. Henderson et al., 2010, which suggests 15–20 ‰ shifts in δD over the last 10,000 years).

Hydrogen isotope and total water analyses of tephra and ash

All volcanic glass samples from this study were analyzed for both δD and H_2O_t on the TCEA continuous flow and sampling system at the University of Oregon stable isotope laboratory (e.g. Bindeman et al., 2012). Prior to analysis, tephra samples were lightly crushed, placed in a water-filled beaker, and sonicated for ~60 min to remove any clays that, if present, may be attached to the glass. The samples were then dried and individual glass shards smaller than ~0.5 mm were picked under microscope to ensure that the glass was pristine. We first experimented with pretreating samples with 8% HF twice for 30 seconds (Cerling et al., 1985; Sarna-Wojcicki and Davis, 1991; Cassel et al., 2012), but found that such a procedure yields greater scatter (Fig. A1; see Appendix C for all Chapter IV supplemental figures) and abandoned this approach because our samples are fresh and do not contain any secondary 'gel' layer as for the above mentioned studies. Our results, which are similar to those from Dettinger and Quade (2015) that show glass samples pretreated with HF having variable δD effects in glass that are not well understood, we chose not to pretreat any samples in 8% HF. Following sample preparation, 2–12 mg of glass (depending on the expected water content, where the lowest water content samples need the largest mass of glass) were picked using a binocular microscope and packaged in silver foil. Ash samples were sieved to keep the 50–250 μm size fraction, as demonstrated by experimentation with glass standards to yield the best reproducibility (Bindeman et al., 2012). Some ash samples contain too many small phenocrysts (microphenocrysts or microlites) to be completely separated from the glass. For these samples, a modal percent of minerals was approximated, and the wt.% H_2O_t was corrected following the analysis (Table 3). These small phenocrysts were all determined to be anhydrous, so a correction was only needed for the wt.% H_2O_t and not for the δD value. Prior to analysis, all samples were heated in a vacuum-sealed oven overnight at 130 °C to remove any adsorbed waters on the outer surface of the glass (e.g. Nolan and Bindeman, 2013). Samples were then immediately transferred to a TCEA autosampler (typically within 10–15 min), loaded and purged with He carrier gas in an autosampler.

Table 3
Relative vesicularity and percent microlites of glass samples

Sample Name	Volcano	Age (ka)	Relative vesicularity (1–10)	Microlites (%)
99163/9	Avachinsky	3.500	2	1
99201/1	Avachinsky	7.150	3	5
VF-74-200	Fuego	0.040	10	15
VF-74-45	Fuego	0.040	10	15
808 KAR 4	Karymsky	7.900	8	0
Margomulyo-1p	Kelud	0.001	5	2
Campling-4p	Kelud	0.001	5	2
98032/4	Khangar	7.000	7	3
80013/4	Kizimen	7.500	6	0
KLV5-1	Klyuchevksoy	0.050	3	30
KLV5-10	Klyuchevksoy	3.100	2	35
KLV5-11	Klyuchevksoy	3.200	3	30
KLV5-12	Klyuchevksoy	3.400	1	40
KLV5-13	Klyuchevksoy	3.600	2	20
KLV5-15	Klyuchevksoy	4.700	4	35
KLV5-18a	Klyuchevksoy	5.700	4	30
KLV5-22	Klyuchevksoy	7.300	2	50
KLV5-3	Klyuchevksoy	1.000	2	40
KLV5-5	Klyuchevksoy	1.600	2	20
KLV5-6	Klyuchevksoy	2.300	4	10
KLV5-7	Klyuchevksoy	2.600	4	20
KLV5-8	Klyuchevksoy	2.700	4	30
KLV5-9	Klyuchevksoy	2.800	4	20
8880/5	Ksudach	1.800	8	0
8889/2	Ksudach	6.400	8	0
97KAM-03a	Kurile Lake	7.600	9	0
97KAM11	Kurile Lake	7.600	5	1
97KAM29AL	Kurile Lake	7.600	5	2
97KAM29DL	Kurile Lake	7.600	9	0
97KAM29HW	Kurile Lake	7.600	9	0
97KAM32D1	Kurile Lake	7.600	6	2
97KAM-21CG	Kurile Lake	7.600	9	1
97KAM-29AB	Kurile Lake	7.600	8	2
97KAM29DB	Kurile Lake	7.600	8	2
CLD205J	Llaima	10.00	8	0
2013MM-1	Mt. Mazama	7.700	7	0
2013MM-10	Mt. Mazama	7.700	7	0
2013MM-11	Mt. Mazama	7.700	7	0

The first part of this study included standardization using three mica reference standards during each set of analyses (NBS30 biotite, δD = -65.7 ‰, and two other in

Table 3

Sample Name	Volcano	Age (ka)	Relative vesicularity (1–10)	Microlites (%)
2013MM-12	Mt. Mazama	7.700	7	0
2013MM-13	Mt. Mazama	7.700	7	0
2013MM-14	Mt. Mazama	7.700	7	0
2013MM-15	Mt. Mazama	7.700	7	0
2013MM-16	Mt. Mazama	7.700	7	0
2013MM-18	Mt. Mazama	7.700	7	0
2013MM-2	Mt. Mazama	7.700	7	0
2013MM-3	Mt. Mazama	7.700	7	0
2013MM-4	Mt. Mazama	7.700	7	0
2013MM-5	Mt. Mazama	7.700	7	0
2013MM-6	Mt. Mazama	7.700	7	0
2013MM-7	Mt. Mazama	7.700	7	0
2013MM-8	Mt. Mazama	7.700	7	0
2013MM-9	Mt. Mazama	7.700	7	0
2014MM-1	Mt. Mazama	7.700	7	0
Mazama-WMC	Mt. Mazama	7.700	8	0
42-Cordova	Mt. Spurr	0.022	10	30
57-Ashton	Mt. Spurr	0.022	10	30
98-10	Opala	0.300	8	0
98-33/2	Opala	3.500	7	0
98KAM2.3	Optr	4.600	7	0
98KAM2.4	Optr	1.500	8	0
CLD155A	Puyehue-Cordon Caulle	4.500	7	0
KF149B	Rungwe	4.000	8	0
KF155D	Rungwe	2.000	7	0
96025/4	Shiveluch	1.000	5	5
97044/1	Shiveluch	0.050	4	5
97049/2	Shiveluch	1.450	4	5
97051/2	Shiveluch	2.800	5	5
CLD064B	Sollipulli	3.000	7	0

house standards calibrated relative to NBS30 in three other labs: BUD Butte (MT) quartz monzonite biotite, δD = -161.8 ‰, and RUH2 muscovite, δD = -98.2 ‰), which nearly span the range of our unknowns. Following each set of analyses, a three point calibration using the offsets between the measured and nominal δD values for the mica standards was performed to correct for day to day analytical variations in δD values. These same analyses were also used to determine the total water content in the glass. NBS30, with a known wt.% H_2O_t of 3.5 was used as a standard for water concentration corrections.

In order to present our results relative to VSMOW, we ran glass samples in the latter part of this study against water (VSMOW, W62001, and GISP) sealed in silver cups (Qi et al., 2010). Due to a recent study by Qi et al. (2014), which demonstrated that the NBS30 nominal δD value is 15–21 ‰ heavier than previously proposed, we ran all of our mica standards (NBS30, BUD, and RUH2) directly against these waters sealed in silver cups, which have δD values spanning the relevant δD range to our solid unknowns, to calibrate the water content in our glasses for our lab specifically relative to a water-based VSMOW scale. For further information on the correction of the NBS30 standard, see Qi et al. (2014), which is what we base our lab specific corrections on. Through seven different analytical sessions of calibration between our mica standards and the three water standards, we obtain a conversion equation of: $\delta D_{mica\ corrected} = 0.9888\delta D_{initial} + 15.385$, with an R^2 of 0.99179. We use this conversion equation to correct all of our mica data, which provided a correction of +16–17 ‰ to our old mica-based normalization, depending on the δD value. The data below are all reported with respect to VSMOW and other waters.

SEM imaging of volcanic tephra to determine surface to volume ratios and bubble wall thicknesses

Six tephra units shown in Table 4 with known water content and δD were imaged with Back-Scattered Electrons (BSE). These tephra were chosen to provide a range of vesicularity and bubble wall thickness for mafic units of various ages from the same volcano (Klyuchevskoy), as well as for a range in compositions from the same compositionally diverse eruption (Kurile Lake). These six tephra were photographed under high magnification using a FEI Quanta 200 SEM microscope at 20 keV, allowing sub-micron resolution (Fig. 4). The photographs were converted to black and white in Adobe Photoshop and checked to make sure all black regions were vesicles (Fig. 5). If they were not, they were changed to white, and vice versa. A separate image was then created so that the entire tephra clast, including vesicles, was all one color. This allowed for the entire area of the tephra clast and vesicles to be determined. Another image was

Table 4
Tephra data for BSE imaged tephra from Kurile Lake and Klyuchevskoy volcanoes in Kamchatka, Russia

Unit	Volcano	Age (ka)	composition	Region of Clast	Area (mm^2)	Total Perimeter (mm)	Number	Number Density	Average Bubble Wall Thickness (mm)
KLV5-1	Klyuchevskoy	0.05	basaltic andesite	Total Image	34.0	92.8	1	27	0.103
				Minerals	0.71	8.08	7		
				Vesicles	15.6	450	899		
				Glass	17.7				
KLV5-8	Klyuchevskoy	2.7	basaltic andesite	Total	23.7	63.4	1	28	0.075
				Minerals	0.72	7.29	5		
				Vesicles	12.1	248	650		
				Glass	10.9				
KLV5-22	Klyuchevskoy	7.3	basaltic andesite	Total	24.6	52.6	1	72	0.051
				Minerals	1.23	12.4	13		
				Vesicles	13.8	442	1695		
				Glass	9.62				
97KAM29AL	Kurile Lake	7.6	rhyolite	Total	36.8	109	1	736	0.017
				Minerals	0.16	3.80	6		
				Vesicles	13.1	2078	26983		
				Glass	23.6				
97KAM29DB	Kurile Lake	7.6	basalt	Total	96.7	159	1	77	0.058
				Minerals	32.7	224	129		
				Vesicles	32.9	1447	4953		
				Glass	31.2				
97KAM21CG	Kurile Lake	7.6	andesite	Total	31.0	59.4	1	161	0.030
				Minerals	4.80	55.0	35		
				Vesicles	9.08	554	4215		
				Glass	17.2				

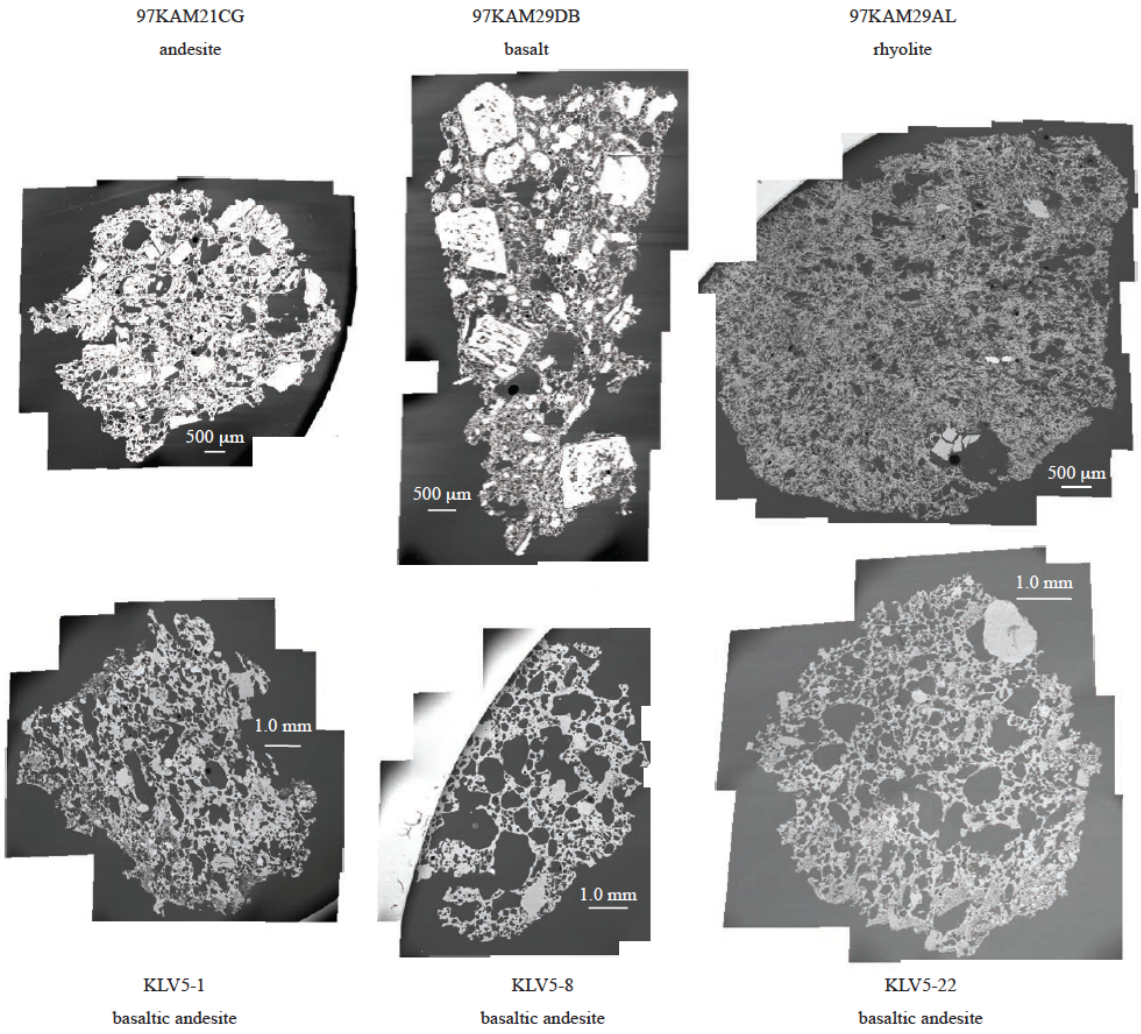

Figure 4. BSE images of tephra used for basalt-andesite-rhyolite texture comparisons. Note the similarities of bubble number densities and bubble wall thicknesses in the Klyuchevskoy basaltic andesites (KLV5 units). The Klyuchevskoy units typically have fewer, yet larger, vesicles. In contrast, the basalt from the Kurile Lake eruption (97KAM29DB) generally has a larger number of smaller vesicles, which is likely due to the greater explosivity of the eruption. The rhyolite sample from the Kurile Lake eruption (97KAM29AL) has the largest number density and smallest bubble wall thicknesses in comparison to any of the basalts or andesites in this study (see Tables 3–4).

created with just the minerals shown in black, so these areas could be removed from any subsequent calculations. All images were imported into the image-processing program NIH ImageJ, which was used to determine the number of vesicles, the area of each vesicle, the perimeter of each vesicle, the total area of the tephra clast including the

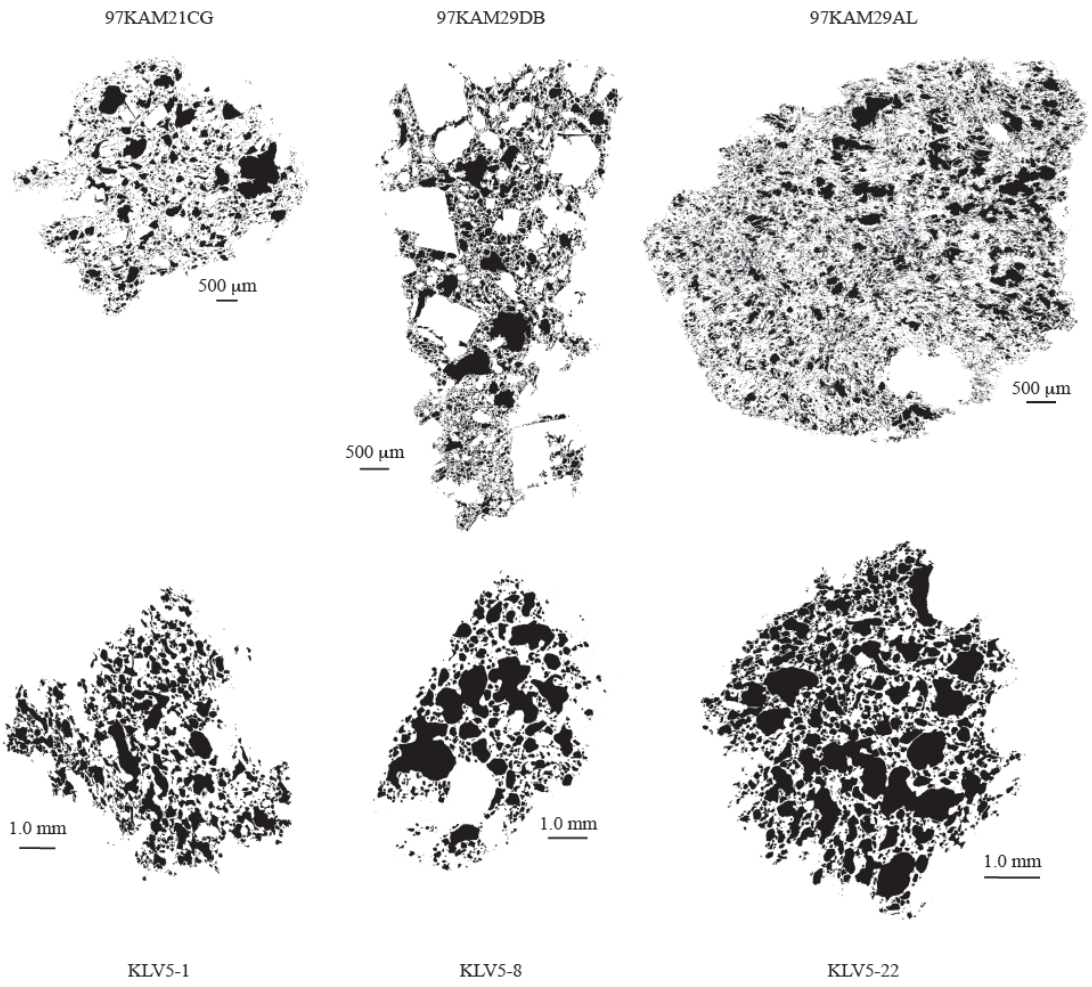

Figure 5. Black and white vesicle images of tephra clasts that were created from the BSE images in Fig. 4. These images were used to determine the number, area, and perimeter of the vesicles for each tephra clast in ImageJ (see Fig. 6).

vesicles and the glass, and the area of the minerals (Fig. 6). The perimeter of each vesicle was assumed to create a circle, and the radius of each vesicle was calculated from: $R = \frac{P}{2\pi}$, where R is the radius of the assumed circle in mm and P is the perimeter in mm. Following Giachetti and Gonnermann (2013), we assumed that the vesicles are distributed evenly across the tephra clast (i.e., we use the hexagonal close-packing assumption of Princen (1979) and Proussevitch et al. (1993)) and estimated the average

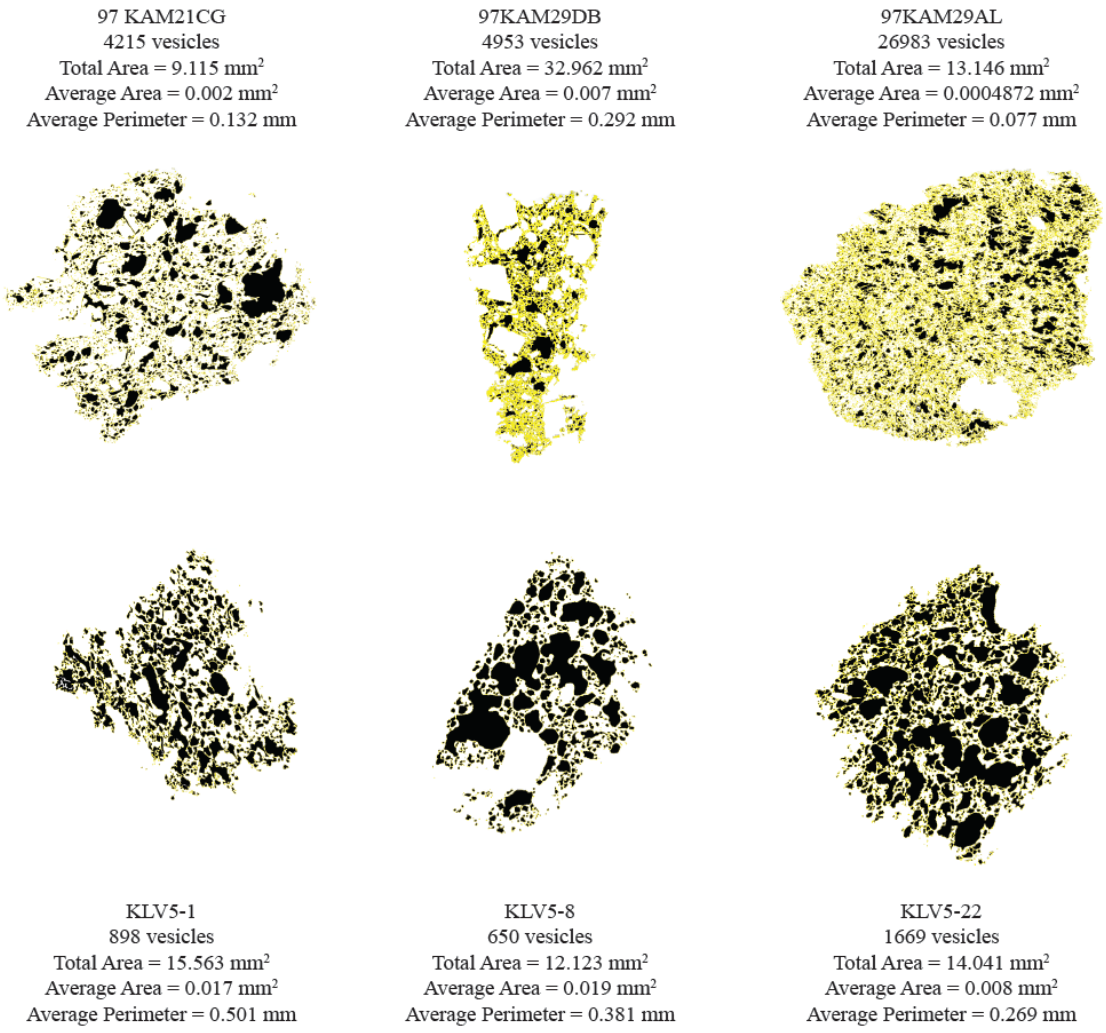

Figure 6. Results from ImageJ analyses of the black and white images of each tephra clast (see Fig. 5) showing the number, area, and perimeter of the vesicles. Each vesicle counted and analyzed by ImageJ is outlined in yellow.

bubble wall thickness for each tephra clast using the equation: $S = \frac{R}{\phi^{\frac{1}{3}}}$, where S is the average thickness of the bubble wall in mm, ϕ is the vesicularity, and R is again the radius in mm. As a check, these values were compared to the SEM tephra clast images (Figs. 4–6) to ensure that they are indeed reasonable.

RESULTS

We report data from Holocene ash and tephra and provide a range of water concentrations and D/H from 0–10 ka volcanic glass of both mafic and felsic composition to better understand hydration rates and corresponding D/H trends with secondary hydration.

Water concentration and hydrogen isotopes in felsic and mafic ashes and scoria

Recently deposited felsic ash samples

The recently deposited ash from the 1992 eruption of Mt. Spurr (42-Cordova and 57-Ashton), the 1974 eruption of Volcán de Fuego (VF-74-45 and VF-74-200), and the 2014 eruption of Kelud (Margomulyo-1p and Campling-4p) are used to gain a better understanding of the quantity of residual undegassed magmatic water dissolved in the glass that volcanic ash is deposited with, and the δD of these associated dissolved waters. These glasses were all collected either during or recently following eruption, so they are assumed to contain only magmatic water, and provide a constraint on the H_2O_t and D/H of primary magmatic water. These data plot within the magmatic degassing trend in Figure 2. The H_2O_t of these samples ranges from 0.1–0.6 wt.% H_2O_t and the δD ranges from -69 to -93 ‰.

Mass balance relations

Results above indicate that unaltered volcanic ash can contain as much as ~0.6 wt.% magmatic water. Although these quantities vary from one tephra layer to the next (0.1–0.6 wt.%), the average water content is 0.3 wt.%. Using these data, we can account for

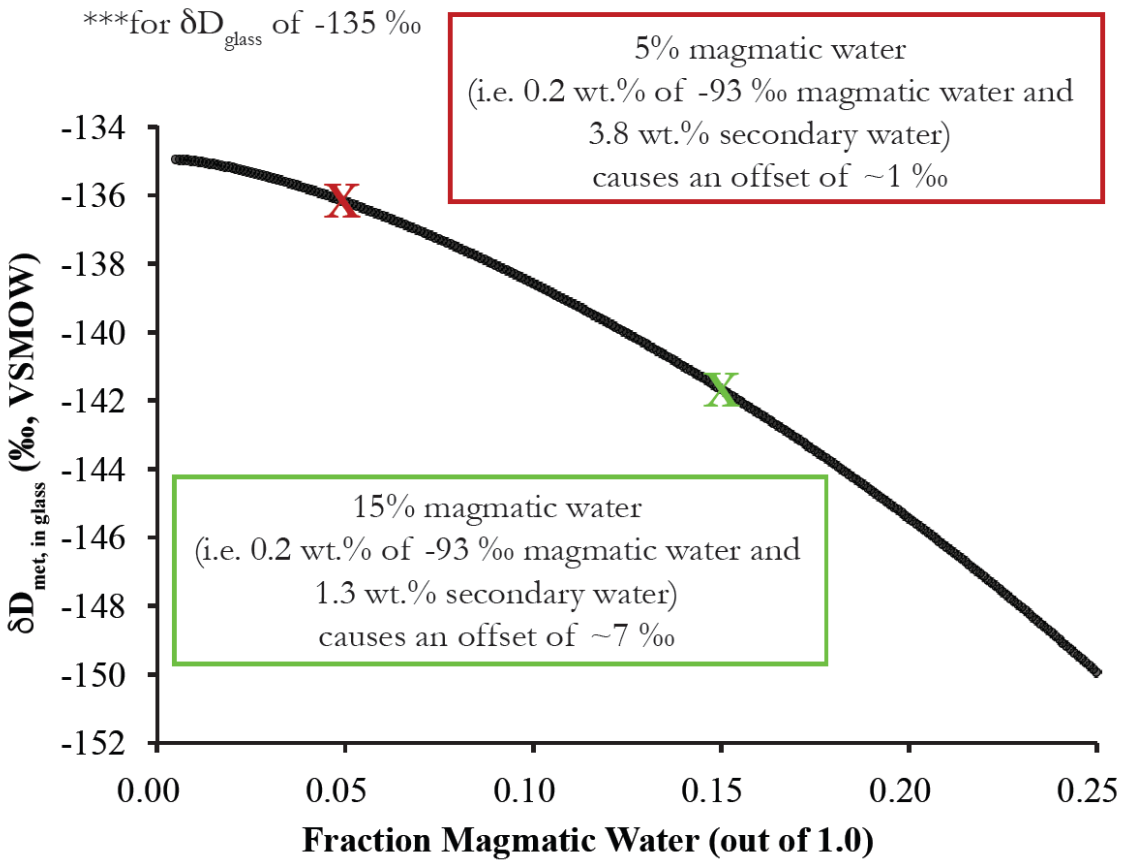

Figure 7. Relationship between the amount of primary magmatic water left in the glass and the δD of the total water (secondary and primary) as determined by TCEA, based on Equations (2) and (3). We do not factor in the variations in OH^- and H_2O_{mol}. For this calculation, we varied the δD of the primary magmatic water with the H_2O_t wt.% of the primary magmatic water during degassing based on degassing trends of Newman et al. (1988) and Castro et al. (2014) using the equation:

$$\delta D_{mag} = 13.8 \ln(H_2O_{t,mag}) - 71 \quad (4)$$

where δD_{mag} is the δD of the magmatic water during degassing in ‰, and $H_2O_{t,mag}$ is the wt.% H_2O_t of the magmatic water. Given the δD_t that is output by the TCEA results, we calculate the offset provided by residual magmatic water on the actual δD of the secondary water, assuming there is no shift in the δD of the primary magmatic water during secondary hydration. The plot here shows actual δD_{met} waters for a δD_t value of -135 ‰ for different fractions of magmatic water (out of 1.0), and provides the necessary shift in δD values needed to obtain the actual δD_{met} value.

the influence of primary magmatic water using mass balance equations:

$$H_2O_t = H_2O_{t,met} + H_2O_{t,mag} \quad (2)$$

$$\delta D_t \approx F_{met}\left(\delta D_{met} - \Delta_{water-glass}\right) + (1 - F_{met})\left(\delta D_{mag}\right) \quad (3)$$

where *F* is the fraction by weight of water in glass that is meteoric, *t,met* designates the total secondary meteoric water (hydroxyl and molecular), *t,mag* designates the total primary magmatic water, and $\Delta_{water\text{-}glass}$ is equal to δ_{water}-δ_{glass}. These mass balance equations describe the variations between the quantity of residual magmatic water left in the glass following deposition, and the relative quantity of secondary hydration. This relation is illustrated in Figure 7, which shows the affect that residual magmatic water can have on the total δD values during analysis of the glass, indicating a need for a correction for primary magmatic water during δD analyses of hydrated volcanic glass, which will be discussed further below.

Hydration of mafic glass

Water concentration versus the age of volcanic scoria from Klyuchevskoy volcano show that there is a general trend of slightly increasing wt.% H_2O_t and decreasing δD (‰) with age (Figs. 8, A2). The youngest samples, with ages younger than ~0.2 ka, have ~0.4 wt.% H_2O_t on average. The older samples, ages 4.7 to 7.3 ka, have slightly higher water concentrations (~0.4 to 1.0 wt.%). Given the low δD of precipitation in Kamchatka (-136 ‰; Bowen, 2015; Bowen and Revenaugh, 2003), the decrease in δD with increasing age and water content is an isotopic indication of very slight secondary hydration.

In addition to the stratigraphic sequence of the Klyuchevskoy scoria, we analyzed mafic tephra (≤ 63 wt.% SiO_2) with a range in age and water concentrations from around Kamchatka and Tanzania to obtain further hydration and δD trends of mafic tephra worldwide (Tables 1–2; Fig. 1). Although the majority of these tephra were more

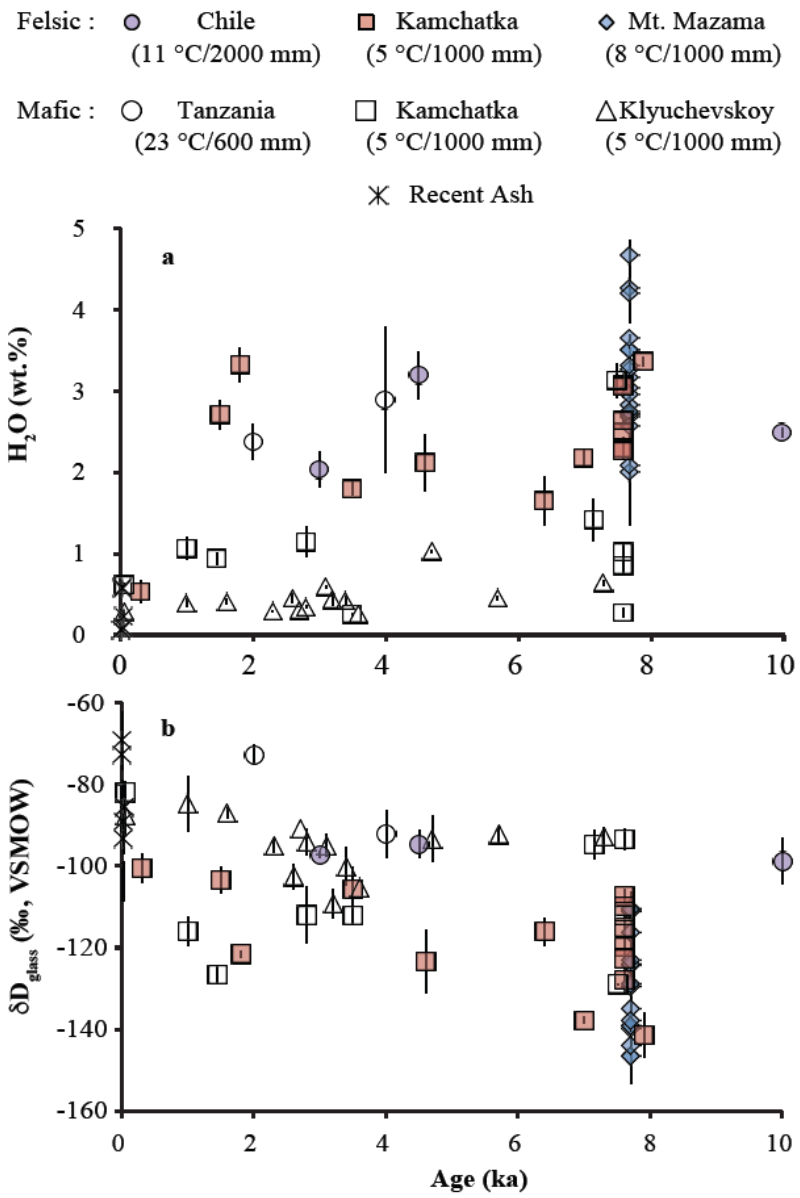

Figure 8. Water concentration (wt.%) and δD (‰) trends of water in glass (±1σ) with time. The mean annual temperature (MAT) in °C and average annual precipitation in mm are listed for each region in the legend. (a) H_2O_t (wt.%) trends of mafic and felsic tephra with age. This plot illustrates a distinction between the hydration rate of basaltic tephra (slower) and rhyolitic tephra (faster), where rhyolitic tephra already contains above 1.5 wt.% H_2O_t after ~1500 years. (b) δD_{glass} trends of mafic and felsic tephra with age. Since the majority of tephra around the world are hydrated with meteoric water with a lower δD (‰) than the residual primary magmatic water (when factoring in the fractionation between water in glass and meteoric water from Friedman et al. (1993a)), the predominant trend shown during secondary hydration is a decrease in the δD (‰) of the water in the glass. This causes felsic (hydrated) tephra to have a lower δD (‰) value after a few thousand years than the majority of the mafic (not as hydrated) tephra.

hydrated than the Klyuchevskoy scoria, their water contents generally do not exceed 2.0 wt.% H_2O_t, even for the tephra that are up to 7.6 ka. Only three glass samples have higher water concentrations: the 2.0 and 4.0 ka eruption of Rungwe and the 7.5 ka eruption of Kizimen. The trend of decreasing δD (‰) with increasing wt.% of added secondary H_2O_t is most clear up to ~1.5 wt.% H_2O_t, after which the δD values become more scattered (-129 – -73 ‰). This is likely due to the differing δD of local meteoric water, as the scatter is mostly due to the hydrated Tanzania samples from a lower latitude, where we see δD of precipitation that is near 100 ‰ heavier than at the higher latitude regions. (Figs. 1–2).

Hydration of felsic glass

Felsic tephra from varying climates all show a clear trend of rapid increase in water and decreasing δD within the first 1500 years, when compared to the recently deposited tephra (Fig. 8). Water concentrations of the felsic glasses range from ~0.5 wt.% H_2O_t at 300 years and have up to ~3.0 wt.% H_2O_t after 2700 years (Fig. 8). After ~2700 years, the water content generally stays near or above ~2.0 wt.% (± 1.0 wt.% H_2O_t). This is in exception to three of the Mt. Mazama glass samples, which have higher H_2O_t between 4.0 and 5.0 wt.% (Figs. 2, 8). Besides the recent ash, the youngest felsic glass analyzed here is the 300 year old Opala ash from Kamchatka with 0.5 wt.% H_2O_t, which is on the higher end of undegassed water concentrations of the recently deposited ash described above. At higher water contents (~2.0–3.5 wt.% H_2O_t), we observe a large range of δD values (~-147– -95 ‰), which is again a reflection of the range in δD (‰) of precipitation around the world (Figs. 1–2).

Surface area as determined by SEM images of basalt versus rhyolite tephra

We examined clast textures and differences in surface areas of mafic versus felsic tephra on BSE images. The basalt-basaltic andesite units from Kurile Lake and Klyuchevskoy have the lowest number density of vesicles (25–77 mm^{-2}). Furthermore, the Klyuchevskoy basaltic andesites consistently have lower vesicle number densities (25–72

mm^{-2}) than all the Kurile Lake tephra clasts. The andesite from the Kurile Lake eruption has a moderate number density (161 mm^{-2}) and the rhyolite from the Kurile Lake eruption has the highest density of vesicles (736 mm^{-2}) (Table 4). Similarly, the rhyolite tephra has the smallest average bubble wall thickness (0.02 mm), while the average bubble wall thickness for the basalt and basaltic andesites is 0.07 mm.

DISCUSSION

Mass balance analysis in distinguishing between magmatic and meteoric water

The importance of creating a magmatic water correction to better obtain the meteoric water δD signal is illustrated in Figure 7. The wt.% residual H_2O_t and δD values are likely different at each volcano, so the magmatic correction needed for each volcano is likely different (and can be independently estimated using the youngest deposits), but we assume that similar looking tephra layers in the same section from a single volcano, such as Klyuchevskoy, can have identical residual H_2O_t and δD. To define a correction to remove the δD (‰) value of the primary magmatic water, we took an average δD (‰) and H_2O_t (wt.%) of the mafic tephra that have ages less than or equal to 1.0 ka and H_2O_t below 0.6 wt.%. The water concentration limit is based on the highest water concentration of the recently erupted ash (Mt. Spurr) and an age limit that is based on the low water concentration and high δD that we see for ash samples less than 1000 years old, indicating a lack of secondary hydration in these tephra. This provides an average δD and H_2O_t for nine degassed tephra of -83 ‰ (±7.7, 1 σ) and 0.32 wt.% (±0.2, 1 σ), respectively. Since we have a series of tephra from Klyuchevskoy volcano, we created a separate correction for the two Klyuchevskoy glasses of -86 ‰ δD (±2.2, 1 σ) and 0.35 wt.% H_2O_t (±0.1, 1 σ), which was determined by the two youngest Klyuchevskoy units (0.05 and 1.0 ka). Six units (basalt-basaltic andesites) are older than 1.0 ka, but have less total water than the correction factor (7.6 ka Kurile Lake, 3.5 ka Avachinsky, 2.3 ka Klyuchevskoy, 2.7 ka Klyuchevskoy, 2.8 ka Klyuchevskoy, 3.6 ka Klyuchveskoy). These units with low water concentrations are assumed to contain only primary magmatic water

and were excluded from further analysis of secondary water determination when using the correction.

δD trends of secondary hydration as compared to local δD of precipitation

We compare the δD (‰) of the water in our glasses to local δD (‰) of meteoric waters, while taking into account the 0.9668 fractionation between meteoric water and water in volcanic glass, where glass is depleted in deuterium (Friedman et al., 1993a) (Fig. 9). Furthermore, we initially use the fractionation factor determined by Friedman et al. (1993a), which is intended for felsic glasses, on mafic glasses, and compare them to local meteoric waters to see if the fractionation factor is similar for mafic glasses, which is discussed further below. We also take into account our correction for total water and δD of primary magmatic water in this section, and do not discuss the isotopic characteristics of samples with water contents equal to or less than the magmatic water correction.

Prior to a magmatic water correction, our δD_{glass} values are typically heavier than their associated local meteoric waters (Fig. 9a, 10a). This can be explained if the water is mostly magmatic, as is illustrated in Figures 2 and 7, since magmatic water remaining in the glass is commonly heavier in δD than the local meteoric water at higher latitudes (Fig. 1). This is particularly characteristic for many of the recently erupted ash and scoria samples with only magmatic water present in them that do not fall on the 1:1 line (Fig. 9a). The only exception are the glasses from Volcán de Fuego and Kelud, which both fall near the 1:1 line and are both located near the equator (Fig. 1). They therefore have heavier local precipitation δD (‰) similar to the range of δD (‰) values of mostly degassed magmas (Figs. 2, 9a). Thus, as is illustrated in Figure 2, the two types of water mask each other. The recent ash that is far from the 1:1 line is from the Alaskan Mt. Spurr, which is located at a northern latitude (Fig. 1), and therefore has local δD (‰) values of precipitation that are significantly lighter than average degassed magmas. This is also true for all Holocene Kamchatkan scoria and ash studied by us (Figs. 1, 9a, 10a). After applying the magmatic water correction, the mafic glasses fall within an average of

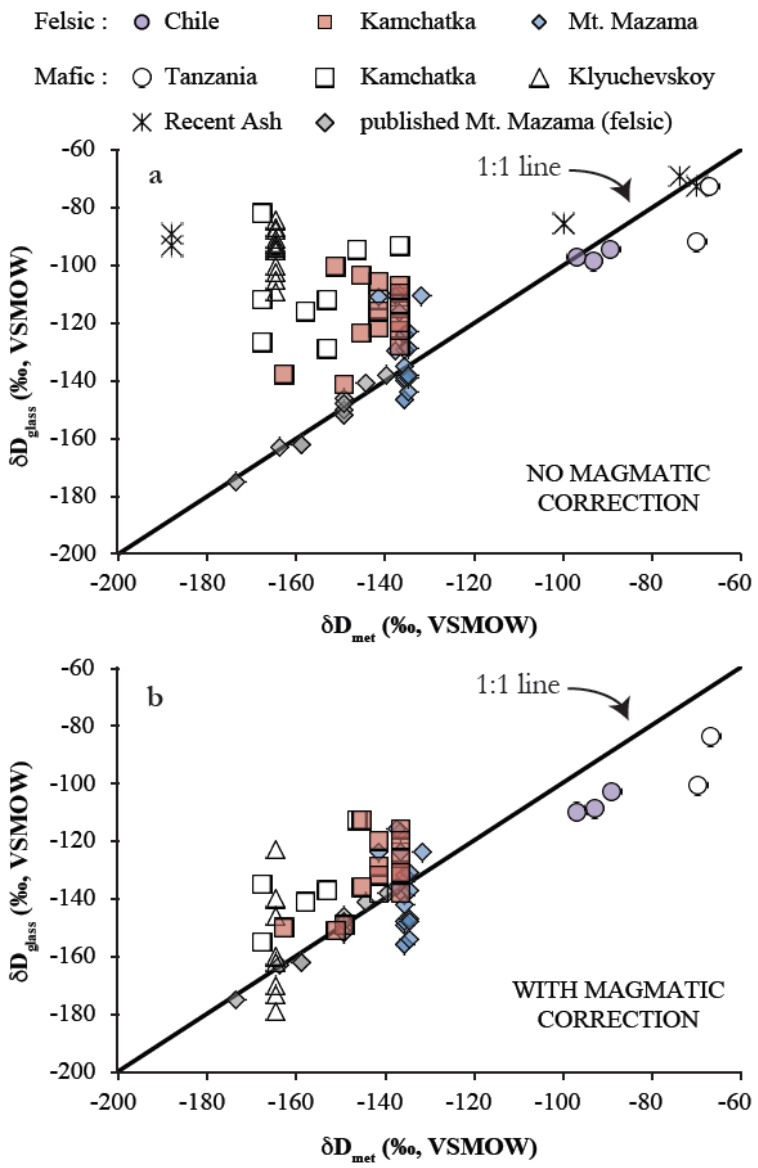

Figure 9. δD_{glass} (‰) in comparison to local δD_{met} (‰). The 1:1 line compares the δD (‰) of the water extracted from the volcanic glass (our analyses) to the δD (‰) of current local meteoric water based on interpolated data from waterisotopes.org (Bowen and Revenaugh, 2003; Bowen, 2015). The fractionation between water in glass and meteoric water (Friedman et al., 1993a) has already been taken into account. (a) Results when an average magmatic water δD (‰) value is not excluded from the δD_{glass} (‰) value. Results here show an average offset of +24 ‰ from current local meteoric waters for all data. (b) Results showing the improved correlation when the average magmatic water δD (‰) value is removed from the δD_{glass} (‰) value. The average offset for both mafic and felsic glasses following the magmatic water δD (‰) correction is +4 ‰. Glasses used to create the magmatic correction and glasses with water concentrations less than the magmatic correction are excluded from (b). Published Mt. Mazama data is from Friedman et al. (1993b).

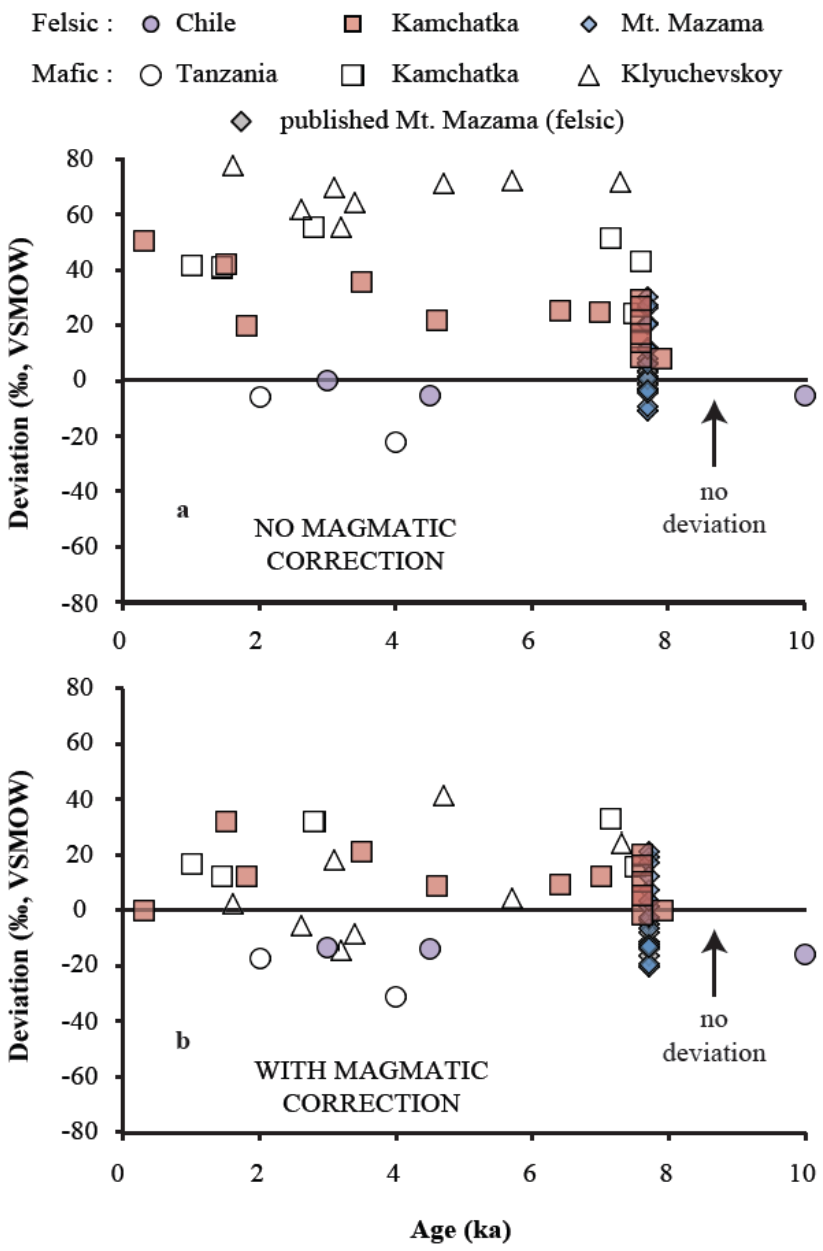

Figure 10. Deviation from the δD (‰) of local meteoric waters in relation to the age of the glass. The black line running through 0 ‰ designates no deviation from the δD of local meteor water (Bowen and Revenaugh, 2003; Bowen, 2015), when taking into account the Friedman et al. (1993a) fractionation between water in glass and meteoric water. (a) Results when an average magmatic water δD (‰) value is not excluded from the δD_{glass} value. Nearly all δD glass data fall above the correlation line. (b) Results showing the improved correlation when the average magmatic water δD (‰) value is removed from the δD_{glass} value. The correction causes more data to fall near the correlation line. Glasses used to create the magmatic correction and glasses with water concentrations less than the magmatic correction are excluded from part (b). Published Mt. Mazama data are from Friedman et al. (1993b).

13 ‰ of the 1:1 line, now deviating an average of 43 ‰ less from the 1:1 line than they did prior to the magmatic water correction (Figs. 9–10).

A natural experiment of secondary hydration of basaltic tephra is provided by the δD values of multiple tephra layers from Klyuchevskoy volcano in Kamchatka (0.05–7.3 ka), which lie above the 1:1 line prior to any magmatic water correction (Fig. 9a). Despite the fact that the majority of the water in the Klyuchevskoy glasses is higher δD undegassed magmatic water, we observe that the total water is increasing slightly, and the δD (‰) values are gradually decreasing with the increasing age of the tephra (Figs. 8, A2). This indicates a slow process of rehydration of up to 0.6 wt.% H_2O_t at 7.3 ka. After applying the correction, there is an average of 60 ‰ less deviation from the 1:1 line (Fig. 9b).

Water extracted from the postglacial 7.7 ka Mt. Mazama glasses and other Holocene felsic glass (0.3–10 ka) are, on average, within ~15 ‰ of the 1:1 line prior to the magmatic water correction (Fig. 9a). Following the magmatic water correction, the data are within an average of 4 ‰ of the 1:1 line. The lesser improvement in fit (although still significant) between the mafic and felsic samples is due to the difference in percentage of magmatic water, where the mafic tephra have a higher percentage of magmatic water than the secondarily hydrated felsic tephra. Although the improvement is smaller in the felsic samples, the magmatic water correction still creates an improvement in the correlation between the water in the glass and the surrounding meteoric water (Figs. 9, 10).

When splitting the glass samples into low water concentration (<1.5 wt.% H_2O_t) and high water concentration (>1.5 wt.% H_2O_t) sets, there was an average of 46 ‰ less deviation from the expected δD_{met} value for the low water concentration samples and an average of 7 ‰ less deviation for the high concentration samples following the correction. This separation of water concentrations is also nearly represented by a separation of mafic versus felsic glasses, where only one rhyolite fell into the low water category (0.3 ka Opala) and three andesites (Rungwe and Kizimen) fell into the high water category, due to the tendency for rhyolites to become hydrated more rapidly.

Fractionation between meteoric water and volcanic glasses of mafic and felsic composition

We compare the D/H of water from our analyses to the local D/H of precipitation for each glass to calculate the fractionation between meteoric water and mafic and felsic glasses in varying climatic regions (Fig. A3). To do this, we utilize our magmatic corrected δD values and compare these values to the local δD of precipitation from Bowen and Revenaugh (2003) and Bowen (2015). We conduct this exercise separately for mafic and felsic glasses, and also for regions with different climates (hot/cold and wet/dry). We report fractionations as $10^3\ln\alpha_{glass\text{-}water}$, where:

$$\alpha_{glass-water} = \frac{(1000 - \delta D_{glass})}{(1000 - \delta D_{water})} \quad (5)$$

glass designates the D/H ratio of water extracted from volcanic glass and *water* designates the D/H ratio of liquid meteoric water.

We determine an average global $10^3\ln\alpha_{glass\text{-}water}$ of -33 (±15; 1σ) for all our hydrated felsic glasses, in which we include glasses older than 2.0 ka with water concentrations greater than 1.5 wt.% (Fig. A3), which is similar to the -34 $10^3\ln\alpha_{glass\text{-}water}$ = -34 from Friedman et al. (1993a). However, it is curious that Friedman et al. (1993a) did not conduct a magmatic correction on their glasses. Their method, however, utilized water contained within hydrated glass spheres from volcanic eruptions, and compared the δD of the liquid water within the hollow sphere (presumed to represent environmental water) to the δD of the water extracted from the glass to determine their $10^3\ln\alpha_{glass\text{-}water}$. Their difference in methodology leads to differing assumptions and causes our comparisons to become difficult. If we include all felsic glasses, except those used in the magmatic water correction, the $10^3\ln\alpha_{glass\text{-}water}$ is slightly smaller at -31 (±16; 1σ). Figure A3 also illustrates the $10^3\ln\alpha_{glass\text{-}water}$ of -20 (±17; 1σ) for all our felsic glasses prior to the magmatic correction, which does not agree with the $10^3\ln\alpha_{glass\text{-}water}$ of Friedman et al. (1993a). We also find variations in the $10^3\ln\alpha_{glass\text{-}water}$ value when we split these same data up into separate climatic regions. The average $10^3\ln\alpha_{glass\text{-}water}$ for the cold and wet

climate of Kamchatka (MAT of ~5 °C and average annual precipitation of ~1000 mm) is -20 (±11; 1σ). The average $10^3\ln\alpha_{glass\text{-}water}$ for the warm and wet climate of Chile (MAT of ~11 °C and annual precipitation of ~2000 mm) is -50 (±2; 1σ). We also include the Pacific Northwest of the United States (Mt. Mazama pumices), which cover a range of climatic settings. Most of the pumices were collected near Crater Lake National Park, which is located in a cold (~8 °C MAT) and wet (~1000 mm annual precipitation) environment. The average $10^3\ln\alpha_{glass\text{-}water}$ for these pumices is -37 (± 15; 1σ). Two of the Mt. Mazama samples were collected farther to the east (Mazama-WMC, 2014MM-1), in a dryer setting (~300 mm annual precipitation), and yield an average $10^3\ln\alpha_{glass\text{-}water}$ of -29 (±28; 1σ). Although we find a similar fractionation to Friedman et al. (1993a) for all of our tephra, we observe large variations in all our $10^3\ln\alpha_{glass\text{-}water}$ averages, represented here as large standard deviations. In addition, counter to what would be expected, we see larger fractionations in warm and wet settings, although we only have 3 samples from a warm and wet region, and two from a dry region, which are not significant enough to build a final conclusion.

Our global data set for the hydrated mafic glasses is significantly smaller than that for the felsic glasses (Fig. A3). If we only include glasses with >1.5 wt.% H_2O_t that are older than 2000 years, we have just three glasses to create our average $10^3\ln\alpha_{glass\text{-}water}$ of -45 (±27; 1σ). We do not consider three glasses significant enough to make a final conclusion on mafic fractionations. Our global average for all mafic $10^3\ln\alpha_{glass\text{-}water}$ is -23 (±23; 1σ), which is smaller than our (and Friedman et al., 1993a) estimate for the felsic $10^3\ln\alpha_{glass\text{-}water}$. Unlike for the felsic glasses, we find the $10^3\ln\alpha_{glass\text{-}water}$ of the larger data set of the mafic glasses that has been corrected for residual magmatic water to be more robust. This is due to there being only a few hydrated mafic glasses in this study. If we determine the $10^3\ln\alpha_{glass\text{-}water}$ for the mafic glasses, prior to the magmatic correction, it becomes +19 (±32; 1σ), which is likely due to the prevalence of magmatic water in the mafic glasses with heavier δD values, signifying the importance of the magmatic correction. Similar to the felsic glasses, we compare fractionations between regions of cold and wet versus hot and dry climates. For the cold and wet region of Kamchatka, the average $10^3\ln\alpha_{glass\text{-}water}$ is -19 (±19; 1σ), and for the hot and dry region of Tanzania (MAT

of ~23 °C and annual precipitation of ~600 mm) the average $10^3 \ln\alpha_{glass\text{-}water}$ is -60 (±11; 1σ). This indicates a similar trend of greater fractionations for hot and dry climates in the mafic glasses. Also similar to the felsic trend, we have minimal samples to base this trend on, and therefore, it is uncertain if this trend is significant.

Hydration of basalt versus rhyolite

There is a clear distinction between the hydration rates of basalt and rhyolite glass (Fig. 8). This difference is likely due either to the difference in diffusion rates of water into basaltic glass and rhyolitic glass, differences in vesicularities, or both. Due to the long time (1000s of years) needed for room temperature hydration, there are no experiments on rates of room temperature hydration of basalt or rhyolite tephra. Therefore, experimental data for rhyolite and basalt diffusivities only go to 400 °C (Zhang and Behrens, 2000).

As we documented above (Fig. 4, Table 4), rhyolitic tephra has a significantly higher vesicle number density (736 mm^{-2}) relative to basalts–andesites (27–161 mm^{-2}). The important implication of this difference in bubble number densities is that surface area increases with an increase in bubble number density, which we examine further below.

Hydration rates of coeval tephra across differing climates

We compare the H_2O_t of tephra of similar age and relative vesicularities across different climatic regions and do not observe consistent differences in hydration rates of felsic or mafic tephra (Fig. 8). In terms of the felsic samples, the Chilean glasses were hydrated in the warmest and wettest climate and we compare these tephra to the cooler climates of Kamchatka and Oregon (United States). We compare the youngest Chilean glass (CLD064B; 3 ka) with a similarly aged Kamchatkan glass from Opala (98-33/2) that has similar vesicularity (Table 3) and find similar water concentrations. However, when we compare an older Chilean glass (CLD155A) with a similar vesicularity to the 4.6 ka Optr

glass (98KAM2.3), we do not find similar water concentrations (3.2 wt.% H_2O_t relative to 2.1 wt.% H_2O_t). Based on the random differences in water concentrations between the few tephra of the warm and wet Chilean climate that we can compare to specific Kamchatkan samples, we cannot conclude that there are any consistent differences in rates of hydration for felsic glasses of differing climates (i.e. cold versus warm). However, we only have a few warm samples to work with, and therefor more research should be done to clarify these results.

We can utilize a similar comparison of the mafic Tanzanian glasses, which were hydrated in a warmer and dryer climate to the cold and wet climate of the Kamchatkan glasses (Fig. 8a; Table 3). However, specific age and vesicularity comparisons are difficult, due to the few samples we have from warm and dry climates. The 2.0 ka Rungwe tephra (KF155D) is bracketed by the 1.0 and 2.8 ka Shiveluch glasses (96025/4 and 97051/2), which both have lower relative vesicularities and lower water concentrations. We compare the older (4.0 ka) Rungwe glass (KF149B) to the 2.8 ka Shiveluch tephra and the 7.5 ka Kizimen tephra (80013/4), which have lower relative vesicularities, and lower and higher water concentrations, respectively. Again, based on the random differences in total water concentrations for both the mafic and felsic glasses that we see here, there does not appear to be any consistent differences in hydration rates of mafic or felsic glasses hydrated in different climatic regions. However, we don't have very many dry climate samples to work with, and more research should be done to clarify these results.

Simplified model for diffusion of water through vesicular glass

A longstanding experimental challenge is the measurement of the diffusivity of water in volcanic glass at ambient temperature. Because the rate of diffusion is so slow, and therefore difficult to investigate with experiments, one approach is to measure the thickness of hydration rinds on obsidians of known age (e.g. Anovitz et al., 2004). In this section, we develop a complementary approach in which we model the hydration versus

time data presented in Figure 8 to obtain an order-of-magnitude estimate of the low-temperature diffusivity of H_2O_t in both vesicular rhyolite and basaltic scoria.

The key observations we focus our attention on are: 1) the H_2O_t in rhyolitic pumices increases between 0 and 2 ka; 2) most of the basaltic scoria are considerably less hydrated than their rhyolitic counterparts; 3) there is no systematic relationship between age and H_2O_t in rhyolitic or basaltic tephra older than 2 ka; and 4) basaltic scoria older than 1.5 ka are more hydrated than modern basalts. It is important to note at the outset that we do not have independent constraints on the solubility of water in basalt and rhyolite at low temperature, and we make the assumption that the solubility of water in mafic and felsic glasses is similar.

We model the diffusive influx of water into a glass wall between two bubbles in 1D to estimate the rate at which the glass wall becomes hydrated as a function of the diffusivity of water and average vesicle wall thickness (Fig. 11a–b). An alternative way to think of this is that we are representing a 1–10 mg aliquot of ash as a square slab with a thickness that is represented by an average bubble wall thickness. At an equivalent mass, thinner-walled tephra clasts will have a greater surface area. In the model, the glass wall initially has 0.1 wt.% water and we assume a 5 wt.% fixed concentration of water at the boundaries, which is near our highest water content after 10,000 years. The fixed concentration boundary conditions imply that the clast as a whole is highly permeable such that environmental water can penetrate into most of the pores. Although the water concentration of 5 wt.% at the boundaries is fixed, the diffusivity within the model will vary with time as the water concentration changes.

The two parameters in the model that determine the rate of hydration versus time are (1) the length that water has to travel to hydrate the glass (average bubble wall thickness) and (2) the diffusivity of water. Because hydration rinds are observed to have relatively sharp boundaries due to the water-concentration dependence of diffusivity (Eq. 1 and surrounding discussion), similar to what is seen in studies involving glass corrosion (e.g. Gin et al., 2013; Steefel et al., 2015), we adopt the formulation for the water

concentration dependent rhyolite diffusion equation from Zhang and Behrens (2000):

$$D_{H_2O_t} = Xexp(m)\left\{1 + exp\left[56 + m + X\left(-34.1 + \frac{44{,}620}{T} + \frac{57.3P}{T}\right) - \sqrt{X}\left(0.091 + \frac{4.77\times10^6}{T^2}\right)\right]\right\} \quad (6)$$

Figure 11 (next page). Comparison and explanation of our model results for water concentration dependent diffusion. (a–b) illustration of the hexagonal close-packing assumption that we utilize in our vesicle and glass layout for our model. The difference between (a) and (b) illustrates the typical difference in bubble wall thicknesses between the rhyolite (a) and basalt (b). (c) Example of our model results for 97KAM29AL (7.6 ka Kurile Lake Rhyolite). 97KAM29AL has an average bubble wall thickness of 17 μm (shown on the x-axis). At the start of the model run, the entire bubble wall has 0.1 wt.% H_2O_t, with 5 wt.% H_2O_t at the boundaries. As hydration proceeds (0.5–7.6 ka shown here), the hydration front produces a 'bulldozing effect' that steadily progresses into the center of the bubble wall, as is shown in the 0.5, 2.0, 5.0, and 7.6 ka markings in gray. The length of hydration (L) for each of our tephra samples was calculated by subtracting the average bubble wall thickness (17 μm here) by the distance to the 0.1 wt.% non-hydrated region of the bubble wall (9.6 μm after 7,600 years here). (d) To determine the proper distance needed for hydration, the known bubble wall thickness from the SEM images was entered into our model (17 μm for 97KAM29AL), along with the known age (7.6 ka for 97KAM29AL), and the diffusivity constant was adjusted until the known water concentration from the TCEA analyses was obtained (2.3 wt.% here). This is shown here by the trend of increasing water with time to end at 2.3 wt.% H_2O_t after 7,600 years. (e) Results show that there is a decrease in hydration rate with a decrease in temperature and that our model results are similar to those for natural rhyolitic glass hydration at 15 and 20 °C. This is shown by our tephra (from Kurile Lake and Klyuchevskoy) having similar lengths of hydration for similarly aged samples at 15 and 20 °C. Given the slightly lower temperature of our Kamchatka samples (~5 °C mean annual temperature), it is reasonable that our samples have a slightly slower hydration rate than the samples at 15–20 °C. We did not determine the hydration distance of KLV5-1 (0.05 ka Klyuchveskoy scoria) based on its young age, and likely negligible secondary hydration. Prior studies are from Friedman et al. (1966; 100 °C), Mazer et al. (1991; 175 °C), Anovitz et al. (2004; 75 °C), Riciputi et al. (2002; 20 °C), and Eerkens et al. (2008; 15–20 °C). Higher degree temperatures listed in the legend are approximate and based on the average temperature for the study.

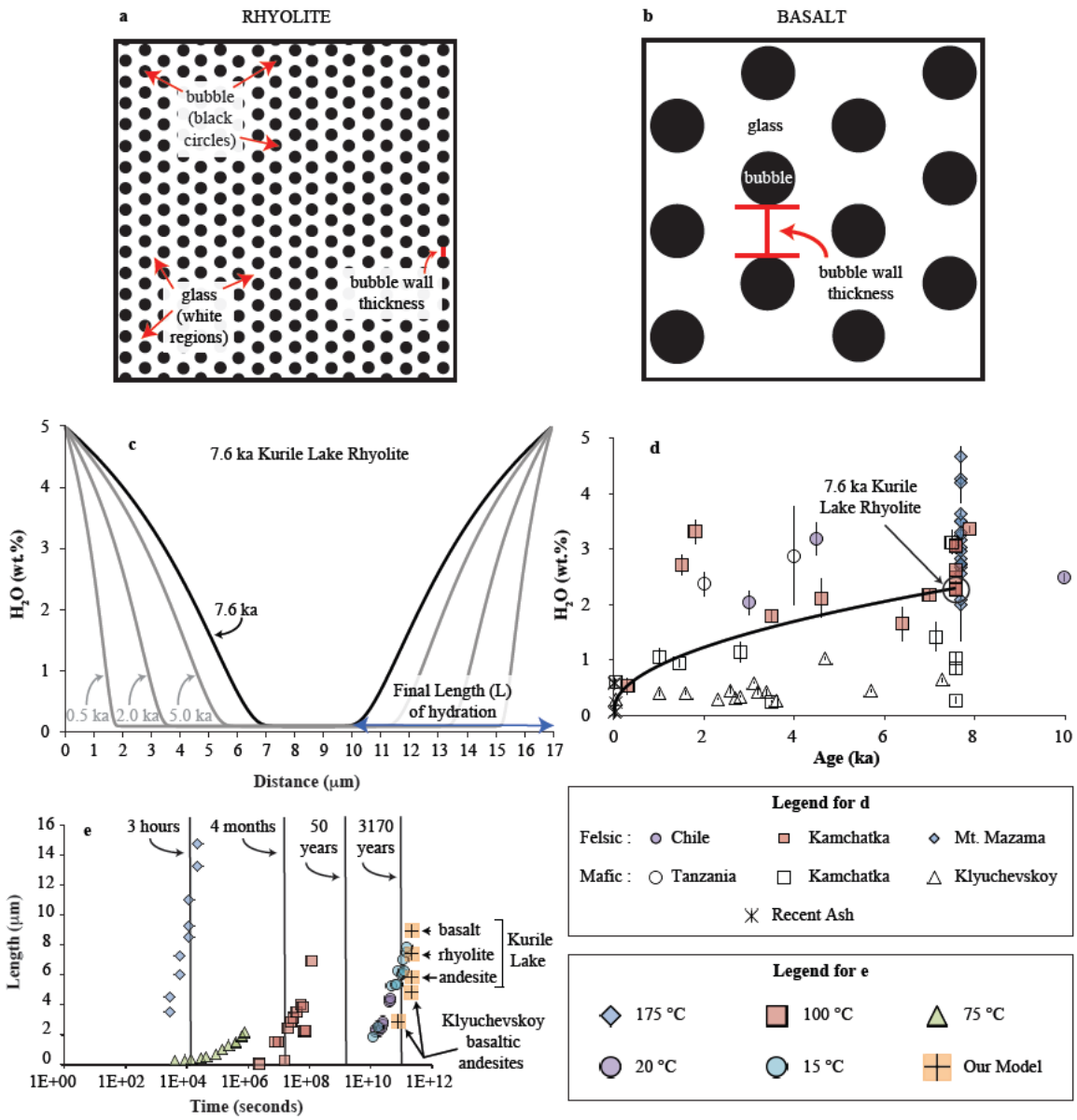

where D is a water concentration diffusion coefficient in $\mu m^2/s$ for molecular water, m = *-20.79-5030/T-1.4P/T*, T is the temperature in Kelvin, P is the pressure in MPa, and X is the mole fraction of H_2O_t on a single oxygen basis. This equation, however, is based on experimental and literature data at temperatures above ~400 °C, and we therefore only utilize it for its dependence on water concentrations at 400 °C, while making the assumption that the functional form is still the same at a much lower temperature. Since diffusion is much slower at 25 °C, we scale the diffusivity by a constant prefactor, which

turns out to be between 10^{-8} and 10^{-10}, in order to match the trend of increasing H_2O_t with age. The constant prefactor is the only free parameter, as we use average bubble wall thicknesses inferred from the imaged tephra clasts in Figure 4 and Table 4.

Figure 11c–d shows an example diffusion simulation for the 7.6 Kurile Lake rhyolite. The initial diffusivity (at 0.1 wt.% H_2O_t) required to yield an average water concentration of 2.3 wt.% after 7.6 ka is on the order of 10^{-4} μm^2/year. Hereafter, we report diffusivities at 0.1 wt.% water because this is the value that governs the length scale of diffusion according to Eq. 1. The value of 10^{-4} μm^2/year for the Kurile Lake rhyolite is somewhat sensitive to the solubility of water, or the assumed concentration of water at the boundary. For example, assuming a boundary concentration of 3 wt.% increases the diffusivity needed to match 2.3 wt.% at 7600 years by one order of magnitude to 10^{-3} μm^2/year.

We applied the same approach to modeling each of the six imaged tephra clasts for which we have SEM images of bubble wall thickness. The youngest Klyuchveskoy basaltic andesite (KLV5-1, 0.05 ka) was not included in this analysis, since the water in this clast is likely all magmatic water, based on its age, δD, and low water concentration. All diffusivities for these samples are within the same order of magnitude (10^{-4} μm^2/year; results not shown). Lengths that we determine from our model produce similar rates of secondary hydration (1–10 μm/1000 years) as were documented by Friedman et al. (1966). Figure 11e shows the length of hydration taken from the modeled 1D diffusion profile versus age for each of the five samples. Also shown is the temperature-dependence of the rate of hydration as determined from several different studies, and the results are generally consistent except for the discrepancy between 75 and 100 °C. The results from our five samples compare favorably to samples that were naturally hydrated at 15–20 °C. The slightly slower rate of hydration for our tephra samples from Kamchatka could be attributed to a number of factors, but it is noteworthy that the mean annual temperature of Kamchatka is about 5 °C, which could theoretically cause slightly slower hydration than at 15–20 °C.

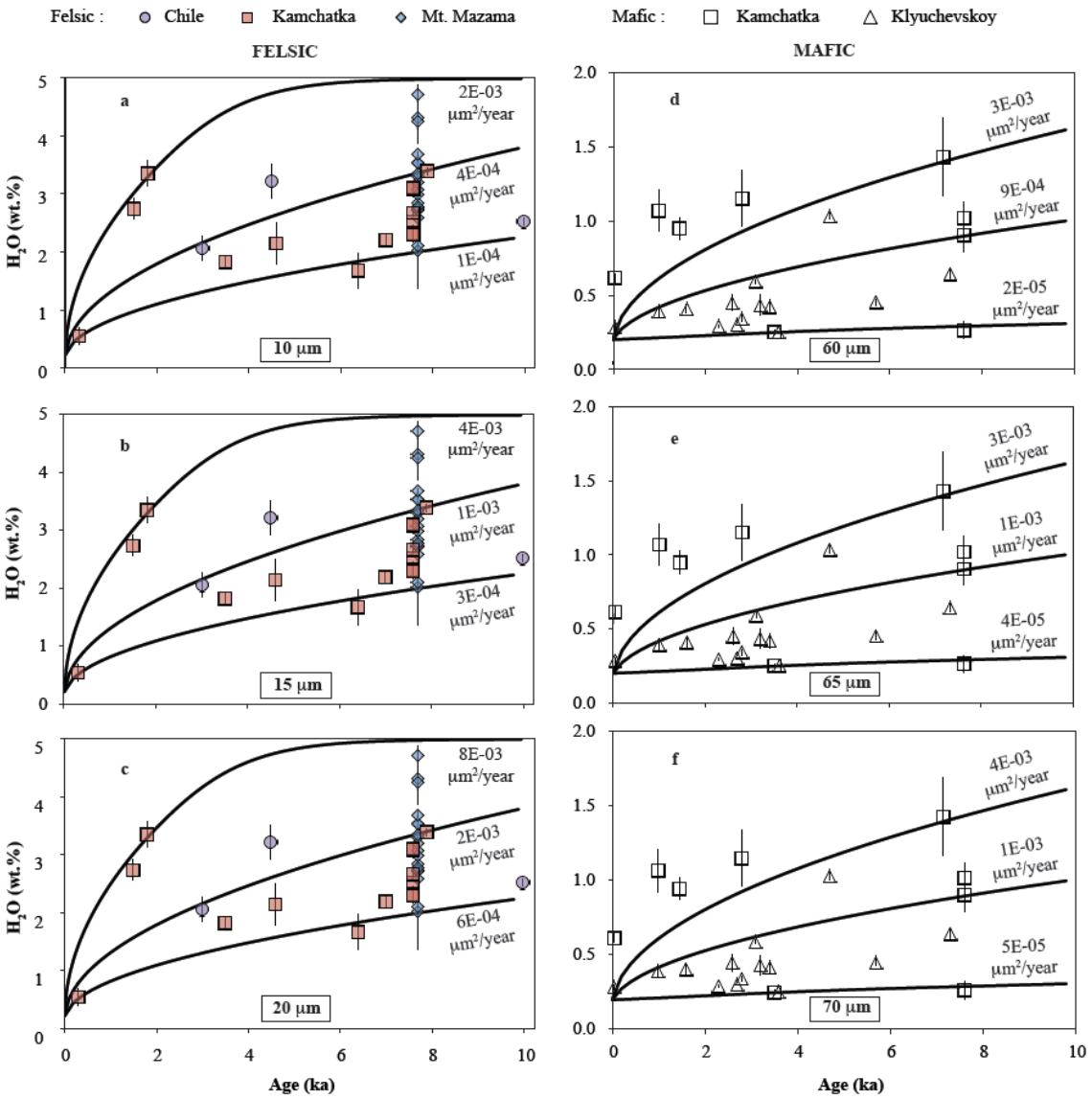

Figure 12. Modeling results from our diffusion code for felsic (a–c) and mafic (d–f) glasses in comparison to our data for water concentration (±1σ) versus age. For the felsic glasses, the bubble wall thickness was varied between 10, 15, and 20 µm, and the diffusivities were subsequently varied at each of these average bubble wall thicknesses until the trend lines matched our data. For the basalts, the bubble wall thickness was varied between 60, 65, and 70 µm. Diffusivities listed in the figure are the initial diffusivity at 0.1 wt.% H_2O_t.

Figure 12 shows the tradeoff between diffusivity and vesicularity (or average bubble wall thickness) for the entire sample set, with the exception of three mafic samples with >2 wt.% water. For the felsic tephra, we vary the bubble wall thicknesses

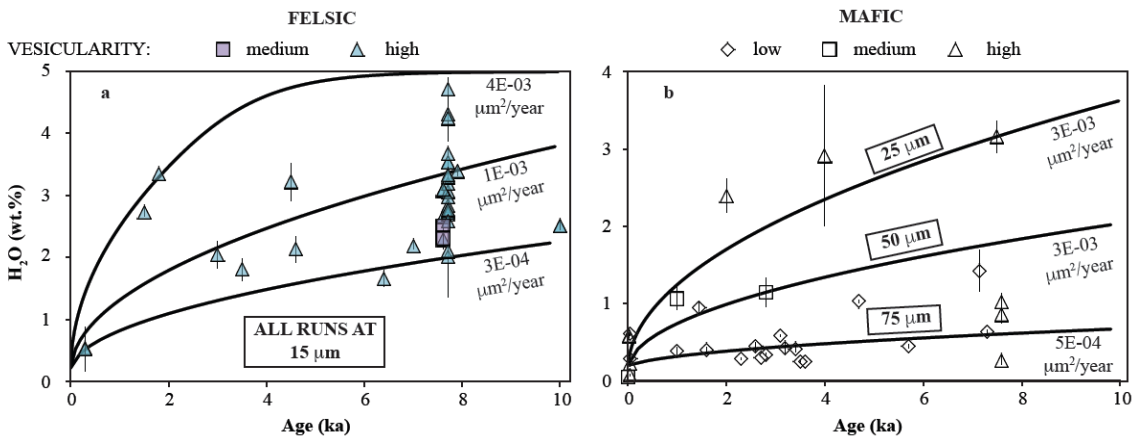

Figure 13. Modeling results from our diffusion code for felsic (a) and mafic (b) glass against our data for water concentration (±1σ) versus age. Vesicularities were split into three groups: 1) highly vesicular samples, with relative vesicularities from 7–10; 2) moderately vesicular, with a relative vesicularity of 5; and 3) low vesicularity samples, with relative vesicularities from 1–4. Relative vesicularities are listed in Table 3. Given the vesicular nature of the felsic samples, runs were only conducted at 15 μm bubble wall thickness. Based on the wide range of vesicularities for the mafic samples, highly vesicular data were matched to 25 μm bubble walls, moderately vesicular data were matched to 50 μm bubble walls, and low vesicularity data were matched to 75 μm bubble walls. Results here show similar orders of magnitude diffusion for mafic and felsic samples, when relative vesicularities are accounted for.

from 10–20 μm, based on the Kurile Lake rhyolite. For the mafic tephra, we vary the bubble wall thicknesses from 60–70 μm, based on the average bubble wall thicknesses for the mafic tephra (Fig. 12). Each panel corresponds to a specified bubble wall thickness, and the curves that bracket the data represent different diffusivities. Based on this comparison, we find that diffusivities for both felsic and mafic glass range between 10^{-3} and 10^{-5} μm^2/year, with the upper bounds for both the felsic and mafic glass having diffusivities ~10^{-3} μm^2/year, the lower bound of the felsic glasses having diffusivities of ~10^{-4} μm^2/year, and the lower bound of the mafic glasses having diffusivities ~10^{-5} μm^2/year (Figure 12).

In Figure 12, the symbols represent geographic setting. In Figure 13, we use symbols corresponding to the relative vesicularity. The first thing to note is that the highest water content samples have high vesicularity, whereas the lowest water content

samples span the full range from low to high vesicularity. This is true for both mafic and felsic samples. Note that we plot results for a larger range of bubble wall thicknesses than used in Figure 12, which is necessary to fit the highest water content mafic samples.

When comparing diffusivities, we still see no significant difference between mafic versus felsic glasses at low temperatures. Therefore, we conclude that rhyolite tephra becomes hydrated more rapidly than basaltic tephra because of higher reactive surface areas arising from higher permeability and smaller average bubble wall thickness. Although the vast majority of the felsic tephra hydrate faster than the mafic tephra in this study, there are three mafic samples (the 2.0 and 4.0 ka Rungwe glass and the 7.5 ka Kizimen glass) that became hydrated at a similar rate to some of the felsic tephra. These tephra all have higher vesicularities than most other mafic tephra, which provides a larger surface area for hydration (Table 3). Rust and Cashman (2011) compiled the relative bubble number densities of basalt and rhyolite tephra and showed that rhyolite tephra have consistently higher bubble number densities (and therefore surface areas), regardless of the mass eruption rate, than mafic tephra. Their compilation also showed that mafic tephra have bubble number densities that increase with increasing mass eruption rates, which correlates with our results of only a few of the mafic tephra being hydrated at similar rates to the felsic tephra.

Furthermore, when plotted versus age, there is a range of hydration rates for basaltic glasses, with the Klyuchevskoy basalts being hydrated at the slowest rates (Fig. 8). There are two potential explanations for this difference: 1) The lower explosivity of the Klyuchevskoy eruptions translates to fewer vesicles, and therefore, thicker bubble walls (Table 4; Figs. 4–6). This would cause water to take longer to penetrate through all the glass; and/or 2) The presence of microlites causes water to diffuse through longer effective pathways, and thus slowly through the pyroclast. Both thicker bubble walls and abundance of microlites have been documented in the Klyuchevskoy tephra, which explains the unusually slow hydration rate of the Klyuchevskoy tephra.

Modeling D/H diffusion during secondary hydration

To further understand the δD trends of secondary hydration, we created a similar code to incorporate the D/H trends during diffusion of water into volcanic glass at ambient temperature for the 7.6 ka Kurile Lake rhyolite (97KAM29AL). We use the same model set up from water-based diffusion model, except the starting conditions are now based on the relative deuterium concentrations from the δD of our magmatic correction (-83 ‰) at 0.1 wt.% H_2O_t, and the boundary conditions are based on the current local δD of precipitation (-107 ‰) while including the fractionation between water in glass and meteoric water from Friedman et al. (1993a) for a δD boundary condition of -137 ‰. We then compare this model to the δD values of our samples that have been magmatic corrected (Fig. 14), and note that our model produces similar results to the schematic curve from Figure 2, and the magma corrected δD value of our 7.6 ka Kurile Lake rhyolite. This correlation illustrates both the robustness of our model, and the ability to produce the local δD of precipitation using water extracted from volcanic glass following a magmatic correction.

CONCLUSIONS

1) We demonstrate the characteristics of the hydrogen isotope variations of secondary hydration of volcanic glass, which illustrates a decrease in the δD value with increasing water in nearly all environments except equatorial.

2) We propose a correction for pre-existing undegassed magmatic water when determining paleoenvironments, where younger tephra from the same section can be used to constrain the δD and concentration of residual magmatic water of older tephra clasts. If younger tephra from the same section are not available, our average δD of -83 ‰ and H_2O_t of 0.32 wt.% still aid in the correlation between δD_{glass} and the local δD_{met}.

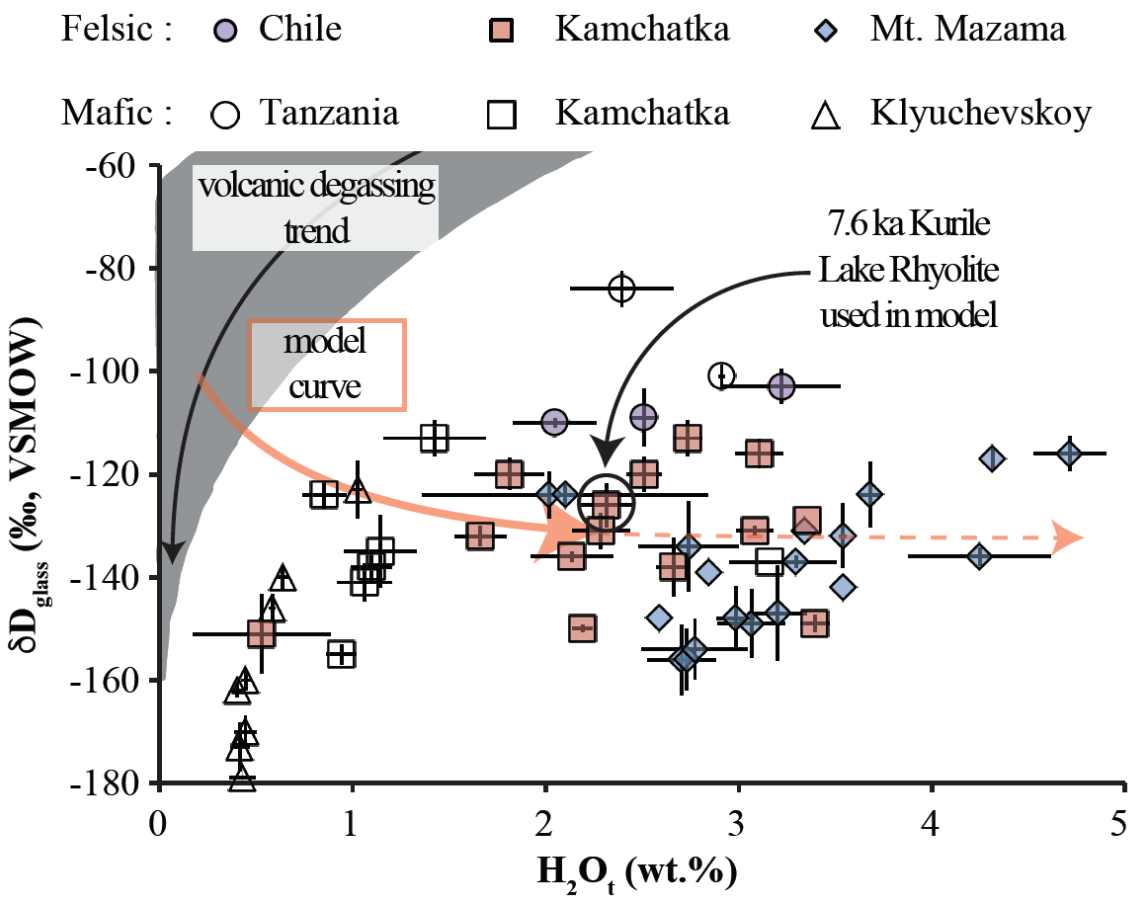

Figure 14. Modeling results from our δD diffusion code. The δD_{glass} values in this figure are magmatic corrected. Note the lower δD values for the δD_{glass} samples, and the similarity between the model curve and our schematic curve in Figure 2. The model was run up to the 2.3 wt.% H_2O_t of the 7.6 ka Kurile Lake rhyolite (97KAM29AL) using the local precipitation annual δD (‰) value from waterisotopes.org, along with the fractionation between water in glass and meteoric water (Friedman et al., 1993a). The continued dashed line following the solid model curve is a projected continuation of the model trend.

3) We show that δD values of water in felsic volcanic glass (≤ ~10,000 years), when compared to present meteoric water, yield uncertainties of 4 ‰ from the current δD of meteoric water after a magmatic correction.

4) Following our magmatic correction, we calculate values of $10^3 ln\alpha_{glass\text{-}water}$ that average -33 for hydrated felsic glasses, which is similar to the $10^3 ln\alpha_{glass\text{-}water}$ value

determined by Friedman et al. (1993a). We also identify a smaller average $10^3 \ln\alpha_{glass\text{-}water}$ for all mafic glasses across differing climates of -23.

5) We demonstrate that felsic glass typically becomes mostly hydrated after ~1500 years with 1.5–3.5 wt.% H_2O_t, but mafic glass is typically still not hydrated beyond 1.5 wt.% H_2O_t even after 7000 years.

6) When corrected for greater bubble number density of rhyolites, we empirically estimate, using our tephrochonological sample set, that the diffusivity of water into felsic glass is within the same order of magnitude as mafic glass.

7) We estimate the initial (at 0.1 wt.% H_2O_t) diffusion coefficient for water in felsic and mafic glass at ambient temperatures and pressures to be between 10^{-3} and 10^{-4} μm^2/year. This equates to a constant prefactor for the Zhang and Behrens (2000) rhyolite diffusion equation at 400 °C ranging between 10^{-8} and 10^{-10}, and similar rates of secondary hydration (1–10 μm/1000 years) as indicated by Friedman et al. (1966).

BRIDGE

In this chapter (Chapter IV), I utilized naturally hydrated volcanic tephra to understand the rates of secondary hydration of volcanic glass over a 10,000 year timescale. I used water concentrations, hydrogen isotopic ratios, and simple diffusion modeling to determine that felsic tephra are hydrated more rapidly than mafic tephra primarily due to the difference in relative vesicularities of the two types of eruptions. I also determined that the hydrogen isotopic trend of secondary hydration typically involves a decrease in δD values, except near equatorial regions.

In the following chapter (Chapter V), I will focus on the earliest stages of secondary hydration through utilizing the well-characterized 1980 summer eruptions of Mount St. Helens. I will utilize δD and water concentrations, as were done in the previous chapter, but will focus in on a 35 year time frame and will also utilize $\delta^{18}O$ glass

values to understand what is needed to cause secondary hydration within 35 years of deposition.

CHAPTER V

ISOTOPIC INSIGHTS INTO THE DEGASSING AND SECONDARY HYDRATION RATES OF VOLCANIC GLASS FROM THE 1980 ERUPTIONS OF MOUNT St. HELENS

In preparation for submission to Bulletin of Volcanology as co-authored material with Ilya N. Bindeman, Alexa Van Eaton, and Richard Hoblitt. I conducted the majority of this work, with advising by Ilya Bindeman. I drafted all the figures and the writing is mine, with assistance by Ilya Bindeman. Alexa Van Eaton helped to develop this project. Richard Hoblitt provided samples collected in 1980 that were utilized in this study, and provided significant background information about the 1980 summer eruptions of Mount St. Helens. Alexa Van Eaton and Richard Hoblitt assisted with fieldwork.

INTRODUCTION

Volcanic glass from explosive eruptions usually retains small amounts of undegassed magmatic water (0.1–0.6 wt.%), with water concentrations reaching up to 1.6 wt.% for rapidly quenched bombs (Newman et al., 1988; Castro et al., 2014; Seligman et al., 2016). Transport in the eruption plume may also affect the water content of the glass, due to increased solubility of water in glass with decreasing temperature during cooling (Westrich and Eichelberger, 1994; Watkins et al., 2012). However, the most significant changes occur after emplacement into the depositional environment. During this time, meteoric water can slowly diffuse into the glass structure, increasing the total water content and changing its isotopic signature. Mid-high latitude meteoric waters have lower δD (‰) values compared to magmatic water, in addition to the ~30 ‰ offset between volcanic glass and environmental water during hydration, allowing secondary waters to impart distinguishable hydrogen isotopic ratios during secondary hydration (Friedman et al., 1993; Seligman et al., 2016). This process is important for a number of applications. First, increased water content (secondary waters) lowers the melting point of volcanic ash, which is relevant to current experimental studies of engine turbine safety during ash-aircraft encounters (Song et al., 2016). Secondly, meteoric waters are a source of error for

volcanological studies that assume water in volcanic glass is entirely magmatic and aim to understand degassing and relative explosivity of eruptions (e.g. Newman et al., 1988; Mastin et al., 2004; Underwood et al., 2013; Castro et al., 2014; Giachetti et al., 2015). The opposite is true for paleoclimate studies (e.g. Shane and Ingraham, 2002; Mulch et al., 2007; Cassel et al., 2014) – primary magmatic water is a source of error when using δD and water content of secondarily hydrated volcanic glass as a proxy for past elevation or climates (Seligman et al., 2016), and for archeological dating of obsidian artifacts (e.g. Riciputi et al., 2002).

Lack of experimental constraints on the rates of secondary hydration requires these types of studies to rely on approximations. Friedman et al. (1966) estimated that over 1000s of years water diffuses 20–100 μm into obsidian at 5 °C and 1000 μm at 100 °C. This corresponds to diffusion coefficients of 10^{-17} m^2s^{-1} at 5 °C and 10^{-13} m^2s^{-1} at 100 °C. Giachetti and Gonnermann (2013) used the TGA (ThermoGravimetric Analysis) technique and compiled data for known water concentrations of 0.0005–22.5 ka intermediate to silicic volcanic glass ranging from approximately 0–4 wt.% H_2O_t (total water as H_2O including OH^- and H_2O_m) to model the rate of secondary hydration of glasses of intermediate–felsic silica content. They concluded that, at surface temperatures, water diffuses into volcanic glass at a rate of approximately 10^{-23} m^2s^{-1} (± one order of magnitude), which is slower than the earlier ambient temperature diffusion coefficients of Friedman et al. (1966), but faster than the water-concentration-dependent model of diffusivity from Seligman et al. (2016). Diffusion is thought to proceed most rapidly in the beginning of hydration due to a more drastic concentration gradient (e.g. Zhang and Behrens, 2000; Anovitz et al., 2004) – however, hydration rates at this initial stage have never been studied. A simple calculation shows that at a room temperature rate of diffusion of 10^{-23} m^2s^{-1}, it will take 3171 years for hydration to advance 1 micron into the glass, making it impractical to conduct such an experiment.

To address this issue, we have designed a natural experiment to assess the amount of secondary hydration in Mount St. Helens 1980 pumice, before and after 35 years of exposure to meteoric water. A diffusivity of 10^{-23} m^2s^{-1} (Giachetti and Gonnermann, 2013) predicts that water in-diffusion should migrate 0.03–0.33 μm into glass over 35 years. This suggests that we could have the resolution to detect a potential shift in water

concentration and δD, if the bubble wall thicknesses are small enough (a few μm) to allow for a fast enough increase in wt.% water over 35 years.

Sampling strategy and aims

On August 22, 1980, bulk samples were collected from deposits erupted from Mount St. Helens on May 18, June 12, July 22, and August 7 and placed in dry storage at the U.S. Geological Survey's Cascades Volcano Observatory. The existence of these baseline samples provides the opportunity to determine how much natural rehydration has occurred in the Mount St. Helens deposits during the past 35 years. Consequently, during the summer of 2015 (35 years later) we collected pumice clasts from these same deposits as close as possible to their original 1980 collections sites (Fig. 1) to compare to the archived samples. The depth that samples were collected during our 2015 excursion varied from surface deposits to 10 m deep. It is important to note that samples coming from the 2015 collections are likely from a portion of the original deposit that slightly deeper into it due to subsequent erosion over the past 35 years. Fresh tephra deposits are eroded quite rapidly following eruptions, as was observed in the Valley of Ten Thousand Smokes (VTTS) by the Griggs expedition in 1915 (Griggs, 1922).

To characterize the primary degassing (1980) and secondary hydration (2015) history of the two sample sets, we analyzed the total water concentration (H_2O_t), hydrogen isotopic ratio (δD) of extracted water, and bulk glass silicate oxygen isotopic ratio of the glass ($\delta^{18}O_{BG}$). While more recent work has been done to constrain the degassing trends of rhyolitic eruptions of Mono Craters (Newman et al., 1988) and Chaitén (Castro et al., 2014), analysis of small quantities of fresh groundmass glass was more problematic for crystal-rich dacites, such as Mount St. Helens. Thus, our study additionally characterizes the degassing trend for a type-example arc stratovolcano.

ANALYTICAL TECHNIQUES

All glass samples analyzed in this study were analyzed for both δD and H_2O_t on the TCEA-MAT253 continuous flow and sampling system at the University of Oregon stable isotope laboratory (e.g. Bindeman et al., 2012), and laser fluorination for $\delta^{18}O_{BG}$ (Tables 1–2). Importantly, our methods permit analyses of milligram quantities of water-poor

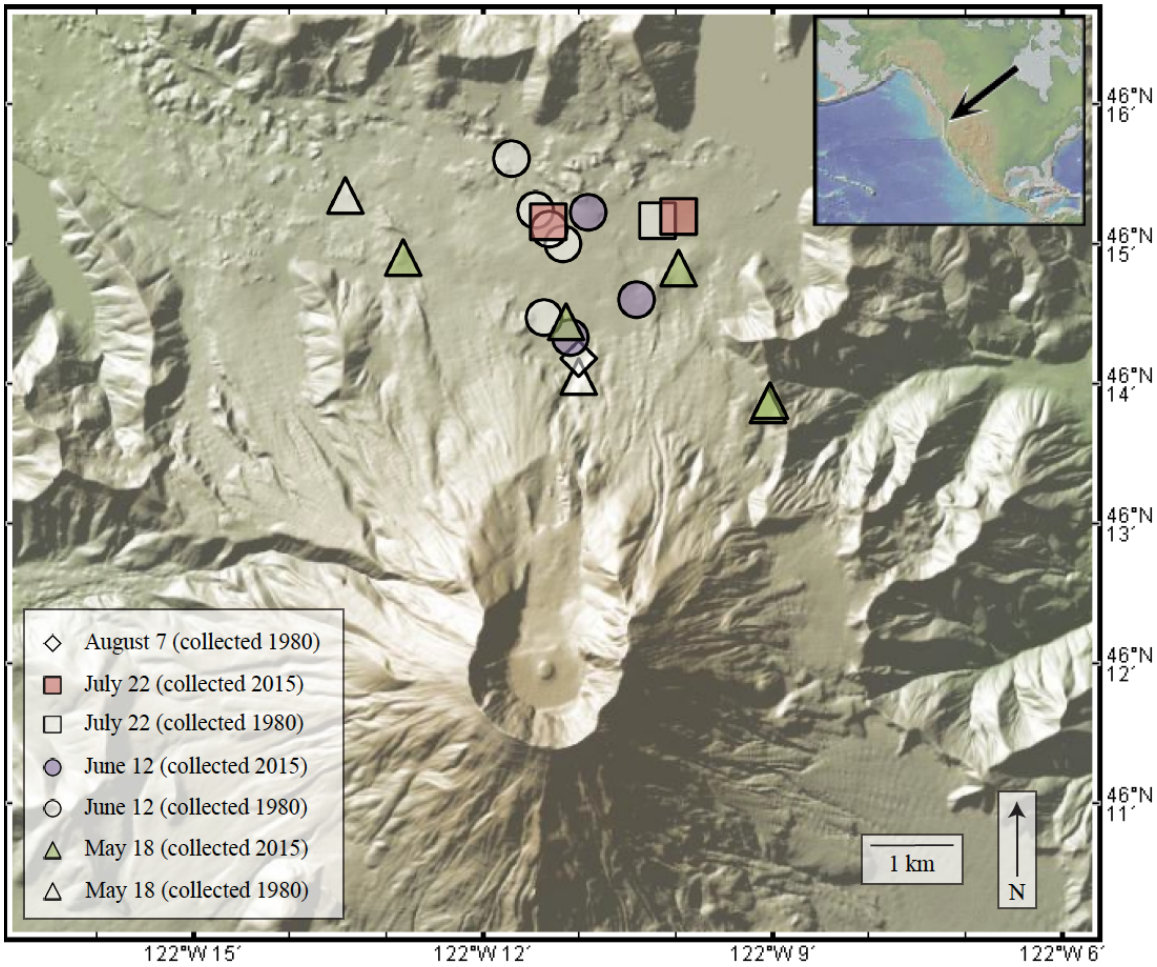

Figure 1. Map showing sample collection sites for tephra collected in 1980 (while filled) and those collected in 2015 (colored). Colors and symbol shapes on this map match the all subsequent figures. This map was created using GeoMapApp as the underlying base map (the Global Multi-Resolution Topography (GMRT) synthesis). GPS coordinates for sample locations can be found in Table 1.

glass (down to 0.1 wt.%) with δD precision within several per mil. This is a factor of 100 reduction in sample size, as compared to conventional methods. Since less material is needed, we are able to analyze the most pristine glass concentrate.

Prior to analysis, tephra samples were lightly crushed, placed in a water-filled beaker, and sonicated for ~60 min to remove any clays that could be attached to the glass (e.g. Dettinger and Quade, 2015; Seligman et al., 2016). The samples were then dried and 2–12 mg of glass smaller than ~0.5 mm were picked under microscope and packaged in silver foil. Prior to analysis, all samples were heated in a vacuum-sealed oven overnight at 130 °C to remove any adsorbed waters on the outer surface of the glass (e.g. Nolan and

Table 1
Location, sample type, and time exposed of glass samples

Sample Name	Unit	Days Exposed	Location N	Location E
5-18-1980_PF	May 18, 1980 PF	32	-122.184	46.234
SH233BLA	May 18, 1980 blast dacite	96	-122.224	46.255
SH233B	May 18, 1980 blast dacite	96	-122.224	46.255
SH233BLB	May 18, 1980 blast dacite	96	-122.224	46.255
SH233BLC	May 18, 1980 blast dacite	96	-122.224	46.255
2015Sel-MSH1A	May 18, 1980 blast dacite	12883	-122.214	46.247
2015Sel-MSH1B	May 18, 1980 blast dacite	12883	-122.214	46.247
2015Sel-MSH1C	May 18, 1980 blast dacite	12883	-122.214	46.247
2015Sel-MSH4	May 18, 1980 PF	12883	-122.187	46.241
2015Sel-MSH5	May 18, 1980 PF	12884	-122.167	46.247
2015Sel-MSH12	May 18, 1980 airfall pumice	12884	-122.150	46.231
2015Sel-MSH11	May 18, 1980 PF	12884	-122.150	46.231
2015Sel-MSH13	May 18, 1980 blast dacite	12884	-122.150	46.231
6-12-1980_PF	June 12, 1980 pyroclastic flow	2	-122.195	46.262
H81-4	June 12, 1980 pyroclastic flow	21	-122.187	46.253
H81-10	June 12, 1980 pyroclastic flow	21	-122.190	46.241
H81-2	June 12, 1980 pyroclastic flow	21	-122.186	46.251
SH229A	June 12, 1980 pyroclastic flow	71	-122.189	46.254
2015Sel-MSH2A	June 12, 1980 pyroclastic flow	12858	-122.186	46.239
2015Sel-MSH2B	June 12, 1980 pyroclastic flow	12858	-122.186	46.239
2015Sel-MSH7	June 12, 1980 pyroclastic flow	12859	-122.182	46.254
2015Sel-MSH8	June 12, 1980 pyroclastic flow	12859	-122.182	46.254
2015Sel-MSH10A	June 12, 1980 pyroclastic flow	12859	-122.173	46.243
2015Sel-MSH10B	June 12, 1980 pyroclastic flow	12859	-122.173	46.243
2015Sel-MSH10C	June 12, 1980 pyroclastic flow	12859	-122.173	46.243
SH231A	July 22, 1980 pyroclastic flow (upper)	32	-122.169	46.253
SH230	July 22, 1980 pyroclastic flow (lower)	32	-122.169	46.253
SH230LA	July 22, 1980 pyroclastic flow (lower)	32	-122.169	46.253
SH231BLA	July 22, 1980 pyroclastic flow (upper)	32	-122.169	46.253
SH230LB	July 22, 1980 pyroclastic flow (lower)	32	-122.169	46.253
SH231BLB	July 22, 1980 pyroclastic flow (upper)	32	-122.169	46.253
SH230LC	July 22, 1980 pyroclastic flow (lower)	32	-122.169	46.253

Bindeman, 2013). Samples were then loaded and purged with He carrier gas in an autosampler. We standardize the hydrogen isotope analyses using mica standards (NBS30, BUD, and RUH2) that have been calibrated relative to water sealed in silver

Table 1 continued

Sample Name	Unit	Days Exposed	Location N	Location E
SH231BLC	July 22, 1980 pyroclastic flow (upper)	32	-122.169	46.253
2015Sel-MSH3A	July 22, 1980 pyroclastic flow	12818	-122.186	46.239
2015Sel-MSH3C	July 22, 1980 pyroclastic flow	12818	-122.186	46.239
2015Sel-MSH6A	July 22, 1980 pyroclastic flow	12819	-122.167	46.253
2015Sel-MSH6B	July 22, 1980 pyroclastic flow	12819	-122.167	46.253
2015Sel-MSH6C	July 22, 1980 pyroclastic flow	12819	-122.167	46.253
2015Sel-MSH9	July 22, 1980 pyroclastic flow	12819	-122.187	46.253
SH232A	August 7, 1980 pyroclastic flow	16	-122.184	46.238

[a]see images in Fig. 4 and Appendix for sample descriptions, whole = average of full clast sample, outer = sample from outer portion of clast, inner = sample from inner portion of clast, halfway =

cups (VSMOW, W62001, and GISP; Qi et al., 2010). NBS30, with a known wt.% H_2O_t of 3.5 was used as a standard for water concentration corrections.

Select samples were also analyzed for their bulk $\delta^{18}O$ of the silicate at the Stable Isotope Laboratory at the University of Oregon to better understand the shift in the bulk rock $\delta^{18}O$ value due to any weathering. Glass separates were picked from select samples using a binocular microscope, with most weights ranging from 1–2 mg. Glass samples were analyzed one at a time by introducing them into a fluorination chamber separate from a custom-built airlock sample chamber. We used CO_2 laser fluorination with a BrF_5 reagent, and day-to-day variability was corrected using an in-house Gore Mt. Garnet ($\delta^{18}O$ = 6.52 ‰) standard. The generated gas was passed through a series of LN_2 cryogenic traps that caused the BrF_5 reaction products to be frozen, and then through a mercury diffusion pump to strip away any F2 gas that could not be cryogenically frozen. This left pure O_2, which was converted to CO_2 in a platinum-graphite converter. The yield was measured as being near 100% for all utilized samples, and the CO_2 gas was analyzed on an MAT 253 mass spectrometer in a dual inlet mode.

RESULTS

H_2O_t and δD trends of Mount St. Helens glasses

Field photographs of select samples are shown in Appendix Figures 1–6 (see Appendix D for all Chapter V supplements). Figure 2 compares the 1980 and 2015 datasets analyzed in four analytical sessions on the TCEA: 1980 and 2015 samples were intermixed within analytical sessions to ensure a lack of day to day variations. All water concentrations and

Table 2
Sample type, water content, and isotopic ratios of glass samples

Sample Name	Unit	Days Exposed	clast type[a]	H_2O_t (wt.%)	δD (‰)	$\delta^{18}O$ (‰)
5-18-1980_PF	May 18, 1980 PF	32	whole	0.3	-98.8	--
SH233BLA	May 18, 1980 blast dacite	96	outer	0.2	-78.6	--
SH233B	May 18, 1980 blast dacite	96	whole	0.2	-92.3	--
SH233BLB	May 18, 1980 blast dacite	96	halfway	0.2	-88.6	6.9
SH233BLC	May 18, 1980 blast dacite	96	inner	0.2	-77.1	--
2015Sel-MSH1A	May 18, 1980 blast dacite	12883	outer	0.4	-69.1	--
2015Sel-MSH1B	May 18, 1980 blast dacite	12883	halfway	0.3	-69.3	--
2015Sel-MSH1C	May 18, 1980 blast dacite	12883	inner	0.3	-75.25	--
2015Sel-MSH4	May 18, 1980 PF	12883	whole	2.1	-109.8	6.1
2015Sel-MSH5	May 18, 1980 PF	12884	whole	0.3	-94.6	--
2015Sel-MSH12	May 18, 1980 airfall pumice	12884	sample from pit to compare to 11	0.3	-74.1	--
2015Sel-MSH11	May 18, 1980 PF	12884	surface sample to compare to 12	0.3	-79.1	--
2015Sel-MSH13	May 18, 1980 blast dacite	12884	whole	0.5	-86.2	6.4
6-12-1980_PF	June 12, 1980 pyroclastic flow	2	whole	0.5	-94.1	6.8
H81-4	June 12, 1980 pyroclastic flow	21	whole	0.2	-74.9	--
H81-10	June 12, 1980 pyroclastic flow	21	whole	0.4	-72.1	--
H81-2	June 12, 1980 pyroclastic flow	21	whole	0.2	-76.5	--
SH229A	June 12, 1980 pyroclastic flow	71	whole	0.2	-80.4	--
2015Sel-MSH2A	June 12, 1980 pyroclastic flow	12858	outer	0.5	-122.9	6.6
2015Sel-MSH2B	June 12, 1980 pyroclastic flow	12858	inner	0.4	-116.0	6.5
2015Sel-MSH7	June 12, 1980 pyroclastic flow	12859	friable portion of clast to compare to 8	0.5	-76.2	--
2015Sel-MSH8	June 12, 1980 pyroclastic flow	12859	hearty portion of clast to compare to 7	0.4	-60.5	6.9

Table 2 continued

Sample Name	Unit	Days Exposed	clast type[a]	H_2O_t (wt.%)	δD (‰)	$\delta^{18}O$ (‰)
2015Sel-MSH10A	June 12, 1980 pyroclastic flow	12859	pumice clast (compare to 10B and 10C)	0.6	-71.0	--
2015Sel-MSH10B	June 12, 1980 pyroclastic flow	12859	vesicular (vesicular portion of large clast to compare to 10C)	0.2	-75.1	--
2015Sel-MSH10C	June 12, 1980 pyroclastic flow	12859	dense (dense portion of large clast to compar to 10B)	0.3	-61.4	--
SH231A	July 22, 1980 pyroclastic flow (upper)	32	whole	0.1	-79.8	--
SH230	July 22, 1980 pyroclastic flow (lower)	32	whole	0.2	-86.8	--
SH230LA	July 22, 1980 pyroclastic flow (lower)	32	outer	0.2	-81.5	6.9
SH231BLA	July 22, 1980 pyroclastic flow (upper)	32	outer	0.2	-86.9	--
SH230LB	July 22, 1980 pyroclastic flow (lower)	32	halfway	0.2	-81.8	--
SH231BLB	July 22, 1980 pyroclastic flow (upper)	32	halfway	0.2	-85.0	--
SH230LC	July 22, 1980 pyroclastic flow (lower)	32	inner	0.2	-82.3	--
SH231BLC	July 22, 1980 pyroclastic flow (upper)	32	inner	0.1	-72.8	--
2015Sel-MSH3A	July 22, 1980 pyroclastic flow	12818	outer	1.8	-123.8	6.0
2015Sel-MSH3C	July 22, 1980 pyroclastic flow	12818	inner	1.9	-129.0	--
2015Sel-MSH6A	July 22, 1980 pyroclastic flow	12819	outer	0.5	-66.4	--
2015Sel-MSH6B	July 22, 1980 pyroclastic flow	12819	halfway	0.2	-73.7	--
2015Sel-MSH6C	July 22, 1980 pyroclastic flow	12819	inner	0.4	-67.2	--
2015Sel-MSH9	July 22, 1980 pyroclastic flow	12819	whole	0.4	-75.2	--
SH232A	August 7, 1980 pyroclastic flow	16	whole	0.2	-99.2	--

[a]see images in Fig. 4 and Appendix for sample descriptions, whole = average of full clast sample, outer = sample from outer portion of clast, inner = sample from inner portion of clast, halfway = sample from in between outer and inner portion of clast

hydrogen isotopic ratios in our datasets range from 0.14 – 2.05 wt.% ± 0.44 1σ, and -61 – 129 ‰ ± 17 1σ, respectively (Fig. 2). However, there are some notable differences between the 1980 and 2015 glasses. Samples collected in 1980 were from the deposit's outer surfaces and were then stored in dry conditions in the lab. The 1980 samples have smaller water concentrations (0.14 – 0.45 wt.%, ± 0.08 1σ) and δD ranges (-72 – -99 ‰, ± 8 1σ) than those recollected for the same units and at approximately the same sites in 2015 (water concentrations 0.19 – 2.05 wt.%, ± 0.56 1σ; δD -61 – -129 ‰, ± 22 1σ). This causes small, yet consistent differences between the average water concentration of glasses collected in 1980 and those collected in 2015 (Fig. 3). We note that all samples collected in 2015 have higher average water concentrations and δD for their respective units, than those collected in 1980.

Furthermore, there are five data points that have lower δD values, which fall outside of the average range of the Mount St. Helens glasses, and also outside the

---

Figure 2 (next page). δD_{glass} (‰) in relation to the H_2O_t of water extracted from glass. The volcanic degassing trend (Newman et al., 1988; Castro et al., 2014) is shown in the background to illustrate typical δD and water concentrations of rhyolitic glasses that contain only magmatic water. The secondary hydration trend is a schematic representation from Seligman et al. (2016) and illustrates the general trend of hydrogen isotopes with increasing secondary hydration. The meteoric water value is based on dome and crater snowpack in 1988 (Hoblitt and Harmon, 1993) and regional springs (Barnes, 1984), and includes the -30 ‰ fractionation from Friedman et al. (1993) between meteoric water and water in glass. Note that most of the glasses have water concentrations and δD values within the 'volcanic degassing' trend, and depths of less than 0.5 km. However, the subsurface samples collected near gas escape pipes (Fig. 5), and some from Underwood et al. (2013) shown in asterisks, have lower δD values and higher water concentrations, causing them to fall outside the 'volcanic degassing' trend and along the secondary hydration trend. Data points in **a** are separated by unit, while data points in **b** are separated by relative vesicularity. In **b** note the low vesicularity of the June 12 data that just barely fall outside the 'volcanic degassing' trend. These data were also collected in the deep deposit and have a depleted δD value that is accompanied by a lower water concentration, relative to the July 22 and May 18 samples that also fall outside the 'volcanic degassing' trend. This difference is likely due to the difference in relative vesicularity. Published amphibole data is from Underwood et al. (2013); published glass data is from Underwood et al. (2013) and Halliday et al. (1983); published Yellowstone obsidian data is from Loewen and Bindeman (2015). Depth contours for equilibrium water concentration at saturation were calculated using VolatileCalc (Newman and Lowenstern, 2002). Data variability is a reflection of sample heterogeneity.

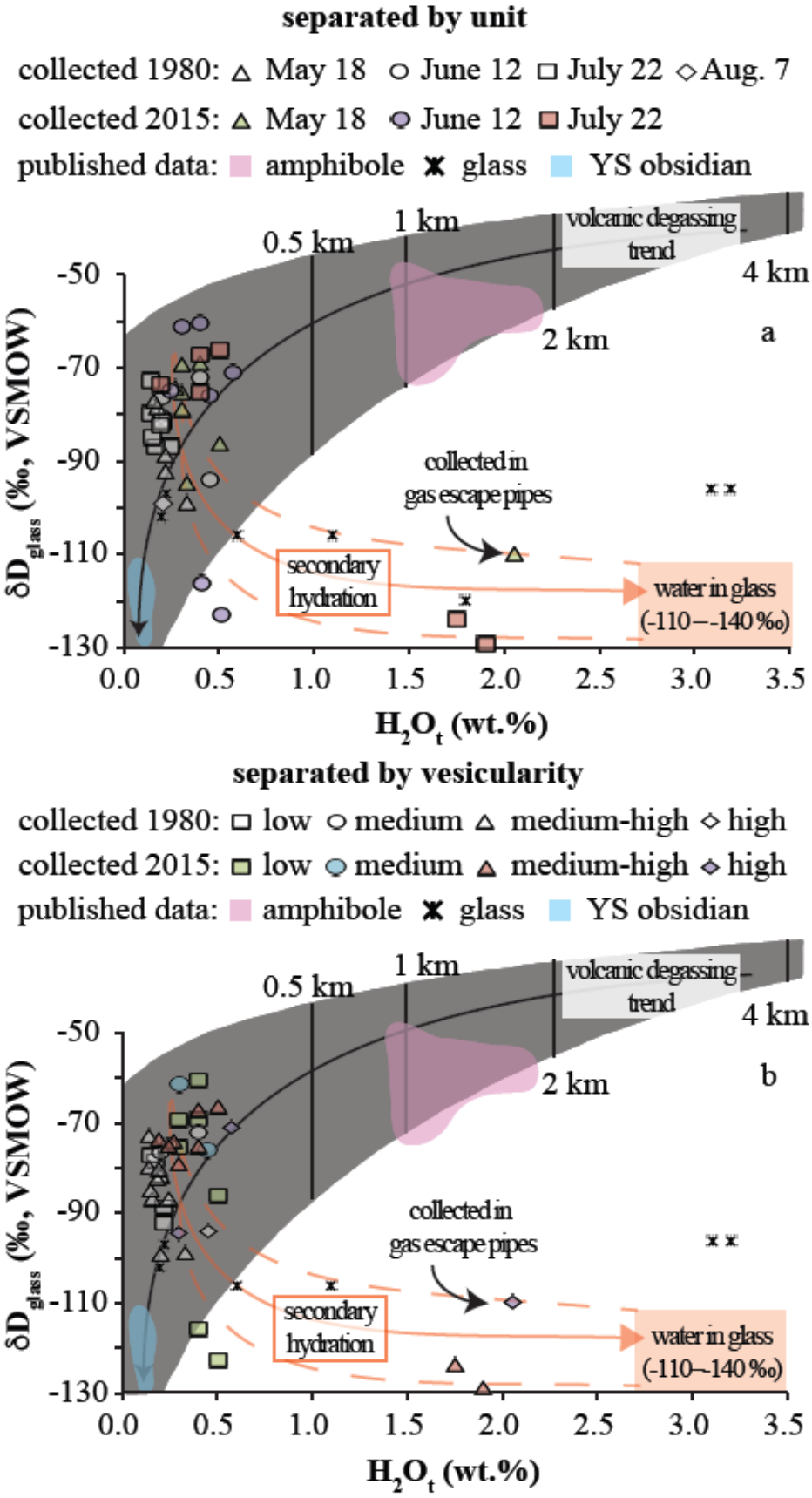
separated by unit
collected 1980: May 18 June 12 July 22 Aug. 7
collected 2015: May 18 June 12 July 22
published data: amphibole glass YS obsidian
0.5 km
1 km
2 km
4 km
volcanic degassing trend
a
collected in gas escape pipes
secondary hydration
water in glass (-110–-140 ‰)
δD glass (‰, VSMOW)
H2Ot (wt.%)
separated by vesicularity
collected 1980: low medium medium-high high
collected 2015: low medium medium-high high
published data: amphibole glass YS obsidian
b

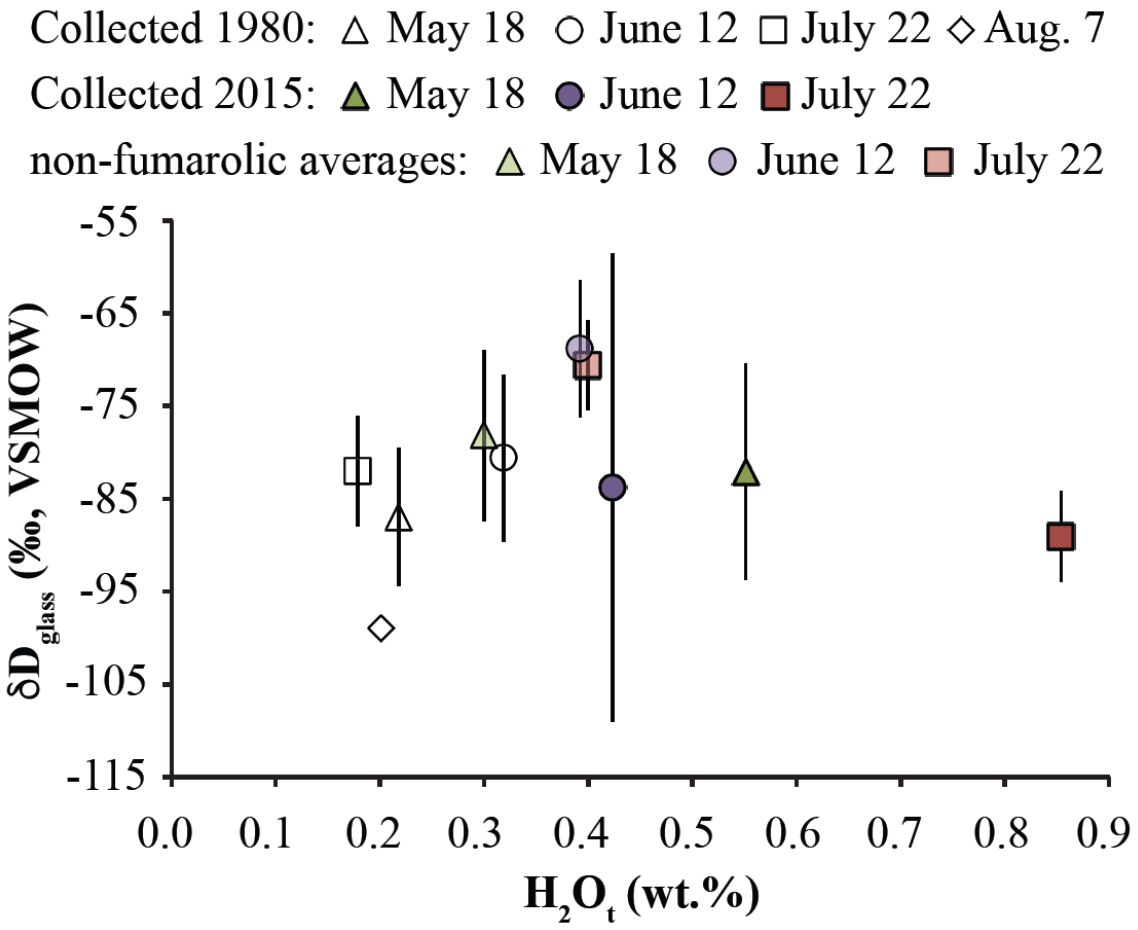

Figure 3. Average δD_{glass} versus water concentration for each of the units (May 18, June 12, July 22, and August 7) collected in 1980 and 2015. There is a slightly elevated water concentration for all of the samples collected in 2015, relative to those collected in 1980. Note that no standard deviation was included in this plot for the water variations, because the water concentration standard deviations are large, and make the plot difficult to read. In addition, the largest change in average water concentration is from the July 22 samples, which is due to the low average water concentration of the tephra deposited in 1980, relative to the two glasses analyzed from the thick tephra deposit. Average values for the tephra collected in 2015 that don't include any of the tephra collected near the gas escape pipes or in the deeper deposits are included with a paler shade than the rest of the averages. If these averages are compared to the 1980 averages, there is a 0.1–0.2 wt.% increase in average water. Also note the small increase in average δD between the 1980 samples and the 2015 non-fumarolic samples, which we attribute to prolonged surface degassing from deeper in the deposits that hydrated the more surficial 2015 samples, but did not have time to hydrated the 1980 samples.

volcanic degassing trend. All five were collected in 2015. Two of the data points falling outside the volcanic degassing trend are from the same clast collected from the June 12 eruption (2015Sel-MSH2A and 2015Sel-MSH2B), where one sample was taken from the

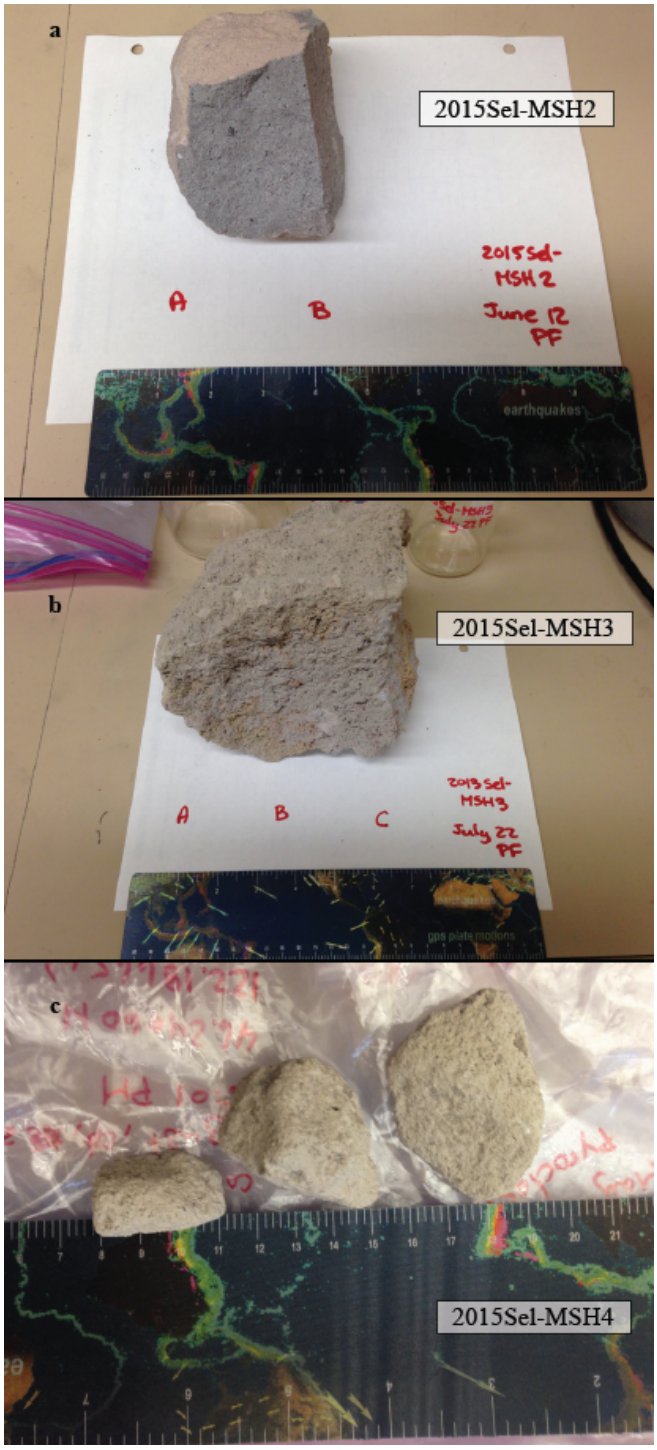

Figure 4. Select sample photographs illustrating relative vesicularity ranges and the locations that samples were taken. **a** photograph of sample 2015Sel-MSH-2 (June 12) showing the locations where samples A and B were collected from the dense clast. **b** photograph of sample 2015Sel-MSH-3 (July 22) showing the locations where samples A, B, and C were collected. **c** photograph of sample 2015Sel-MSH4 (May 18). Note the relative differences in vesicularity between the June 12 dense clast and the more vesicular July 22 and May 18 clasts.

center of a dense clast, and one was taken from the outer rim (Fig. 4). This is also the case for the two data points from the July 22 eruption, which both have low δD values and high water concentrations, where one sample was taken from the center (2015Sel-MSH3C), and one was taken from the outer rim (2015Sel-MSH3A) of a more porous tephra clast (Fig. 4). The data point from the May 18 eruption is from one smaller tephra clast (Fig. 4). The interesting feature of these three samples is that they were all subsurface samples collected from a deep erosional outcrop in the pumice plain north of Mount St. Helens (Fig. 5).

$\delta^{18}O$ bulk silicate trends of Mount St. Helens glasses

We also analyzed our Mount St. Helens glasses that have large ranges in D/H and H_2O_t for their $\delta^{18}O_{BG}$ values, where some groundmass glass contains trace quantities of microlites. $\delta^{18}O_{BG}$ values of samples of differing vesicularity collected from the deposits of the 1980 summer eruptions are identical within uncertainty (6.8–6.9 ‰). These values overlap with the $\delta^{18}O_{WR}$ ($\delta^{18}O$ whole rock) values (6.8–6.9 ‰) of the lowest water content (0.26–0.29 wt.%) and densest (2.38–2.58 g/cm^3) black dacite from the 1980 cryptodome from Hoblitt and Harmon (1993), suggesting that the primary magmatic $\delta^{18}O$ value of the 1980 eruption is between 6.8 and 6.9 ‰. The overall constant and normal to high $\delta^{18}O$ values of glass (within ± 0.08 ‰ uncertainty) corroborate the known relative compositional constancy during the May–August 1980 eruptions (e.g. Blundy et al., 2008), which suggests that there were no significant changes in magma type throughout the eruptive sequences, or interaction with waters or surrounding rocks in the conduit during the eruptions, except shallow volatile loss (Fig. 2), which would only minimally enrich the $\delta^{18}O_{BG}$, given the small $1000\ln\alpha_{glass\text{-}water}$ (0.4 ‰) at 500 °C (Zheng, 1991; 1993).

However, we note lowering $\delta^{18}O_{BG}$ values for some of the glasses collected in 2015, which correlates with increases in water concentration (Fig. 6). It is important to note that these samples are always within or near a deposit containing narrowly pyramidal structures that are interpreted to be gas escape pipes (Fig. 5b). We observe that water-poor samples collected from the surface have nearly identical $\delta^{18}O_{BG}$ values

Figure 5. Photographs from the field showing the deeper deposits of the May 18, June 12, and July 22 samples. **a** photograph of the view back towards Mount St. Helens of the sample location for 2015Sel-MSH-4 (May 18). The sample location of 2015Sel-MSH-2 (June 12) and 2015Sel-MSH-3 (July 22) is approximately 180 meters back up the drainage towards Mount St. Helens (around the corner). **b** Photograph of sample location for 2015Sel-MSH-4 (May 18) as collected in the field. Note the gas escape pipe that the samples were collected in. **c** photograph of sample location for 2015Sel-MSH-2 (June 12) and 2015Sel-MSH-3 (July 22) as collected in the field.

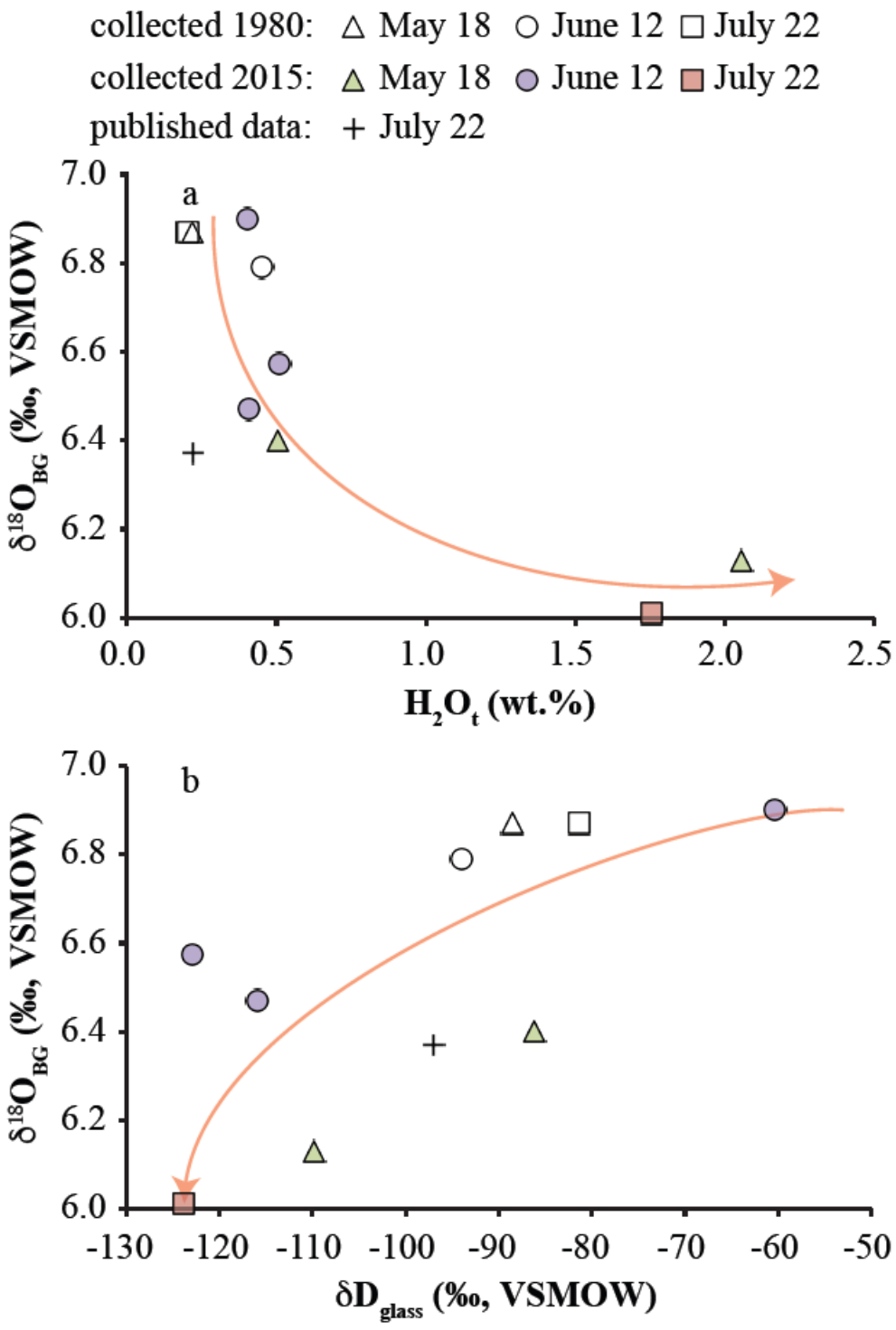

Figure 6. $\delta^{18}O_{BG}$ trends relative to total water concentration and δD_{glass} values. Note that the higher water concentration glasses (with lower δD_{glass} values shown in Figure 2) have correlated drops in their $\delta^{18}O_{BG}$ values. Trends of decreasing $\delta^{18}O_{BG}$ and δD_{glass} values, along with increases in H_2O_t (wt.%) are indicative of localized water-rock interactions. The published datum is from Halliday et al. (1983).

(average = 6.8 ‰, range = 6.4–6.9 ‰), but near gas escape pipes they reach 6.1 ‰ average $\delta^{18}O_{BG}$ values, with a range from 5.9 – 6.6 ‰.

Temperature of emplacement

Banks and Hoblitt (1981) used thermocouples and direct-reading, electronically compensated, digital voltmeters starting two days after the May 18 paroxysmal eruption of Mount St. Helens to determine the emplacement temperatures of the deposits of the May 18, June 12, and July 22 eruptions. Temperature readings of the May 18 pyroclastic flow deposits range from 297–418 °C, with an estimated emplacement temperature of 307 °C based on two temperature measurements that were separated by 850 m. Temperatures of the June 12 pyroclastic flow deposits ranged between 361 and 602 °C just 15 hours after their emplacement. Importantly, temperature measurements for the June 12 eruption from Hoblitt et al. (1985) indicate that at depths of ~6 m into the pyroclastic flows, temperatures were still above 500 °C in December of 1980, showing the slow rate of cooling within these deposits. The temperature readings for the July 22 pyroclastic flow deposits were nearly 660 °C within 35 minutes of the eruption. Also importantly, the temperature profiles show that the deposits became saturated with steam as water infiltrated the deposit. We conclude that conditions conducive to rehydration of pyroclastic deposits – extended exposure to high-temperature water vapor – are apt to be found beneath the surface, in deep deposits.

DISCUSSION

H_2O_t and isotopic trends of the Mount St. Helens glasses

We use our dataset from both 1980 and 2015 below to discuss the δD-H_2O trends pertinent to magmatic degassing and the earliest stages of secondary hydration. Figure 2 illustrates the water concentration and hydrogen isotopic ratio differences between the samples collected in 1980 and 2015. The majority of samples fall within the volcanic degassing trend, including all samples collected in 1980 and most of the samples collected in 2015.

The roles of emplacement temperature and fumarolic activity

The hydrated May 18 clast was collected within a gas escape pipe, and the June 12 and July 22 samples were collected from this same deep outcrop, just 180 meters to the south (Fig. 5). Interestingly, the May 18 and July 22 samples from this outcrop have been pulled off the volcanic degassing trend by rehydration. The June 12 sample is off the degassing trend, but has not undergone rehydration. Note in Fig. 2b that the June 12 clast has a much lower vesicularity than the July 22 and May 18 samples (Fig. 4). Although water was not able to diffuse into the glass of the clast, likely due to the low vesicularity, it appears that hydrogen isotopes were able to exchange. Therefore, exchange of hydrogen isotopes is apparently the earliest step in the secondary hydration process. Despite 35 years of exposure to meteoric water, most glasses have not had enough time to allow water to diffuse into the glass. Diffusion of water is only obvious in high-vesicularity glasses exposed to water at elevated temperatures. Although high vesicularity is apparently necessary to hydrate the tephra near gas-escape pipes, there is no clear correlation between the δD of the water extracted from the glasses and the relative vesicularity (Appendix Fig. 7–8).

Distinguishable trends of surface tephra samples

As is shown in Figure 2b, we group our tephra into four separate categories of relative vesicularity and utilize different relative average bubble wall thicknesses from the four density categories of Cashman and McConnell (2005). This provides us with relative distances (bubble wall thicknesses) for our vesicularity groups that water needs to migrate across to hydrate the tephra clast (low = 50 μm, medium = 21 μm, medium-high = 14 μm, and high = 6 μm), where the bubble wall thicknesses were determined using Figure 3 of Cashman and McConnell (2005). We utilize these bubble wall thicknesses and the estimated rates of the diffusivity of water in glass at ambient temperature to see if there should be a recognizable shift in water concentration in our glasses.

We note from Figure 3 that the glasses collected in 2015 have a higher average water concentration that those collected in 1980 (also see Appendix Fig. 9). To test if this is a significant signal, we start with the highest vesicularity tephra that has the thinnest average bubble wall (6 μm) as shown by Cashman and McConnell (2005). Using the

water-concentration-dependent model of diffusivity from Seligman et al. (2016), even the most vesicular tephra will not have gained enough water to have a recognizable shift in water concentration. However, if we utilize the fastest rate of diffusion estimate from Giachetti and Gonnermann (2013), which shows that water could migrate up to 0.33 μm into the glass over 35 years, and the thinnest bubble wall (6 μm), this could lead to an increase of up to 0.5 wt.% H_2O_t in the glass, which is far above the detection limit of our instrument (± 0.05 wt.%). Even though there is only a small (0.1–0.2 wt.%) increase in average water concentration for the May 18th, June 12th, and July 22nd eruptions, when the high water samples collected from the deep outcrop are excluded in the average (shown in Figure 3 as the paler shaded symbols), there is still a possibility for a distinguishable migration of water into the glass. Furthermore, the only tephra that have become hydrated above 1.0 wt.% H_2O_t fall into the two highest relative vesicularity groupings (Fig. 2b, Appendix Figs. 7–8), which indicates the need for higher vesicularity to promote secondary hydration. Consequently, we suggest that the Mount St. Helens glasses have acquired a small, but detectable amount of meteoric water in 35 years.

Curiously, we also note a small increase in average δD values (2015: -73 ‰, 1980: -87 ‰) for the surface tephra samples, which is in contrast to the expected decrease in δD associated with secondary hydration (Fig. 2). During our sample collection in 2015, we noted that many of the 1980 sample locations had been eroded away, so we had to collect from slightly deeper regions of the flow that are now exposed at the surface. The 1980 samples were collected soon following eruption, when the deposits were still warm and continuing to degas. Subtly higher δD values are peculiar and require that the hydrating water was higher in δD than either the local meteoric water or the magmatic water. Four explanations are possible: 1) hydration happened because warm residual or surface water within a deposit lost light hydrogen during evaporation; 2) hydration of the sampled deposit happened because of escaping magmatic water during continuous degassing, but this process is likely not possible above the glass transition (see Fig. 2); 3) hydration was from water that had a complex exchange with local vegetation promoting the loss of isotopically light H_2 and CH_4; or 4) degassing of deeper deposits released water that was enriched in deuterium, which hydrated overlying deposits, causing the overlying deposits to become enriched in deuterium and H_2O_t. Regardless of the exact

cause, it is significant that we have discovered an important heterogenization of the H_2O and δD values of this erupted tephra deposit, putting important constraints into the future sampling of tephra deposits for either secondary hydration or degassing purposes.

Trends of $\delta^{18}O_{BG}$ with δD and H_2O_t around gas escape pipes

Our three samples that lie outside the volcanic degassing trend were collected relatively deep within outcrops (~10 m) and show signs of fumarolic activity (Fig. 5). While subtly recognizable in the field, our measurements unambiguously identify these features as gas escape pipes because the pumice is hydrated up to 2 wt.% H_2O_t and all samples not collected from this deposit show less hydration and less of a depletion of δD (Figs. 2, 6). Given the measured temperatures cited above and the thickness of the deposit, we compute that it would take ~10–20 years to conductively cool the interior of such a deposit from 500 to 50 °C, and shorter if flushed with water, which was likely the case given the presence of hot springs for several years after the 1980 eruptions. In a similar setting, but with an ~200 m thick deposit, long-lived fumaroles were observed by the 1916 Griggs expedition four years after the 1912 Katmai eruption, and the fumaroles were still present through 1930 (Griggs, 1922; Fierstein and Hildreth, 1992).

We compare our $\delta^{18}O$ versus water trends with those from Holt and Taylor (1997) for the >80 m thick Owen's Gorge section of the more densely welded 0.76 Ma Bishop Tuff. Holt and Taylor (1997) note localized $\delta^{18}O_{WR}$ zones as low as -5 ‰ near regions of prior fumarolic activity, but their study did not involve hydrogen isotopes nor total water measurements that would have constrained values of secondary hydration by meteoric water. They utilize these low $\delta^{18}O_{WR}$ zones in their deposit to infer time-averaged interaction temperatures of 400–600 °C over 10–25 years. In a different study, Holt and Taylor (2001) measured less extreme $\delta^{18}O_{WR}$ (-0.1 ‰) values in the uppermost 10–15 m of the 200 m thick 1912 ash-flow sheet in the Valley of Ten Thousand Smokes, Alaska. This deposit, which is much more porous and permeable than the Bishop tuff, required localized (10–15 years) of high temperature (450–645 °C) fumarolic activity according to Holt and Taylor (2001).

Our trends illustrate decreasing $\delta^{18}O_{BG}$ with increasing water (Fig. 6a), even though our $\delta^{18}O_{BG}$ values aren't as depleted. However, in addition to the $\delta^{18}O_{WR}$ data

from Holt and Taylor (1997; 2001), we have low $\delta^{18}O_{BG}$ values that correlate with decreases in δD and increases in wt.% H_2O_t in our Mount St. Helens glasses (Fig. 6), allowing us to visualize the earliest stages of hydration when $\delta^{18}O$ is not significantly affected, as is shown by our strongly curved δD versus $\delta^{18}O$ trend (Fig. 6). Therefore, the muted low $\delta^{18}O$ signal that our data show, relative to Holt and Taylor (1997; 2001), is likely due to the fact that the less voluminous and thinner Mount St. Helens deposits cooled more quickly, providing less time to hydrate and exchange oxygen.

The similarly low (-11 – -15 ‰) $\delta^{18}O$ and (-70 – -111 ‰) δD value of meteoric water surrounding the Bishop Tuff, Katmai, and Mount St. Helens makes high temperature interactions with a cooling (300–500 °C) deposit proceed at $1000\ln\alpha_{glass\text{-}water}$ ranges between 3.1–0.4 ‰ (for 300 and 500 °C respectively) for oxygen isotopes using calculated CIPW norms and mineral-water fractionations from Zheng (1991; 1993). Thus, the percolating ~ -13 ‰ meteoric water will always decrease any normal $\delta^{18}O$ values.

An additional, and alternative, explanation for the higher $\delta^{18}O$ values of the Mount St. Helens glasses is that the subsurface Mount St. Helens loosely welded studied samples were emplaced at a cooler temperature than the 80 m thick Owen's Gorge deposit of the Bishop Tuff. The latter was clearly emplaced above the glass transition temperature, allowing its fiamme to become flattened, and the whole deposit to become densely welded, unlike what is observed for the Mount St. Helens deposits. This indicates a higher temperature of deposition (near 650–700 °C) for the Bishop Tuff versus the lower temperature (near 300 °C) for the Mount St. Helens deposits reported by Banks and Hoblitt (1981). The importance of this difference is in comparing the $1000\ln\alpha_{glass\text{-}water}$ at 700 °C (-0.4 ‰) versus the $1000\ln\alpha_{glass\text{-}water}$ at 300 °C (+3.1 ‰), making the water-rock interaction at high temperature more efficient at lowering the rock's $\delta^{18}O$ value. It is unlikely that full equilibrium is achieved in natural settings, and thus our measured higher $\delta^{18}O$ values are likely a reflection of two things: 1) incomplete exchange, especially for shorter cooling times of the Mount St. Helens deposits, and/or 2) colder temperature of emplacement of the Mount St. Helens deposits, which favors a higher $\delta^{18}O$ reaction product.

Magmatic degassing of an archetypal arc volcano

With the exception of the secondarily hydrated samples that we discussed above, we utilize δD-H_2O relationships to discuss trends in magmatic degassing, which so far has been done only at a handful of volcanoes around the world. Isotopic insight into a volcano are important to constrain the depth that gas separates from the magma (e.g. Fig. 2) and if crystallization driven degassing for microlite-rich dacites of arc volcanos and Mount St. Helens specifically (Blundy and Cashman, 2005) affects the δD-water relationships shown in Fig. 2. We thus compare our trends of δD versus H_2O_t for the Mount St. Helens glasses to data from Underwood et al. (2013) and one datum from Halliday et al. (1983). Given the amphibole data from Underwood et al. (2013), we can derive a degassing trend to obtain the range of δD and H_2O_t values for the Mount St. Helens deposits (Fig. 2). It is notable that this trend overlaps well with earlier datasets for the crystal-poor rhyolitic volcanoes of Mono Craters (Newman et al., 1988) and Chaitén (Castro et al., 2014). This suggests that separation of water from the bulk magma is: 1) shallow, and 2) similar to rhyolites that don't contain abundant microlites.

Seismic data from Mount St. Helens prior to and during the 1980 eruption suggests magma storage at a depth of 7–14 km (Scandone and Malone, 1985). It is notable that we do not achieve the very low δD values proposed in the deep permeable foam model of Taylor et al. (1983) or Eichelberger et al. (1986) developed for the obsidians of Glass Mt., CA. Rather, the Mount St. Helens glasses come to 0.5 wt.% water before the δD values begin to decrease, and they never reach δD values much below -100‰, suggesting relatively short-lived shallow degassing. We can better understand these trends through the use of VolatileCalc (Newman and Lowenstern, 2002), which permits us to add pressure information onto Figure 2. Figure 2 illustrates that the episode of gas-bulk magma separation at Mount St. Helens must have occurred at a depth less than 0.5 km, which is also illustrated by the moderate δD values of our glasses, when we compare our -70 – -100 ‰ δD values to those of the Yellowstone lavas that erupted slowly (Loewen and Bindeman, 2015), which had significantly more time to degas and therefore have significantly lower (<-110 ‰) δD values. This shallow depth agrees with the shallow degassing and rapid magma ascent of the Mount St. Helens summer eruptions determined by Cashman and McConnell (2005), based on textures, glass composition,

and volatile contents of melt inclusions. Cashman and McConnel (2005) utilize the high water content of melt inclusions and the highly vesicular nature of many tephra clasts to suggest that magma storage was deeper than 8 km until shortly before the eruption, which we also note from our moderate δD values.

CONCLUSIONS

1. We note a distinguishable 0.1–0.2 wt.% increase in average water concentration for each unit collected from the surface in 2015 relative to tephra collected from the same unit in 1980. The minor increase in water concentration is associated with an average δD increase of 15 ‰, which we conclude is associated with degassing of deeper deposits that hydrated the overlying deposits with heavier δD water vapor. Since time was needed for this process, the samples collected in 1980 contain less water and have lower δD values.

2. In contrast, the subsurface tephra associated with gas escape pipes, indicate that elevated heat is required for larger amounts (>1.0 wt.% H_2O_t) of secondary hydration to occur within a 35 year time span, leading to a decrease in δD values.

3. Our muted fumarolic activity relative to what is found at the Bishop Tuff and Katmai results in the reduced depletions of our $\delta^{18}O_{BG}$ values, which do not show as significant a decrease as those from the thicker deposits from the Bishop Tuff and Katmai.

4. We do not find δD values as depleted as those found in lava eruptions that are able to degas for longer periods, and therefore able to lower the δD value of the residual hydrogen. We conclude that our data is consistent with eruptions driven by shallow degassing (0.5 km separation of water from the bulk magma) from a magma that is rapidly rising from depth, which would not allow water to degas significantly prior to eruption.

5. Furthermore, our conclusions show that tephra collected from deeper deposits are more likely to become secondarily hydrated more rapidly, which is important for volcanological and engine turbine safety research, which do not focus on secondary waters. In addition, our research shows that paleoclimate studies should focus on surface deposits, since tephra collected from deeper within deposits are likely to be hydrated at

elevated temperatures, which leads to smaller fractionations between water and glass (less than the expected 30 ‰ ambient temperature fractionation).

BRIDGE

In this chapter (Chapter V), I used δD, $\delta^{18}O$, and water concentrations to characterize the earliest stages of secondary hydration utilizing the well-characterized 1980 eruptions of Mount St. Helens. I determined that, while small increases in water (0.1–0.2 wt.%) are possible within 35 years, a higher heat source is required to significantly increase the water concentration of glass. I also utilized δD and water concentrations to denote the need for magma storage at depth prior to a rapid rise in magma before the 1980 eruptions of Mount St. Helens.

In the following chapter (Chapter VI), I will focus on method development for the TCEA to analyze oxygen isotopic ratios of water extracted from silicates. This new method is based on previous work by Nolan and Bindeman (2013), which proposed that oxygen isotopes of water extracted from volcanic glass is actually a more reliable means of determining paleoclimates. Using this motivation, I begin to develop this method as a means of understanding oxygen isotopes of water extracted from silicates through the use of mass balance and $\delta^{13}C$ corrections.

CHAPTER VI

$\delta^{18}O$ ANALYSES OF HYDROUS VOLCANIC GLASS USING THE TCEA: NEW STANDARDS AND METHODOLOGY

In preparation for submission to Geochimica et Cosmochimica Acta as co-authored material with Ilya N. Bindeman. I conducted the majority of this work, with advising by Ilya Bindeman. I drafted all the figures and the writing is mine, with assistance by Ilya Bindeman.

INTRODUCTION

Oxygen isotopes in hydrous portions of hydrous silicates

Investigation of oxygen isotopes in the hydrous portion of silicates and sulfates (e.g. kaolinite, illite, micas, alunite) in addition to the bulk $\delta^{18}O$ analysis of these phases spans several decades (Savin, 1967; Hamza and Epstein, 1980; Bechtel and Hoernes, 1990; Girard and Savin, 1996; Gilg et al., 2004). These early efforts used conventional off-line stable isotopic methods. They targeted internal silicate-OH $\delta^{18}O$ fractionation as an internal thermometer and at the same time (if the silicate portion of the mica $\delta^{18}O$ was measured), the temperature of last equilibration, perhaps in an analogy to modern day clumped isotope methods (Eiler, 2007).

In order to extract hydrogen-bound oxygen from these OH-bearing materials, two chief methods were employed: partial low-temperature fluorination using F_2 gas, and thermal dehydroxylation by heating in a resistance furnace conducted at 800–1000 °C (Hamza and Epstein, 1980; Bechtel and Hoernes, 1990; Girard and Savin, 1996). Both methods, coupled with measurements of the silicate residue, yielded good mass balance constraints and largely consistent results (within 1–2 ‰ $\delta^{18}O$ uncertainties). The first two studies found that both fluorination and thermal dehydroxylation yielded overlapping results, while the latter suggested that dehydroxylation is preferred. These authors, including Clayton et al. (2009), suggested that there is no isotopic exchange upon rapid water loss from the sample. Therefore, the resulting $1000\ln\alpha_{silicate\text{-}OH}$ fractionation reflects the true difference between the oxygen in the OH and in the silicate. However, since only

half of the oxygen is extracted as H_2O from the OH^- sites during dehydroxylation, this difference must be corrected using the fractionation at the temperature of extraction, as we do below.

Dehydroxylation of Fe-bearing minerals and glasses may be more complicated than for Fe-free or Fe-poor samples and involves Fe reduction:

$$2OH + FeO_{silicate} + 2C = H_2O + Fe_{silicate} + 2CO \quad \text{1a}$$

$$2OH + Fe_2O_{3_{silicate}} + C = 2FeO_{silicate} + CO \quad \text{1b}$$

Therefore, previous investigators avoided chlorites and other micas rich in Fe due to the difficult to quantify effects.

Another approach to understand water (and OH^-) fractionation in silicates is to use an increment method involving oxygen bonding environments and the associated dependence on temperature. Using these methods, Schütze (1984) and Zheng (1993) computed OH-silicate fractionations as a function of temperature. Additionally, Girard and Savin (1996) and Bechtel and Hoernes (1990) observed that their experimentally determined OH-silicate fractionations agree with these calculations at 200–300 °C, but disagreements were larger at low (environmental) temperatures, which predict, for example, 40 ‰ offsets between the silicate and the OH- portion of kaolinite (Zheng, 1993). The closure temperature of investigated samples was not discussed by either of these authors and their samples were sourced from hydrothermal deposits in plutonic environments.

We here attempt to investigate the meaning of $\delta^{18}O$ of water extracted from rapidly quenched, mostly felsic pyroclastic rocks. We use the TCEA reduction furnace in which samples are dehydroxilated in seconds at 1450 °C and measured in a continuous flow mode. Given previously positive results described above of thermal extraction for longer times and at lower temperatures, which show no fractionation, and the much smaller size of our samples (a few mg), we consider the TCEA to be a superior technique to retrieve the true unfractionated $\delta^{18}O$ value of hydrogen-based oxygen in glasses.

We target rocks that have only primary magmatic water (both H_2O_m and OH^-) and those that have experienced secondary hydration by mostly molecular water; many of these samples have been previously investigated for D/H and H_2O_t (Seligman et al., 2016;

Martin et al., 2016). As we have either measured or estimated the proportion of OH^- and H_2O_m, we are able to provide a mass balance relationship with respect to both molecular water and hydroxyl.

Oxygen isotopes of the hydrous portion of silicate glass

Concentrations of water in silicate glass and its hydrogen isotopic ratio have been used to understand a variety of volcanic processes including the sources of magmatic water, fluid-rock interactions, magmatic degassing, and the cycle of water through subduction zones (e.g., Kyser and O'Neill, 1984; Taylor, 1986; Giggenbach, 1992; Pineau et al., 1999; Shaw et al., 2008; De Hoog et al., 2009; Walowski et al., 2015). Although many studies have been able to document the $\delta^{18}O$ values of bulk rocks and mineral phases there are no studies of the $\delta^{18}O$ value of water extracted from solid samples. The reason oxygen isotopes have not yet been implemented is because of the unknown reliability of analyses, and the meaning of the oxygen isotopes of water extracted from volcanic glass.

Water in silicate glass can be quenched magmatic, consisting of H_2O_m and OH^- and secondary, which is added to volcanic glass below the glass transition as mostly H_2O_m (Newman et al., 1986; Silver et al., 1990; Ihinger et al., 1999; Giachetti et al., 2015).

Below, we document our work on the $\delta^{18}O$ analyses of water extracted from volcanic glass using rapid thermal decomposition and reduction in a Thermal Conversion Elemental Analyzer (TCEA)-MAT253 mass spectrometer system in which milligram quantities of hydrous samples are rapidly heated to 1450 °C and reduced to H_2 and CO gases (Fig. 1). Previous work developed by Sharp et al. (2001), Cassel et al. (2014), and Mulch (2006), among others, investigated primarily hydrogen isotope analyses of organic and inorganic hydrous minerals. In addition, the TCEA is routinely used to analyze oxygen isotopes in phosphates (e.g. Vennemann et al., 2002) and sulfates (e.g. Bao and Marchant, 2006), etc. We test if analyses of hydrous glasses will be a practical approach to understanding magmatic processes of volcanic degassing and secondary hydration, which can be correlated with the already well-understood hydrogen isotopic ratios.

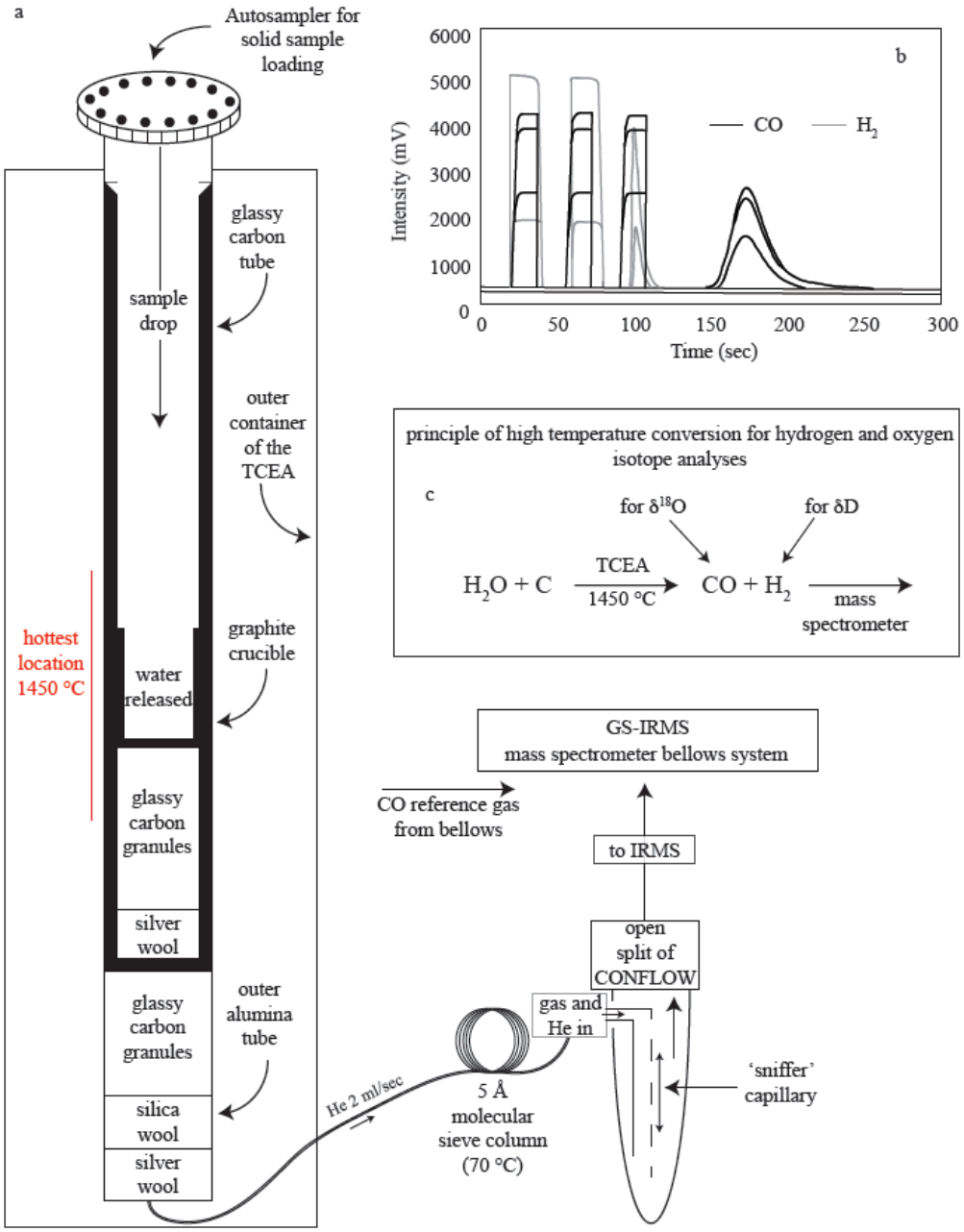

Figure 1. Schematic of the TCEA set up for oxygen and hydrogen isotopic analyses. a) Schematic of the TCEA set up and how the sample travels through the TCEA to the mass spectrometer for analysis. Solid samples are initially loaded in an autosampler above the reaction furnace. One at a time, samples are dropped into the reaction furnace and rapidly heated to 1450 °C. They are then passed through a 5 Å molecular sieve column, through an open split, and into the mass spectrometer, where the reference gas is introduced from the bellows system of the dual inlet (see text for a detailed description). b) example of the analysis peaks for CO and H_2 analyses. The peaks shown here are from NBS30 analyses. c) Illustration of the principle of high temperature conversion for hydrogen and oxygen isotope analyses on the TCEA.

Oxygen isotopes of secondary water in volcanic glass

In addition to the importance of understanding the $\delta^{18}O$ of magmatic water in volcanic glass, glasses that have been hydrated by surrounding, typically low-$\delta^{18}O$, meteoric water also contain important information in their $\delta^{18}O$ values. It is well understood that as climate fluctuates between warmer and colder temperatures the $\delta^{18}O$ and δD values of precipitation change. This shift in water isotopic ratios is also true for precipitation at higher versus lower latitudes, over topographic changes, or farther into continental interiors versus near the coast (Dansgaard, 1964; Rowley et al., 2001). Utilizing these isotopic variations, researchers have traditionally focused on analyses of the δD and $\delta^{18}O$ in a variety of solids as proxies for paleoenvironmental studies to determine the paleoclimate or paleoelevation of a region. Sheppard and Gilg (1996) and Mulch (2006) focused on the δD of water in clays, while Chamberlain and Poage (2000) focused on the $\delta^{18}O$ of water in clays. Bao et al. (2000) utilized oxygen isotopic ratios of goetite to document paleoclimate signals. Snell et al. (2014) utilized clumped isotopes of carbon and oxygen (Δ^{47}) of carbonates to determine temperature fluctuations. In addition, hydrogen isotopic ratios of secondarily hydrated glass have been used by multiple researchers (e.g. Friedman et al., 1993b; Cassel et al., 2014) to determine paleoelevations of regions across the United States.

The use of hydrogen isotopic ratios (δD) of secondarily hydrated volcanic glass to understand paleoenvironmental conditions and water isotope values is based on the assumption that, following deposition, ash is hydrated to 2–4 wt.% water within hundreds to a few thousand years and that this water does not equilibrate or shift with changing surrounding waters because there are no thermodynamically favorable forces to change it (Friedman et al., 1966; 1993b). If this assumption holds true, it means that the hydrogen isotopic ratio of water contained within volcanic glass reflects the isotopic value of meteoric water with an approximately -30 ‰ offset (Friedman et al., 1993a), and this ratio does not change with time as the subsequently surrounding δD of precipitation changes. Researchers have utilized this concept to use the hydrogen isotopic values of water in glass as a century to millennia averaged paleoclimate indicator (Shane and Ingraham, 2002; Mulch et al., 2008; Cassel et al., 2014). However, recent experimental

work by Nolan and Bindeman (2013) used naturally hydrated ash from the 7.7 ka Mt. Mazama eruption and placed it in ^{2}H and ^{18}O doped waters at 70, 40, and 20 °C for up to three years and showed that the hydrogen isotopes of the water in the glass began to equilibrate with surrounding deuterated waters on a timescale of hours to days at 70 °C, and months at 40 °C. Following five years, the 20 °C dataset showed an increase in δD of approximately 20 ‰, and the experiment is still running. While hydrogen isotopes were able to exchange between ash and surrounding waters, the total water concentration and the $\delta^{18}O$ of the extracted water remained unchanged, suggesting preferential mobility of D and H at least at 40 and 70 °C. This experiment places limitations on paleoclimate or paleoaltimetry studies if the δD of precipitation has changed since the ash was deposited, and proposes that previous research using the δD of water extracted from secondarily hydrated glass needs to be further experimentally evaluated. However, to be able to utilize the $\delta^{18}O$ of water in glass for paleoenvironmental studies, further studies are needed, which is what we detail below.

METHODOLOGY

Samples and analytical strategy

Samples used for this research are listed in Tables 1–3, and details of the oxygen isotope analyses of the magmatic glasses are listed in Table 4. We analyze volcanic glass with low water concentrations from Mount St. Helens (June 12, 1980), Volcán de Fuego (1974), Mt. Spurr (1992), and the 7.7 ka Cleetwood rhyolite from Mt. Mazama. In addition, we analyze synthetically hydrated rhyolite (R2) and dacite (D2) glasses from Bindeman et al. (2013) that were hydrated at 850 °C (R2) and 900 °C (D2) with water from Fiji (δD = -41.8 ‰, $\delta^{18}O$ = -5.3 ‰) for one hour. We also analyzed a hydrous rhyolitic glass (1.77 wt.% water; IDDP-1) from the Iceland Deep Drilling Project that was quenched almost instantaneously at a depth of approximately 2.1 km after being intercepted by a drill core. We present new isotopic results for this material as it was described in detail by (Zierenberg et al., 2012). In addition, we analyze glasses that were secondarily hydrated at ambient temperature and pressure. These include volcanic glass from the 7.7 ka Mt. Mazama eruption (Table 2), which were variably degassed and now

Table 1
Data and location information from isotopic analyses of volcanic glasses and micas

Sample Name	unit	Location	composition	$\delta^{13}C$ (‰)	$\delta^{18}O_{RAW}$ (‰)	$\delta^{18}O_{TCEA}$ (‰)	$\delta^{18}O_{H2Om}$ (‰)	$\delta^{18}O_{OH}$ (‰)	$\delta^{18}O_{Total}$ (‰)
Cleetwood	Cleetwood rhyolite	Mount Mazama	rhyolite	-26.05	-13.5	-6.4	6.8	-0.4	-0.1
6_12_1980	12-Jun-80	Mount St. Helens	dacite	-23.66	-7.4	-6.6	7.3	-1.4	-0.5
IDDP	Krafla	Iceland	rhyolite	-25.27	-11.1	-9.0	3.0	-9.0	-5.0
D2	synthetic dacite[a]	Kamchatka	dacite	-25.26	-4.3	-1.8	5.3	-3.6	0.2
R2	synthetic rhyolite[a]	Heise	rhyolite	-25.28	-7.4	-4.0	4.0	-6.3	-1.8
VF-74-45	1974	Volcán de Fuego	basalt	-24.10	0.4	-0.2	7.4	3.3	3.3
42-Cordova	1992	Mt. Spurr	dacite	-25.09	-3.1	-0.5	6.2	1.8	2.4
57-Ashton	1992	Mt. Spurr	dacite	-25.35	-3.1	-1.9	6.2	0.9	1.6
BUD	mica standard	Butte (MT)	NA	-24.71	-4.4	-3.6	NA	1.4	NA
NBS30	mica standard	California batholith	NA	-24.64	-3.5	-2.6	NA	1.9	NA
Kaolinite	kaolinite powder	Sigma-Aldrich	NA	-23.27	7.7	8.8	NA	--	NA
Brucite	NA	Austria	NA	-22.33	2.9	2.2	NA	--	NA

[a]experimentally synthesized glasses from Bindeman et al. (2013)

have different amounts of water (Nolan and Bindeman, 2013). We also analyze glasses from the 630 ka Lava Creek Tuff eruption of the Yellowstone hotspot from Bindeman et al. (2007), which have been collected in climatically different regions across the western United States (Table 2). In addition, we analyze secondarily hydrated glasses from the postglacial 8 ka Hrafntinnusker eruption in Iceland (Martin et al., 2016).

Hydrogen isotope and total water analyses of volcanic glass

All glass samples in this study were previously analyzed for both δD and H_2O_t on the Thermal Conversion Elemental Analyzer (TCEA) continuous flow and sampling system at the University of Oregon stable isotope laboratory (e.g. Bindeman et al., 2012; Martin et al. 2016) to determine the hydrogen isotopic ratio and total water concentration prior to any oxygen isotope analyses (Table 5). Prior to analysis, tephra samples were lightly crushed, placed in a water-filled beaker, and sonicated for ~60 min to remove any clays or particulates with large surface/volume ratio that, if present,

Table 2
Data and location information from oxygen isotopic analyses of volcanic glasses that have been hydrated by meteoric waters

Sample Name	unit	composition	$\delta^{13}C$ (‰)	$\delta^{18}O_{RAW}$ (‰)	$\delta^{18}O_{TCEA}$ (‰)	H_2O_t wt.%	$SiOH/H_2O_m$	$\delta^{18}O_{H2Ot}$ (‰)
Mazama0[a]	Mt. Mazama (7.7 ka)	rhyolite	-25.57	-7.3	-4.5	2.90	0.5	-2.3
Mazama2[b]	Mt. Mazama (7.7 ka)	rhyolite	-24.46	-5.3	-4.7	1.30	1.2	-1.5
Mazama3[c]	Mt. Mazama (7.7 ka)	rhyolite	-22.62	0.5	-2.6	0.40	4.7	1.3
Mazama4[d]	Mt. Mazama (7.7 ka)	rhyolite	-24.34	-5.2	-4.9	1.40	1.1	-1.8
Mazama5[e]	Mt. Mazama (7.7 ka)	rhyolite	-24.22	-3.2	-3.2	0.80	2.1	0.2
Mazama6[f]	Mt. Mazama (7.7 ka)	rhyolite	-23.00	0.1	-2.3	0.50	3.3	1.2
Mazama7[g]	Mt. Mazama (7.7 ka)	rhyolite	-22.87	-0.2	-2.9	0.50	4.0	1.0
IB01-2[h]	Lava Creek Tuff (630 ka)	rhyolite	-24.94	1.9	3.0	2.26	--	--
IB01-3[i]	Lava Creek Tuff (630 ka)	rhyolite	-25.38	-1.9	0.1	1.94	--	--
IB04-3[j]	Lava Creek Tuff (630 ka)	rhyolite	-24.85	2.8	3.7	2.40	--	--
IB01-1[k]	Lava Creek Tuff (630 ka)	rhyolite	-25.38	-1.7	0.2	2.15	--	--
IB04-4[l]	Lava Creek Tuff (630 ka)	rhyolite	-24.89	4.3	6.3	2.52	--	--
IB01-5[m]	Lava Creek Tuff (630 ka)	rhyolite	-25.22	-4.3	-1.2	1.74	--	--
HSK1[n]	Hrafntinnusker (8 ka Iceland)	rhyolite	-25.12	-2.1	0.9	5.50	--	--
HSK3[n]	Hrafntinnusker (8 ka Iceland)	rhyolite	-26.20	-3.6	1.2	4.70	--	--
HSK4[n]	Hrafntinnusker (8 ka Iceland)	rhyolite	-25.17	-6.5	-3.4	3.60	--	--
HSK7[n]	Hrafntinnusker (8 ka Iceland)	rhyolite	-24.86	-5.3	-2.9	3.50	--	--

[a]reference glass (Nolan and Bindeman, 2013); [b]heated from 0–500 °C in 25 min (Nolan and Bindeman, 2013); [c]heated at 500 °C for 1 hour (Nolan and Bindeman, 2013); [d]heated at 500 °C for 5 min (Nolan and Bindeman, 2013) [e]heated at 500 °C for 10 min (Nolan and Bindeman, 2013); [f]heated at 500 °C for 20 min (Nolan and Bindeman, 2013); [g]heated at 500 °C for 30 min (Nolan and Bindeman, 2013); [h]from Bindeman et al. (2007) collected in Springtown, NE; [i]from Bindeman et al. (2007) collected in Iowa; [j]from Bindeman et al. (2007) collected in Iowa; [k]from Bindeman et al. (2007) collected in Springtown, NE; [l]from Bindeman et al. (2007) collected in Lake Tecopa, CA; [m]from

Table 3
$\delta^{18}O$ and $\delta^{13}C$ data for mica standards

Sample Name	$\delta^{13}C$ (‰)	$\delta^{18}O_{RAW}$ (‰)	$\delta^{18}O_{TCEA}$ (‰)	$\delta^{18}O$ water standard corrected (‰)
BUD	-25.14	-7.1	-4.9	--
BUD	-25.18	-6.5	-4.2	--
BUD	-25.11	-6.8	-4.6	--
BUD	-25.08	-6.4	-4.4	--
BUD	-25.29	-6.8	-4.3	--
BUD	-25.30	-5.4	-2.9	--
BUD	-25.43	-5.7	-2.9	--
BUD	-24.52	-4.1	-3.2	--
BUD	-25.09	-4.6	-2.5	--
BUD	-25.72	-6.2	-2.9	--
BUD	-25.19	-6.5	-4.2	--
BUD	-26.30	-6.1	-1.6	--
BUD	-26.14	-6.0	-1.8	--
BUD	-24.09	-8.4	-8.3	--
BUD	-24.16	-6.9	-6.7	--
BUD	-23.73	-6.7	-7.4	--
BUD	-23.78	-5.2	-5.7	--
BUD	-24.30	-6.3	-5.8	--
BUD	-24.20	-6.0	-5.7	--
BUD	-24.34	-6.9	-6.3	--
BUD	-24.32	-5.8	-5.2	--
BUD	-25.00	-6.5	-4.6	-4.9
BUD	-25.00	-5.5	-3.6	-3.8
BUD	-25.00	-5.4	-3.5	-3.7
BUD	-25.31	-6.1	-3.6	-3.8
BUD	-25.21	-4.8	-2.5	-2.7
BUD	-23.13	-4.9	-7.1	-6.2
BUD	-23.43	-1.6	-3.2	-1.9
BUD	-24.99	-4.5	-3.0	-2.0
BUD	-21.84	-0.4	-5.2	-3.8
NBS30	-25.14	-4.1	-1.9	--
NBS30	-25.77	-3.4	0.1	--
NBS30	-25.14	-4.8	-2.6	--
NBS30	-24.94	-2.8	-1.0	--
NBS30	-24.95	-3.3	-1.5	--
NBS30	-25.10	-5.0	-2.9	-3.1
NBS30	-25.40	-4.3	-1.6	-1.8
NBS30	-25.20	-4.4	-2.1	-2.3

Table 3 continued

Sample Name	$\delta^{13}C$ (‰)	$\delta^{18}O_{RAW}$ (‰)	$\delta^{18}O_{TCEA}$ (‰)	$\delta^{18}O$ water standard corrected (‰)
NBS30	-24.95	-5.1	-3.3	-3.5
NBS30	-24.67	-5.0	-3.8	-4.0
NBS30	-23.01	-0.7	-3.1	-1.7
NBS30	-23.40	-1.7	-3.4	-2.2
NBS30	-23.94	-2.3	-2.9	-1.7
NBS30	-23.36	-2.6	-4.4	-3.2
RUH	-25.18	-10.0	-7.8	--
RUH	-25.13	-10.0	-7.9	--
RUH	-24.98	-9.7	-7.9	--
RUH	-24.64	-7.9	-6.7	--
RUH	-24.59	-7.6	-6.6	--

may be attached to the glass. The samples were then rinsed with acetone and dried at 130 °C in air and 2–12 mg of vesicular glass fragments smaller than ~0.5 mm were picked under microscope and packaged in silver foil cups. Prior to analysis, all samples wrapped in silver foil were heated in a vacuum-sealed oven overnight at 130 °C to remove any adsorbed waters on the outer surface of the glass (e.g. Nolan and Bindeman, 2013). Samples were then rapidly loaded (within 5 min) and purged with He carrier gas in a TCEA autosampler (Fig. 1). The samples were analyzed for their D/H after an H3 factor correction in a separate analytical session from the CO run. The D/H analyses were used to determine the total water and δD value using NBS30 mica with a known H_2O_t of 3.5 wt.% and a δD value of -47 ‰ following the correction of Qi et al. (2014). Companion papers by Martin et al. (2016) and Seligman et al. (2016) present more details of standardization of the quoted δD and water values using water standards.

Oxygen isotope analysis of CO gas

Samples for TCEA analyses using the CO method were prepared similar to those for hydrogen isotope analyses. Tephra samples were lightly crushed and sonicated for 60 min, and then dried, picked under a microscope, and packaged in silver foil. Prior to analysis, all samples were heated in a vacuum-sealed oven overnight at 130 °C, and loaded and purged with He carrier gas in an autosampler. Samples were dropped one at a

Table 4
Sources for magmatic temperature, chemistry, and speciation used for $\delta^{18}O$ calculations

Sample Name	magmatic temperature	chemistry data	relative H_2O_m and OH^-	bulk silicate $\delta^{18}O$
Cleetwood	Druitt and Bacon (1989)	Nolan and Bindeman (2013)	Newman and Lowenstern (2002)	measured
6_12_1980	used similar temperature as Blundy and Cashman (2005)	Halliday et al. (1983)	Newman and Lowenstern (2002)	measured
IDDP	Zierenberg et al. (2012)	Zierenberg et al. (2012)	Zierenberg et al. (2012)	Zierenberg et al. (2012)
D2	Bindeman et al. (2013)	Seligman et al. (2014)	Ihinger et al. (1999)	Bindeman et al. (2013)
R2	Bindeman et al. (2013)	Watts et al. (2011)	Ihinger et al. (1999)	Bindeman et al. (2013)
VF-74-45	Rose et al. (1978)	Rose et al. (1980)	Newman and Lowenstern (2002)	measured
42-Cordova	estimated from Nye and Turner (1990)	Swanson et al. (1995)	Newman and Lowenstern (2002)	estimated from Nye and Turner (1990)
57-Ashton	estimated from Nye and Turner (1990)	Swanson et al. (1995)	Newman and Lowenstern (2002)	estimated from Nye and Turner (1990)

time into the reduction furnace (Fig. 1) and rapidly heated to 1450 °C, allowing water to be released off the solid and instantaneously converted to CO gas through high temperature reduction with the surrounding glassy carbon (e.g. Brand et al., 1994). The conversion to CO gas likely helps to drive the water extraction reaction by reducing the number of reaction products. This approach is perhaps better than the dehydroxilation techniques described above that are conducted at lower temperatures and involve cryogenic freezing of the extracted water prior to conversion to CO or CO_2 gas. The CO gas was then passed through a 0.6 m long, short packed, 5 Å molecular sieve column, and then through an open split and into the mass spectrometer. Analyses of the CO gas are conducted relative to a reference gas from the University of Ottawa G.G. Hatch Stable Isotope Laboratory with a known $\delta^{18}O$ value of -5.5 ‰ relative to SMOW, which is introduced from the bellows system of a dual inlet continuous flow run method (Fig. 1). Calibration of the final value is performed using solid and liquid standards with known $\delta^{18}O$ VSMOW values (see below).

Table 5
δD and H_2O_t data from Seligman et al. (2016) to compare to new $\delta^{18}O_{Total}$ data

Sample Name	unit	Location	δD (‰)	H_2O_t wt.%	$\delta^{18}O_{Total}$ (‰)
Cleetwood	Cleetwood rhyolite	Mount Mazama	-125	0.21	-0.1
6_12_1980	12-Jun-80	Mount St. Helens	-94	0.47	-0.5
IDDP	Krafla	Iceland	-118	1.77	-5.0
D2	synthetic dacite[a]	Kamchatka	-76	2.33	0.2
R2	synthetic rhyolite[a]	Heise	-61	2.43	-1.8
VF-74-45	1974	Volcán de Fuego	-86	0.10	3.3
42-Cordova	1992	Mt. Spurr	-89	0.57	2.4
57-Ashton	1992	Mt. Spurr	-93	0.58	1.6

[a]experimentally synthesized glasses from Bindeman et al. (2013)

Oxygen isotope analyses of bulk $\delta^{18}O$ using laser fluorination

Glass separates that did not already have a known $\delta^{18}O_{BG}$ ($\delta^{18}O$ value of the bulk glass) were also analyzed for their bulk silicate $\delta^{18}O$ at the University of Oregon stable isotope laboratory. Glass separates were picked from select samples using a binocular microscope, with most weights ranging from 1–2 mg, and loaded into stainless steel cubes with threads on all sides. The carousel of glass samples were degassed in a vacuum and then introduced one at a time into a separate fluorination chamber from a custom-built airlock sample chamber. The two chambers are separated by a ball valve and movement is enacted using specially designed rods that move in and out through greased O-rings that can still maintain a vacuum within the chamber. We used CO_2 laser fluorination with a BrF_5 reagent, and day-to-day variability was corrected using an in-house Gore Mt. Garnet ($\delta^{18}O$ = 6.52 ‰) standard. The generated gas was passed through a series of LN_2 cryogenic traps that caused the BrF_5 reaction products to be frozen, and through a mercury diffusion pump to strip away any F_2 gas that could not be cryogenically frozen, leaving pure O_2, which was then converted to CO_2 in a platinum-graphite converter. The yield was measured as being near 100% for all samples used in this study, and the CO_2 gas was analyzed on an MAT 253 mass spectrometer in a dual inlet mode with an estimated overall precision of the whole procedure of ± 0.1 ‰.

RESULTS

Water in glass: method development and the meaning of oxygen isotope ratios

Oxygen isotopic ratios of extracted water were determined on the TCEA through high temperature (1450 °C) reduction with the surrounding glassy carbon in a He atmosphere upon the release of water from the sample:

$$hydrous\ glass = anhydrous\ glass + H_2O \quad (2a)$$

$$H_2O + C \rightarrow H_2 + CO \quad (2b)$$

As is shown by Brand et al. (1994), the reaction is fully shifted to the right and extraction is quantitative. The first step of the reaction involves melting and diffusion of water from the glass. Bindeman et al. (2012) and Martin et al. (2016) used experimentally synthesized glasses to verify complete extraction of water through FTIR analysis of glass separates, in addition to illustrating mineral size fraction effects for glass separates smaller than 250 μm. These results confirmed earlier experimentation by Sharp et al. (2001) who suggested that micas and hydrous organic components pyrolize by breaking down to their constitutive oxides and metals.

An important consideration for volcanic glass is that magmatic water is quenched in volcanic glass and present as both OH^- and H_2O_m. These proportions are determined based on the total water concentration and the magmatic temperature (see Fig. 2; Newman et al., 1986; Ihinger et al., 1999; Newman and Lowenstern, 2002), and thus we must consider water extraction from both the molecular and hydroxyl components. It is important to note that according to Equation (2), 100 % of the molecular water is extracted and converted to CO, but based on mass balance principles, only half of the water present as OH^- is converted to H_2O_m and then CO gas upon thermal heating to 1450 °C in accordance to the below reaction:

$$2OH^- = H_2O_m + O^{2-}_{silicate} \quad (3)$$

This indicates that half of the OH^- bound oxygen remains in the silicate upon completion of devolatilization.

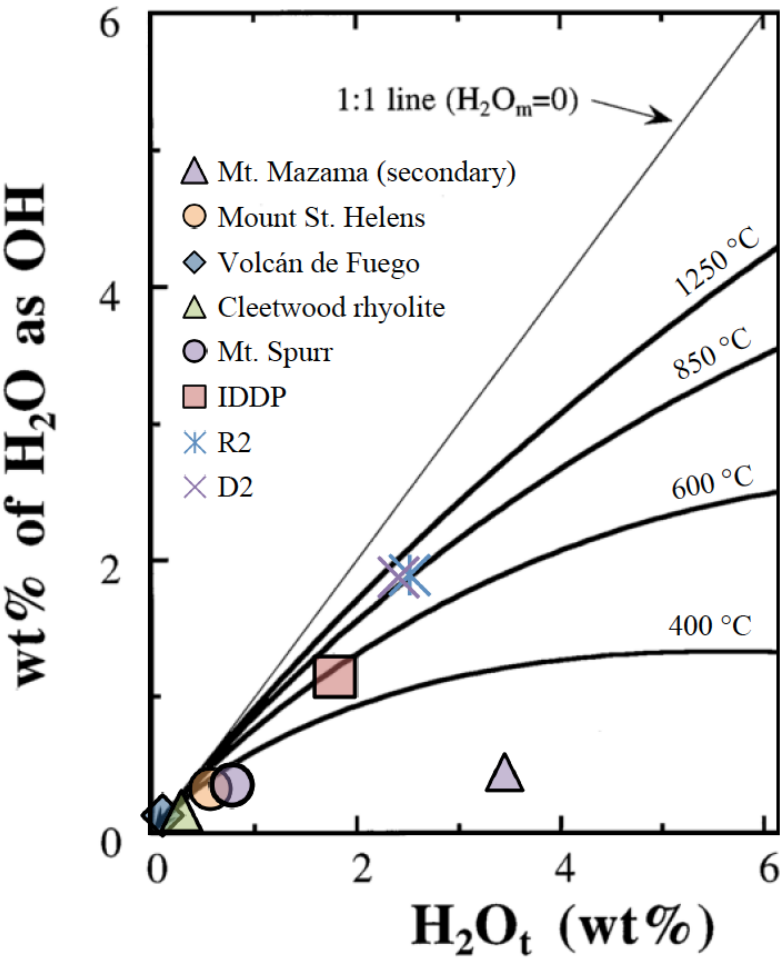

Figure 2. Relative quantities of H_2O_t and OH^- (modified from Ihinger et al., 1999), illustrating the larger relative quantities of OH^- at higher temperatures in contrast to the larger quantities of H_2O_m at lower temperatures. We include our magmatic glasses, where the relative quantities of OH^- and H_2O_m were either measured, or calculated using VolatileCalc (Newman and Lowenstern, 2002), or this plot (R2 and D2 glasses). We also include the hydrous 7.7 ka Mt. Mazama glass from Nolan and Bindeman (2013) that has not been variably heated (see Table 2). Note the larger relative proportions of H_2O_m in the secondarily hydrated glass.

This presence of both forms of water in magmatically quenched glass creates an extra step in determining the total $\delta^{18}O$ of water extracted from samples and analyzed for CO in the TCEA due to the need to determine: 1) the relative quantities of OH^- and H_2O_m present in the sample; and 2) any associated isotopic fractionation between the oxygen in the molecular water and the oxygen in the hydroxyl groups.

Oxygen isotope calibration and standards for CO analyses

Thermal decomposition in the TCEA is a rapid process that takes seconds and extracts 100 % of the total water of hydrous silicate samples as is shown by us and previous researchers (Sharp et al., 2001; Bindeman et al., 2012; Seligman et al., 2016; Martin et al., 2016). However, this extraction likely carries many types of instrumental mass fractionations; in the glassy carbon rod, along the 1/8 inch wide tubing during the He flow transport, and in the open slit of the CONFLOW upon sampling by the sniffing capillary (Fig. 1). We thus must rely on a series of standards that are run together with unknowns to correct for these fractionations. For that we use a series of mica standards (OH^- component only) calibrated versus water standards sealed in silver cups, as explained in the adjusted values below.

In order to standardize our oxygen isotope measurements of volcanic glass on the TCEA we analyzed: 1) ~0.125 mg water standards sealed in silver cups provided by Drs. Haiping Qi and Tyler Coplen from the Reston USGS Stable Isotope Laboratory (see Qi et al., 2010). These waters have known $\delta^{18}O$ and δD, and include VSMOW ($\delta^{18}O$ and δD = 0 ‰), W62001 ($\delta^{18}O$ = -6.25 ‰, δD = -41.1 ‰), and GISP ($\delta^{18}O$ = -19.8 ‰, δD = -190.0); and 2) the three mica standards (BUD, NBS30, and RUH2), which are already used as hydrogen isotope standards for CO on the TCEA (Fig. 1). Both waters and mica overlap in their δD and $\delta^{18}O$ values. In separate analytical sessions, we: i) ran water standards, mica standards, and glasses in the same session (3 sessions total) to determine the $\delta^{18}O$ in these micas relative to VSMOW, to then be able to ii) run the micas as their own standards versus glass utilizing the correction in (i).

Correcting versus not correcting for kinetic isotope fractionation

As illustrated in Eq. 2b, TCEA analyses for $\delta^{18}O$ are conducted on a CO molecule. Therefore, any isotopic fractionation and non-systematic variations that we observe (e.g. Fig. 1) are for the most part related to kinetics of CO molecule behavior in a long pipework and Conflow within the He flow capillary. A common practice in stable isotope analyses using the CO molecule is to ignore the $\delta^{13}C$ values and correct the resulting $\delta^{18}O$ values by concurrently run standards with known $\delta^{18}O$ values (Sharp et al., 2001). We want to explore this procedure further by discussing the merits of correcting the final

data for their ^{13}C variations. Although fractionation of oxygen isotopic ratios by a kinetic principle in a laminar He flow is a hypothesis requiring confirmation, we further test its merits below.

From general kinetic principles, the mass dependent fractionation between $^{18}O/^{16}O$ is twice that of $^{13}C/^{12}C$ fractionation. As $\delta^{13}C$ values should be constant for each run day (and mostly related to the value of our carbon reactor, crucibles, and granules) we can utilize the $\delta^{13}C$ data as a check for kinetic fractionation within our instrument. After choosing a single value for a day, we take twice the difference between the measured and nominal value for that day and subtract or add the $\Delta\delta^{18}O$ for that day to each analysis.

To correct for day-to-day variation, the situation is unfortunately more complex, as it depends on the relative combination of the sources of carbon in the generated CO gas as well as variations in the analytical conditions. The $\delta^{13}C$ value of the carbon materials within our system were analyzed at the University of New Mexico and vary within ~3 ‰. The different sources of glassy carbon within the TCEA have $\delta^{13}C$ values of: -22.25 ‰ (carbon tube), -25.87 ‰ (glassy carbon granules), -24.02 ‰ (old factory crucibles used prior to January 19, 2016), and -24.57 ‰ (new homemade crucibles used after January 19, 2016). Most of the source of the carbon is likely coming from the crucible itself where the silver cup sample is landing (Fig. 1), but each of these sources of carbon likely contribute to the final $\delta^{13}C$ of the CO molecule. Given the variability of the $\delta^{13}C$ sources listed above, we cannot calculate a global average to correct for day to day variations, but note that within a single run for our instrument, the $\delta^{13}C$ value should stay approximately constant, which allows for correction of the $\delta^{18}O$ of the CO molecule by assuming a certain constant $\delta^{13}C$ value for each session.

Figure 3a illustrates the raw $\delta^{13}C$ value for the CO gas produced after analysis of glass, mica, and water samples for different days of analysis. We know that the $\delta^{13}C$ value should stay relatively constant with each analytical session, depending on the

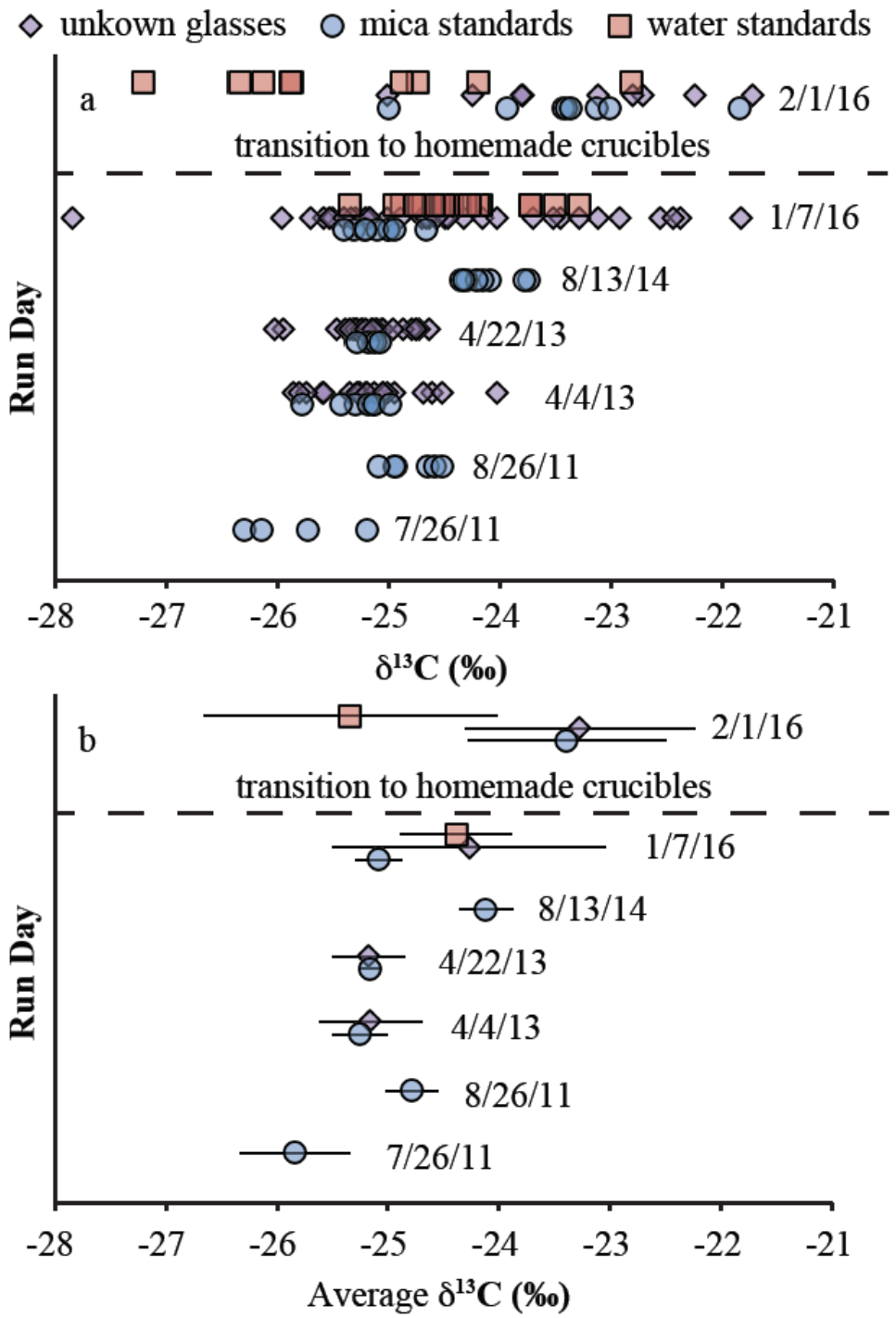

Figure 3. Results showing the trends of $\delta^{13}C$ values for each day of analyses for hydrous glasses, mica standards, and water standards. Note the shift from the use of factory made crucibles to homemade crucibles. The larger span in $\delta^{13}C$ values for the 2016 analyses is likely due to the greater number of samples analyzed. a) all the $\delta^{13}C$ data points individually for each day of analysis; b) average $\delta^{13}C$ values for each sample type (micas, waters, and glasses) along with the associated standard deviation.

material providing the carbon for the CO molecule. The majority of $\delta^{13}C$ values were between -24 and -25 ‰, and the standard deviation increases following the transition to the homemade crucibles (Fig. 3b). However, it is also important to note that more samples have been analyzed, and are therefore contributing to the standard deviation in the two most recent days of analysis.

The data spread and standard deviations of mica and water standards run on different days are shown in Figure 4. The scatter in mica $\delta^{18}O$ values is spread within several per mil, which did not always decrease following normalization to a single $\delta^{13}C$ value, as the spread in mica $\delta^{18}O$ values is likely related to both analytical and natural variability (Fig. 4). We also plot the BUD mica standard versus mass to see if any variability that we notice could be explained by the difference in water extraction from samples of varying weight on different days of analysis (Fig. 5). However, even when masses up to 5 mg of BUD were run, relative to the usual 1–2 mg, we see no trend of deviating $\delta^{18}O$ values of extracted waters with differences in masses, illustrating that variations are not due to the difference in the amount of water extracted, or the difference in masses of the residual silicate.

$\delta^{18}O$ of water within high-temperature silicate glass and mica

High temperature IDDP glass

Unlike micas, where all the water is present as OH^-, volcanic glass has a mixture of H_2O_m and OH^- in either known or expected proportions based on their high temperature partitioning (Fig. 2) (Ihinger et al., 1999; Newman and Lowenstern, 2002). The CO analysis on the TCEA reports a bulk $\delta^{18}O$ for water extracted from a solid (H_2O_m and OH^-), but records only half the $\delta^{18}O$ of the OH^- present in the solid (Eq. 2). It is, however, possible to resolve this using mass balance relationships, and by employing some simple assumptions about the temperature-dependent fractionations (Zheng, 1991; 1993; Zhao and Zheng, 2003).

Two initial assumptions must be made: 1) the water present as H_2O_m has a $\Delta^{18}O_{glass\text{-}H2Om}$ fractionation from the melt that can be computed using a known chemical composition at a known temperature that the melt was quenched at (e.g. Zheng, 1991; Zheng, 1993; Zhao and Zheng, 2003); 2) the half of the OH^- that is left in the silicate has

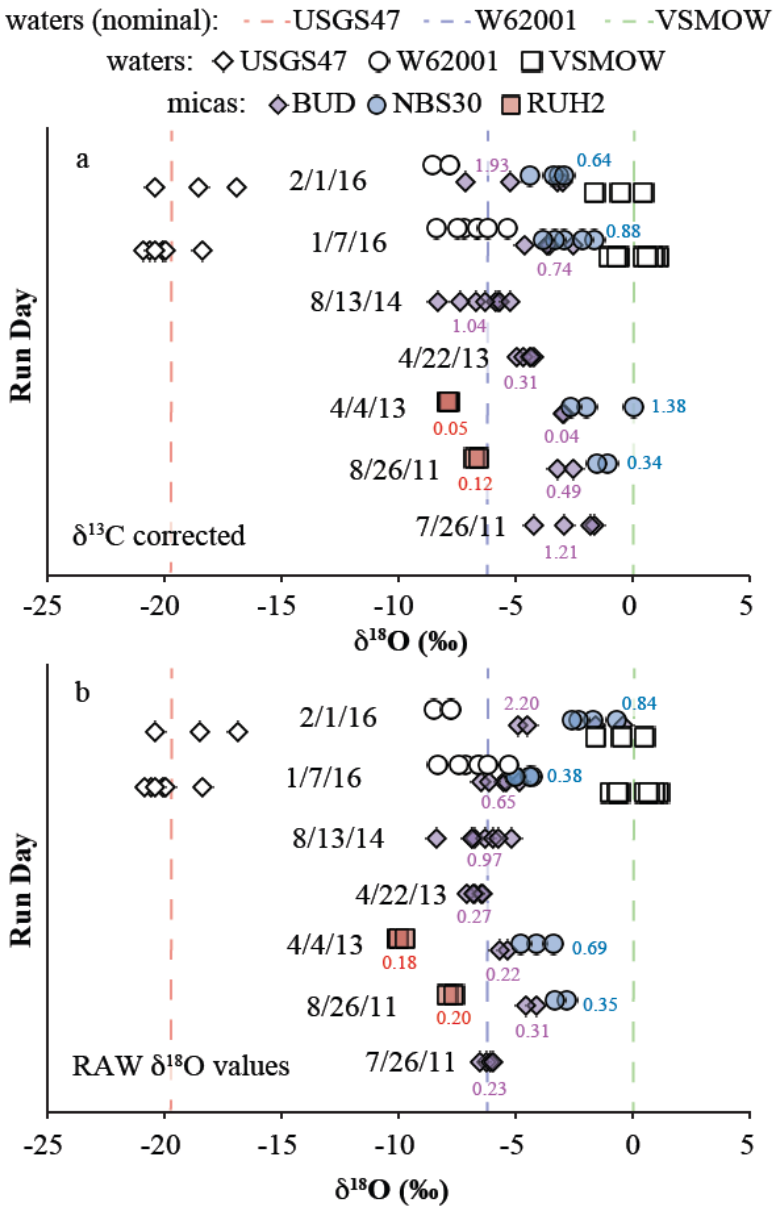

Figure 4. $\delta^{18}O$ (‰) values of the mica (BUD, NBS30, and RUH2) and water (USGS47, W62001, VSMOW) standards on each day of analysis, illustrating the variability of $\delta^{18}O$ values and displaying typical session-to-session variability. The standard deviation for each set of data is listed in the color associated with the sample type (BUD, NBS30, VSMOW, etc.) near the respective data set, and the nominal $\delta^{18}O$ value of the water standards are shown as vertical dashed lines. a) $\delta^{18}O$ (‰) values of micas here have been corrected for $\delta^{13}C$ variations (to account for kinetic fractionation of generated CO gas where $H_2O + C = CO + H_2$ in a continuous flow pipework and CONFLOW, see methods). As the mica $\delta^{18}O$ values are not water standard corrected in this Figure, they are not relative to VSMOW, but do show per mil variations. However, the water standards are relative to VSMOW. b) $\delta^{18}O$ (‰) values of micas prior to the $\delta^{13}C$ correction. Note that the $\delta^{13}C$ correction does not always improve the variability of the $\delta^{18}O$ values. Also note that no $\delta^{13}C$ correction is made for the water standards.

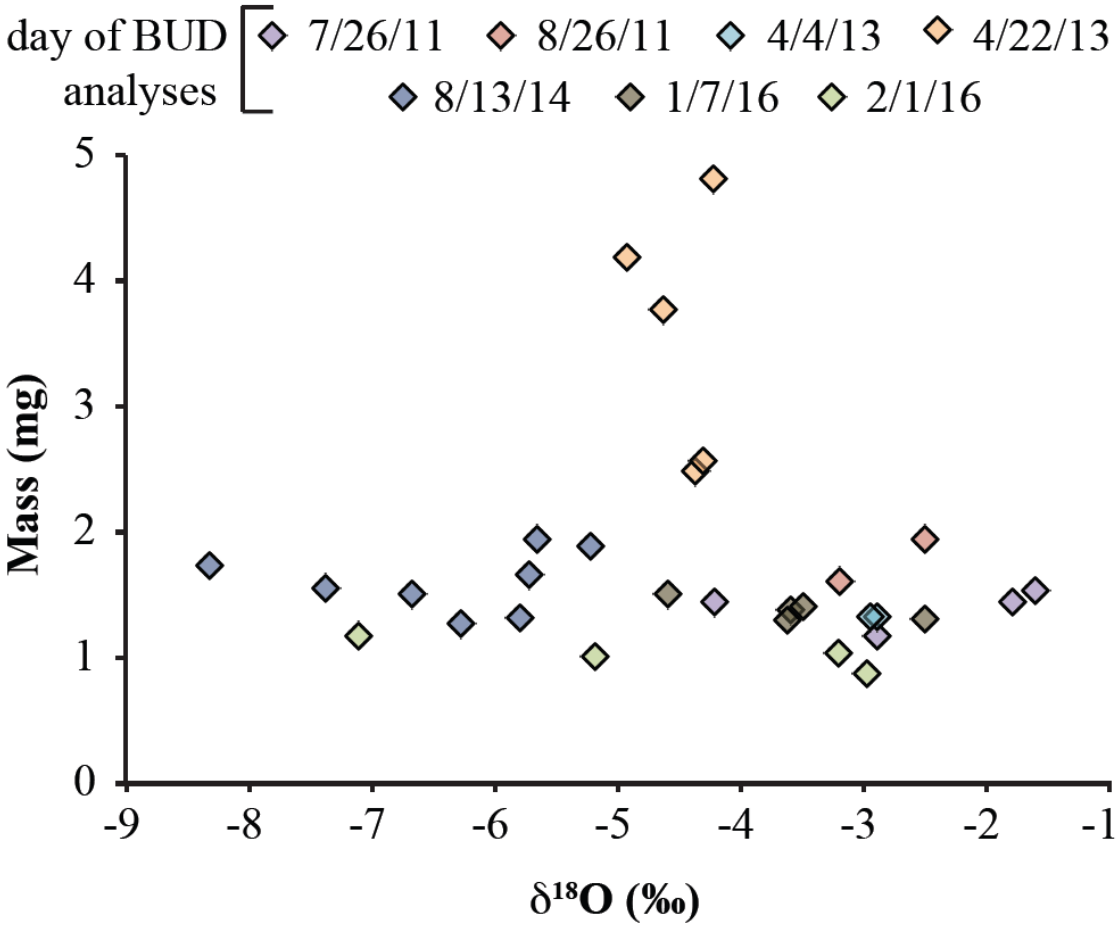

Figure 5. $\delta^{18}O$ (‰) values of the BUD mica standard relative to the mass (mg) that was analyzed for each day of analysis. Typically, 1–2 mg of mica are analyzed during TCEA analyses, but to see if the mass analyzed had any effect on the $\delta^{18}O$ value of the analysis, BUDs of variable weights (up to ~5 mg) were analyzed. We see no trend in $\delta^{18}O$ values with differing masses of analyzed solids, although $\delta^{18}O$ values of BUD are variable on different days of analysis. Except for the 8/13/2014 and 2/1/2016 run days, we see little variations during a single session of analysis (± 2.5 ‰).

a fractionation from the silicate that can be calculated given a known composition at the temperature of its extraction at 1450 °C. Utilizing these assumptions, we can determine the $\delta^{18}O$ of the molecular water and the OH^- that is left in the silicate, and use mass balance to determine the $\delta^{18}O$ of the total water.

We thus analyzed hydrous volcanic glass quenched at high temperature with a range of known H_2O_m and OH^- concentrations (Fig. 2). One set of these glasses consists of a rhyolite that was uniquely intercepted at high temperatures by the Iceland Deep Drilling Project (IDDP) at 2.1 km depth (Zierenberg et al., 2012). These rhyolites have

known relative H_2O_m and OH^- concentrations that were measured by FTIR, a known chemical composition, and a known melt temperature (Zierenberg et al., 2012). Isotope fractionations between water and silicate at temperatures greater than 800 °C are sub-permil (e.g. Friedman and O'Neil, 1977) and depend on the proportions of major oxides. We utilize known $1000\ln\alpha_{rhyolite\text{-}water}$ from Zhao and Zheng (2003) at the melt temperature of 885 °C from Zierenberg et al. (2012), which is 0.1 ‰ (essentially zero given our uncertainty). Then, using the bulk $\delta^{18}O$ (3.1 ‰) and the calculated $1000\ln\alpha_{rhyolite\text{-}water}$ at 885 °C we can determine the $\delta^{18}O$ of the molecular water ($\delta^{18}O_{H2Om}$ = 3.0 ‰).

Similarly, to determine the $\delta^{18}O_{OH\rightarrow silicate}$ ($\delta^{18}O$ of the hydroxyl that is left in the silicate during analysis), we use the same steps to calculate the fractionation between the glass and the half of the OH^- that was left behind ($1000\ln\alpha_{rhyolite\text{-}water}$) at 1450 °C, which provides no detectable fractionation (0.0 ‰), so the water extracted at 1450 °C has the same $\delta^{18}O$ as the silicate (3.1 ‰). The next step is to calculate the isotope fractionation associated with the reaction from Equation 2 above to determine the $\delta^{18}O_{OH\rightarrow H2Om}$ (the OH^- that is analyzed by the TCEA). The $\delta^{18}O_{OH\rightarrow H2Om}$ can now be computed based on known mass balance relationships. We already know that:

$$\delta^{18}O_{TCEA} = F_{H_2O_m}\times\delta^{18}O_{H_2O_m} + F_{OH\rightarrow H_2O_m}\times\delta^{18}O_{OH\rightarrow H_2O_m} \quad (4)$$

where $\delta^{18}O_{TCEA}$ is the total water that is analyzed by the TCEA (H_2O_m and ½ of the OH^-), F_{H2Om} and $\delta^{18}O_{H2Om}$ are the fraction and the isotope value of the molecular water respectively, $F_{OH\rightarrow H2Om}$ is the fraction of the total water that is present as OH^- and is converted to H_2O_m during analysis and analyzed by the TCEA (half of the total OH^-, see Eq. 2), and $\delta^{18}O_{OH\rightarrow H2Om}$ is the $\delta^{18}O$ of the ½ of the OH^- that is extracted from the glass and contributes to the total water that is analyzed by the TCEA. Rearranging, it is possible to see that the $\delta^{18}O$ of the OH^- that is released to form a CO molecule in the TCEA can be calculated by:

$$\delta^{18}O_{OH\rightarrow H_2O_m} = \frac{\left(F_{H_2O_m} + F_{OH\rightarrow H_2O_m}\right)\times\delta^{18}O_{TCEA} - F_{H_2O_m}}{F_{OH\rightarrow H_2O_m}} \quad (5)$$

Using the relationships for the IDDP glass provided above, the equilibrium value of $\delta^{18}O_{H2Om}$ (3.0 ‰), and the mass balance of Eq. 4, we can predict that the total $\delta^{18}O$ of the OH^- present in the IDDP volcanic glass is -9.0 ‰.

The next step is to calculate the $\delta^{18}O$ of the total water using another mass balance relationship:

$$\delta^{18}O_{Total-glass} = \left(F_{H_2O_m}\right)\times\delta^{18}O_{H_2O_m} + F_{OH^-}\times\delta^{18}O_{OH^-} \quad (6)$$

where $\delta^{18}O_{Total\text{-}glass}$ is the $\delta^{18}O$ of the total water (hydrogen-associated oxygen) present in a solid that has both OH^- and H_2O_m present prior to analysis, F_{OH-} and $\delta^{18}O_{OH-}$ are the fraction of the water present as OH^- and the $\delta^{18}O$ of the total OH^- respectively. Once the total OH^- is added to the analysis, this creates a $\delta^{18}O_{Total\text{-}glass}$ for IDDP of -5.0 ‰.

Extraction of water from mica

This same mass balance can be utilized for micas, which only contain OH^-, and no molecular water. Since all the water in micas is present as OH^-, the mass balance is much simpler, as we can disregard H_2O_m. We thus assume that despite the prior history of the closure temperature for micas, the fractionation that matters for our calculations is the high temperature extraction reaction.

Based on the relatively small proportion of water in relation to the oxygen in the silicate, the bulk $\delta^{18}O$ value of the mica silicate can be taken as a proxy of the anhydrous silicate. If we take BUD as an example (Table 1), the $\delta^{18}O_{TCEA}$ of the extracted water value was -3.6 ‰. We then utilized the known bulk $\delta^{18}O$ mica value of 5.1 ‰, and the fractionation computed by the increment method between the OH^- group in biotite and water vapor as H_2O at the temperature of our extraction (1450 °C) from Zheng (1993). Using this information, we obtain a $\Delta^{18}O_{silicate\text{-}OH}$ of -1.3 ‰. Thus, the $\delta^{18}O$ value of the half of the oxygen from the OH^- that is left in the silicate upon extraction is +6.4 ‰, making the anhydrous mica reside a bit heavier than the starting biotite upon thermal decomposition. Determining the $\delta^{18}O_{Total}$ for micas, is then much simpler because the final $\delta^{18}O_{Total\text{-}mica}$ can be determined as:

$$\delta^{18}O_{Total-mica} = \frac{1}{2}(\delta^{18}O_{TCEA}) + \frac{1}{2}(\delta^{18}O_{OH\rightarrow silicate}) \quad (7)$$

where $\delta^{18}O_{Total\text{-}mica}$ is the $\delta^{18}O$ of the total OH^- present in a silicate.

Our mass balance demonstrates that, similar to glasses, the $\delta^{18}O_{Total}$ of the micas is 2–6 ‰ heavier than the extracted water $\delta^{18}O_{TCEA}$ value (Fig. 6), depending on the relative proportion of OH^- (e.g. Girard and Savin, 1996; Clayton and Mayeda, 2009). This is because the oxygen left in the silicate upon disproportionation of the OH^- (Eq. 3) is expectedly enriched in the heavy isotope of oxygen (^{18}O) relative to the extracted and departed water. Therefore, the oxygen left in the silicate during extraction does not have a $\delta^{18}O$ value that is much different than the bulk silicate $\delta^{18}O$ value.

Oxygen isotope trends of the high temperature IDDP glass

The IDDP glass (Iceland Deep Drilling Project) is from a depth of 2.1 km and was quenched almost instantaneously after a drill core intercepted it (Zierenberg et al., 2012), therefore providing a rare natural experiment of quench at depth. The $\delta^{18}O_{Total}$ and δD_{Total} values for the IDDP glass are lower than would be expected for its high water concentration, in relation to the typical volcanic degassing trend. The main difference in the IDDP glass, relative to the other magmatic glasses, is that it was rapidly quenched at depth, and therefore able to hold its high water concentration. Furthermore, low δD values (near -120 ‰) as seen for the IDDP glass are typically seen in glasses with less than 1.0 wt.% H_2O_t, instead of nearly 2 wt.%, which is present in the IDDP glasses. Therefore, another low δD (and $\delta^{18}O$) source must be present.

The IDDP glass is from the Krafla geothermal field, where the geothermal fluids primarily consist of low δD and $\delta^{18}O$ meteoric waters ($\delta^{18}O$ = -12.5 ‰, δD = -90 ‰) (Sveinbjörnsdóttir et al. 1986). Given the high temperature (885 °C), and the abundant low $\delta^{18}O$ and low δD local meteoric waters, the high water concentration and low $\delta^{18}O_{Total}$ and δD_{Total} values of the IDDP glass agree with a trend of secondary hydration at elevated temperatures (885 °C) (i.e. hydrothermal circulation). Therefore, it is likely that the low $\delta^{18}O$ (and δD) values of the IDDP glass were acquired through prior episodes of hydrothermal circulation, and subsequent partial melting of previously hydrothermally

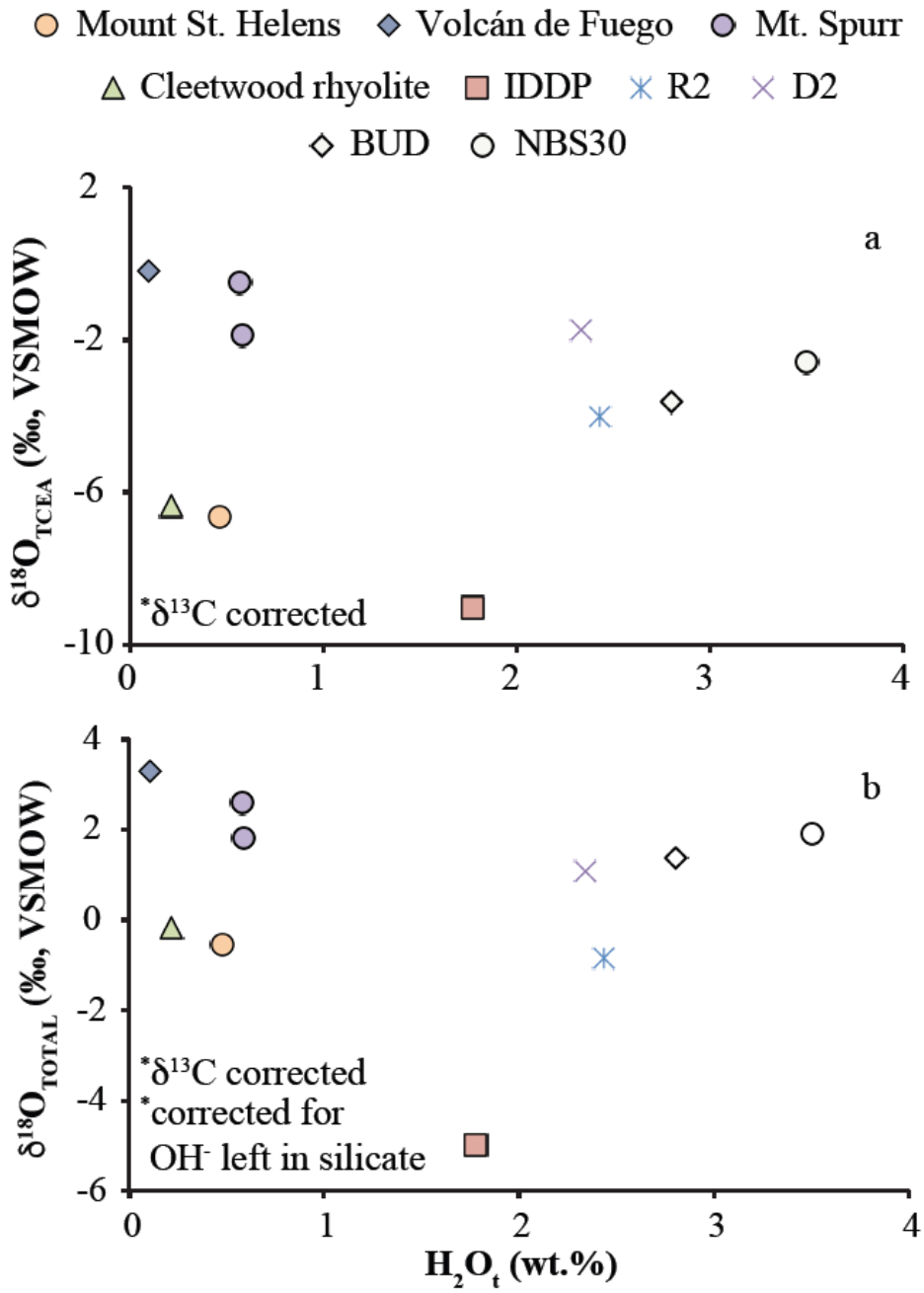

Figure 6. $\delta^{18}O$ values of water extracted from hydrous silicates relative to the H_2O_t (wt.%) of the silicate a) $\delta^{18}O_{TCEA}$ values of water extracted from glasses and micas, plotted relative to the H_2O_t (wt.%) of the silicate. Values here have been corrected for $\delta^{13}C$ variations and are standard corrected, but have not been corrected for the half of the OH^- that remains in the silicate during thermal extraction. b) $\delta^{18}O_{Total}$ values of the same silicates from (a) relative to the H_2O_t (wt.%). These values have been fully corrected and therefore represent the total $\delta^{18}O$ of the water present in the silicate prior to analysis. Note the large shift in $\delta^{18}O$ values following the total water correction to more positive $\delta^{18}O$ values. The only visible difference in (a) and (b) is the $\delta^{18}O$ scale, and the relative shift in $\delta^{18}O$ from (a) to (b) is based on the relative quantities of OH^- in the silicate.

altered rocks associated with the Krafla eruptive center, similar to processes documented at Yellowstone (e.g. Watts et al., 2011; Drew et al., 2013; Colón et al., 2015).

Oxygen isotope trends of synthetically hydrated R2 and D2 glasses

The R2 (rhyolite) and D2 (dacite) glasses were synthesized at 850 °C (R2) and 900 °C (D2) for one hour with Fiji water (δD = -41.8 ‰, $\delta^{18}O$ = -5.3 ‰) in a study by Bindeman et al. (2013). The one hour of heating is sufficient to redistribute water in accordance to high-temperature partitioning, which should only take minutes (Zhang et al., 1997).

These data were processed in the same manner as the IDDP glass discussed above, except since there is no known $1000\ln\alpha_{dacite\text{-}water}$, we utilize known mineral assemblages based on CIPW norm calculations and mineral-water fractionations from Zheng (1991; 1993) to calculate the fractionation between D2 and its associated waters. Although we do not know the $\delta^{18}O$ of the initial magmatic water of the R2 and D2 glasses, Bindeman et al. (2013) reported low H_2O in the starting powders of: 0.5 wt.% H_2O_t and -121 ‰ δD (D2) and 0.7 wt.% H_2O_t and -112 ‰ δD (R2), suggesting that these powders, which were prepared from Pleistocene rocks, contained secondarily absorbed water. Following synthesis with ~2 wt.% Fiji water (-5.3 ‰), the measured $\delta^{18}O_{WR}$ of R2 was 4.1 ‰ and D2 was 5.0 ‰. The $\delta^{18}O_{Total}$ of the water extracted from the glasses following the synthesis for R2 was -0.9 ‰ (850 °C synthesis) and D2 was +1.1 ‰ (900 °C synthesis). We can also see that, for the temperatures given in Figure 7, the synthesis resulted in a smaller $\Delta^{18}O_{silicate\text{-}H2Ot}$ (‰) than for the rest of the magmatic glasses.

Other silicate glasses

Here, we report observed trends of $\delta^{18}O$ of magmatic water extracted from mafic and silicic volcanic glass as well as $\delta^{18}O$ values of the total water extracted from BUD and NBS30 micas (Tables 1, 3). Figure 6a shows the $\delta^{18}O$ value of the water extracted from the volcanic glass and the micas that were analyzed by the TCEA, following the $\delta^{13}C$ corrections. These values are raw $\delta^{18}O_{TCEA}$ values that have not been corrected for the OH^- left in the silicate. Figure 6b shows the $\delta^{18}O_{Total}$ values, which have been $\delta^{13}C$ and

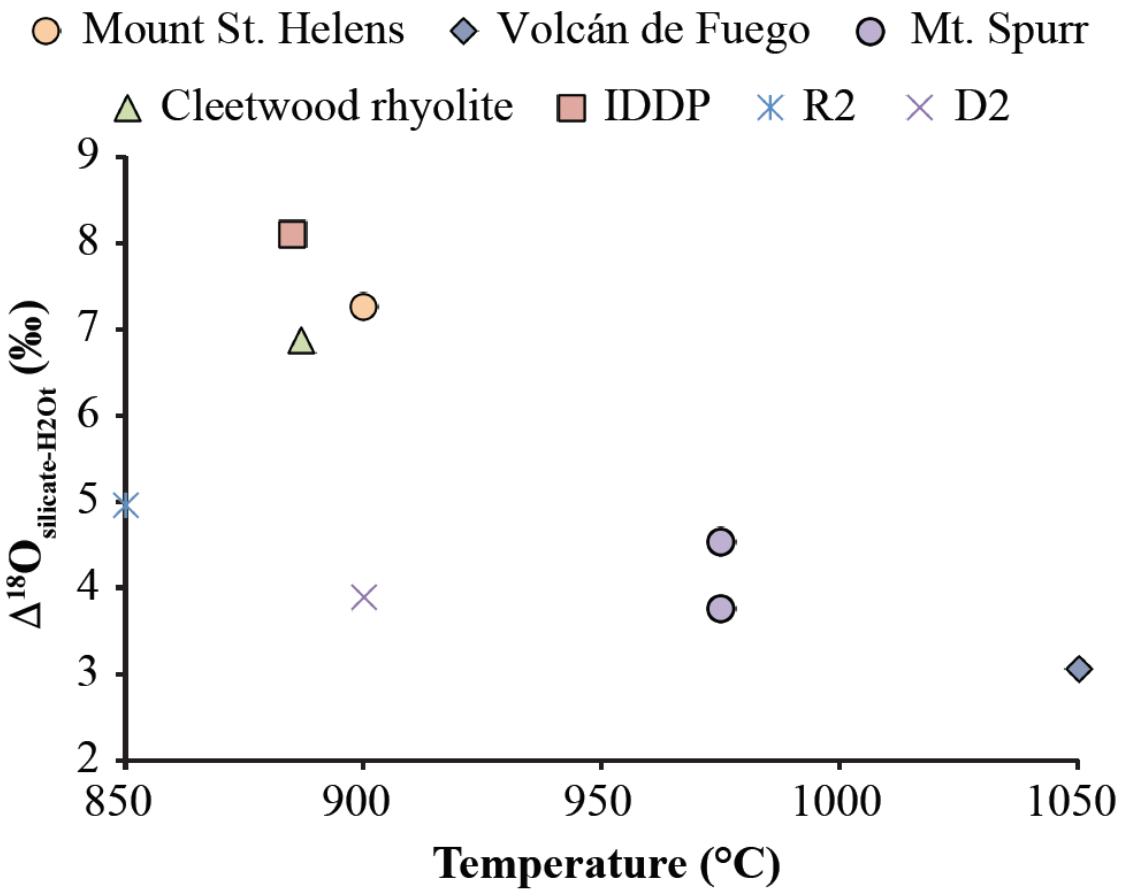

Figure 7. $\Delta^{18}O_{silicate\text{-}H2Ot}$ relative to the magmatic temperature (taken from previous literature, see Table 4) showing a clear decrease in fractionation between the silicate and the extracted water with increasing magmatic temperature.

standard corrected, as discussed in section *3.3.1* and *3.3.2*. In many cases, the relative quantities of OH^- and H_2O_m had not been determined prior to $\delta^{18}O$ analyses. When this was the case, they were determined using VolatileCalc (Newman and Lowenstern, 2002) (Table 4). When comparing Figure 6a ($\delta^{18}O_{TCEA}$) to Figure 6b ($\delta^{18}O_{Total}$), the primary distinction is a trend towards heavier $\delta^{18}O$ values (-5.0 – +3.3 ‰) following the correction for the $\delta^{18}O_{OH\rightarrow silicate}$ from lighter $\delta^{18}O_{TCEA}$ values (-9.0 – 0.0 ‰). This is due to disproportionation in which light oxygen is extracted along with the H_2O_m during rapid heating, leaving behind the heavier oxygen during analysis.

There is a positive trend between magmatic temperatures and the $\Delta^{18}O_{silicate\text{-}H2Ot}$ (the oxygen isotope fractionation between the silicate and the total water) (Fig. 7). The highest temperature glass (Volcán de Fuego) has the smallest $\Delta^{18}O_{silicate\text{-}H2Ot}$ (3.0 ‰) and

the lowest temperature glass (IDDP) has the largest $\Delta^{18}O_{silicate\text{-}H2Ot}$ (8.1 ‰). The R2 and D2 glasses fall slightly off the trend.

$\delta^{18}O$ of water extracted from secondarily hydrated glasses

Above, we utilized magmatic glasses that contain magmatic water partitioned at high temperature between H_2O_m and OH^- sites, which are quenched from the temperature of a magma that is relatively well known (Fig. 2). Below, we briefly discuss what we can determine from our $\delta^{18}O$ analyses of water extracted from secondarily hydrated glasses. Unlike micas that contain OH^- only and high-temperature glasses that contain both OH^- and H_2O_m, secondarily hydrated glasses contain primarily H_2O_m from rain and snow that is added below the glass transition. This is based on the higher temperatures that would be needed to repartition to OH^- during secondary hydration (e.g. Giachetti et al., 2015). Additionally, if magmatic glasses are quenched at a known high temperature, known silicate-water fractionations can be used to determine the $\delta^{18}O$ of the H_2O_m and OH^- contained in the glass.

Although we have not measured the relative proportions of OH^- and H_2O_m, and therefore the $\delta^{18}O_{H2Om}$ and the $\delta^{18}O_{OH}$ of water extracted from all of our secondarily hydrated glasses, we can determine the $\delta^{18}O_{Total\text{-}glass}$ from Equation 6 if the relative proportions of OH^- and H_2O_m are known or assumed. This procedure was utilized by Seligman et al. (2016) for D/H in ash and leads to an improvement in the meteoric water estimate. In one end member case, it can be assumed that the proportion of OH^- is very small (<0.1–0.2 wt.%), as was measured for Yellowstone lavas (Loewen and Bindeman, 2015). In this case, nearly all the water is present and extracted as H_2O_m. The other end member involves the proportion of OH^- being higher (Martin et al., 2016), and requires a primary magmatic water correction (Seligman et al., 2016).

Secondary water has an unknown $\Delta^{18}O_{glass\text{-}meteoric\ water}$ fractionation. Hydrogen, for example, becomes ~30 ‰ lighter when added to the glass structure (Friedman et al., 1993a). Unlike hydrogen, which does not have a partner in the glass to exchange with, silicate oxygen in the glass is predominant and thus added water can: 1) kinetically fractionate upon addition (possibly $1/8^{th}$ that of hydrogen), or 2) exchange and

equilibrate, which would lead to large $\Delta^{18}O_{glass\text{-}H2Om}$, and therefore an increase in $\delta^{18}O$ with increasing hydration.

Table 2 presents analyses of all secondarily hydrated glasses analyzed in this study. Fig. 8a illustrates the $\delta^{18}O_{TCEA}$ values relative to the total water concentration (determined in a separate run that also determined the glass δD value) of each of these glasses. These are $\delta^{18}O_{TCEA}$ values, so they have not been corrected for the OH^- that remains in the silicate. There are two different types of samples shown in Figure 8. All glasses were hydrated by meteoric water, but the Mt. Mazama glasses have also been progressively heated to remove variable amounts of water off the glasses (Table 2), which is likely the cause of the opposing trends shown in Figure 8.

$\delta^{18}O$ of water in glass and local precipitation

Figure 8 demonstrates a rather diverse set of $\delta^{18}O$ water values, but we can still observe four general trends: 1) Most $\delta^{18}O_{TCEA}$ and $\delta^{18}O_{Total}$ values are generally isotopically negative, and lower in $\delta^{18}O$ than their associated bulk silicate; 2) This is in exception to

---

Figure 8 (next page). $\delta^{18}O$ values of water extracted from secondarily hydrated glasses relative to the H_2O_t (wt.%) of the silicate. a) $\delta^{18}O_{TCEA}$ values of extracted waters for the secondarily hydrated glass samples relative to their total water concentrations. Values here have been corrected for $\delta^{13}C$ variations and are standard corrected, but have not been corrected for the half of the OH^- that remains in the silicate during thermal extraction: $2OH^- = H_2O_m + O^{2-}_{silicate}$, see text for explanation. Therefore, these values are relative to VSMOW, but represent the total water extracted from the glass with some offset from the $\delta^{18}O_{Total}$ related to this reaction. All glasses here contain secondary waters, but the glasses from the Mt. Mazama eruption have been variably degassed, which is likely the cause of the differing trends. b) $\delta^{18}O_{Total}$ values for the Mt. Mazama and Hrafntinnusker glasses, which are the only secondarily hydrated glasses in this study that have known relative OH^- and H_2O_m concentrations. The Mt. Mazama glass with the highest water concentration is most representative of the original $\delta^{18}O$ of the waters that the glass was hydrated with, since it did not go through the progressive heating sequence. Note that during progressive heating, ^{16}O is degassed preferentially relative to ^{18}O. This is opposite the trend shown for the Hrafntinnusker glasses, which show an increase in $\delta^{18}O_{Total}$ with increasing hydration. c) $\delta^{18}O_{Total}$ versus δD for the Hrafntinnusker glasses, illustrating the opposing trends between oxygen and hydrogen isotopes during secondary hydration, where ^1H is preferred for hydrogen isotopes during secondary hydration, but ^{18}O appears to be preferred for oxygen isotopes. The local $\delta^{18}O$ and δD of precipitation is from waterisotopes.org.

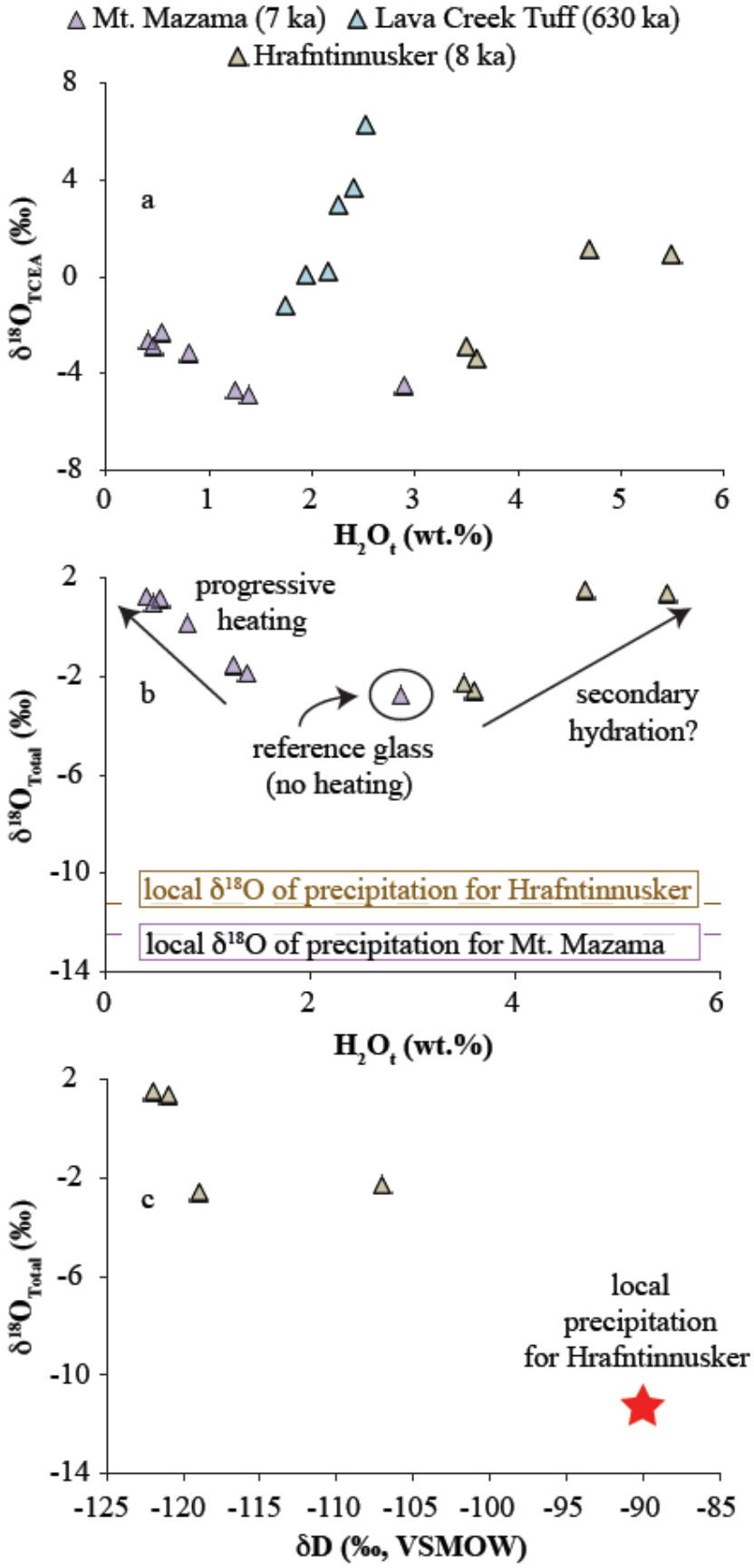
Mt. Mazama (7 ka)
Lava Creek Tuff (630 ka)
Hrafntinnusker (8 ka)
a
$\delta^{18}O_{TCEA}$ (‰)
H_2O_t (wt.%)
b
progressive heating
reference glass (no heating)
secondary hydration?
local δ18O of precipitation for Hrafntinnusker
local δ18O of precipitation for Mt. Mazama
$\delta^{18}O_{Total}$ (‰)
H_2O_t (wt.%)
c
local precipitation for Hrafntinnusker
$\delta^{18}O_{Total}$ (‰)
δD (‰, VSMOW)

nearly all LCT glasses, and the most hydrated Iceland glasses that have positive $\delta^{18}O$ values; 3) All $\delta^{18}O_{Total}$ values are heavier than the -11.2 ‰ (Hrafntinnusker) and -12.5 ‰ (Mt. Mazama) local meteoric waters; 4) For the LCT (only $\delta^{18}O_{TCEA}$) and the Hrafntinnusker glasses, an increase in H_2O_t leads to an increase in the $\delta^{18}O$ of the extracted water. This result is opposite the outcome shown for δD during secondary hydration (Seligman et al., 2016) where the addition of water leads to either a constant or decreasing δD (Fig. 8c).

The secondarily hydrated Hrafntinnusker glasses

Since the relative concentrations of the H_2O_m and the OH^- of the 8 ka Hrafntinnusker glasses were determined by Martin et al. (2016) using the DRIFT method, we can determine the $\delta^{18}O_{Total}$ values for these glasses, which are shown in Figure 8b, relative to their total water concentration. Here we can see that the $\delta^{18}O_{Total}$ values increase in the Hrafntinnusker glasses with an increase in total water concentration, which causes the $\delta^{18}O$ of the water in the glass to become progressively more different from the local $\delta^{18}O$ of precipitation with an increase in secondary hydration. Similar to what is shown for the magmatic glasses, we see an increase in $\delta^{18}O$ values once the $\delta^{18}O_{TCEA}$ value has been corrected for the residual OH^- that is left in the silicate during analysis (Figs. 8a, b).

Progressively degassed sample set

Nolan and Bindeman (2013) used the KBr pellet technique to measure the relative abundances of H_2O_m and OH^- of the 7.7 ka Mt. Mazama glasses. However, these samples are different from the 8 ka Hrafntinnusker glasses, since the 7.7 ka Mt. Mazama glasses were progressively heated and degassed for minutes in temperatures ranging from 300–800 °C and thus likely: 1) lost H_2O_m preferentially, and/or 2) repartitioned the remaining magmatic H_2O_m to the OH^- groups in the glass, although the latter result is less certain. Figure 8b compares the $\delta^{18}O_{Total}$ of the Mt. Mazama glasses to the H_2O_t and the local $\delta^{18}O$ of precipitation. The step heating procedure is thought to release the H_2O_m earliest, which is also thought to be the lightest $\delta^{18}O$ secondary water, since it is not as strongly bound to the silicate as the OH^- (Newman et al., 1986; Silver et al., 1990; Giachetti et al.,

2015). This process could explain the negative trend of increasing $\delta^{18}O$ of residual water. It is notable that the samples that have been heated the least, with the highest water concentration, have the $\delta^{18}O_{Total}$ values closest to the current $\delta^{18}O$ of precipitation. However, since we do not yet know the fractionation that takes place during secondary hydration in terms of the oxygen isotopes at ambient temperature, we cannot determine the $\delta^{18}O_{H2Om}$.

DISCUSSION

Prior oxygen isotope analyses of water in silicates in comparison to our results

In order to investigate sources of water and the origins of these fractionations of water in meteorites after their formation in carbonaceous chondrites, Clayton and Mayeda (2009) conducted step heating dehydration of mostly OH-bearing silicates (brucite, serpentine, and meteorites) to determine the $\delta^{18}O$ and $\delta^{17}O$ of water extracted from each of these samples, relative to the $\delta^{18}O$ of the residual solid. Similar to our results, where the residual solid is isotopically heavier relative to the extracted water, Clayton and Mayeda (2009) found that step heating produced large kinetic isotope effects during oxygen isotope analyses, where the oxygen liberated during analysis is enriched in ^{16}O, while the oxygen left in the residual solid is enriched in ^{18}O.

Furthermore, Hamza and Epstein (1980) used step fluorination to determine the $\delta^{18}O$ of OH^- extracted from OH-bearing minerals. Similar to Clayton and Mayeda (2009), Hamza and Epstein (1980) note an increase in the $\delta^{18}O$ of extracted OH^- with continued heating. Hamza and Epstein (1980) conducted partial fluorination at increasing temperatures (0–450 °C) on kaolinite, biotite, muscovite, chlorite, and phlogopite. In addition, Zheng (1993) used the modified increment method to calculate the $\Delta^{18}O_{silicate\text{-}OH}$ value for a range of hydroxyl-bearing silicates, including muscovite, kaolinite, and biotite at temperatures ranging from 0–1200 °C. They found that the OH-bearing silicates are enriched in ^{18}O relative to the associated hydroxyl group, but that the OH-bearing silicate is depleted in ^{18}O relative to its anhydrous counterpart.

In Figure 9 we compare our $\Delta^{18}O_{mica\text{-}OH}$ values for our biotites (BUD and NBS30) to those determined by Zheng (1993) and Hamza and Epstein (1980). Our $\Delta^{18}O_{biotite\text{-}OH}$

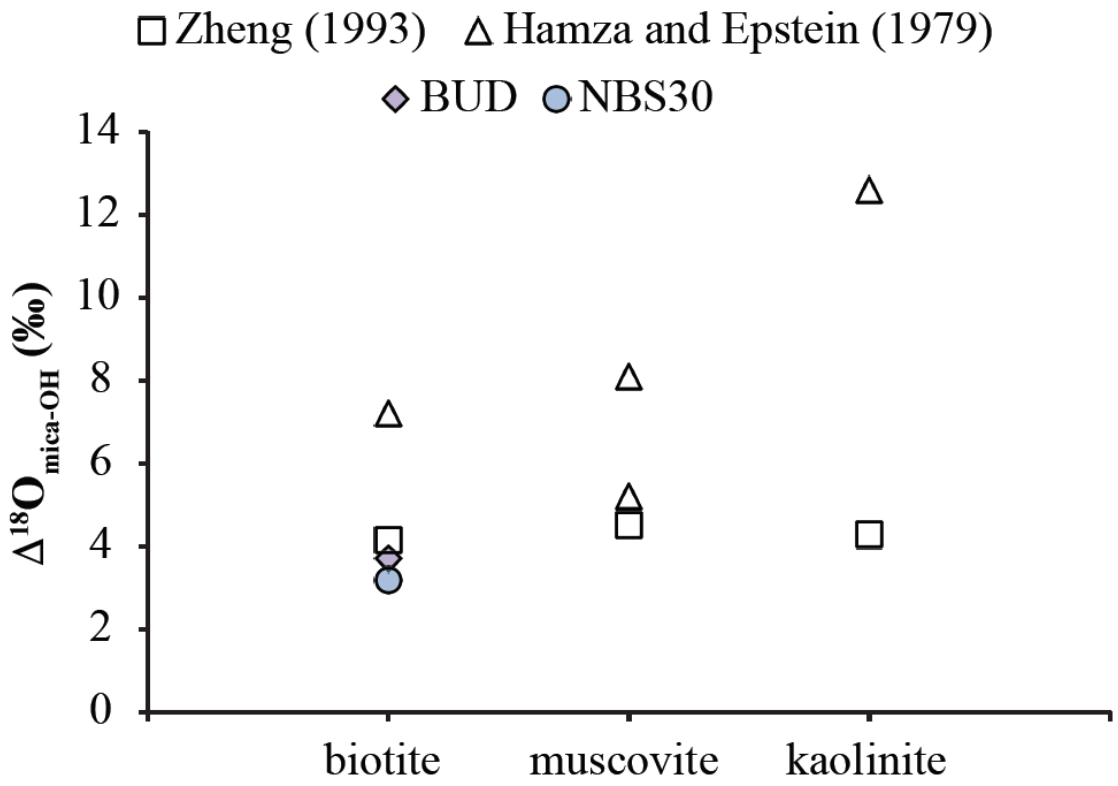

Figure 9. Comparison of our $\Delta^{18}O_{mica\text{-}OH}$ values with those from Zheng (1993) and Hamza and Epstein (1980) for biotite, muscovite, and kaolinite. Our biotite fractionations overlap well with those from Zheng (1993), while Hamza and Epstein (1980) fractionations are larger than ours and those from Zheng 1993.

values are very similar to those determined by Zheng (1993) using the increment method (within 0.5 ‰). However, the $\Delta^{18}O_{biotite\text{-}OH}$ value from Hamza and Epstein (1980) using partial fluorination is around 4 ‰ heavier than our values.

Understanding the $\delta^{18}O$ values of water extracted from volcanic glasses

High temperature mafic and felsic silicates and associations with δD values

The primary trend in the oxygen isotopic ratios of extracted waters is based on the relationship between the hydrogen-bound oxygen and the oxygen in the silicate. Since the $\delta^{18}O_{H2Om}$ values are calculated based off the $\delta^{18}O$ value of the associated silicate at its magmatic temperature (see section *3.3.1* above), we see heavier $\delta^{18}O_{Total}$ values for the more mafic, higher temperature glasses (Volcán de Fuego), relative to the more felsic, lower temperature glasses (Mount St. Helens and Mt. Mazama). This is in contrast to

trends shown for hydrogen isotopes, and is very likely due to the presence of oxygen in the silicate that is reacting with the hydrogen-bound oxygen.

Figure 10a does not show any clear trends between δD and $\delta^{18}O$ in the water extracted from the glasses. Shifts in δD with continued degassing illustrate a decrease in δD with decreasing H_2O_t (wt.%) (Newman et al., 1988; Castro et al., 2014), which is based on the preferential degassing of ^2H relative to ^1H. As was discussed above, the degassing of oxygen isotopes is more complicated due to interactions between the oxygen of the water and the oxygen of the silicate. Therefore, we must take into account the fractionations between water and glass for basalt, andesite, dacite, and rhyolite glasses, which are all based on relationships between water and the associated minerals that make up the silicate. $1000\ln\alpha_{rhyolite\text{-}water}$ equilibrium relationships lead to lighter $\delta^{18}O$ values of associated waters in relation to the silicate. However, $1000\ln\alpha$ fractionations for more mafic glasses have the opposite relationships, due to the differing mineral assemblages of basalts, andesites, and dacites, relative to rhyolites. Therefore, it appears that rhyolites should have degassing trends that generally correlate with hydrogen isotope trends, while more mafic magmas should have degassing trends that oppose those of hydrogen isotopic ratios.

$\delta^{18}O_{Total}$ trends in relation to δD trends of secondary hydration

Figure 8b illustrates a trend of increasing $\delta^{18}O_{Total}$ values with increasing wt.% H_2O_t in the secondarily hydrated 8 ka Hrafntinnusker glasses. This trend also illustrates that increased secondary hydrated caused the $\delta^{18}O_{Total}$ value of water extracted from the Hrafntinnusker glasses to become more different than the $\delta^{18}O$ of local precipitation. Although we are still not completely certain of the process that occurs during secondary hydration in terms of the oxygen isotopic ratios, as was discussed in section 3.4, there are two primary possibilities for oxygen isotopic fractionation during secondary hydration: 1) kinetic fractionation (possibly $1/8^{th}$ that of hydrogen), or 2) exchange and equilibration with the silicate, which would lead to large, positive $\Delta^{18}O_{glass\text{-}H2Om}$, and therefore an increase in $\delta^{18}O$ with increasing hydration. Figure 8b illustrates that the likely trend with secondary hydration in terms of the oxygen isotopic ratio is the latter, which leads to

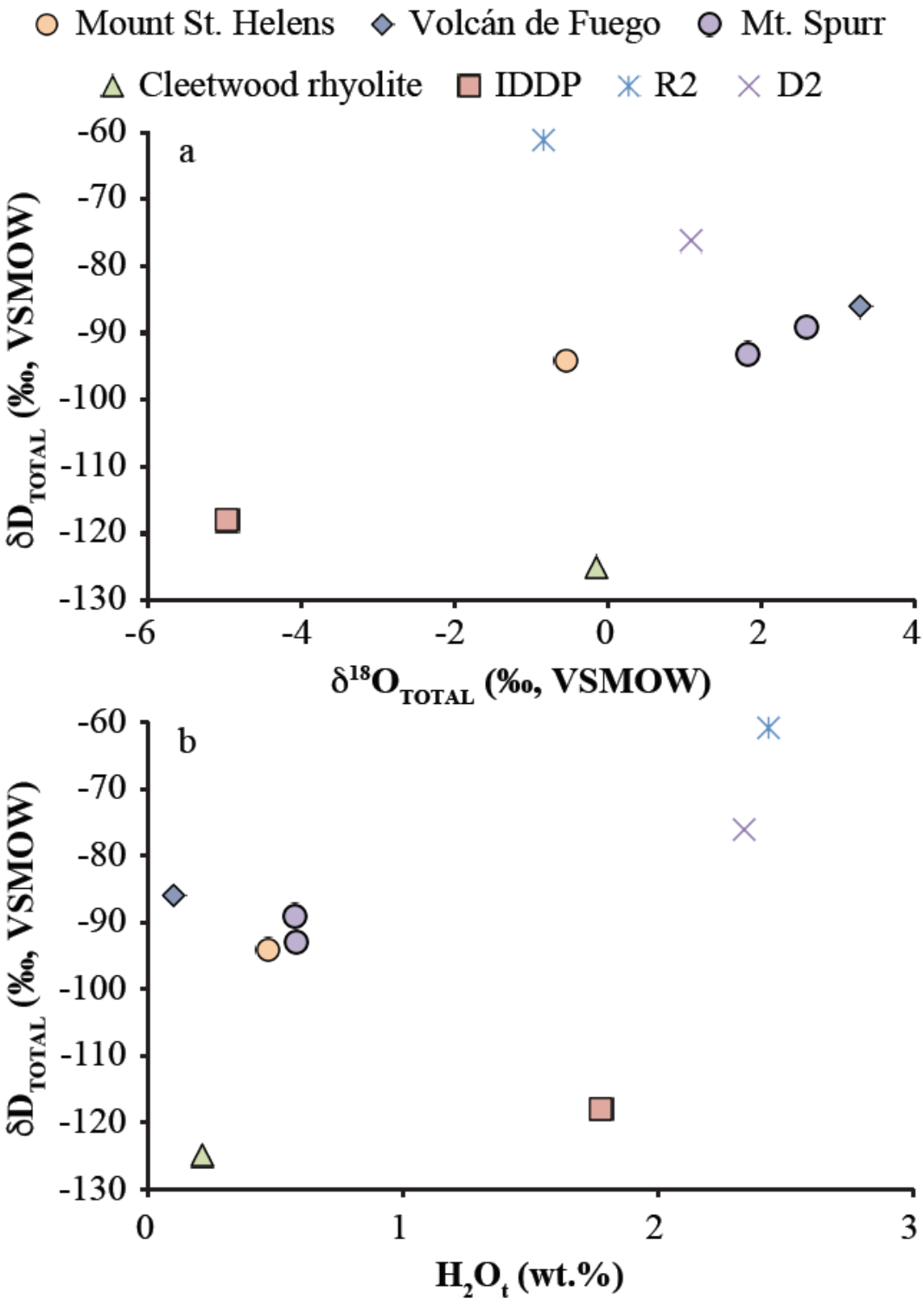

Figure 10. Water isotopes relative to water concentration. a) δD relative to the $\delta^{18}O$ of water extracted from our glasses, showing no consistent correlations between the two. b) δD_{Total} relative to the total water concentration, which shows the trends between the hydrogen isotopes and the total water concentration.

heavier $\delta^{18}O$ values with increased hydration. This is opposite the trend we see for hydrogen isotopic ratios, which leads to lower δD values with increased hydration.

CONCLUSIONS

We developed an approach to determine the $\delta^{18}O$ of H_2O_m, OH^-, and H_2O_t of water extracted from volcanic glasses. Following corrections the residual OH^- that is left in the silicate during analysis, the $\delta^{18}O$ of water extracted from silicate glasses can be determined using the TCEA. The trends for oxygen isotopes of magmatic glasses illustrate that oxygen isotopic ratios during volcanic degassing are likely different for rhyolitic versus more mafic magmatic melts. In addition, we show that secondary hydration of volcanic glass likely leads to increases in $\delta^{18}O$ values with increased hydration, which is opposite the secondary hydration trend for hydrogen isotopic ratios. These analyses have the potential to open up new pathways in isotopic investigations of water-rock interactions prior to and following volcanic eruptions.

CHAPTER VII

SUMMARY

In this dissertation I explored processes from the initial formation of large-scale volcanic eruptions all the way to the process of secondary hydration of volcanic glass, which is used for paleoenvironmental studies. Through the use of oxygen and hydrogen isotopes, this research has provided insights into the full life of magmas, from their initial formation to secondary hydration.

In Chapter II, I used isotopic ratios ($^{87}Sr/^{86}Sr$, $^{143}Nd/^{144}Nd$, and $\delta^{18}O$), major element compositions, and MELTS and EC-AFC modeling to determine that the explosive eruptions from Gorely volcano in Kamchatka, Russia were formed through partial melting of the underlying Akhomten Massif. I also used $^{40}Ar/^{39}Ar$ dating to determine that the Gorely eruptive center is a longer-lived center than was previously thought, with explosive eruptions dating back to over 300 ka.

In Chapter III, I used isotopic ($\delta^{18}O$ and εHf) and trace element ratios to determine that the 30 Ma Crooked River caldera is the oldest known caldera associated with the Yellowstone hotspot. I also used these same ratios in addition to the known geologic instabilities beneath the Wildcat Mountain and Tower Mountain calderas to determine that their magmas were formed through small-scale delamination of the underlying crust.

Chapter IV details my work to better understand what happens to volcanic glass once it is deposited on the Earth's surface, in terms of the in-diffusion of meteoric water. This chapter is important for studies involving the secondary hydration of volcanic glass used for paleoclimate studies. This chapter documents the rate that water diffuses into volcanic glass at ambient temperature and pressure, and the D/H ratios that are associated with secondary hydration. It also details the need for corrections for pre-existing magmatic water D/H ratios if researchers want to utilize the D/H of secondarily hydrated volcanic glass to match local meteoric water.

In Chapter V, I document the D/H trends associated with the earliest stages of secondary hydration of volcanic glass using the well-described 1980 eruptions of Mount

St. Helens. I compare the D/H, water concentration, and $\delta^{18}O$ trends of tephra collected in 1980 and compare these tephra to tephra from the same units, which were recently collected in 2015. I document that the only samples that show significant shifts in water concentrations (>1 wt.%) are those that were collected near gas escape pipes and from thicker deposits, illustrating the need for a longer-lived heat source to hydrate glass within 35 years. Using the water concentration and D/H ratios of the non-hydrated glasses, I was also able to document that the magmas that sourced the 1980 eruptions did not have significant amounts of time to degas prior to eruption, and therefore the magma needed to rise rapidly from deeper depths prior to eruption.

In Chapter VI, I developed a new method for the analyses of oxygen isotopic ratios of hydrous volcanic glass on the TCEA. I propose new mica standards for these analyses that are calibrated against water standards sealed in silver cups. I document that these analyses are possible, provided corrections for instrumental mass fractionation using $\delta^{13}C$, and that the trends of $\delta^{18}O$ with increasing secondary hydration are opposite those of δD.

APPENDIX A

CHAPTER II SUPPLEMENTARY PHOTOS, FIGURES, AND TABLES

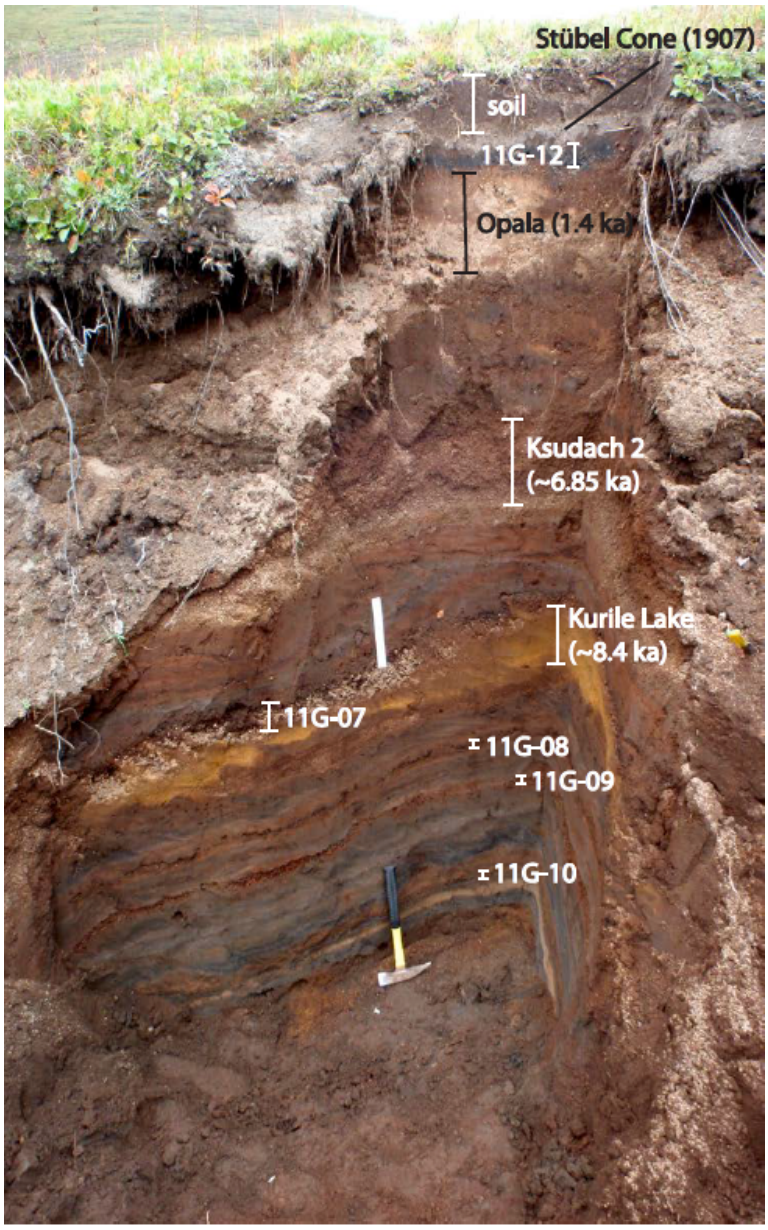

Figure A3. The above photograph and those on the next three pages are stratigraphic position of tephra samples, including tephra marker layers used to date tephra samples. The tephra sections for 11G-20, and 11G-19 and 11G-18 are separated by a drainage. Sample 11G-20 is younger than samples 11G-19 and 11G-18 based on its orientation above Optr, while 11G-19 and 11G-18 are located below Optr. Sample 11G-19 is stratigraphically located ~2 m above 11G-18.

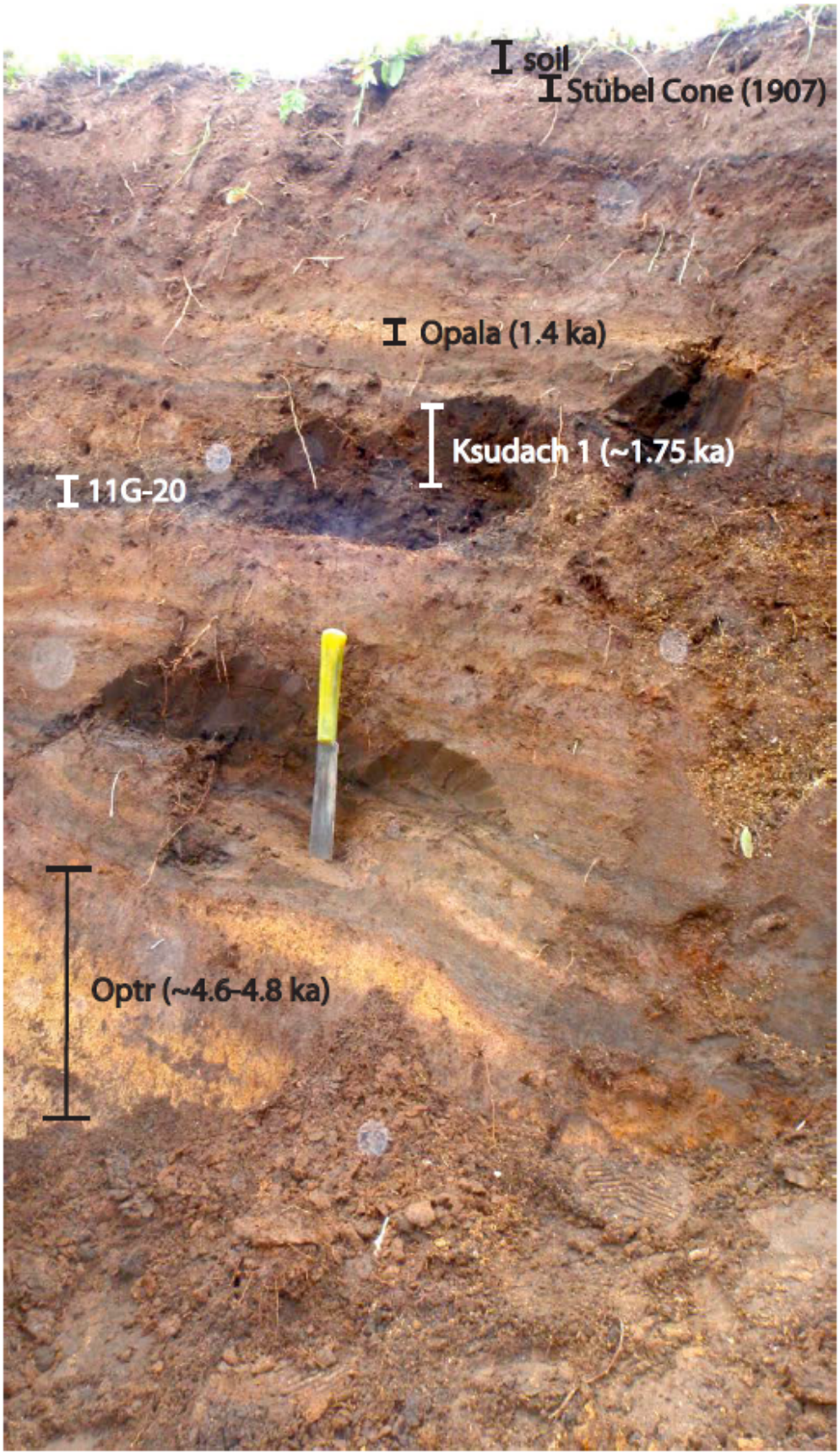
soil
Stübel Cone (1907)
Opala (1.4 ka)
Ksudach 1 (~1.75 ka)
11G-20
Optr (~4.6-4.8 ka)

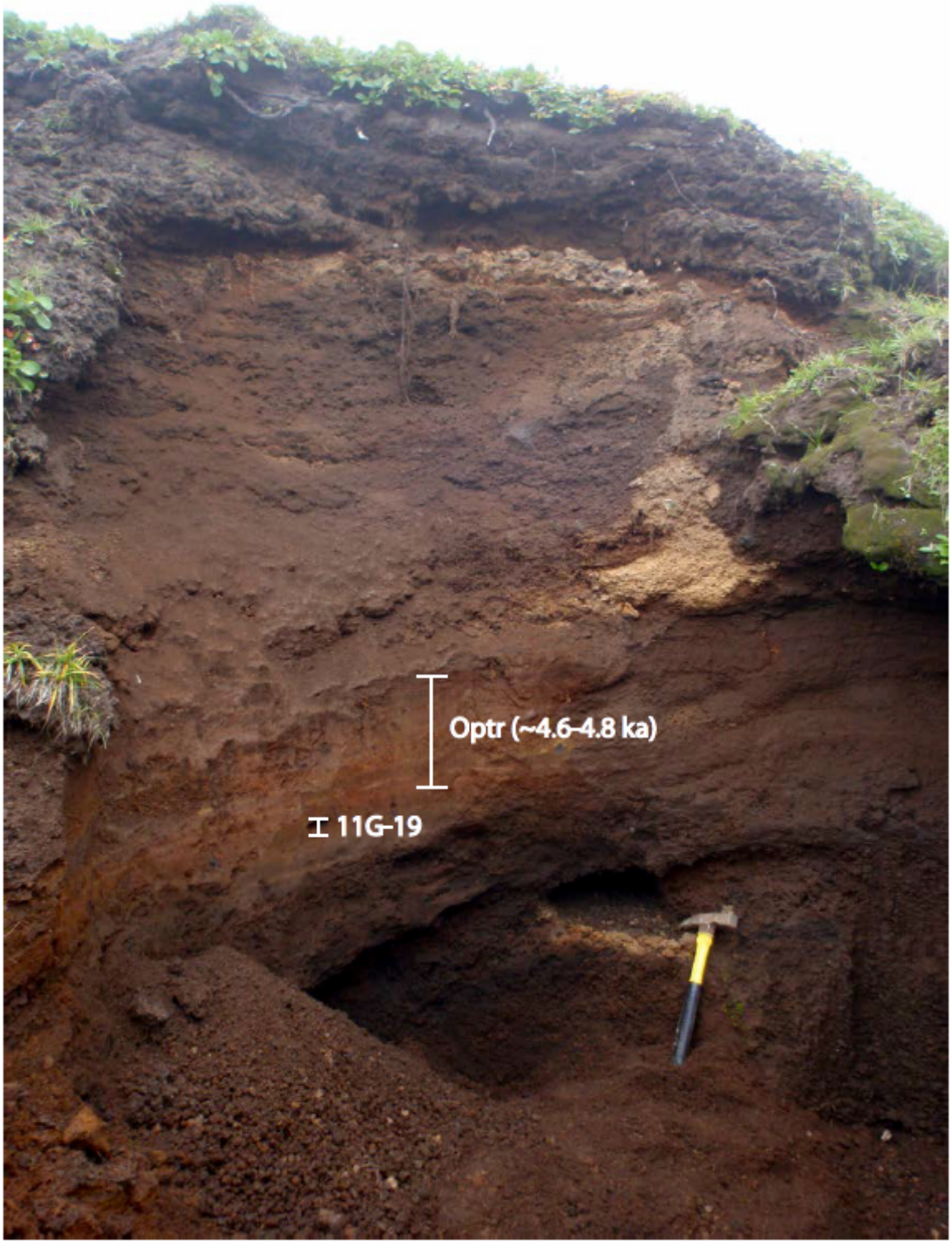
Optr (~4.6–4.8 ka)
11G-19

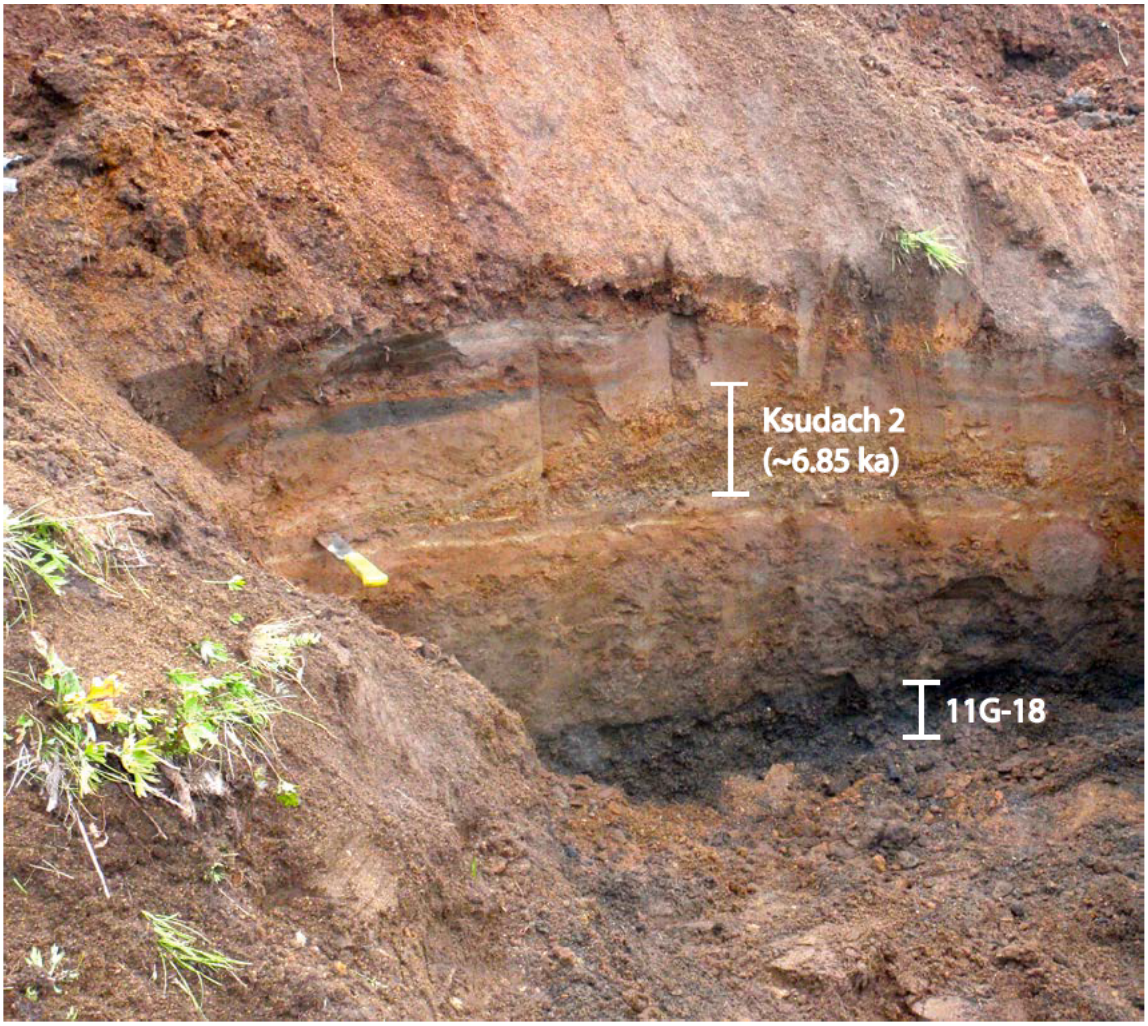
Ksudach 2
(~6.85 ka)
11G-18

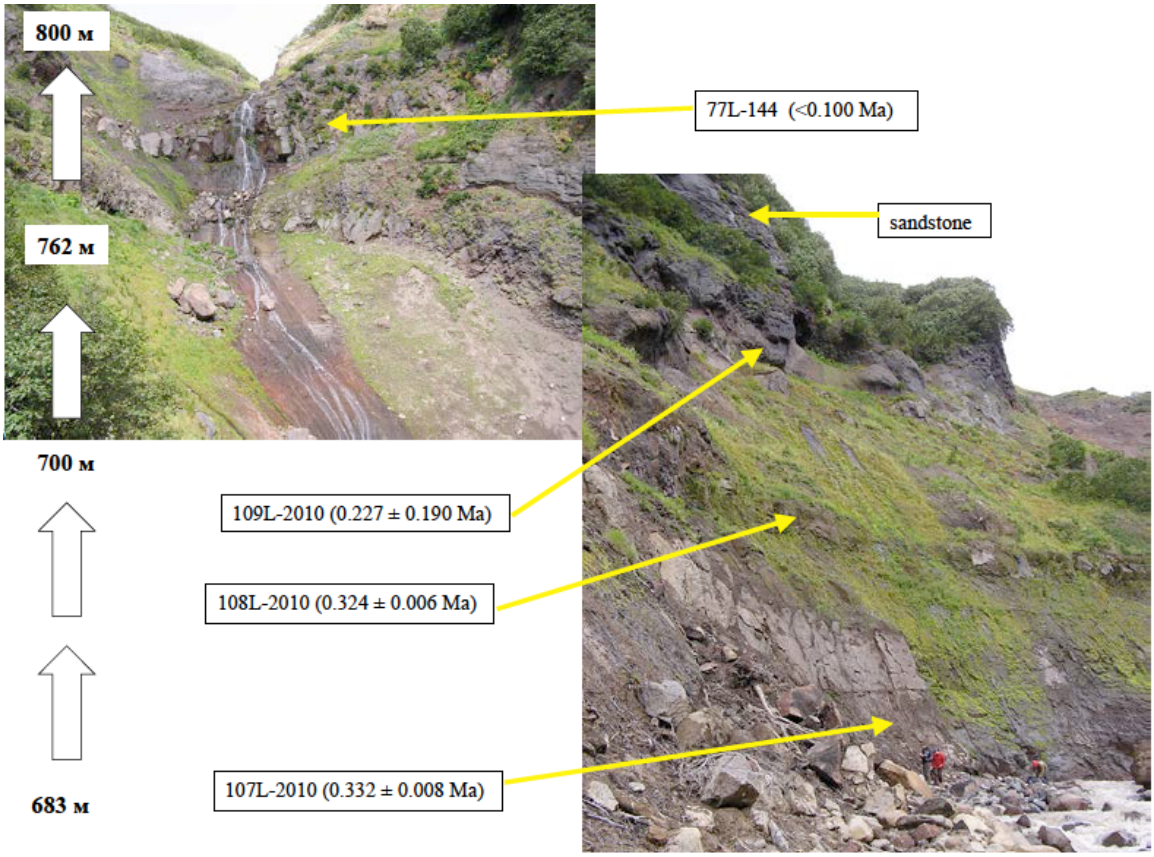

Figure A2. Location, age, and stratigraphic order of samples collected from Opasny (Dangerous) Canyon used in this study. People in lower right-hand corner of figure for scale.

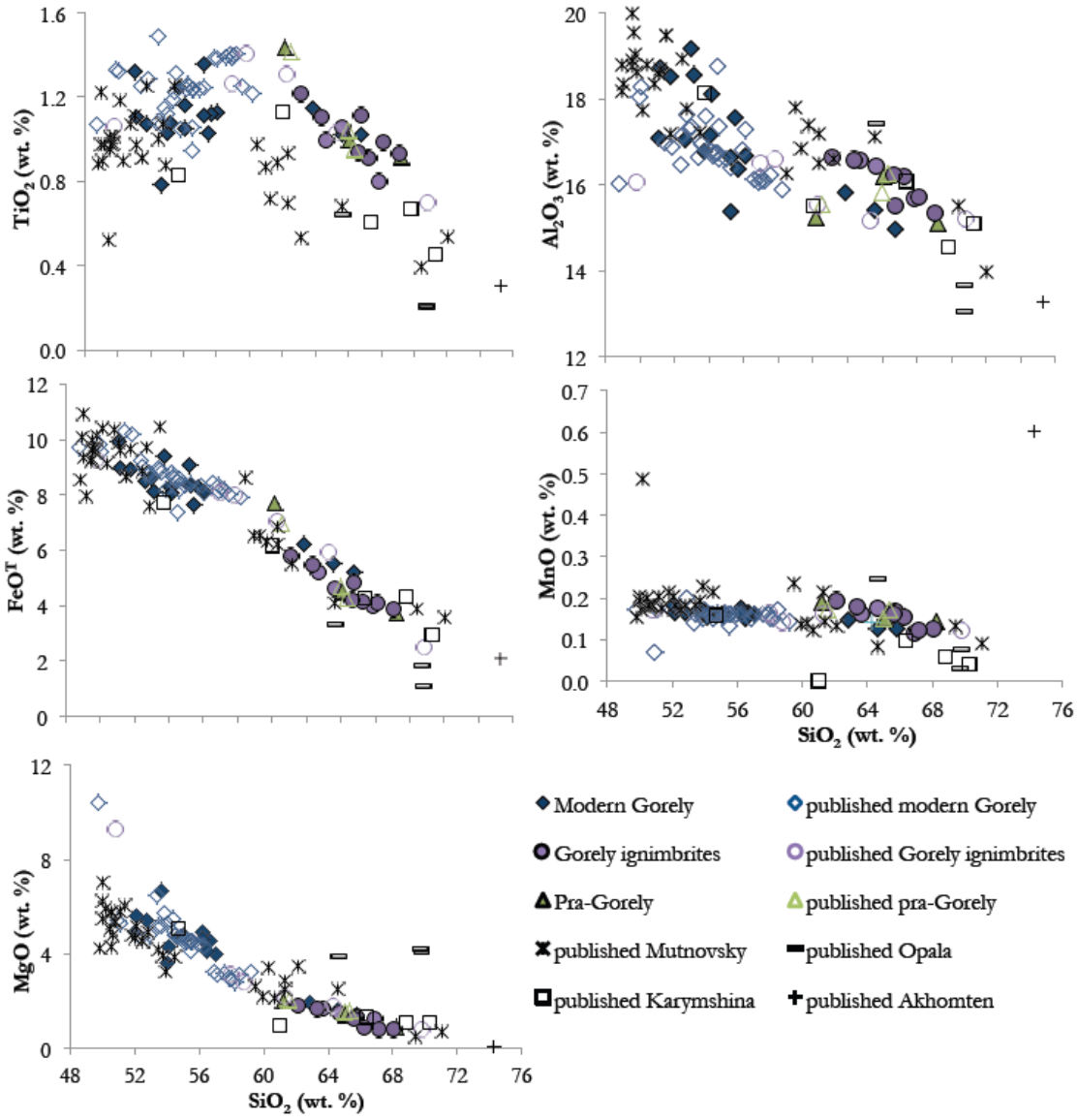

Figure A3. Harker diagrams to complement Figure 5, showing the major element chemistry of Gorely rocks relative to the surrounding felsic centers. Gorely data from other authors includes analyses from Chashchin et al. (2011); Duggen et al. (2007); Kepezhinskas et al. (1997); Pineau et al. (1999); Ishikawa et al. (2001); Popolitov & Volynets (1981). Karymshina data is from Shipley (2011); Mutnovsky data is from Duggen et al. (2007); Bindeman et al. (2004); Kepezhinskas et al. (1997); Hochstaedter et al. (1996); Pineau et al. (1999); Poplitov & Volynets (1991); Opala data is from Bindeman et al. (2004).

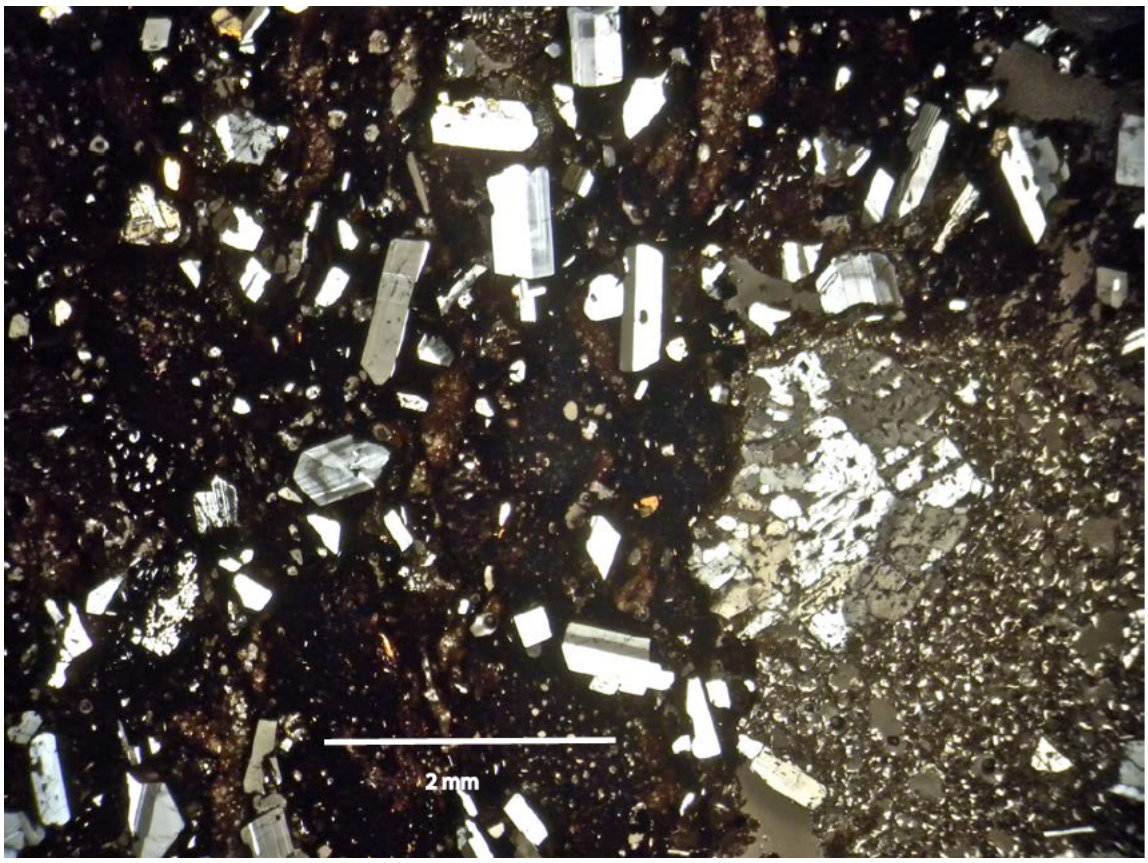

Figure A4. Image of unit 77L-144, showing its variable groundmass texture, which is sporadically distributed throughout the thin section. This type of variable groundmass is seen in many ignimbrite units. This image shows groundmass that is primarily devitrified, but is not consistent throughout the unit.

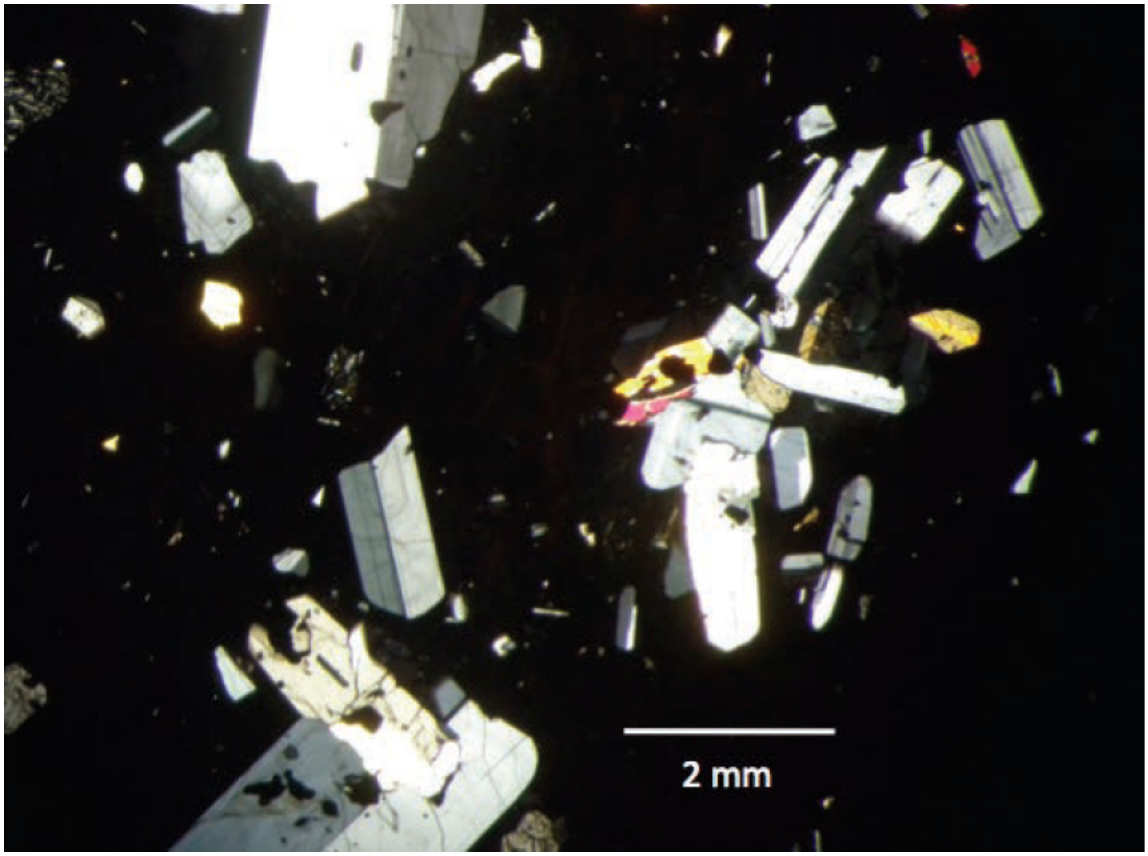

Figure A5. Image of unit 125L-2000, showing its glomeroporphyritic texture, which is representative of the ignimbrite units.

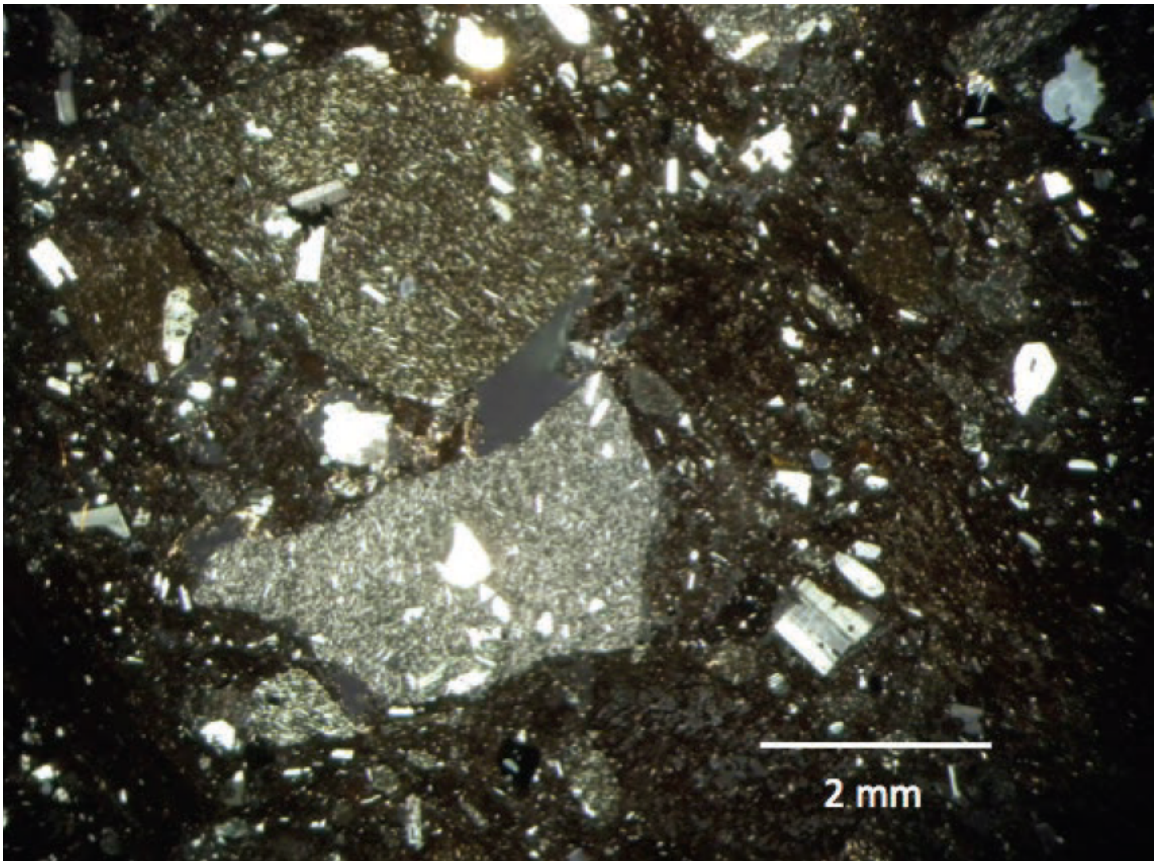

Figure A6. Image of unit 108L-2010, showing multiple mafic enclaves, which are representative of the ignimbrite units.

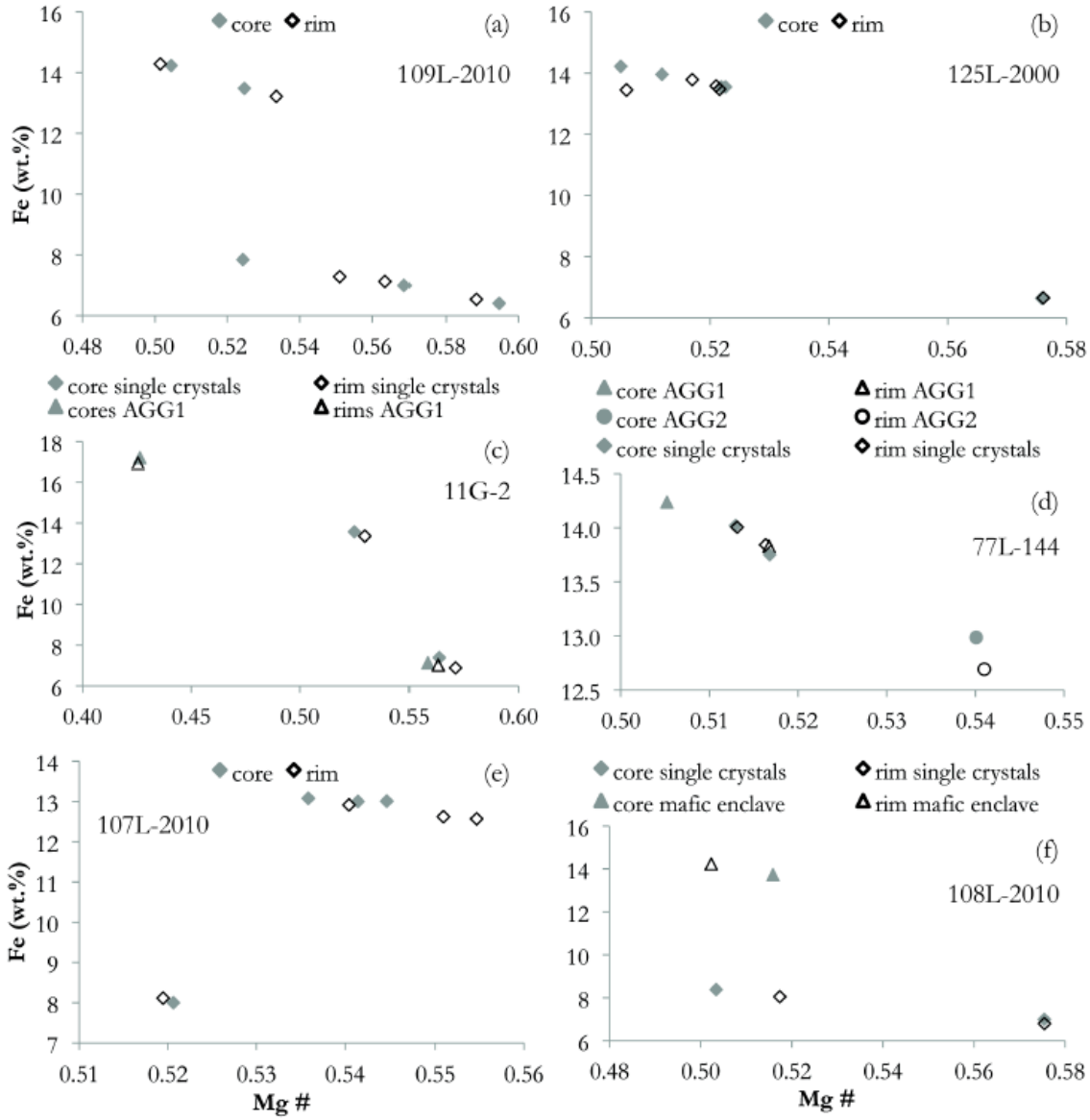

Figure A7. Similar diagrams to Figure 7, but with Zr, which is an incompatible trace element, on the x-axis. The thick, black arrow on each graph is a linear trend for the Gorely dacites, pointing back to a possible initial source, if a consistent fractionating trend is occurring. The trend is not as clear as shown in Figure 7, but Rb and Ba still show a clear offset from the Gorely basalts. Error bars are denoted for our analyses as a 2σ replicate LOD. Data is from this work and others: Duggen et al. (2007); Kepezhinskas et al. (1997); Ishikawa et al. (2001).

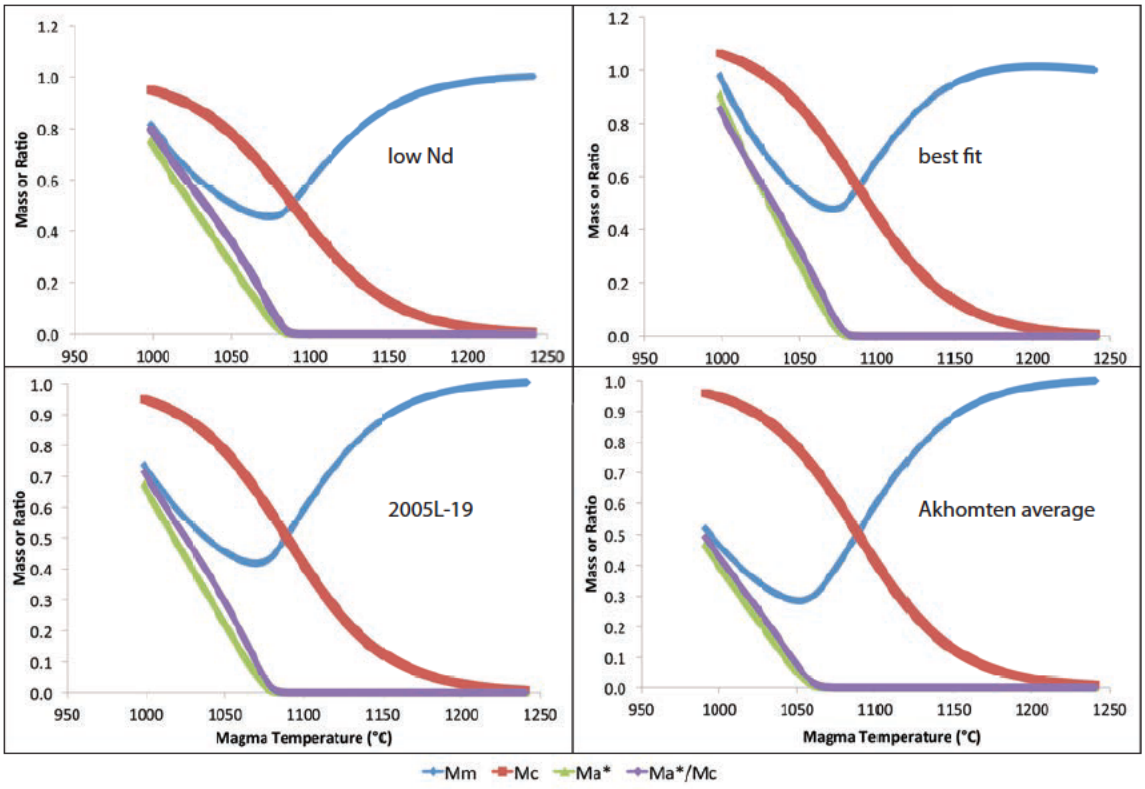

Figure A8. EC-AFC results in terms of the change in magmatic temperature and the resulting 'mass of melt in magma body' (M_m), 'mass of cumulates' (M_c), 'mass of anatectic melt' (M_a*), and the ratio between the 'mass of anatectic melt' and the 'mass of cumulates' (M_a*/M_c). Results are shown for each of the four models (low Nd, best fit, 2005L-19, and the average Akhomten).

Table A1: Summary of $^{40}Ar/^{39}Ar$ experiments and U-Pb ages

Sample no.	K/Ca total	total fusion age (ka)	2σ	$^{40}Ar/^{36}Ar$	2σ	MSWD	isochron age (ka)	2σ	N	^{39}Ar %	MSWD	plateau age (ka)	2σ	U-Th-Pb age (Ma)	1σ	number of grains
109L-2010	0.65	173	31	294.9	2.1	0.06	235	36	5 of 11	70.9	0.11	**227**	**19**			
108L-2010	0.49	325	11	293.1	2.9	0.76	335	16	6 of 9	90.7	1.31	**324**	**10**			
107-2010	1.81	332	7	296.5	2.1	0.22	326	13	9 of 10	98.3	0.31	**332**	**6**			
11G-3a xenocryst core														54.5	1.1	1
11G-3a xenocryst rim														37.5	0.7	1
89L-9														11.2	0.1	11
111L-2010														4.11	0.09	11
418L-1972														4.04	0.08	12
59L-11														4.01	0.08	11

*$^{40}Ar/^{39}Ar$ Ages calculated relative to 28.201 Ma for the Fish Canyon sanidine (Kuiper et al., 2008) using decay constants of Min et al. (2000)

**Age in bold is preferred $^{40}Ar/^{39}Ar$ age

Table A2: location, type, and analytical methods of each unit

Sample no.	Latitude	Longitude	Sample Type	XRF	$^{87}Sr/^{86}Sr$	$^{144}Nd/^{143}Nd$	$^{40}Ar/^{39}Ar$	U-Pb	$\delta^{18}O$	Thin Section
11G-1	N52°32'19.6"	E158°12'08.5"	ignimbrite	X	X	X			X	
11G-2	N52°32'19.6"	E158°12'08.5"	ignimbrite	X					X	X
11G-3	N52°32'53.6"	E158°12'04.5"	pumice	X					X	
11G-4	N52°35'37.7"	E158°00'45.9"	lava	X					X	
11G-5	N52°31'25.7"	E157°59'07.4"	lava	X					X	
11G-6	N52°31'25.7"	E157°59'07.4"	lava	X					X	X
11G-7	N52°31'25.7"	E157°59'07.4"	tephra	X					X	
11G-8	N52°31'25.7"	E157°59'07.4"	tephra	X					X	
11G-9	N52°31'25.7"	E157°59'07.4"	tephra	X					X	
11G-10	N52°31'25.7"	E157°59'07.4"	tephra	X					X	
11G-12	N52°31'25.7"	E157°59'07.4"	tephra	X					X	
11G-13	N52°35'06.8"	E158°03'34.9"	lava	X					X	X
11G-14	N52°35'06.8"	E158°03'34.9"	lava	X					X	X
11G-15	N52°35'14.3"	E158°05'03.6"	lava	X					X	
11G-16	N52°34'59.9"	E158°05'17.9"	lava	X					X	
11G-17	N52°34'35.0"	E158°05'16.5"	lava	X					X	
11G-18	N52°35'10.4"	E158°03'04.4"	tephra	X					X	
11G-19	N52°35'10.4"	E158°03'04.4"	tephra	X					X	
11G-20	N52°35'10.4"	E158°03'04.4"	tephra	X					X	
11G-21	N52°32'16.8"	E157°58'31.3"	bomb	X					X	X
11G-23			lava	X					X	
11G-24	N52°33'29.5"	E158°03'21.2"	lava	X					X	X
107L-2010	N52°28'16.7"	E158°05'48.0"	ignimbrite	X	X	X	X		X	X
108L-2010	N52°28'17.2"	E158°05'47.4"	ignimbrite	X			X		X	X
109L-2010	N52°28'17.5"	E158°05'43.8"	ignimbrite	X	X	X	X		X	X
125L-2000	N52°30'01.4"	E158°07'57.1"	ignimbrite	X			X		X	X
77L-144	N52°28'19.9"	E158°05'43.4"	ignimbrite	X	X	X	X		X	X
2005L-19	N52°37'31.0"	E158°05'49.7"	ignimbrite	X	X	X			X	X
07L-53	N52°34'23.2"	E157°57'52.3"	ignimbrite	X					X	X
07L-54	N52°35'00.1"	E158°03'31.4"	lava	X			X		X	X
89L-9	N52°27'31.6"	E158°24'16.1"	Massif	X				X		
111L-2010	N52°30'37.3"	E158°12'59.2"	ignimbrite					X		
418L-1972	N52°37'7.3"	E158°19'18.3"	ignimbrite					X		
59L-2011	N52°52'47.5"	E157°45'24.3"	ignimbrite					X		
53L-11			ignimbrite					X		
59L-11			ignimbrite					X		

Table A3: Summary of MELTS modeling

liquidus T (°C)	1241
P (kbar)	1
$f(O_2)$	NNO
SiO_2	48.16
TiO_2	1.26
Al_2O_3	17.51
Fe_2O_3	2.00
Cr_2O_3	0.03
FeO	8.42
MnO	0.07
MgO	9.34
NiO	0.01
CoO	0.01
CaO	8.91
Na_2O	2.33
K_2O	0.73
P_2O_5	0.25
H_2O	0.97
Total	100.00

Mineral assemblage at:

50 wt.% SiO_2
Fo_{77}
An_{79}
Spinel

55 wt.% SiO_2
OPX En_{93}
CPX En_{21}
An_{73}
Spinel

60 wt.% SiO_2
OPX En_{93}
CPX En_{17}
An_{63}
Spinel

65 wt.% SiO_2
OPX En_{94}
CPX_{14}
An_{49}
Spinel
Apatite

70 wt.% SiO_2
OPX En_{95}
An_{31}
Spinel
Apatite

Table A4: Summary of EC-AFC modeling - Best fit run

	Sr	Nd	O	T (°C)	Specific Heat (J/kg*K)	Enthalpy (J/kg)
magma concentration	474	15				
magma bulk D	1.7	0.031				
assimilant concentration	474	15				
assimilant bulk D	1.7	0.2				
isotopic ratio (magma)	0.7032	0.51302	6.2			
isotopic ratio (assimilant)	0.7036	0.51320	4.0			
liquidus (magma)				1241		
initial T (magma)				1241		
liquidus (assimilant)				1000		
initial T (assimilant)				500		
solidus				900		
magma					1484	396000
assimilant					1370	270000
equilibration temperature				998.73		

Table A5: Summary of EC-AFC modeling - Average Akhomten

	Sr	Nd	O	T (°C)	Specific Heat (J/kg*K)	Enthalpy (J/kg)
magma concentration	474	6				
magma bulk D	1.5	0.03				
assimilant concentration	474	9				
assimilant bulk D	1.5	0.03				
isotopic ratio (magma)	0.70320	0.513030	6.2			
isotopic ratio (assimilant)	0.70356	0.513093	4.3			
liquidus (magma)				1241		
initial T (magma)				1241		
liquidus (assimilant)				1000		
initial T (assimilant)				500		
solidus				900		
magma					1484	396000
assimilant					1370	270000
equilibration temperature				963.91		

Table A6: Summary of EC-AFC modeling - First ignimbrite

	Sr	Nd	O	T (°C)	Specific Heat (J/kg*K)	Enthalpy (J/kg)
magma concentration	474	11				
magma bulk D	1.5	0.03				
assimilant concentration	474	11				
assimilant bulk D	1.5	0.02				
isotopic ratio (magma)	0.70320	0.51303	6.20			
isotopic ratio (assimilant)	0.70343	0.51309	4.85			
liquidus (magma)				1241		
initial T (magma)				1241		
liquidus (assimilant)				1000		
initial T (assimilant)				500		
solidus				900		
magma					1484	396000
assimilant					1370	270000
equilibration temperature				988.14		

Table A7: Summary of EC-AFC modeling - Low Nd assimilant

	Sr	Nd	O	T (°C)	Specific Heat (J/kg*K)	Enthalpy (J/kg)
magma concentration	474	11				
magma bulk D	1.5	0.03				
assimilant concentration	474	11				
assimilant bulk D	1.5	0.02				
isotopic ratio (magma)	0.70323	0.51312	NA			
isotopic ratio (assimilant)	0.70356	0.51293	NA			
liquidus (magma)				1241		
initial T (magma)				1241		
liquidus (assimilant)				1000		
initial T (assimilant)				500		
solidus				900		
magma					1484	396000
assimilant					1370	270000
equilibration temperature				998.73		

Appendix A References Cited

Bindeman, I.N., Ponomareva, V., Bailey, J. & Valley, J. (2004). Volcanic arc of Kamchatka: A province with high $\delta^{18}O$ magma sources and large-scale $^{18}O/^{16}O$ depletion of the upper crust. *Geochimica et Cosmochimica Acta* **68**, 841–865.

Chashchin, A.A., Martynov, Y.A., Perepelov, A.B., Ekimova, N.I., Vladimirova, T.P. (2011). Physical and chemical conditions of the formation and evolution of Late Pleistocene–Holocene magmas of the Gorely and Mutnovsky volcanoes, southern Kamchatka. Russian Journal of Pacific Geology 5, 348–367.

Duggen, S., Portnyagin, M.V., Baker, J.A., Ulfbeck, D.G., Hoernle, K.A., Garbe-Schonber, D. & Grassineau, N. (2007). Drastic shift in lava geochemistry in the volcanic-front to rear-arc region of the southern Kamchatkan subduction zone: Evidence for the transition from slab surface dehydration to sediment melting. *Geochimica et Cosmochimica Acta* **71**, 452–480.

Hochstaedter, A.G., Kepezhinskas, P.K. & Defant, M.J. (1996). Insights into the volcanic arc mantle wedge from magnesian lavas from the Kamchatka Arc. *Journal of Geophysical Research* **B101**, 697–712.

Kepezhinskas, P.K., McDermott, F., Defant, M., Hochstaedter, A.G., Drummond, M.S., Hawkesworth, C.J., Koloskov, A.V., Maury, R.C. & Bellon, H. (1997). Trace element and Sr-Nd-Pb isotopic constraints on a three-component model of Kamchatka Arc petrogenesis. *Geochimica et Cosmochimica Acta* **61**, 577–600.

Pineau, F., Semet, M.P., Grassineau, N., Okrugin, V.M. & Javoy, M. (1999). The genesis of stable isotope (O, H) record in arc magmas: The Kamchatkan Case. *Chemical Geology* **153**, 93–124.

Ishikawa, T., Tera, F. & Nakazawa, T. (2001). Boron isotope and trace element systematics of the three volcanic zones in the Kamchatka arc. *Geochimica et Cosmochimica Acta* **65**, 4523–4537.

Poplitov, E.I. & Volynets, O.N. (1981). Geochemical characteristics of quaternary volcanism of the Kurile-Kamchatka island arc. *Nauka Publishers* (in Russian).

Shipley, N.K. (2011). Isotopic and petrologic investigation and model of genesis of large-volume high-silica rhyolites in arc environments: Karymshina caldera, Kamchatka, Russia [MA Thesis]: Eugene, Oregon, University of Oregon, 76 pages.

APPENDIX B

CHAPTER III SUPPLEMENTARY CITATIONS, METHODS, AND FIGURES

Citations for map locations

Figure 1:

The locations of the Crooked River, Wildcat Mountain, Tower Mountain, and Mohawk River calderas are from McClaughry et al. (2009b; 2010). The Siletzia accreted basalt and the 32 Ma location of the Yellowstone hotspot are from Wells et al. (2014). The current Cascade arc (major composite volcanoes shown as triangles) and the Columbia River and Steens basalts are from Coble and Mahood (2012). The location of the ancestral Cascade arc is based on the rotation of Oregon from Wells et al. (1998). The John Day Formation is from Robinson et al. (1990). The younger caldera complexes of the Snake River Plain and Yellowstone Plateau are from Morgan and McIntosh (2005), Watts et al. (2011), and Coble and Mahood (2012). The mapped boundary of the Blue Mountain Province is from Walker (1977), and the two Oligocene-early Miocene calderas in southwestern Oregon are from McClaughry et al. (2009b). The inferred boundary of the Klamath-Blue Mountain gravity-anomaly lineament (KBML) and the inferred geophysical boundary of the Siletzia terrane from Gao et al. (2011) are also shown. The 0.706 dashed line defines the $^{87}Sr/^{86}Sr = 0.706$ boundary, which separates the Mesozoic-Paleozoic accreted terranes to the west and the Precambrian craton to the east (Farmer and Depaolo, 1983; Fleck and Criss, 1985).

Citations for compiled data fields

Figure 2:

a) Data field for the Yellowstone plume basalts is from Bennett (2006); data for the basalts of the ancestral Cascades is from du Bray and John (2011); data for pre-Mazama basalt eruptions are from Bacon (1989) and Bacon et al. (1997); data for the Hawaiian plume are from Garcia et al. (2000), Gaffney et al. (2004), Sisson et al. (2002), Coombs et al. (2004), Xu et al. (2005), Morgan et al. (2007), Xu et al. (2007), Marske et al. (2008), Sisson et al. (2009), Hanano et al. (2010), and van der Zander et al. (2010).

b) Data field for rhyolites of the ancestral Cascades is from du Bray and John (2011); data for the rhyolites of the High Cascades are from Bullen and Clynne (1990), Nakada et al. (1994), Leeman et al. (1990), Smith and Leeman (1987), Sevigny and Brown (1989), Tepper et al. (1993), Lawrence et al. (1984), Conrey et al. (2001), Grove et al. (1988), Borg and Clynne (1998), Reagan et al. (2003), Baker et al. (1991), and Grove et al. (2005); data for rhyolite field of the Yellowstone-Snake River Plain are from Drew et al. (2013), Christiansen and McCurry (2008); data for John Day Formation field come from this study, Obermiller (1987), Patridge (2009), and McClaughry et al., 2009b); select ancestral Cascades tuffs are from McClaughry et al. (2010); data for the Wildcat Mountain caldera rhyolites are from this study, Ferns and McClaughry (2007), and McClaughry and Ferns (2006b); data for the Tower Mountain caldera are from Ferns et al., 2003, Ferns, 1999, and Ferns and Taubeneck, 1994; data for the Crooked River caldera are from this study, Obermiller (1987), McClaughry et al. (2009b,c), Patridge (2009), Ferns and McClaughry (2006a; 2006b), McClaughry and Ferns (2006b), McClaughry and Ferns (2006a; 2006b), Weidenheim (1981), Smith et al. (1998), Bingert (1984), and Thormahlen (1984)

MORB normalized trace element diagrams

MORB normalized diagrams of Pearce (1983) are used to compare compositions of basalts of Crooked River (CR) (this study; Patridge, 2009; Smith et al., 1998; Obermiller, 1987; Smith, 1986a; Thormahlen, 1984; Weidenheim, 1981; McClaughry and Ferns, 2006b), Wildcat Mountain (WM) (this study; Ferns and McClaughry, 2006a; 2006b; McClaughry and Ferns, 2006b; Patridge, 2009; Obermiller, 1987; Smith et al., 1998; Smith, 1986a; Bingert, 1984), and Tower Mountain (TM) (this study; Ferns et al., 2003; Ferns and Taubeneck, 1994; Ferns, 1999) to basalts from the ancestral Cascades (du Bray and John 2011), Yellowstone Plateau basalts (Bennett, 2006), pre-Mazama basalts (Bacon, 1989; Bacon et al., 1997), the basalt of Mt. Tom of the Mohawk River eruptive center of the ancestral Cascades (McClaughry et al., 2010), and OIB (Sun and McDonough, 1989).

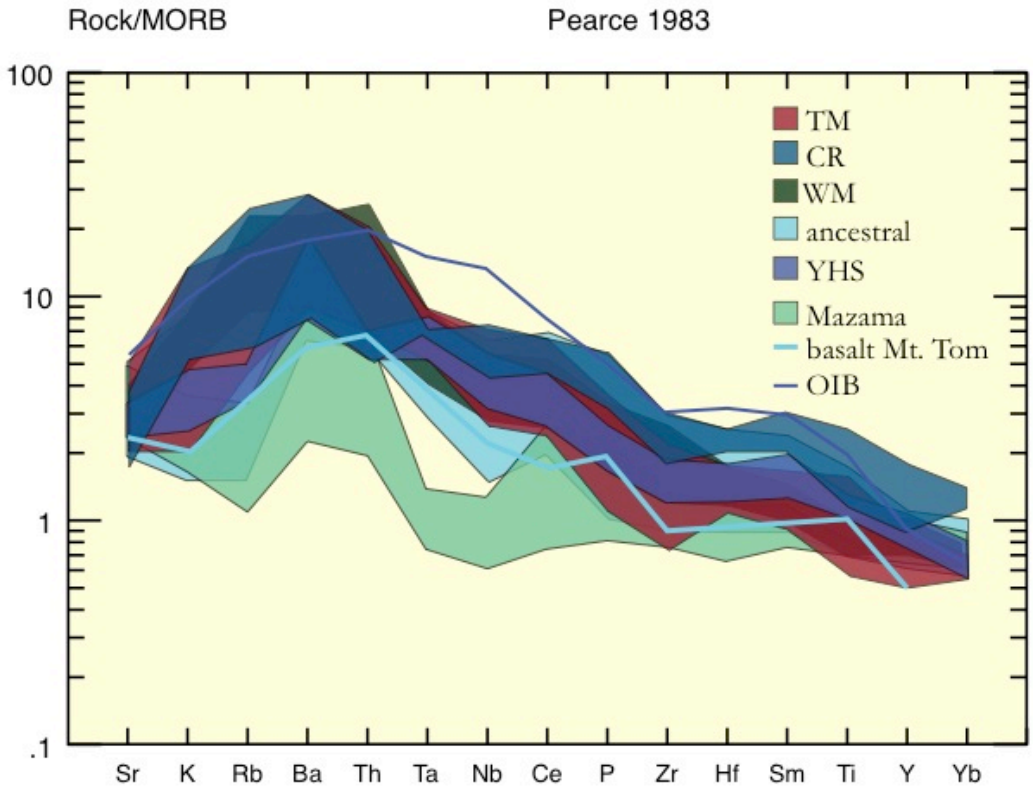
Rock/MORB
Pearce 1983
100
10
1
.1
TM
CR
WM
ancestral
YHS
Mazama
basalt Mt. Tom
OIB
Sr K Rb Ba Th Ta Nb Ce P Zr Hf Sm Ti Y Yb

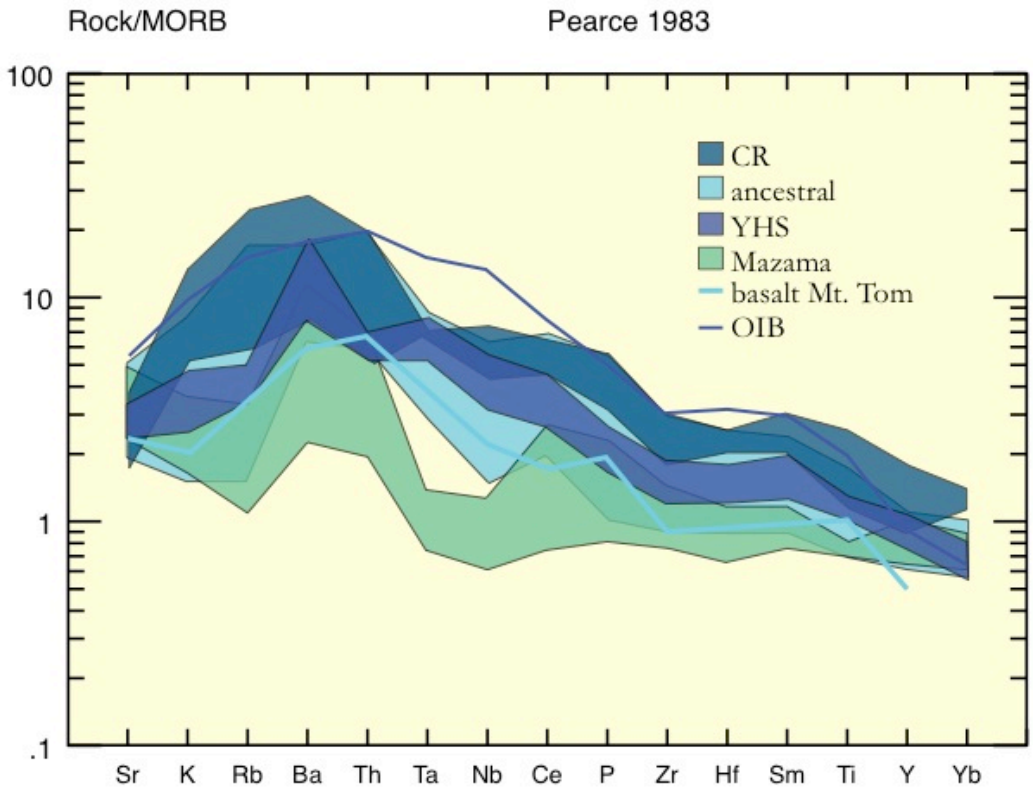
Rock/MORB
Pearce 1983
100
10
1
.1
CR
ancestral
YHS
Mazama
basalt Mt. Tom
OIB
Sr K Rb Ba Th Ta Nb Ce P Zr Hf Sm Ti Y Yb

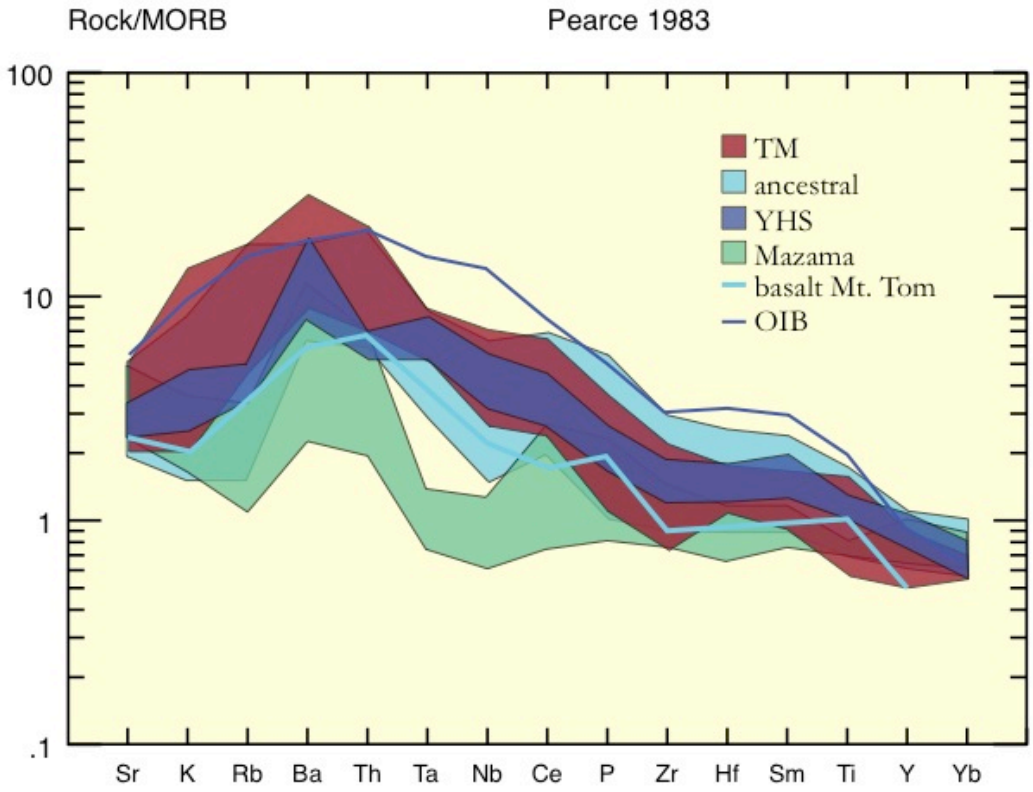
Rock/MORB
Pearce 1983
100
10
1
.1
TM
ancestral
YHS
Mazama
basalt Mt. Tom
OIB
Sr K Rb Ba Th Ta Nb Ce P Zr Hf Sm Ti Y Yb

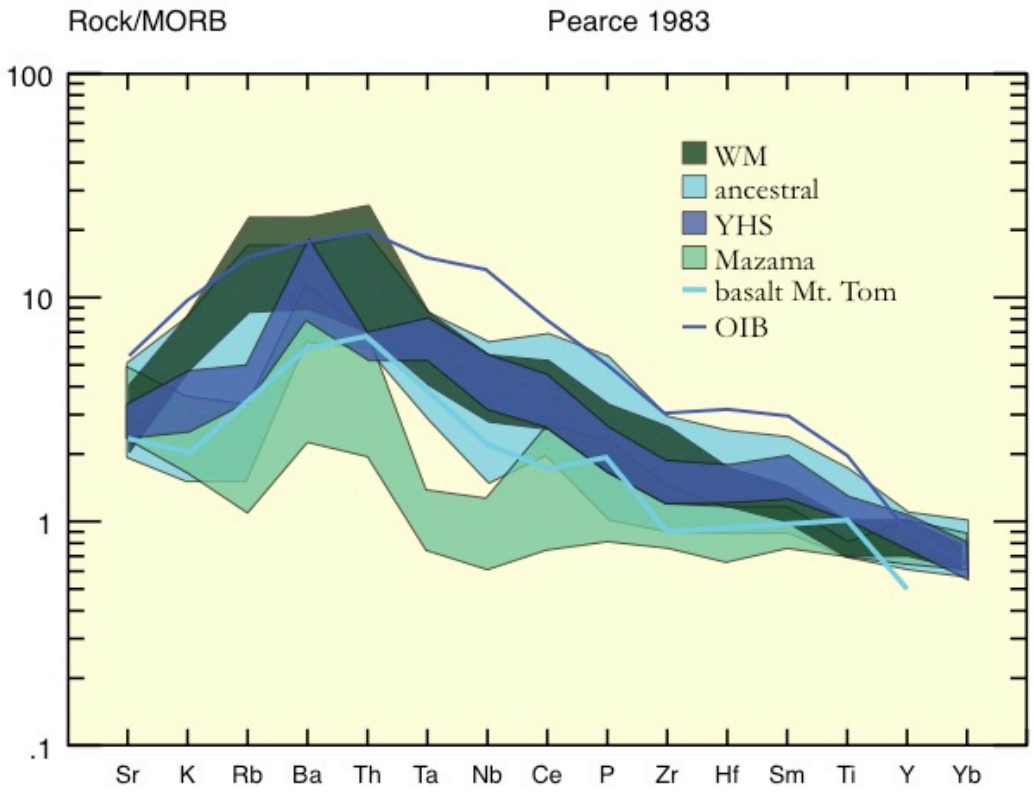
Rock/MORB
Pearce 1983
100
10
1
.1
WM
ancestral
YHS
Mazama
basalt Mt. Tom
OIB
Sr K Rb Ba Th Ta Nb Ce P Zr Hf Sm Ti Y Yb

Laser fluorination analytical methods

$\delta^{18}O$ compositions of 1–2 mg of quartz, plagioclase, pyroxene, olivine, amphibole, and bulk zircon phenocrysts were determined in the stable isotope laboratory at the University of Oregon. Individual grains (0.75–2 mg) were picked from each sample using a binocular microscope. Grains from the 0.5 to 1 mm size fraction were selected for analysis. Samples were analyzed using CO_2-laser fluorination (e.g. Bindeman, 2008) using Gore Mt. Garnet ($\delta^{18}O$ of 5.75‰) as a standard. The gas to be analyzed was purified through a series of steps involving reactions with BrF_5 and multiple LN_2 cryogenic traps that captured BrF_5 reaction products in a mercury diffusion pump acting as a getter for F_2 gas. The remaining purified O_2 was then converted to CO_2 in a small platinum-graphite converter and the yield was measured as a means to quantify any sample loss. The isotopic ratio of $^{18}O/^{16}O$ in the CO_2 gas was determined on a MAT 253 mass spectrometer.

SIMS analytical methods

$\delta^{18}O$ compositions of cores and rims of mounted and imaged zircon crystals were further refined in situ using the Cameca 1280R ion microprobe at the Canadian Centre for Isotopic Microanalysis, University of Alberta, Canada (±0.16‰ 2σ). Zircons were cast in epoxy and their mid-sections exposed by diamond grinding and polishing. Scanning electron microscopy (SEM) was conducted utilizing a Zeiss EVO MA15 operating at 15 kV and ~3 nA, and equipped with a broadband, high-sensitivity cathodoluminescence (CL) detector to reveal internal grain structures. The zircon array, cut out to form a ~4 x 6 mm epoxy block, was pressed into the center of custom indium receptacle along with two similar blocks comprising zircon reference materials (RMs). Au was sputtered onto the mount (M1248) surface to a thickness of 30 nm prior to SIMS.

SIMS analyses utilized a Cameca IMS1280 multicollector instrument with 20 keV Cs^+ primary ions (2.5 – 3.0 nA, ⌀12 μm) and extraction of O^- secondary ions through 10 kV. Charge compensation utilized normal incidence low energy electrons. The primary beam was rastered around the spot for 60 s prior to acquisition and rastered 5 x 5 μm during acquisition. Entrance slit and field aperture were 122 μm and 5 x 5 mm,

respectively, with 100x image magnification of the transfer optics. Energy filtering was not employed. Secondary ion collection utilized dual Faraday cups at L'2 ($^{16}O^-$, ~3E9 ions/s) and H'2 ($^{18}O^-$, ~6.5E6 ion/s), with mass resolutions of 2000 and 2275, respectively, which are sufficient to resolve spectral interferences. Each analysis required 4.5 min, including pre-analysis sputtering, automated secondary ion tuning, and a total of 90 s peak counting. The analysis sequence consisted of four unknowns followed by one analysis of CCIM reference zircon S0081 ($\delta^{18}O_{VSMOW}$ = +4.87); after each group of eight unknowns, TEM2 (S0022) zircon ($\delta^{18}O_{VSMOW}$ = +8.20; Black et al., 2004) was analyzed. Data for 46 analyses of S0081 were processed collectively for session IP13082 and document minor instrumental mass fractionation drift (+0.1‰), yielding a linear time-corrected session standard deviation of ±0.07‰. Uncertainties propagated to unknowns include within-spot, between-spot, and between-session components, which together yield a median value of ±0.16‰ (2σ) per analysis. The weighted mean $\delta^{18}O$ value of TEM2 (S0022) zircon for this session is +8.26 ±0.03 (N= 27; MSWD = 1.02).

Lu-Hf analyses of zircon

The Lu-Hf isotopes composition of zircon was determined for some of these same O spots at the Radiogenic Isotope and Geochronology Lab (RIGL) at Washington State University (±0.8–2.0 eHf). Following oxygen isotopic analyses, the mounts were lightly repolished before laser ablation-multicollector-inductively coupled plasma-mass spectrometry (LA-MC-ICPMS) analyses were conducted to determine Lu-Hf isotopic composition using a 213 nm New Wave Nd:YAG laser coupled with a Thermo-Finnigan Neptune MC-ICPMS. Analytical methods are described by Fisher et al. (2014) with the exception that U-Pb ages were not concurrently determined. Measured $^{176}Hf/^{177}Hf$ of analyzed unknowns were normalized to the measured $^{176}Hf/^{177}Hf$ of the Mud Tank zircon standard (Woodhead and Hergt, 2005). Typical correction factors were 1.00016. In order to monitor the accuracy of the ^{176}Yb and ^{176}Lu interference correction, analyses of a Yb-rich synthetic zircon (MUNZirc-4) were interspersed with unknowns and yielded a mean $^{176}Hf/^{177}Hf$ of 0.282123 ± 10 (2 σ), which is within error of the value given by Fisher et

al. (2011). Epsilon Hf values were calculated using the CHUR values of Bouvier et al. (2008) and the ^{176}Lu decay constant of Söderlund et al. (2004) ($1.867*10^{-11}$ year−1). Depleted mantle values used are those of Nowell et al. (1998).

U-Pb ages of zircons

Individual zircon cores and rims were analyzed for ^{238}U-^{206}Pb ages using the CAMECA ims 1270 ion microprobe at the University of California, Los Angeles using an ^{16}O primary beam for analyses. Analytical reproducibility was estimated from the standard deviation of replicate analyses of AS3 (1099.1 Ma; Paces and Miller, 1993) and TEM2 (416.8 Ma; Black et al., 2003), which were both used for calibrations of U, Th, and Pb sensitivities. Standards were mounted on the same disk as the unknowns and in close proximity to the unknowns. 12 to 15 zircons were analyzed from three units of the Crooked River caldera. Standards were analyzed approximately once for every 5 unknowns. Although the reproducibility between analyses for each unit has standard deviations of ~1 or less, the uncertainty for each analysis is typically high (~5 Ma). These large errors are likely due to a combination of high common Pb and low U content of the zircons. For this reason, we do not rely on any of these ages for our conclusions, although we include the new ages in our figures.

Appendix B References Cited

Albright, L.B., III, Woodburne, M.O., Fremd, T.J., Swisher, C.C., III, MacFadden, B.J., Scott, G.R., III. (2008). Revised chronostratigraphy and biostratigraphy of the John Day Formation (Turtle Cove and Kimberly Members), Oregon, with implications for updated calibration of the Arikareean North American Land Mammal Age. *J. Geology* **116**, 211–237.

Bacon, C.R. (1989). Calc-alkaline, shoshonitic, and primitive tholeiitic lavas from monogenetic volcanoes near Crater Lake, Oregon. *Journal of Petrol*ogy **31**, 135-166.

Bacon, C.R., Bruggman, P.E., Christiansen, R.L., Clynne, M.A., Donnelly-Nolan, J.M., Hildreth, W. (1997). Primitive magmas at five Cascade volcanic fields: Melts from hot, heterogeneous sub-arc mantle. *The Canadian Mineralogist* **35**, 397-423.

Baker, M.B., Grove, T.L., Kinzler, R.J., Donnelly-Nolan, J.M., Wandless, G.A. (1991). Origin of compositional zonation (high-alumina basalt to basaltic andesite) in the Giant Crater Lava Field, Medicine Lake Volcano, Northern California. *Journal of Geophysical Research* **B96**, 21819–21842.

Bennett, K.M. (2006). Petrogenesis of Pleistocene basalts of the Norris-Mammoth Corridor, Yellowstone National Park [Masters thesis]: University of Nevada, Las Vegas, 124 p.

Bindeman, I. (2008). Oxygen isotopes in mantle and crustal magmas as revealed by single crystal analysis. *Reviews in Mineralogy and Geochemistry* **69**, 445–478.

Bingert, N.J. (1984). Geology of the northeast one-quarter of the Prineville Quadrangle, North-Central Oregon [Masters thesis]: Oregon State University, 141 p.

Black, L.P., Kamo, S.L., Allen, C.M., Aleinikoff, J.N., Davis, D.W., Korsch, R.J., Foudoulis, C. (2003). TEMORA 1: a new zircon standard for Phanerozoic U-Pb geochronology. *Chemical Geology* **200**, 155–170.

Black, L. P., Kamo, S. L., Allen, C. M., Davis, D., Aleinikoff, J. N., Valley, J.W., Mundil, R., Campbell, I.H., Korsch, R.J., Williams, I.S., Foudoulis, C. (2004). Improved $^{206}Pb/^{238}U$ microprobe geochronology by the monitoring of a trace-element-related matrix effect; SHRIMP, ID-TIMS, ELA-ICP-MS and oxygen isotope documentation for a series of zircon standards. *Chemical Geology* **205**, 115–140.

Borg, L.E., Clynne, M.A. (1998). The petrogenesis of felsic calc-alkaline magmas from the southernmost Cascades, California: Origin by partial melting of basaltic lower crust. *Journal of Petrology* **39**, 1197–1222.

Bouvier, A., Vervoort, J.D., Patchett, P.J. (2008). The Lu-Hf and Sm-Nd isotopic composition of CHUR: Constraints from unequilibrated chondrites and implications for the bulk composition of terrestrial planets. *Earth and Planetary Science Letters* **273**, 48–57.

Bullen, T.D., Clynne, M.A. (1990). Trace element and isotopic constraints on magmatic evolution of Lassen Volcanic Center. *Journal of Geophysical Research* **B95**, 19671–19691.

Christiansen, E.H., McCurry, M. (2008). Contrasting origins of Cenozoic silicic volcanic rocks from the western Cordillera of the United States. *Bulletin of Volcanology* **70**, 251–267.

Coble, M.A., Mahood, G.A. (2012). Initial impingement of the Yellowstone plume located by widespread silicic volcanism contemporaneous with Columbia River flood basalts. *Geology* **40**, 655–658.

Conrey, R.M., Hooper, P.R., Larson, P.B., Chesley, J.T., Ruiz, J. (2001). Trace element and isotopic evidence for two types of crustal melting beneath a high Cascade volcanic center, Mt. Jefferson, Oregon. *Contributions to Mineralogy and Petrology* **141**, 710–732.

Coombs, M.L., Clague, D.A., Moore, G.F., Cousens, B.L. (2004). Growth and collapse of Waiane volcano, Hawaii, as revealed by exploration of its submarine flanks. *Geochemistry Geophysics Geosystems* **5**, 1–30.

Drew, D., Bindeman, I., Watts, K., Schmitt, A., Fu, B., McCurry, M. (2013). Crustal-scale recycling in caldera complexes and rift zones along the Yellowstone hotspot track: O and Hf isotopic evidence in diverse zircons from voluminous rhyolites of the Picabo volcanic field, Idaho. *Earth and Planetary Science Letters* **381**, 63–77.

du Bray, E.A., John, D.A. (2011). Petrologic, tectonic, and metallogenic evolution of the ancestral Cascades magmatic arc, Washington, Oregon, and northern California. *Geosphere* **7**, 1102-1133.

Farmer, G.L., Depaolo, D.J. (1983). Origin of Mesozoic and Tertiary granite in the western United States and implications for Mesozoic crustal structure: 1. Nd and Sr isotopic studies in the geocline of the northern Great Basin. *Journal of Geophysical Research* **88**, 3379–3401.

Ferns, M.L. (1999). Geologic map of the Fly Valley 7.5' quadrangle, Union County, Oregon. *Oregon Department of Geology and Mineral Industries Geologic Map Series* **GMS-113**, scale 1:24,000.

Ferns, M.L., McClaughry, J.D. (2006a). Preliminary geologic map of the Huston Lake 7.5' quadrangle, Crook County, Oregon. *Oregon Department of Geology and Mineral Industries Open-File Report* **O-06-21**, scale 1:24,000.

Ferns, M.L., McClaughry, J.D. (2006b). Preliminary geology map of the Powell Buttes 7.5' quadrangle, Crook County, Oregon. *Oregon Department of Geology and Mineral Industries Open-File Report* **O-06-24**, scale 1:24,000.

Ferns, M.L., McClaughry, J.D. (2007). Preliminary geologic map of the Hensley Butte and Salt Butte 7.5' quadrangles, Crook County, Oregon. *Oregon Department of Geology and Mineral Industries Open-File Report* **O-07-11**, scale 1:24,000.

Ferns, M.L., McConnell, V., Madin, I. (2003). Transition from tholeiitic flood basalt magmatism to calc-alkaline and alkaline volcanism along an eruptive axis coincident with the east margin of the Grande Ronde Valley, northeastern Oregon. *Geological Society of America Abstracts with Programs* **35**, 549.

Ferns, M.L., Taubeneck, W.H. (1994). Geology and mineral resources map of the Limber Jim Creek quadrangle, Union County, Oregon. *Oregon Department of Geology and Mineral Indstries Geological Map Series* **GMS-82**, scale 1:24,000.

Fisher, C.M., Hanchar, J.M., Samson, S.D., Dhuime, B., Blichert-Toft, J., Vervoort, J.D., Lam, R. (2011). Synthetic zircon doped with hafnium and rare earth elements: A reference material for in situ hafnium isotope analysis. *Chemical Geology* **286**, 32–47.

Fisher, C.M., Vervoort, J.D., DuFrane, S.A. (2014). Accurate Hf isotope determinations of complex zircons using the "laser ablation split stream" method. *Geochemistry Geophysics Geosystems* **15**, 1–19.

Fleck, R.J., Criss, R.E. (1985). Strontium and oxygen isotopic variations in Mesozoic and Tertiary plutons of central Idaho. *Contributions to Mineralogy and Petrology* **90**, 291–308.

Gaffney, A.M., Nelson, B.K., Blichert-Toft, J. (2004). Geochemical constraints on the role of oceanic lithosphere in intra-volcano heterogeneity at west Maui, Hawaii. *Journal of Petrology* **45**, 1663–1687.

Gao, H., Humphreys, E., Yao, H., van der Hilst, R. (2011). Crust and lithosphere structure of the northwestern U.S. with ambient noise tomography: Terrane accretion and Cascade arc development. *Earth and Planetary Science Letters* **304**, 202-211.

Garcia, M.O., Pietruszka, A.J., Rhodes, J.M., Swanson, K. (2000). Magmatic processes during the prolonged Pu 'u Oo eruption of Kilauea Volcano, Hawaii. *Journal of Petrology* **41**, 967–990.

Grove, T.L, Baker, M.B., Price, R.C., Parman, S.W., Elkins Tanton, L.T., Chatterjee, N., Müntener, O. (2005). Magnesian andesite and dacite lavas from Mt. Shasta, Northern California: Products of fractional crystallization of H_2O-rich mantle melts. *Contributions to Mineralogy and Petrology* **148**, 542–565.

Grove, T.L., Kinzler, R.J., Baker, M.B., Donnelly-Nolan, J.M. (1988). Assimilation of granitic by basaltic magma at Burnt Lava Flow, Medicine Lake Volcano, northern California: Decoupling of heat and mass transfer. *Contributions to Mineralogy and Petrology* **99**, 231–343.

Hanano, D., Weis, D., Scoates, J.S., Aciego, S., Depaolo, D.J. (2010). Horizontal and vertical zoning of heterogeneities in the Hawaiian mantle plume from the geochemistry of consecutive postshield volcano pairs: Kohala-Mahukona and Mauna Kea-Hualalai. *Geochemistry Geophysics Geosystems* **11**, 1–22.

Hladky, F.R., McCaslin, G.R. (2006). Preliminary geologic map of the Springfield 7.5' quadrangle, Lane County, Oregon. *Oregon Department of Geology and Mineral Industries Open-File Report* **O-06-07**, scale 1:24,000.

Lawrence, R.B., Armstrong, R.L., Berman, R.G. (1984). Garibaldi group volcanic rocks of the Salal Creek area, southwestern British Columbia: Alkaline lavas on the fringe of the predominantly calc-alkaline Garibaldi (Cascade) Volcanic Arc. *Journal of Volcanology and Geothermal Research* **21**, 255–276.

Leeman, W.P., Smith, D.R., Hildreth, W., Palacz, Z.A., Rogers, N.W. (1990). Compositional diversity of late Cenozoic basalts in a transect across the southern Washington Cascades: Implications for subduction zone magmatism. *Journal of Geophysical Research* **B95**, 19561–19582.

Marske, J.P., Garcia, M.O., Pietruszka, A.J., Rhodes, J.M., Norman, M.D. (2008). Geochemical variations during Kilauea's Pu 'u Oo eruption reveal a fine-scale mixture of mantle heterogeneities within the Hawaiian plume. *Journal of Petrology* **49**, 1297–1318.

McClaughry, J.D., Ferns, M.L. (2006a). Preliminary geologic map of the Prineville 7.5' quadrangle, Crook County, Oregon. *Oregon Department of Geology and Mineral Industries Open-File Report* **O-06-22**, scale 1:24,000.

McClaughry, J.D., Ferns, M.L. (2006b). Preliminary geologic map of the Ochoco Reservoir 7.5' quadrangle, Crook County, Oregon. *Oregon Department of Geology and Mineral Industries Open-File Report* **O-06-23**, scale 1:24,000.

McClaughry, J., Ferns, M.L., Gordon, C.L., Patridge, K.A. (2009a). Field trip guide to the Oligocene Crooked River caldera: Central Oregon's supervolcano, Crook, Deschutes, and Jefferson Counties, Oregon. *Oregon Geology* **69**, 25–44.

McClaughry, J.D., Ferns, M.L., Streck, M.J., Patridge, K.A., Gordon, C.L. (2009b). Paleogene calderas of central and eastern Oregon: Eruptive sources of widespread tuffs in the John Day and Clarno Formations, *in* O'Connor, J.E., Dorsey, R.J., and Madin, I.P., ed., Volcanoes to vineyards: Geologic field trips through the dynamic landscape of the Pacific Northwest. *Geological Society of America Field Guide* **15**, 407–434.

McClaughry, J.D., Ferns, M.L., Gordon, C.L. (2009c). Field trip guide to the Neogene stratigraphy of the Lower Crooked Basin and the ancestral Crooked River, Crook County, Oregon. *Oregon Geology* **69**, 45–60.

McClaughry, J.D., Ferns, M.L., Gordon, C.L., Patridge, K.A. (2009d). Field trip guide to the Oligocene Crooked River caldera: Central Oregon's supervolcano, Crook, Deschutes, and Jefferson Counties, Oregon *Oregon Geology* **69**, 25–44.

McClaughry, J.D., Wiley, T.J., Ferns, M.L., Madin, I.P. (2010). Digital geologic map of the southern Willamette Valley, Benton, Lane, Linn, Marion, and Polk Counties, Oregon. *Oregon Department of Geology and Mineral Industries Open File Report* **0-10-03**.

Morgan, J.K., Clague, D.A., Borchers, D.C., Davis, A.S., Milliken, K.L. (2007). Mauna Loa's submarine western flank: Landsliding, deep volcanic spreading, and hydrothermal alteration. *Geochemistry Geophysics Geosystems* **8**, 1–42.

Morgan, L.A., McIntosh, W.C. (2005). Timing and development of the Heise volcanic field, Snake River Plain, Idaho, western USA. *Geological Society of America Bulletin* **117**, 288-306.

Nakada, S., Bacon, C.R., Gartner, A.E. (1994). Origin of phenocrysts and compositional diversity in pre-Mazama rhyodacite lavas, Crater Lake, Oregon *Journal of Petrology* **35**, 127–162.

Nowell, G.M., Kempton, P.D., Noble, S.R., Fitton, J.G., Saunders, A.D., Mahoney, J.J., Taylor, R.N. (1998). High precision Hf isotope measurements of MORB and OIB by thermal ionasation mass spectrometry: Insights into the depleted mantle. *Chemical Geology* **149**, 211–233

Obermiller, W.A. (1987). Geologic, structural, and geochemical features of basaltic and rhyolitic volcanic rocks of the Smith Rock-Gray Butte area, central Oregon [Masters thesis]: University of Oregon, 169 p.

Paces, J.B., Miller, J.D. (1993). Precise U-Pb ages of Duluth Complex and related mafic intrusions, northeastern Minnesota: Geochronological insights to physical, petrogenetic, paleomagnetic, and tectonomagmatic processes associated with the 1.1 Ga mid-continent rift system. *Journal of Geophysical Research* **98**, 13997–14013.

Patridge, K.A. (2009). Geochemistry and petrogenesis of John Day Ash Flows near Prineville, Oregon [Masters thesis]: Washington State University, 149 p.

Pearce, J.A. (1983). The role of sub-continental Lithosphere in magma genesis at destructive plate boundaries, *in* Hawkesworth, C.J., and Norry, M.J., ed., Continental basalts and mantle xenoliths, Nantwich, Cheshire. *Shiva Publications*, 230–249.

Reagan, M.K., Sims, K.W., Erich, J., Thomas, R.B., Cheng, H., Edwards, R.L., Layne, G., Ball, L. (2003). Time-scales of differentiation from mafic parents to rhyolite in north American continental arcs. *Journal of Petro*logy **44**, 1703–1726.

Retallack, G.J., Bestland, E.A., Fremd, T.J. (2000). Eocene and Oligocene paleosols of central Oregon. *Geological Society of America Special Paper* **344**, 192.

Retallack, G.J., Orr, W.N., Prothero, D.R., Duncan, R.A., Kester, P.R., Ambers, C.P. (2004). Eocene-Oligocene extinction and paleoclimate change near Eugene, Oregon. *Geological Society of America Bulletin* **116**, 817–839.

Robinson, P.T., Walker, G.W., McKee, E.H. (1990). Eocene(?), Oligocene and lower Miocene rocks of the Blue Mountains region, *in* Walker, G.W., ed., Geology of the Blue Mountains region of Oregon, Idaho, and Washington. *U.S. Geological Survey Professional Paper* **1437**, 29–62.

Seton, M., Muller, R.D., Zahirovic, S., Gaina, C., Torsvik, T., Shephard, G., Talsma, A., Gurnis, M., Turner, M., Maus, S., Chandler, M. (2012). Global continental and ocean basin reconstructions since 200 Ma. *Earth-Sci. Reviews* **113**, 212–270.

Sevigny, J.H., Brown, E.H. (1989). Geochemistry and tectonic interpretation of some metavolcanic rock units of the western north Cascades, Washington. *Geological Society of America Bulletin* **101**, 391–400.

Sisson, T.W., Kimura, J.I., Coombs, M.L. (2009). Basanite-nephelinite suite from early Kilauea: Carbonated melts of phlogopite-garnet peridotite at Hawaii's leading magmatic edge. *Contributions to Mineralogy and Petrology* **158**, 803–829.

Sisson, T.W., Lipman, P.W., Naka, J. (2002). Submarine alkali through tholeiitic shield-stage development of Kilauea Volcano, Hawai'i. *Hawaiian Volcanoes: Deep Underwater Perspectives*, 193–219.

Smith, D.R., Leeman, W.P. (1987). Petrogenesis of Mount St. Helens dacitic magmas. *Journal of Geophysical Research* **B92**, 10313–10334.

Smith, G.A. (1986a). Stratigraphy, sedimentology, and petrology of Neogene rocks in the Deschutes Basin, central Oregon: A record of continental margin volcanism [Doctoral thesis]: Oregon State University, 467 p.

Smith, G.A., Manchester, S.R., Ashwill, M., McIntosh, W.C., Conrey, R.M. (1998). Late Eocene-early Oligocene tectonism, volcanism, and florisitic change near Gray Butte, central Oregon. *Geological Society of America Bulletin* **110**, 759–778.

Söderlund, U., Patchett, P.J., Vervoort, J.D., Isachsen, C.E. (2004). The ^{176}Lu decay constant determined by Lu-Hf and U-Pb isotope systematics of Precambrian mafic intrusions. *Earth and Planetary Science Letters* **219**, 311–324.

Sun, S.S., McDonough, W.F. (1989). Chemical and isotopic systematics of oceanic basalts: Implications for mantle composition and processes. *Geologic Society of London* **42**, 313–345.

Tepper, J.H., Nelson, B.K., Bergantz, G.W., Irving, A.J. (1993). Petrology of the Chiiliwack Batholith, North Cascades, Washington: Generation of calc-alkaline granitoids by melting of mafic lower crust with variable water fugacity. *Contributions to Mineralogy and Petrology* **113**, 333-351.

Thormahlen, D. (1984). Geology of the northwest quarter of the Prineville quadrangle [Masters thesis]: Oregon State University, 116 p.

Van der Zander, I., Sinton, J.M., Mahoney, J.J. (2010). Late shield-stage silicic magmatism at Wai 'anae Volcano: Evidence for hydrous crustal melting in Hawaiian Volcanoes. *Journal of Petrology* **51**, 671–701.

Walker, G.W. (1977). Geologic map of Oregon east of the 121st meridian. *U.S. Geological Survey Map* I-902, scale 1:500,000.

Watts, K., Bindeman, I., Schmitt, A. (2011). Large-volume rhyolite genesis in caldera complexes of the Snake River Plain: Insights from the Kilgore Tuff of the Heise Volcanic Field, Idaho, with comparison to Yellowstone and Bruneau-Jarbidge rhyolites. *Journal of Petrology* **52**, 1–34.

Weidenheim, J.P. (1981). The petrography, structure, and stratigraphy of Powell Buttes, Crook County, central Oregon [Masters thesis]: Oregon State University, 95 p.

Wells, R., Bukry, D., Friedman, R. Pyle, D., Duncan, R., Haeussler, P., Wooden, J. (2014). Geologic history of Siletzia, a large igneous province in the Oregon and Washington Coast Range – Correlation to the geomagnetic polarity timescale and implications for a long-lived Yellowstone Hot Spot. *Geosphere* **10**, 692–719.

Wells, R.E., Weaver, C.S., Blakely, R.J. (1998). Fore-arc migration in Cascadia and its neotectonic significance. *Geology* **26**, 759–762.

Woodhead, J.D., Hergt, J.M. (2005). A preliminary appraisal of seven natural zircon reference materials for *In Situ* Hf isotope determination. *Geostandards and Geoanalytic Research* **29**, 183–195.

Xu, G., Frey, F.A., Clague, D.A., Abouchami, W., Blichert-Toft, J., Cousens, B., Weisler, M. (2007). Geochemical characteristics of west Molokai shield-and postshield-stage lavas: Constraints on Hawaiian plume models. *Geochemistry Geophysics, Geosystems* **8**, 1–40.

Xu, G., Frey, F.A., Clague, D.A, Weis, D., Beeson, M.H. (2005). East Molokai and other Kea-trend volcanoes: Magmatic processes and sources as they migrate away from the Hawaiian Hot Spot. *Geochemistry Geophysics Geosystems* **6**, 1–28.

APPENDIX C

CHAPTER IV SUPPLEMENTARY FIGURES

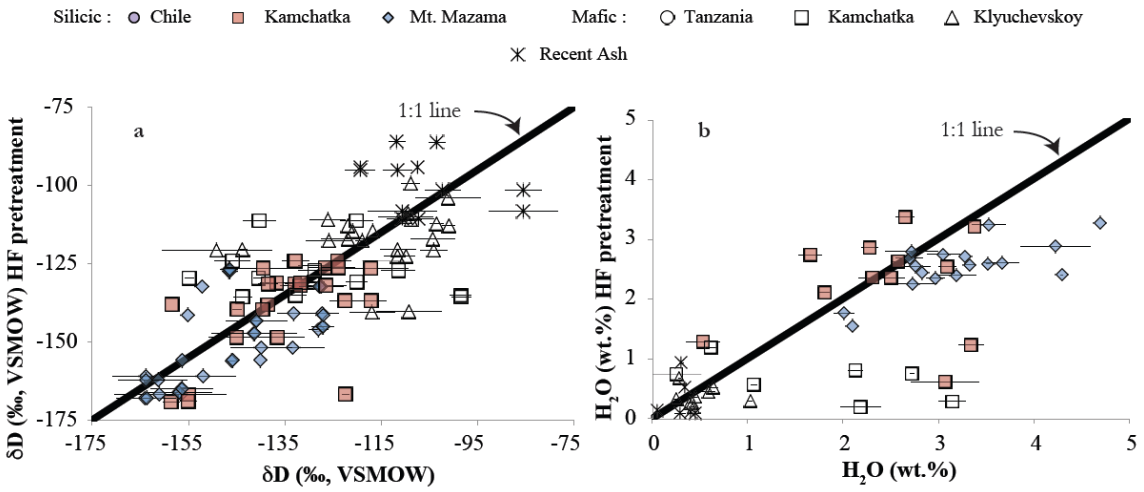

Figure A1. Testing of sample preparation techniques, showing the results of pretreating samples with 8% HF twice for 10 seconds (Y-axis) (e.g. Cassel et al., 2012), versus with a water sonication pretreatment for ~45 minutes (X-axis). Similar to results from Dettinger and Quade (2015), our results illustrate random changes in H_2O_t (wt.%) and δD (‰) from the 8% HF pretreatment.

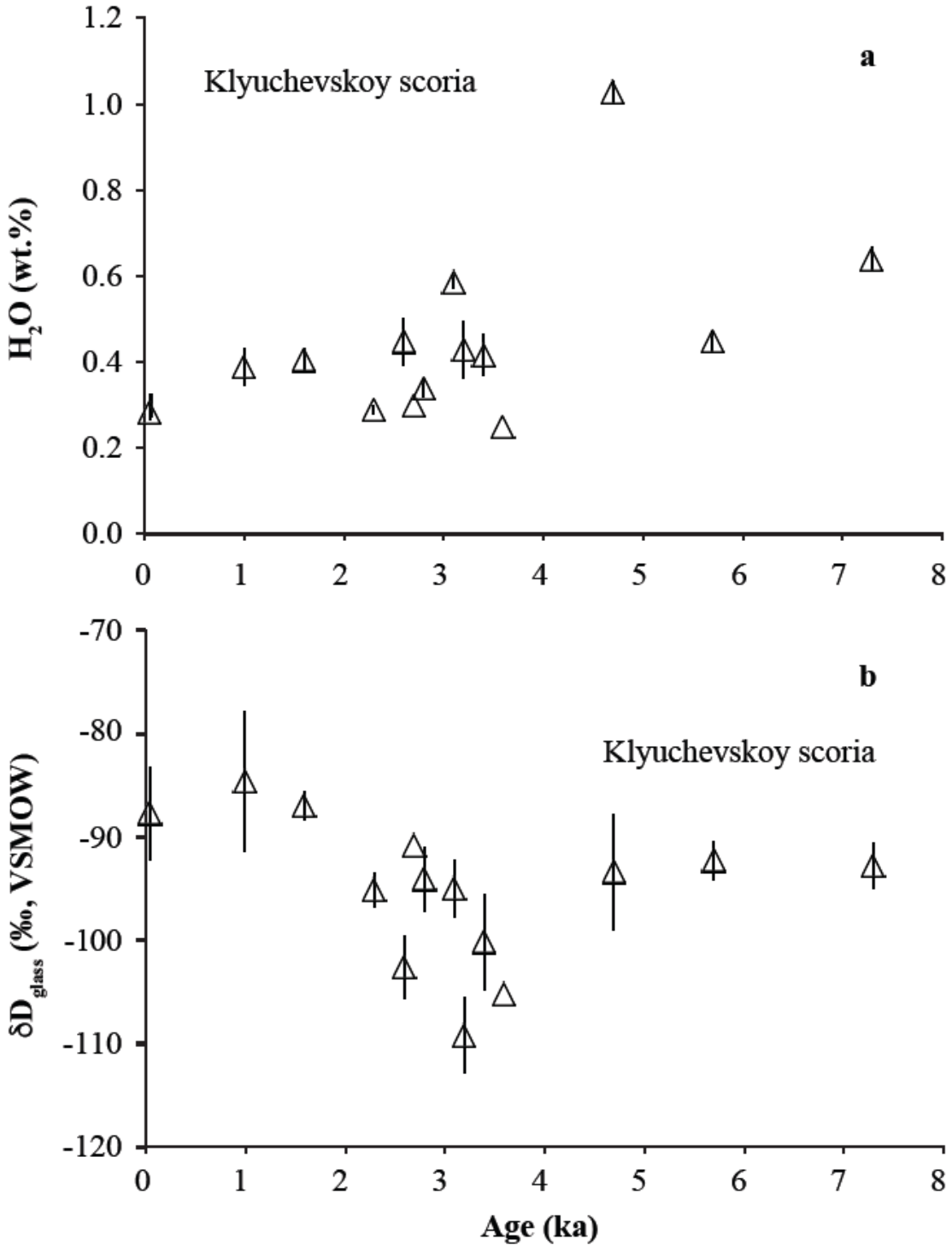

Figure A2. Graphs similar to Fig. 8, but with a zoom in view of the Klyuchevskoy scoria, which have a smaller range in wt.% H_2O_t and δD (‰).

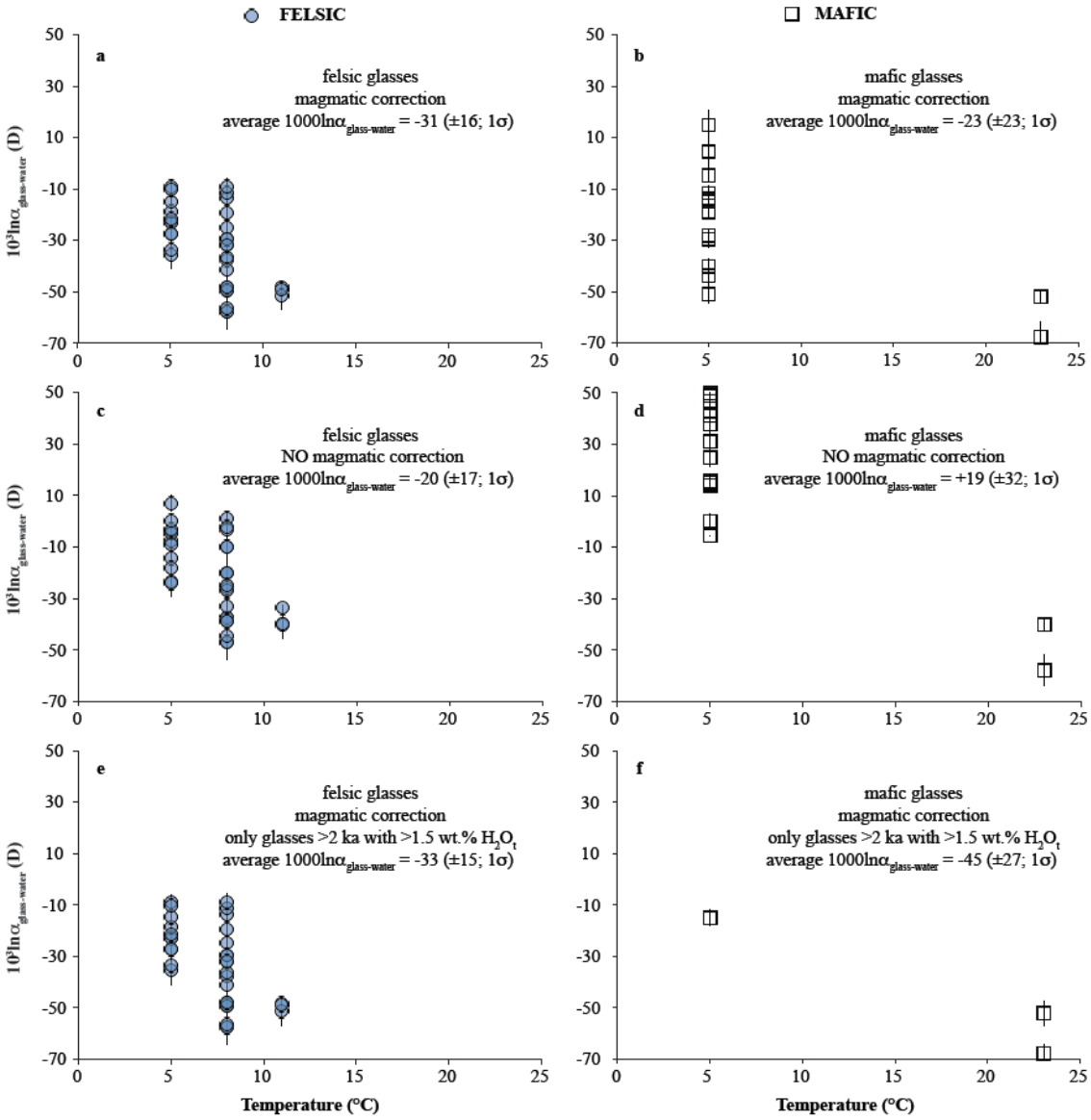

Figure A3. Average $10^3 \ln\alpha_{glass\text{-}water}$ determined at each subset of data, for both mafic and silicic glasses, at the mean annual temperature for each sample location.

Appendix C References Cited

Cassel, E.J., Graham, S.A., Chamberlain, C.P., Henry C.D. (2012) Early Cenozoic topography, morphology, and tectonics of the northern Sierra Nevada and western Basin and Range. *Geosphere* **8**, 229–249.

Dettinger, M.P., Quade, J. (2015) Testing the analytical protocols and calibration of volcanic glass for the reconstruction of hydrogen isotopes in paleoprecipitation. In *Geodynamics of a Cordilleran Orogenic System: The Central Andes of Argentina and Northern Chile* (eds. P.G. DeCelles, M.N. Ducea, B. Carrapa, P.A. Kapp), Geological Society of America **212**, 261–276.

APPENDIX D

CHAPTER V SUPPLEMENTARY FIGURES AND CITATIONS

Figure 1. Photograph of sample 2015Sel-MSH-1 (May 18) as collected in the field.

Figure 2. Photograph of sample 2015Sel-MSH-7 (June 12) as collected in the field. This is the more friable and weathered sample from June 12, as compared to 2015 Sel-MSH-8 (below).

Figure 3. Photograph of sample 2015Sel-MSH-8 (June 12) as collected in the field. This is the heartier and less weathered sample from June 12, as compared to 2015 Sel-MSH-7 (above).

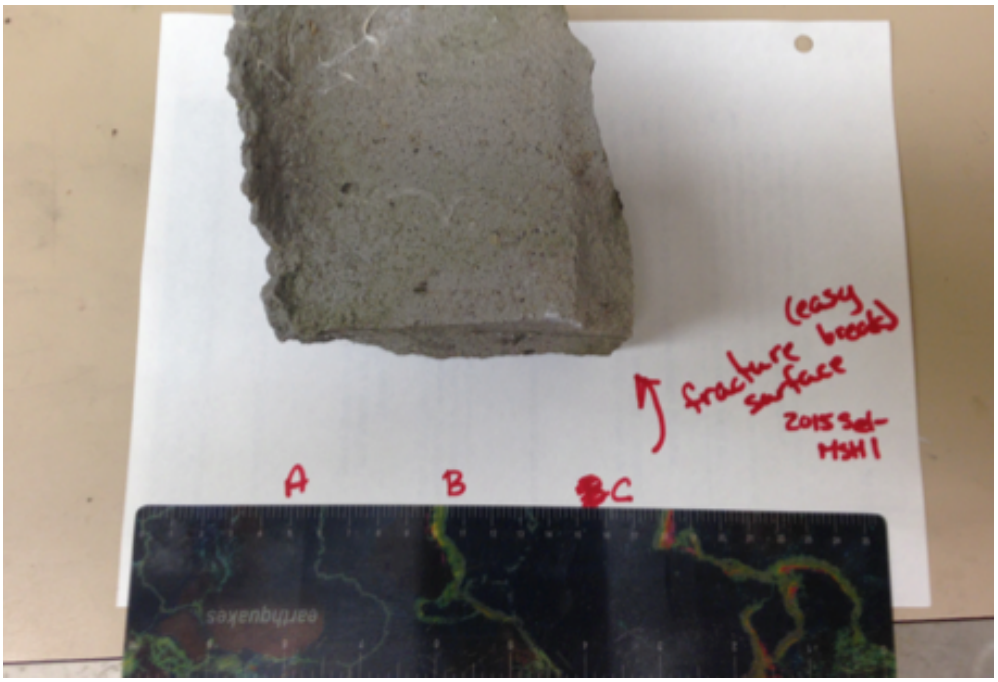

Figure 4. Photograph of sample 2015Sel-MSH-1 (May 18) showing the locations where samples A, B, and C were collected.

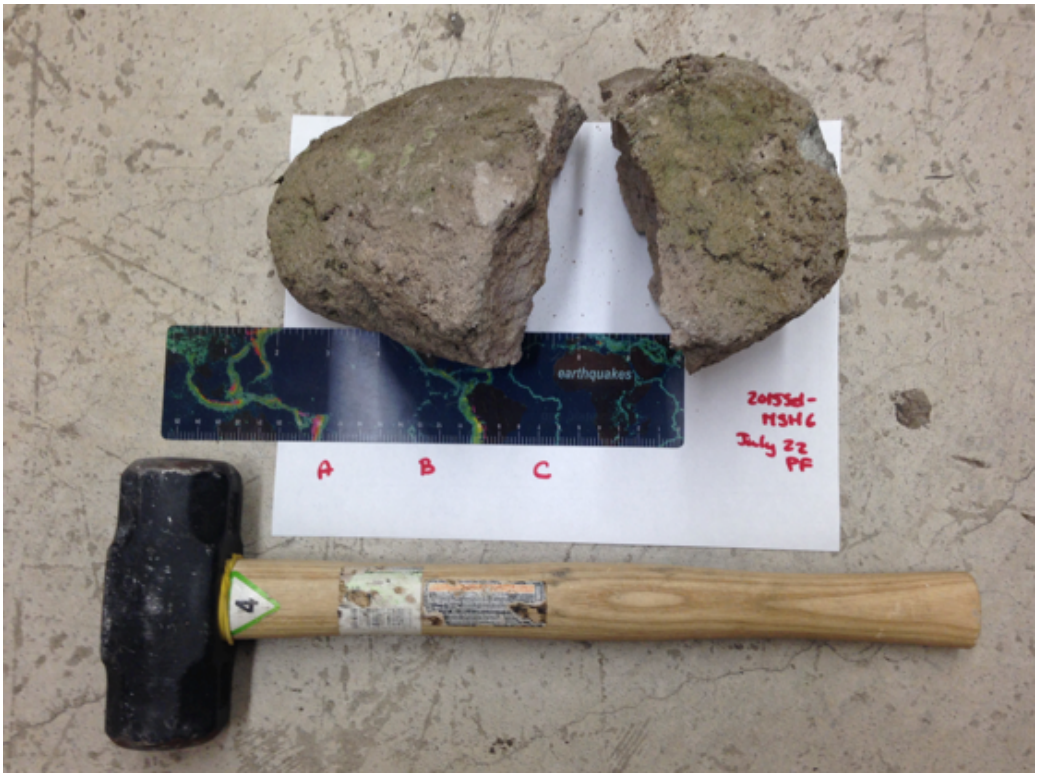

Figure 5. Photograph of sample 2015Sel-MSH-6 (July 22) showing the locations where samples A, B, and C were collected.

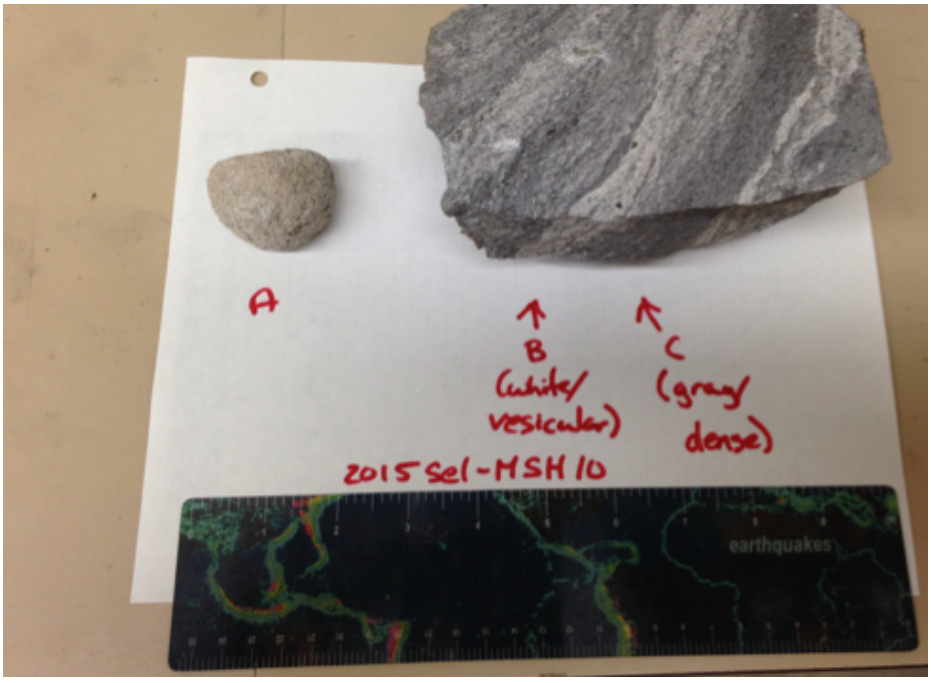

Figure 6. Photograph of sample 2015Sel-MSH-10 (June 12) showing the locations where samples A (pumice clast), B (frothy, more vesicular region), and C (dark gray, more dense region) were collected.

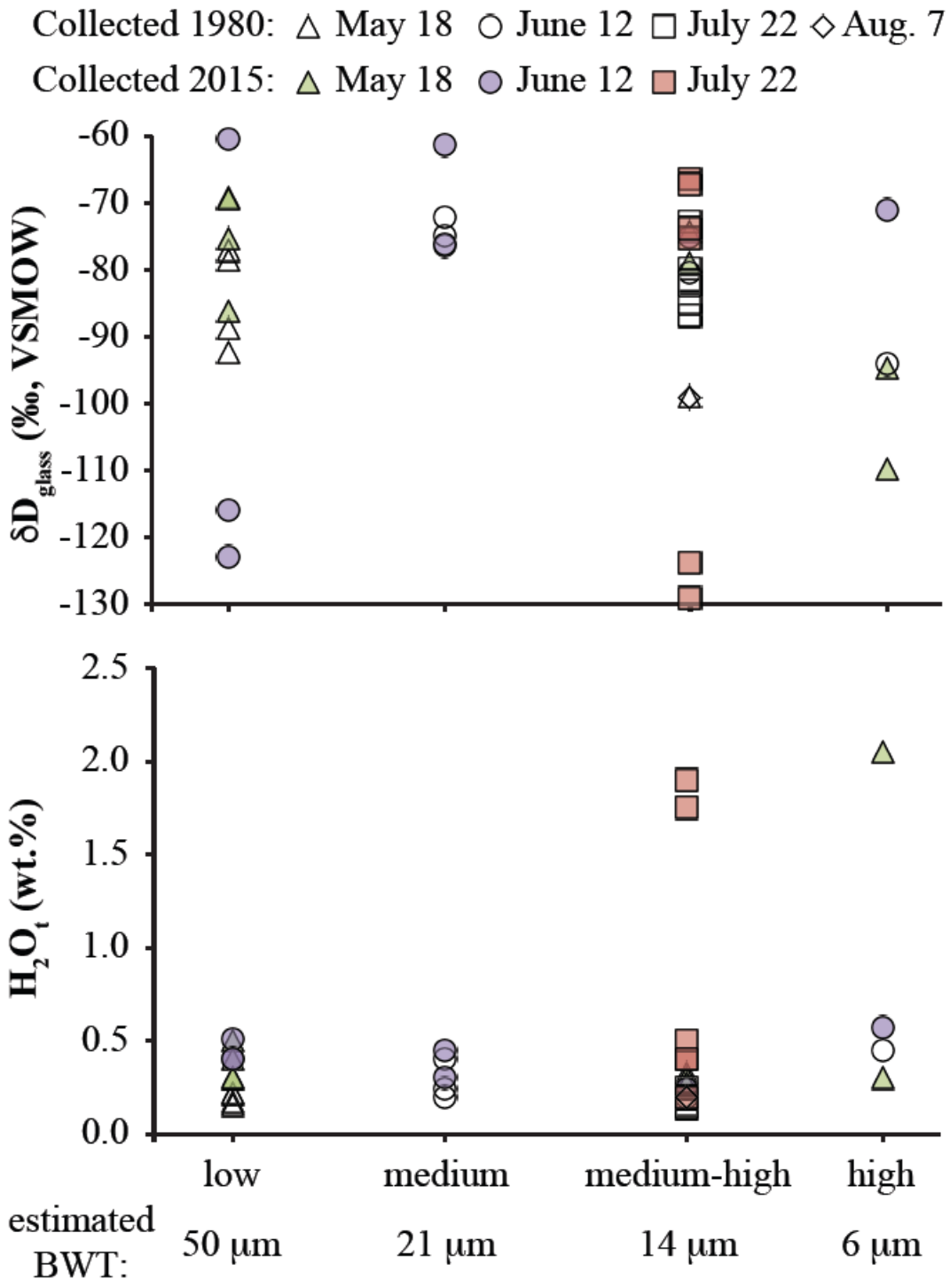

Figure 7. δD_{glass} and H_2O_t relative to the relative vesicularity of the different units collected in 1980 and 2015. As is shown here, there are no significant δD trends in relation to the relative vesicularity of the tephra clasts. Although most of the water concentrations are below 0.6 wt.%, the only higher wt.% water glasses have higher vesicularities. Estimated BWT (bubble wall thickness) is from Cashman and McConnel (2005).

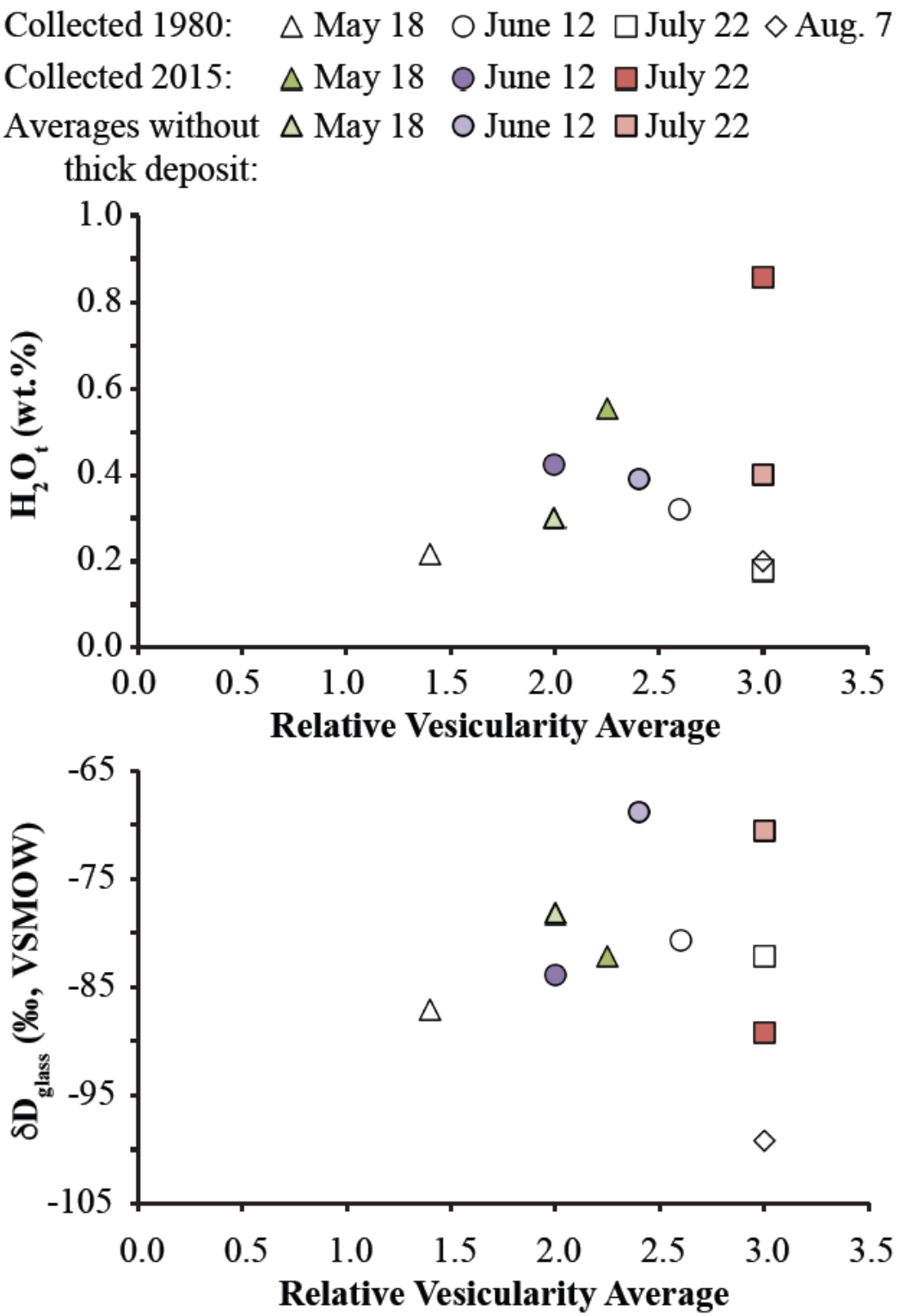

Figure 8. Average δD_{glass} and H_2O_t in relation to the relative vesicularity of the different units collected in 1980 and 2015. As is shown here, there is a clear increase in the wt.% H_2O_t with an increase in relative vesicularity. However the trend in δD is not as clear.

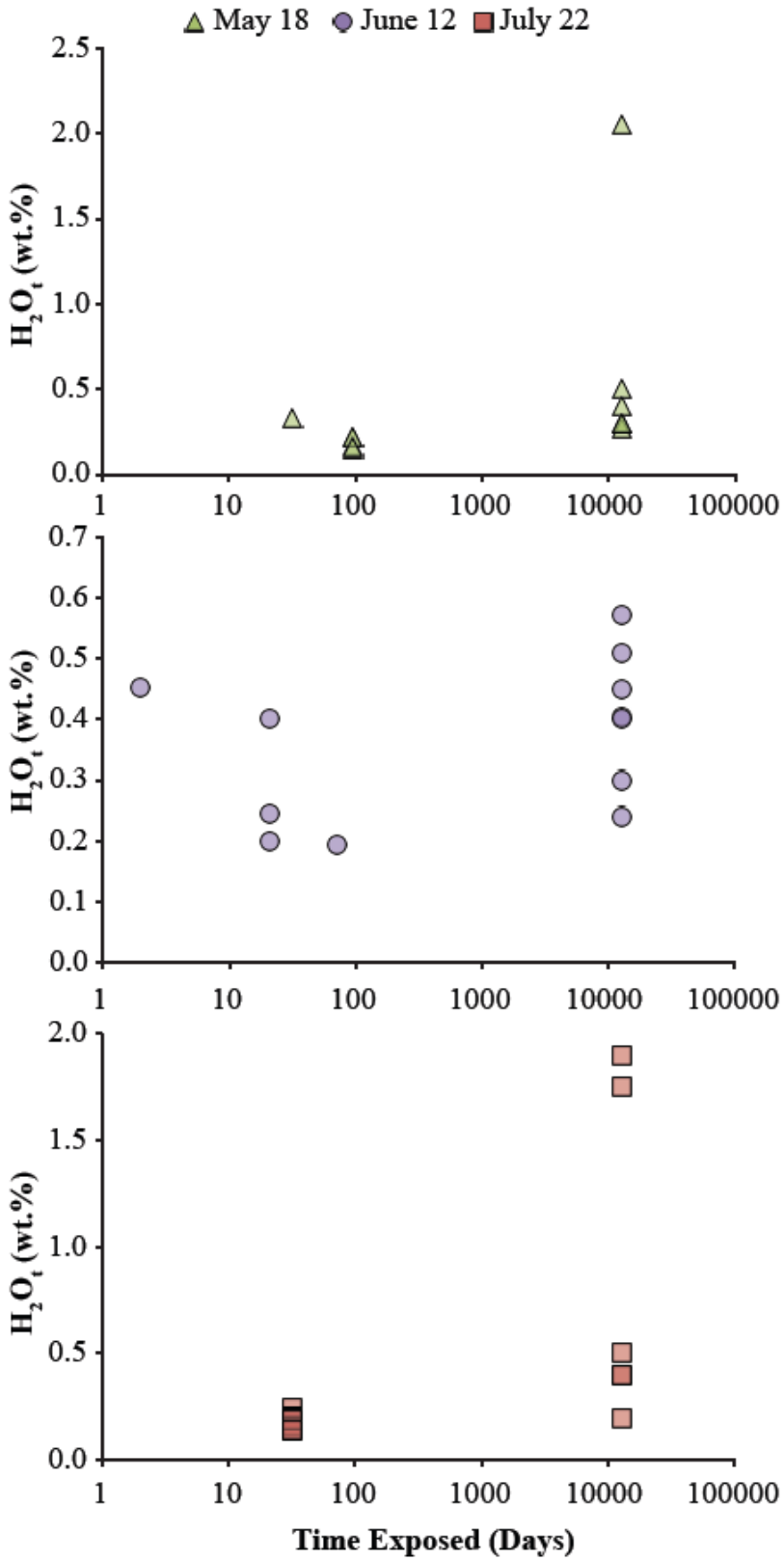

Figure 9. H_2O_t in relation to the days the tephra was left on Earth's surface prior to collection.

Appendix D References Cited

Cashman, K.V., McConnell, S.M. (2005). Multiple levels of magma storage during the 1980 summer eruptions of Mount St. Helens, WA. *Bulletin of Volcanology* **68**, 57–75.

REFERENCES CITED

Chapter I

Atherton, M.P.& Petford, N. (1993). Generation of sodium-rich magmas from newly underplated basaltic crust. *Nature* **362**, 144–146.

Canavan, R.R., Carrapa, B., Clementz, M.T., Quade, J., DeCelles, P.G., Schenbohm, L.M. (2014). Early Cenozoic uplift of the Puna Plateau, Central Andes, based on stable isotope paleoaltimetry of hydrated volcanic glass. *Geology* **42**, 447–450.

Cassel, E.J., Breecker, D.O., Henry, C.D., Larson, T.E., Stockli, D.F. (2014). Profile of a paleo-orogen: High topography across the present-day Basin and Range from 40 to 23 Ma. *Geology* **42**(11), 1007–1010.

Chappell, B.W. & White, J.R. (2001). Two contrasting granite types: 25 years later. *Australian Journal of Earth Sciences* **48**, 489–499.

Friedman, I., Gleason, J., Warden, A. (1993). Ancient climate from deuterium content of water in volcanic glass. *Geophysical Monograph* **78**, 309–319.

Gill, J. (1981). *Orogenic Andesites and Plate Tectonics*. Springer-Verlag: New York.

Grove, T.L. & Kinzler, R.J. (1986). Petrogenesis of andesites. *Annual Review of Earth and Planetary Sciences* **14**, 417–454.

Grove, T.L., Parman, S.W., Bowring, S.A., Price, R.C. & Baker, M.B. (2002). The role of an H_2O-rich fluid component in the generation of primitive basaltic andesites and andesites from Mt. Shasta region, N California. *Contributions to Mineralogy and Petrology* **142**, 375–396.

Grove, T.L., Elkins-Tanton, L.T., Parman, S.W., Chatterjee, N., Müntener, O. & Gaetani, G.A. (2003). Fractional crystallisation and mantle-melting controls on calc-alkaline differentiation trends. *Contributions to Mineralogy and Petrology* **145**, 515–533.

Izbekov, P., Gardner, J.E. & Eichelberger, J.C. (2004). Comagmatic granophrye and dacite from Karymsky volcanic center, Kamchatka; Experimental constraints and magma storage conditions. *Journal of Volcanology and Geothermal Research* **131**, 1–18.

Mulch, A., Sarna-Wojcicki, A.M., Perkins, M.E., Chamberlain, C.P. (2007). A Miocene to Pleistocene climate and elevation record of the Sierra Nevada (California). *Proceedings of the National Academy of Sciences* **105**(19), 6819–6824.

Müntener, O., Kelemen, P.B. & Grove, T.L. (2001). The role of H_2O during crystallisation of primitive arc magmas under upper-most mantle conditions and genesis of igneous pyroxenites: An experimental study. *Contributions to Mineralogy and Petrology* **141**, 643–658.

Musselwhite, D.S., De Paolo, D.J. & McCurry, M. (1989). The evolution of a silicic magma system —isotopic and chemical evidence from the Woods Mountains Volcanic Center, Eastern California. *Contributions to Mineralogy and Petrology* **101**, 19–29.

Nolan, G.S., Bindeman, I.N. (2013). Experimental investigation of rates and mechanisms of isotope exchange (O, H) between volcanic ash and isotopically-labeled water. *Geochimica et Cosmochimica Acta* **111**, 5–27.

Petford, N. & Atherton, M. (1996). Na-rich partial melts from newly underplated basaltic crust: The Cordillera Blanca Batholith, Peru. *Journal of Petrology* **37**, 1491–1521.

Rapp, R.P. & Watson, E.B. (1995) Dehydration melting of metabasalt at 8–32kbar: Implications for continental growth and crust–mantle recycling. *Journal of Petrology* **36**, 891–931.

Riciputi, L.R., Elam, J.M., Anovitz, L.M., Cole, D.R. (2002). Obsidian diffusion dating by Secondary Ion Mass Spectrometry: A test using results from Mound 65, Chalco, Mexico. *Journal of Archaeological Science* **29**(10), 1055–1075.

Rogers, G. & Hawkesworth, C.J. (1989). A geochemical traverse across the North Chilean Andes: Evidence for crust generation from the mantle wedge. *Earth and Planetary Science Letters* **91**, 271–285.

Smith, D.R. & Leeman, W.P. (1987). Petrogenesis of Mount St. Helens dacitic magmas. *Journal of Geophysical Research* **92**, 10313–10334.

Tepper, J.H., Nelson, B.K., Bergantz, G.W. & Irving, A.J. (1993). Petrology of the Chiilwack batholith, North Cascades, Washington. Generation of calc-alkaline granitoids by melting of mafic lower crust with variable water fugacity. *Contributions to Mineralogy and Petrology* **113**, 333–351.

Chapter II

Annen, C., Blundy, J.D. & Sparks, R.S. (2006). The genesis of intermediate and silicic magmas in deep crustal hot zones. *Journal of Petrology* **47**, 505–539.

Asimow P.D. & Ghiorso M.S. (1998). Algorithmic modifications extending MELTS to calculate subsolidus phase relations. *American Mineralogist* **83**, 1127–1131.

Atherton, M.P.& Petford, N. (1993). Generation of sodium-rich magmas from newly underplated basaltic crust. *Nature* **362**, 144–146.

Baboshina, V.A., Tereshchenkov, A.A. & Kharakhinov, V.V. (2000). Tectonic map of the sea of Okhotsk region. *Institute of the Lithosphere of Marginal Seas, Russian Academy of Sciences*, Scale 1:6,500,000, 1 sheet.

Balesta, S.T. (1991). Earth crust structure and magma chambers of the areas of present Kamchatka volcanism. In: Fedotov, S.A. & Masurenkov, Y.P. (eds) *Active volcanoes of Kamchatka*: Nauka, 36–45.

Barr, L.D. & Clark, C.D. (2012). Late Quaternary glaciations in far NE Russia; combining moraines, topography and chronology to assess regional and global glaciation synchrony. *Quaternary Science Reviews* **53**, 72–87.

Basaltic Volcanism Study Project. (1981). Basaltic volcanism on the terrestrial planets. *Pergamon Press, Inc., New York*. 1286 pp.

Bergantz, G.W. & Breidenthal, R.E. (2001). Non-stationary entrainment and tunneling eruptions: A dynamic link between eruption processes and magma mixing. *Geophysical Research Letters* **28**, 3075–3078.

Bindeman, I.N., Davis, A., & Drake, M. (1998). Ion microprobe study of plagioclase-basalt partition experiments at natural concentration levels of trace elements. *Geochimica et Cosmochimica Acta* **62**, 1175–1193.

Bindeman, I. (2008). Oxygen isotopes in mantle and crustal magmas as revealed by single crystal analysis. *Reviews in Mineralogy & Geochemistry* **69**, 445–478.

Bindeman, I.N., Valley, J., Wooden, J. & Persing, H. (2001). Post-caldera volcanism: in situ measurement of U-Pb age and oxygen isotope ratio in Pleistocene zircons from Yellowstone caldera. *Earth and Planetary Science Letters* **189**, 197–206.

Bindeman, I.N., Vinogradov, V.I., Valley, J.W., Wooden, J.L. & Natal'in, B.A. (2002). Archean protolith and accretion of crust in Kamchatka: SHRIMP dating of zircons from Sredinny and Ganal Massifs. *Journal of Geology* **110**, 271–289.

Bindeman, I.N., Ponomareva, V., Bailey, J. & Valley, J. (2004). Volcanic arc of Kamchatka: A province with high $\delta^{18}O$ magma sources and large-scale $^{18}O/^{16}O$ depletion of the upper crust. *Geochimica et Cosmochimica Acta* **68**, 841–865.

Bindeman, I.N., Fu, B., Kita, N. T. & Valley, J. W. (2007). Origin and evolution of Yellowstone silicic magmatism based on ion microprobe analysis of isotopically zoned zircons. *Journal of Petrology* **49**, 163–193.

Bindeman, I.N., Leonov, V.L., Izbekov, P.E., Ponomareva, V.V., Watts, K.E., Shipley, N.K., Perepelov, A.B., Bazanova, L.I., Jicha, B.R., Singer, B.S., Schmitt, A.K., Portnyagin, M.V. & Chen, C.H. (2010). Large-volume silicic volcanism in Kamchatka: Ar-Ar and U-Pb ages, isotopic, and geochemical characteristics of major pre-Holocene caldera-forming eruptions. *Journal of Volcanology and Geothermal Research* **189**, 57–80.

Bohrson, W.A. & Spera, F.J. (2001). Energy-constrained open-system magmatic processes II: Application of energy-constrained assimilation-fractional crystallization (EC-AFC) model to magmatic systems. *Journal of Petrology* **42**, 1019–1041.

Braitseva, O.A., Melekestsev, I.V., Ponomareva, V.V. & Sulerzhisky, L.D. (1995). Ages of calderas, large explosive craters and active volcanoes in the Kuril-Kamchatka region, Russia. *Bulletin of Volcanology* **57**, 383–402.

Brophy J.G. (1991). Composition gaps, critical crystallinity, and fractional crystallization in orogenic (calc-alkaline) magmatic systems. *Contributions to Mineralogy and Petrology* **109**, 173–182.

Chappell, B.W. & White, J.R. (2001). Two contrasting granite types: 25 years later. *Australian Journal of Earth Sciences* **48**, 489–499.

Chashchin, A. (1999). Ignimbrites of Gorely Volcano, southern Kamchatka: Composition and conditions of formation. *Tr. Dal'nevost. Gos. Tekhn. Univ* **121**, 142–148.

Chashchin, A.A., Martynov, Y.A., Perepelov, A.B., Ekimova, N.I., Vladimirova, T.P. (2011). Physical and chemical conditions of the formation and evolution of Late Pleistocene–Holocene magmas of the Gorely and Mutnovsky volcanoes, southern Kamchatka. Russian Journal of Pacific Geology 5, 348–367.

Chayes F. (1963). Relative abundance of intermediate members of the oceanic basalt-trachyte association. *Journal of Geophysical Research* **68**, 1519–1534.

Chiba H., Chacko, T., Clayton, R. & Goldsmith, J. (1989). Oxygen isotope fractionations involving diopside, forsterite, magnetite, and calcite: Application to geothermometry. *Geochimica et Cosmochimica Acta* **53** 2985–2995.

Christiansen, R.L. & Yeats, R.L. (1992). Post-Laramide geology of the U.S. Cordilleran region. In Burchfiel, B.C., Lipman, P.W., Zoback, M.L., (eds), *The Cordilleran Orogen: Conterminous U.S.* **G-3**, 261–406.

Churikova, T.G., Dorendorf, F., Barman, T.R. (2001). Sources and fluids in the mantle wedge below Kamchatka, evidence from across-arc geochemical variation. *Journal of Petrol*ogy **42**, 1567–1593.

Czuppon, G., Lukács, R., Harangi, S., Mason, P., Ntaflos, T. (2012). Mixing of crystal mushes and melts in the genesis of the Bogács Ignimbrite suite, northern Hungary: An integrated geochemical investigation of mineral phases and glasses. *Lithos* **148**, 71–85.

Daly R.A. (1925). The geology of Ascension Island. *American Academy of Arts and Sciences Proceedings* **60**, 1–80.

Deering, C., Bachmann, O., Dufek, J., Gravley, D. (2011). Rift-related transition from andesite to rhyolite volcanism in the Taupo Volcanic Zone (New Zealand) controlled by crystal-melt dynamics in mush zones with variable mineral assemblages. *Journal of Petrology* **52**, 2243–2263.

Deering, D., Vogel, T., Patino, L., Szymanski, D., Alvarado, G. (2012). Magmatic processes that generate chemically distinct silicic magmas in NW Costa Rica and

the evolution of juvenile continental crust in oceanic arcs. *Contributions to Mineralogy and Petrology* **163**, 259–275.

Dorendorf, F., Wiechert, U.H., Wörner, G. (2000). Hydrated sub-arc mantle: A source for the Kluchevskoy volcano, Kamchatka/Russia. *Earth and Planetary Science Letters* **175**, 69–86.

Druitt, T.H., Costa, F., Deloule, E. & Scaillet, B. (2012). Decadal to monthly timescales of magma transfer and reservoir growth at a caldera volcano. *Nature* **482**, 77–82.

Duggen, S., Portnyagin, M.V., Baker, J.A., Ulfbeck, D.G., Hoernle, K.A., Garbe-Schonber, D. & Grassineau, N. (2007). Drastic shift in lava geochemistry in the volcanic-front to rear-arc region of the southern Kamchatkan subduction zone: Evidence for the transition from slab surface dehydration to sediment melting. *Geochimica et Cosmochimica Acta* **71**, 452–480.

Dungan, M.A. & Davidson, J. (2004). Partial assimilative recycling of the mafic plutonic roots of arc volcanoes: An example from the Chilean Andes. *Geology* **32**, 773–776.

Elkins Tanton, L. & Hager, B. (2000). Melt intrusion as a trigger for lithospheric foundering and the eruption of the Siberian flood basalts. *Geophysical Research Letters* **27**, 3937–3940.

Erlich, E.N. & Gorshkov, G.S. (1979). Quaternary volcanism and tectonics in Kamchatka. *Bulletin of Volcanology* **42**, 13–43.

Ewart, A. & Griffin, W. (1994). Application of proton-microprobe data to trace-element partitioning in volcanic-rocks. *Chemical Geology* **117**, 251–284.

Folkes, C.B., de Silva, S.L., Bindeman, I.N., Cas, R. (2013). Tectonic and climate history influence the geochemistry of large-volume silicic magmas: new $\delta^{18}O$ data from the Central Andes with comparison to N America and Kamchatka. *Journal of Volcanology and Geothermal Research* **262**, 90–102.

Gavrilenko, M., Ozerov, A., Kyle, P., Herzberg, C., Carr, M., & Nikulin, A. (in press). Constraints on magma evolution at Gorely volcano, Kamchatka: mantle lithology, fractional crystallization and mixing. *Bulletin of Volcanology*.

Geyer, A. & Bindeman, I. (2011). Glacial influence on caldera-forming eruptions. *Journal of Volcanology and Geothermal Research* **202**, 127–142.

Ghiorso, M., Sack, R.O. (1995). Chemical Mass Transfer in Magmatic Processes. IV. A Revised and Internally Consistent Thermodynamic Model for the Interpolation and Extrapolation of Liquid-Solid Equilibria in Magmatic Systems at Elevated Temperatures and Pressures. *Contributions to Mineralogy and Petrology* **119**, 197–212.

Gill, J. (1981). *Orogenic Andesites and Plate Tectonics*. Springer-Verlag: New York.

Gavrilenko, M. & Ozerov, A. (2010). Geochemical similarities between the pre-caldera and modern evolutionary series of eruptive products from Gorely volcano, Kamchatka. Abstract V21B–2333 presented at 2010 Fall Meeting, AGU.

Gorbatov, A., Kostoglodov, V., Suarez, G. & Gordeev, E. (1997). Seismicity and structure of the Kamchatka subduction zone. *Journal of Geophysical Research* **102**, 17,883–17,898.

Gorbatov, A., Domiguez, J., Suarez, G., Kostoglodov, V. & Gordeev, E. (1999) Tomographic imaging of the P-wave velocity structure beneath the Kamchatka peninsula. *Journal of Geophysical Research* **137**, 269–279.

Gordeev, E.I., Gusev, A.A., Levin, V.E., Bakhtiarov, V.F., Pavlov, V.M., Chebrov, V.N. & Kasahara, M. (2001). Preliminary analysis of deformation at the Eurasia-Pacific-North America plate junction from GPS data. *Geophysical Journal International* **147**, 189–198.

Grove, T.L. & Donnelly-Nolan, J.M. (1986). The evolution of young silicic lavas at Medicine Lake Volcano, California: Implications for the origin of compositional gaps in calc-alkaline series lavas. *Contributions to Mineralogy and Petrology* **92**, 281–302.

Grove T.L., Donnelly-Nolan J.M. & Housh T. (1997). Magmatic processes that generated the rhyolite of Glass Mountain, Medicine Lake volcano, N. California. *Contributions to Mineralogy and Petrology* **127**, 205–223.

Grove, T.L. & Kinzler, R.J. (1986). Petrogenesis of andesites. *Annual Review of Earth and Planetary Sciences* **14**, 417–454.

Grove, T.L., Parman, S.W., Bowring, S.A., Price, R.C. & Baker, M.B. (2002). The role of an H_2O-rich fluid component in the generation of primitive basaltic andesites and andesites from Mt. Shasta region, N California. *Contributions to Mineralogy and Petrology* **142**, 375–396.

Grove, T.L., Elkins-Tanton, L.T., Parman, S.W., Chatterjee, N., Müntener, O. & Gaetani, G.A. (2003). Fractional crystallisation and mantle-melting controls on calc-alkaline differentiation trends. *Contributions to Mineralogy and Petrology* **145**, 515–533.

Hedge, C.E. & Gorshkov, G.S. (1977). Strontium-isotope composition of volcanic rocks from Kamchatka. *Dokl. Akad. Nauk SSSR* **233**, 163–166.

Hildreth, W. & Moorbath, S. (1988). Crustal contribution to arc magmatism in the Andes of Central Chile. *Contributions to Mineralogy and Petrology* **98**, 455–489.

Hochstaedter A., Gill J., Peters R., Broughton P., Holden P. (2001). Across-arc geochemical trends in the Izu-Bonin arc: Contributions from the subducting slab. *Geochemistry Geophysics Geosystems* **2**, Paper number 2000GC000105.

Hochstaedter, A.G., Kepezhinskas, P.K. & Defant, M.J. (1996). Insights into the volcanic arc mantle wedge from magnesian lavas from the Kamchatka Arc. *Journal of Geophysical Research* **B101**, 697–712.

Hourigan, .K., Brandon, M.T., Soloviev, A.V., Kirmasov, A.B., Garver, J.I. & Reiners, P.W. (2009). Eocene arc-continent collision and crustal consolidation in Kamchatka, Russian Far East. *American Journal of Science* **309**, 333–396.

Hughes, G. & Mahood, G.A. (2008). Tectonic controls on the nature of large silicic calderas in volcanic arcs. *Geology* **36**, 627–630.

Humphreys, E. (1995), Post-Laramide removal of the Farallon slab, western United States. *Geology* **23**, 987–990.

Ishikawa, T. & Tera, F. (1997). Source, composition and distribution of the fluid in the Kurile mantle wedge: Constraints from across-arc variations of B/Nb and B isotopes. *Earth and Planetary Science Lett*ers **152**, 123–138.

Ishikawa, T., Tera, F. & Nakazawa, T. (2001). Boron isotope and trace element systematics of the three volcanic zones in the Kamchatka arc. *Geochimica et Cosmochimica Acta* **65**, 4523–4537.

Izbekov, P., Eichelberger, J., Ivanov, B. (2004a). The 1996 eruption of Karymsky volcano, Kamchatka: Historical record of basaltic replenishment of an andesite reservoir. *Journal of Petrology* **45**, 2325–2345.

Izbekov, P., Gardner, J.E. & Eichelberger, J.C. (2004b). Comagmatic granophrye and dacite from Karymsky volcanic center, Kamchatka; Experimental constraints and magma storage conditions. *Journal of Volcanology and Geothermal Research* **131**, 1–18.

Jicha, B.R., Rhodes, J.M., Singer, B.S. & Carcia, M.O. (2012). $^{40}Ar/^{39}Ar$ geochronology of submarine Mauna Loa volcano, Hawaii. *Journal of Geophysical Research* **117**, B09204.

John, D.A., Sisson, T.W., Breit, G.N., Rye, R.O. & Vallance, J.W. (2008). Characteristics, extent and origin of hydrothermal alteration at Mount Rainier Volcano, Cascades Arc, USA: Implications for debris-flow hazards and mineral deposits. *Journal of Volcanology and Geothermal Research* **175**, 289–314.

Johnson, D. M., Hooper, P. R. & Conrey, R. M. (1999). XRF analysis of rocks and minerals for major and trace elements on a single low dilution Li-tetraborate fused bead. *Advances in X-ray Analysis* **41**, 843–867.

Jouzel, J., Lorius, C., Petit, J.R., Genthon, C., Barkov, N.I., Kotlyakov, V.M., Petrov. V.M. (1987). Vostok ice core: a continuous isotope temperature record over the last climatic cycle (160,000 years). *Nature* **329**, 403–8.

Jouzel, J., Barkov, N.I., Barnola, J.M., Bender, M., Chappellaz, J., Genthon, C., Kotlyakov, V.M., Lipenkov, V., Lorius, C., Petit, J.R., Raynaud, D., Raisbeck, G.,

Ritz, C., Sowers, T., Stievenard, M., Yiou, F., Yiou, P. (1993). Extending the Vostok ice-core record of palaeoclimate to the penultimate glacial period. *Nature* **364**, 407–12.

Jouzel, J., Waelbroeck, C., Malaize, B., Bender, M., Petit, J.R., Stievenard, M., Barkov, N.I., Barnola, J.M., King, T., Kotlyakov, V.M., Lipenkov, V., Lorius, C., Raynaud, D., Ritz, C., Sowers. T. (1996). Climatic interpretation of the recently extended Vostok ice records. *Climate Dynamics* **12**, 513–521.

Kepezhinskas, P.K., McDermott, F., Defant, M., Hochstaedter, A.G., Drummond, M.S., Hawkesworth, C.J., Koloskov, A.V., Maury, R.C. & Bellon, H. (1997). Trace element and Sr-Nd-Pb isotopic constraints on a three-component model of Kamchatka Arc petrogenesis. *Geochimica et Cosmochimica Acta* **61**, 577–600.

Kersting, A.B. & Arculus, R.J. (1994). Kamchatka, Russia: The role of high-flux recharged, trapped, and fractionated magma chamber(s) in the genesis of high-Al_2O_3 from high-MgO basalt. *Journal of Petrology* **35**, 1–41.

Kirsanov, I.T. & Melekestev, I.V. (1991). Gorely Volcano. *Active Volcanoes of Kamchatka* **2**, 294–315.

Konstantinovskaya, E.A. (2003). Margins of the east seas: tectonics, structural evolution and geodynamic modeling. *Moscow: Scientific World* **549**, 224 (in Russian).

Kuiper, K.F., Deino, A., Hilgen, F.J., Krijgsman, W., Renne, P.R. & Wijbrans, J.R. (2008). Synchronizing rock clocks of Earth history. *Science* **320**, 500–504.

Lander, A. & Shapiro, M. (2007). The origin of the modern Kamchatka subduction zone. In Eichelberger, J., Gordeev, E., Kasahara, M., Izbekov, P., Lees, J. (eds) *Volcanism and subduction: The Kamchatka region: American Geophysical Union Geophysical Monograph* **172**, 57–64.

Lisiecki, L.E. & Raymo, M.E. (2005). A Pliocene-Pleistocene stack of 57 globally distributed benthic $\delta^{18}O$ records. *Paleocenagraphy* **20**, PA1003.

Marsh B.D. (1981). On the crystallinity, probability of occurrence, and rheology of lava and magma. *Contributions to Mineralogy and Petrology* **78,** 85–98.

Melekhova, E., Annen, C., Blundy, J. (2013). Compositional gaps in igneous rock suites controlled by magma system heat and water content. *Nature Geoscience* **6**, 285–390.

Merle, O., Barde-Cabusson, S., de Vries, B. (2010). Hydrothermal calderas. *Bulletin of Volcanology* **72**, 131–147.

Min, K., Mundil, R., Renne, P. & Ludwig, K. (2000). A test for systematic errors in $^{40}Ar/^{39}Ar$ geochronology through comparison with U/Pb analysis of a 1.1-Ga rhyolite. *Geochimica et Cosmochimica Acta* **64**, 73–98.

Müntener, O., Kelemen, P.B. & Grove, T.L. (2001). The role of H_2O during crystallisation of primitive arc magmas under upper-most mantle conditions and genesis of igneous pyroxenites: An experimental study. *Contributions to Mineralogy and Petrology* **141**, 643–658.

Musselwhite, D.S., De Paolo, D.J. & McCurry, M. (1989). The evolution of a silicic magma system —isotopic and chemical evidence from the Woods Mountains Volcanic Center, Eastern California. *Contributions to Mineralogy and Petrology* **101**, 19–29.

Nagasawa, H. & Schnetzler, C. (1971). Partitioning of rare Earth, alkali, and alkaline Earth elements between phenocrysts and acidic igneous magmas. *Geochimica et Cosmochimica Acta* **35**, 953–968.

Onuma, N., Higuchi, H., Wakita, H., & Nagasaw, H. (1968). Trace element partition between two pyroxenes and the host lava. *Earth and Planetary Science Letters* **5**, 47–51.

Ozerov, A.Yu., Ariskin, A.A., Barmina, G.S. (1995). The problem of genetic relations between high-alumina basalts and high-magnesian basalts of the Klyuchevskoi Volcano, Kamchatka (Trans.). *Doklady Acadamy of Sciences USSR* **350**, 1127–1130.

Petford, N. & Atherton, M. (1996). Na-rich partial melts from newly underplated basaltic crust: The Cordillera Blanca Batholith, Peru. *Journal of Petrology* **37**, 1491–1521.

Petit, J.R., Jouzel, J., Raynaud, D., Barkov, N.I., Barnola, J.M., Basile, I., Bender, M., Chappellaz, J., Davis, M., Delayque, G., Delmotte, M., Kotlyakov, V.M., Legrand, M., Lipenkov, V.Y., Lorius, C., Pepin, L., Ritz, C., Saltzman, E., Stievenard, M. (1999). Climate and atmospheric history of the past 420,000 years from the Vostok ice core, Antarctica. *Nature* **399**, 429–436.

Pineau, F., Semet, M.P., Grassineau, N., Okrugin, V.M. & Javoy, M. (1999). The genesis of stable isotope (O, H) record in arc magmas: The Kamchatkan Case. *Chemical Geology* **153**, 93–124.

Ponomareva, V., Melekestev, I., Braitseva, O., Churikova, T., Pevzner, M., Sulerzhitsky, L. (2007). Late Pleistocene-Holocene volcanism on the Kamchatka Peninsula, Northwest Pacific Region. *Geophysical Monograph Series* **172**, 165–198.

Poplitov, E.I. & Volynets, O.N. (1981). Geochemical characteristics of quaternary volcanism of the Kurile-Kamchatka island arc. *Nauka Publishers* (in Russian).

Putirka, K.D. (2008). Thermometers and Barometers for volcanic systems. *Reviews in Mineralogy and Geochemistry* **69**, 61–120.

Rapp, R.P. & Watson, E.B. (1995) Dehydration melting of metabasalt at 8–32kbar: Implications for continental growth and crust–mantle recycling. *Journal of Petrology* **36**, 891–931.

Reubi, O. & Blundy, J. (2009) A dearth of intermediate melts at subduction zone volcanoes and the petrogenesis of arc andesites. *Nature* **461**, 1269–1273.

Rogers, G. & Hawkesworth, C.J. (1989). A geochemical traverse across the North Chilean Andes: Evidence for crust generation from the mantle wedge. *Earth and Planetary Science Letters* **91**, 271–285.

Rubatto, D. (2002). Zircon trace element geochemistry: Partitioning with garnet and the link between U-Pb ages and metamorphism. *Chemical Geology* **184**, 123–138.

Rudnick, R.L. & Fountain, D.M. (1995). Nature and composition of the continental crust: A lower crustal perspective. *Reviews of Geophysics* **33**, 267–309.

Scholl, D. (2007). Viewing the tectonic evolution of the Kamchatka-Aleutian (KAT) connection with an Alaska crustal extrusion perspective. In Eichelberger, J., Gordeev, E., Kasahara, M., Izbekov, P., Lees, J. (eds) *Volcanism and subduction: The Kamchatka region: American Geophysical Union Geophysical Monograph* **172**, 3–35.

Selyangin, O. (2006). The wonderful world of Mutnovsky and Gorely volcanoes: A guide for volcanologists and travelers. Petropavlovsk-Kamchatsky.

Selyangin, O. & Ponomareva, V. (1999). Structure and evolution of the Gorelovsky volcanic center, southern Kamchatka. *Vulkanol. Seismol* **2**, 3–23.

Sheimovich, V.S. & Karpenko, M.I. (1996). K-Ar volcanism of Southern Kamchatka. *Volcanol. Seismol.* **2**, 86-90.

Shipley, N.K. (2011). Isotopic and petrologic investigation and model of genesis of large-volume high-silica rhyolites in arc environments: Karymshina caldera, Kamchatka, Russia [MA Thesis]: Eugene, Oregon, University of Oregon, 76 pages.

Siebert, L. & Simkin, T. (2002). Volcanoes of the world: An illustrated catalog of Holocene volcanoes and their eruptions: Smithsonian Institution, Global Volcanism Program, Digital Information Series.

Simakin, A. & Bindeman, I.N. (2012). Remelting in caldera and rift environments and the genesis of hot, "recycled" rhyolites. *Earth and Planetary Science Letters* **337–338**, 224–235.

Soloviev, A.V., Shapiro, M.N. & Garver, J.I. (2002a). Lesnaya nappe, northern Kamchatka. *Geotectonics* **36**, 469–482.

Soloviev, A.V., Shapiro, M.N., Garver, J.I., Shcherbinina, E.A. & Kravchenko-Berezhnoy, I.R. (2002b). New age data from the Lesnaya Group: A key to understanding the timing of arc-continent collision, Kamchatka, Russia. *The Island Arc* **11**, 79–90.

Smith, D.R. & Leeman, W.P. (1987). Petrogenesis of Mount St. Helens dacitic magmas. *Journal of Geophysical Research* **92**, 10313–10334.

Sparks, R. & Marshall, L. (1986). Thermal and mechanical constraints on mixing between mafic and silicic magmas. *Journal of Volcanology and Geothermal Research* **29**, 99–124.

Spera, F.J. & Bohrson, W.A. (2001). Energy-constrained open system magmatic processes I: General model and energy-constrained assimilation and fractionation crystallization (EC-AFC) formulation. *Journal of Petrology* **42**, 999–1018.

Steiger, R.H. & Jäger, E. (1977). Subcommission on geochronology: Convention on the use of decay constants in geo- and cosmochronology. *Earth and Planetary Science Letters* **36**, 359–362.

Sun, S.S. & McDonough, W.F. (1989). Chemical and isotopic systematics of oceanic basalts: Implications for mantle composition and processes. *Geological Society of London* **42**, 313–345.

Tatsumi, Y., Kogiso, T., Nohda, S. (1995). Formation of a third volcanic chain in Kamchatka: Generation of unusual subduction-related magmas. *Contributions to Mineralogy and Petrology* **120**, 117–128

Taylor, R.N. & Nesbitt, R.W. (1998). Isotopic characteristics of subduction fluids in an intra-oceanic setting, Izu-Bonin Arc, Japan. *Earth and Planetary Science Letters* **164**, 79–98.

Tepper, J.H., Nelson, B.K., Bergantz, G.W. & Irving, A.J. (1993). Petrology of the Chiilwack batholith, North Cascades, Washington. Generation of calc-alkaline granitoids by melting of mafic lower crust with variable water fugacity. *Contributions to Mineralogy and Petrology* **113**, 333–351.

Thompson, A.B., Matile L. & Ulmer P. (2002). Some thermal constraints on crustal assimilation during fractionation of hydrous, mantle-derived magmas with examples from central Alpine batholiths. *Journal of Petrology* **43**, 403–422.

Tollan, P., Bindeman, I. & Blundy, J. (2012). Cumulate xenoliths from St. Vincent, Lesser Antilles Island Arc: a window into upper crustal differentiation of mantle-derived basalts. *Contributions to Mineralogy and Petrology* **163**, 189–208.

Tolstykh, M.L., Naumov, V.B., Gavrilenko, M.G., Ozerov, A.Y. & Kononkova, N.N. (2012). Chemical composition, volatile components, and trace elements in the

melts of the Gorely Volcanic Center, southern Kamchatka: Evidence from inclusions in minerals. *Geochemistry International* **50**, 522–550.

Tuffen, H. (2010). How will melting of ice affect volcanic hazards in the twenty-first century?. *Philosophical Transactions of The Royal Society A* **368**, 2535–2558.

Turner, S.P., Sims, K.W.W., Reagan, M.K., Cook, C. (2007). A ^{210}Pb-^{226}Ra-^{230}Th-^{238}U study of Klyuchevskoy and Bezymianny volcanoes, Kamchatka. *Geochimica et Cosmochimica Acta* **71**, 4771–4785.

Vinogradov, V.I. (1995) Isotopic evidence of the conversion of oceanic crust to continental crust in the continent-ocean transition zone of Kamchatka. *Geochemistry International* **32**, 70–108.

Vinogradov, V.I. & Vakin (1983). Strontium isotopes of the thermal waters of Kamchatka (Trans.). *Doklady Acadamy of Sciences USSR* **273**, 965–968.

Volynets, O.N., Babanskii, A.D., Gol'tsman, Y. (2000). Variations in isotopic and trace-element composition of lavas from volcanoes of the northern group, Kamchatka, in relation to specific features of subduction. *Geochemistry International* **38**, 974–989.

Walker, J.A., Carr, M.J., Patino, L.C., Johnson, C.M., Feigenson, M.D., Ward, R.L. (1995). Abrupt change in magma generation processes across the Central American arc in southeastern Guatemala: Flux-dominated melting near the base of the wedge to decompression melting near the top of the wedge. *Contributions to Mineralogy and Petrology* **120**, 378–390.

Weismaier, S., Troll, V., Carracedo, J., Ellam, R., Bindeman, I., Wolff, J. (2012). Bimodality of lavas in the Teide-Pico Viejo succession in Tenerife – the role of crustal melting in the origin of recent phonolites. *Journal of Petrology* **53**, 2465–2495.

Chapter III

Atwater, T., Stock, J. (1998). Pacific-North America plate tectonics of the Neogene Southwestern Unites States: An update. *International Geology Review* **40**, 375–402.

Auer, S., Bindeman, I., Wallace, P., Ponomareva, V., Portnyagin, M. (2008). The origin of hydrous, high-d18O voluminous volcanism: diverse oxygen isotope values and high magmatic water contents within the volcanic record of Klyuchevskoy volcano, Kamchatka, Russia. *Contributions to Mineralogy and Petrology* **157**, 209–230.

Bacon, C.R. (1989). Calc-alkaline, shoshonitic, and primitive tholeiitic lavas from monogenetic volcanoes near Crater Lake, Oregon. *Journal of Petrol*ogy **31**, 135-166.

Bacon, C.R., Bruggman, P.E., Christiansen, R.L., Clynne, M.A., Donnelly-Nolan, J.M., Hildreth, W. (1997). Primitive magmas at five Cascade volcanic fields: Melts from hot, heterogeneous sub-arc mantle. *The Canadian Mineralogist* **35**, 397-423.

Bennett, K.M. (2006). Petrogenesis of Pleistocene basalts of the Norris-Mammoth Corridor, Yellowstone National Park [Masters thesis]: University of Nevada, Las Vegas, 124 p.

Bindeman, I.N. (2008). Oxygen isotopes in mantle and crustal magmas as revealed by single crystal analysis. *Reviews in Mineralogy and Geochemistry* **69**, 445–478.

Bindeman, I.N., Leonov, V.L., Izbekov, P.E., Ponomareva, V.V., Watts, K.E., Shipley, N.K., Perepelov, A.B., Bazanova, L.I., Jicha, B.R., Singer, B.S., Schmitt, A.K., Portnyagin, M.V., Chen, C.H. (2010). Large-volume silicic volcanism in Kamchatka: Ar-Ar and U-Pb ages, isotopic, and geochemical characteristic of major pre-Hoocene caldera-forming eruptions. *Journal of Volcanology and Geothermal Research* **189**, 57–80.

Bindeman, I.N., Simakin, A.G. (2014). Rhyolites-Hard to produce, but easy to recycle and sequester: Integrating microgeochemical observations and numerical models. *Geosphere* **10**, 930–957.

Boroughs, S., Wolff, J., Bonnichsen, B., Godchaux, M., Larson, P. (2005). Large-volume, low-$\delta^{18}O$ rhyolites of the central Snake River Plain, Idaho, USA. *Geology* **33**, 821–824.

Burov, E., Guillou-Frottier, L., D'Acremont, E., Le Pourhiet, L., Cloetingh, S. (2007). Plume head-lithosphere interactions near intra-continental plate boundaries. *Tectonophysics* **434**, 15–38.

Camp, V.E., Hanan, B.B. (2008). A plume-triggered delamination origin for the Columbia River Basalt Group. *Geosphere* **4**, 480–495.

Cathey, H., Nash, B., Seligman, A., Valley, J., Kito, N., Allen, C., Campbell, I.H., Vazquez, J., Wooden, J. (2011). Low $\delta^{18}O$ from the Bruneau-Jarbidge eruptive center: A key to crustal anatexis along the track of the Yellowstone hotspot [abs]: *Eos (Transactions, American Geophysical Union)* **92**.

Chorowicz, J. (2005). The East African rift system. *Journal of African Earth Sciences* **43**, 379–410.

Christiansen, E., McCurry, M. (2008). Contrasting origins of Cenozoic silicic volcanic rocks from the western Cordillera of the United States. *Bulletin of Volcanol*ogy **70**, 251–267.

Coble, M.A., Mahood, G.A. (2012). Initial impingement of the Yellowstone plume located by widespread silicic volcanism contemporaneous with Columbia River flood basalts. *Geology* **40**, 655–658.

Darold, A., Humphreys, E. (2013). Upper mantle seismic structure beneath the Pacific Northwest: A plume-triggered delamination origin of the Columbia River flood basalt eruptions. *Earth and Planetary Science Lett*ers **365**, 232–242.

Drew, D., Bindeman, I., Watts, K., Schmitt, A., Fu, B., McCurry, M. (2013). Crustal-scale recycling in caldera complexes and rift zones along the Yellowstone hotspot track: O and Hf isotopic evidence in diverse zircons from voluminous rhyolites of the Picabo volcanic field, Idaho. *Earth and Planetary Science Lett*ers **381**, 63–77.

du Bray, E.A., John, D.A. (2011). Petrologic, tectonic, and metallogenic evolution of the ancestral Cascades magmatic arc, Washington, Oregon, and northern California. *Geosphere* **7**, 1102-1133.

Duncan, R.A. (1982). A captured island chain in the coast range of Oregon and Washington. *Journal of Geophysical Res*earch **87**, 10827–10837.

Elkins-Tanton, L.T. (2005). Continental magmatism caused by lithospheric delamination, *in* Foulger, G.R., Natland, J.H., Presnall, D.C., and Anderson, D.L., ed., Plates, plumes, and paradigms. *Geological Society of America Special Paper* **388**, 449–461.

Elkins-Tanton, L.T., Hager, B.H. (2000). Melt intrusion as a trigger for lithospheric foundering and the eruption of the Siberian flood basalts. *Geophysical Research Lett*ers **27**, 2937–3940.

Ferns, M.L., McClaughry, J.D. (2013). Stratigraphy and volcanic evolution of the middle Miocene to Pliocene La Grande-Owyhee eruptive axis in eastern Oregon, *in* Reidel, S.P., Camp, V.E., Ross, M.E., Wolff, J.A., Martin, B.S., Tolan, T.L., and Wells, R.E., ed., The Columbia River Flood Basalt Province. *Geological Society of America Special Paper* **497**, 401–427.

Fisher, C.M., Vervoort, J.D., DuFrane, S.A. (2014). Accurate Hf isotope determinations of complex zircons using the "laser ablation split stream" method. *Geochemistry Geophysics Geosyst*ems **15**, 1–19.

Gao, H., Humphreys, E., Yao, H., van der Hilst, R. (2011). Crust and lithosphere structure of the northwestern U.S. with ambient noise tomography: Terrane accretion and Cascade arc development. *Earth and Planetary Science Letters* **304**, 202-211.

Gorczyk, W., Hobbs, B., Gerya, T. (2012). Initiation of Rayleigh-Taylor instabilities in intra-cratonic settings. *Tectonophysics* **514–517**, 146–155.

Humphreys, E.D. (1995). Post-Laramide removal of the Farallon slab, western United States. *Geology* **23**, 987–990.

Jicha, B.R., Hart, G.L., Johnson, C.M., Hildreth, W., Beard, B.L., Shirey, S.B., Valley, J.W. (2009). Isotopic and trace element constraints on the petrogenesis of lavas from the Mount Adams volcanic field, Washington. *Contributions to Mineralogy and Petrology* **157**, 189–207.

Johnson, E.R., Wallace, P.J., Granados, H.D., Manea, V.C., Kent, A.J.R., Bindeman, I.N., Donegan, C.S. (2009). Subduction-related volatile recycling and magma generation beneath Central Mexico: Insights from melt inclusions, oxygen isotopes and geodynamic modeling. *Journal of Petrol*ogy **50**, 1729–1764.

Johnston, S.T., Thorkelson, D.J. (2000). Continental flood basalts: Episodic magmatism above long-lived hotspots. *Earth and Planetary Science Letters* **175**, 247–256.

Liu, L., Stegman, D.R. (2012). Origin of Columbia River flood basalt controlled by propagating rupture of the Farallon slab. *Nature* **482**, 386–390.

McClaughry, J., Ferns, M.L., Gordon, C.L., Patridge, K.A. (2009a). Field trip guide to the Oligocene Crooked River caldera: Central Oregon's supervolcano, Crook, Deschutes, and Jefferson Counties, Oregon. *Oregon Geology* **69**, 25–44.

McClaughry, J.D., Ferns, M.L., Streck, M.J., Patridge, K.A., Gordon, C.L. (2009b). Paleogene calderas of central and eastern Oregon: Eruptive sources of widespread tuffs in the John Day and Clarno Formations, *in* O'Connor, J.E., Dorsey, R.J., and Madin, I.P., ed., Volcanoes to vineyards: Geologic field trips through the dynamic landscape of the Pacific Northwest. *Geological Society of America Field Guide* **15**, 407–434.

McClaughry, J.D., Wiley, T.J., Ferns, M.L., Madin, I.P. (2010). Digital geologic map of the southern Willamette Valley, Benton, Lane, Linn, Marion, and Polk Counties, Oregon. *Oregon Department of Geology and Mineral Industries Open File Report* **0-10-03**.

McCurry, M., Rodgers, D.W. (2009). Mass transfer along the Yellowstone hotspot track I: Petrologic constraints on the volume of mantle-derived magma. *Journal of Volcanology and Geothermal Res*earch **188**, 86–98.

Münker, C., Wörner, G., Yogodzinski, G., Churikova, T. (2004). Behaviour of high field strength elements in subduction zones: constraints from Kamchatka-Aleutian arc lavas. *Earth and Planetary Science Letters* **224**, 275–293.

Murphy, J.B., Hynes, A., Johnston, S.R., Keppie, J.D. (2003). Reconstructing the ancestral Yellowstone plume from accreted seamounts and its relationship to flat-slab subduction. *Tectonophysics* **365**, 185–194.

Nash, B., Perkins, M., Christensen, J., Lee, D., Halliday, A. (2006). The Yellowstone hotspot in space and time: Nd and Hf isotopes in silicic magmas. *Earth and Planetary Science Letters* **247**, 143–156.

Nowell, G.M., Kempton, P.D., Noble, S.R., Fitton, J.G., Saunders, A.D., Mahoney, J.J., Taylor, R.N. (1998). High precision Hf isotope measurements of MORB and OIB by thermal ionasation mass spectrometry: Insights into the depleted mantle. *Chemical Geology* **149**, 211–233.

Obrebski, M., Allen, R.M., Xue, M., Hung, S. (2010). Slab-plume interaction beneath the Pacific Northwest. *Geophysical Research Letters* **37**, 1–6.

Pearce, J.A., Harris, N.B., Tindle, A.G. (1984). Trace element discrimination diagrams for the tectonic interpretation of granitic rocks. *Journal of Petrology* **25**, 956–983.

Pearce, J.A., Peate, D.W. (1995) Tectonic implications of the composition of volcanic arc magmas. *Annual Review of Earth and Planetary Sciences* **23**, 251–285.

Pierce, K.L., Morgan, L.A. (1992). The track of the Yellowstone hot spot: Volcanism, faulting, and uplift, *in* Link, P.K., ed., Regional Geology of Eastern Idaho and Western Wyoming. *Memoirs of the Geological Society of America* **179**, 1–53.

Schwartz, J.J., Johnson, K., Miranda, E.A., Wooden, J.L. (2011). The generation of high Sr/Y plutons following Late Jurassic arc-arc collision, Blue Mountains province, NE Oregon. *Lithos* **126**, 22–41.

Seligman, A., Bindeman, I., Jicha, B., Ellis, B., Ponomareva, V., Leonov, V. (2014). Multi-cyclic and isotopically diverse silicic magma generation in an arc volcano: Gorely eruptive center, Kamchatka, Russia. *Journal of Petrology* **55**, 1561–1594.

Seton, M., Muller, R.D., Zahirovic, S., Gaina, C., Torsvik, T., Shephard, G., Talsma, A., Gurnis, M., Turner, M., Maus, S., Chandler, M. (2012). Global continental and ocean basin reconstructions since 200 Ma. *Earth-Science Rev*iews **113**, 212–270.

Steinberger, B., O'Connell, R.J. (1998). Advection of plumes in mantle flow: Implications for hotspot motion, mantle viscosity and plume distribution. *Geophysical Journal International* **132**, 412–434.

Valley, J., Lackey, J., Cavosie, A., Clechenko, C., Spicuzza, Basei, M.A.S., Bindeman, I.N., Ferreira, V.P., Sial, A.N., King, E.M., Peck, W.H., Sinha, A.K., Wei, C.S. (2005). 4.4 billion years of crustal maturation: Oxygen isotope ratios of magmatic zircon. *Contributions to Mineralogy and Petrology* **150**, 561–580.

Watts, K., Bindeman, I., Schmitt, A. (2011). Large-volume rhyolite genesis in caldera complexes of the Snake River Plain: Insights from the Kilgore Tuff of the Heise Volcanic Field, Idaho, with comparison to Yellowstone and Bruneau-Jarbidge rhyolites. *Journal of Petrology* **52**, 1–34.

Wells, R.E., Bukry, D., Friedman, R. Pyle, D., Duncan, R., Haeussler, P., Wooden, J. (2014). Geologic history of Siletzia, a large igneous province in the Oregon and Washington Coast Range – Correlation to the geomagnetic polarity timescale and implications for a long-lived Yellowstone Hot Spot. *Geosphere* **10**, 692–719.

Wells, R.E., Engebretson, D.C., Snavely, P.D., Coe, R.S. (1984). Cenozoic plate motions and the volcano-tectonic evolution of western Oregon and Washington. *Tectonics* **3**, 275–294.

Wells, R.E., Weaver, C.S., Blakely, R.J. (1998). Fore-arc migration in Cascadia and its neotectonic significance. *Geology* **26**, 759–762.

Chapter IV

Anovitz, L.M., Elam, J.M., Riciputi, L.R., Cole, D. R. (2004). Isothermal time-series determination of the rate of diffusion of water in Pachuca obsidian. *Archaeometry* **46**, 301–326.

Anovitz, L.M., Cole, D.R., Fayek, M. (2008). Mechanisms of rhyolitic glass hydration below the glass transition. *Am. Mineral.* **93**, 1166–1178.

Anovitz, L.M., Cole, D.R., Riciputi, L.R. (2009). Low-temperature isotopic exchange in obsidian: Implications for diffusive mechanisms. *Geochimica et Cosmochimica Acta* **73**(13), 3795–3806.

Auer, S., Bindeman, I., Wallace, P., Ponomareva, V., Portnyagin, M. (2009). The origin of hydrous, high-$\delta^{18}O$ voluminous volcanism: diverse oxygen isotope values and high magmatic water contents within the volcanic reord of Klyuchevskoy volcano, Kamchatka, Russia. *Contrib. Mineral. Petrol.* **157**, 209–230.

Bindeman, I.N., Kamenetsky, V., Palandri, J., Vennemann, T. (2012). Hydrogen and oxygen isotope behavior during variable degrees of upper mantle melting: example from the basaltic glasses from Macquarie Island. *Chemical Geology* **310–311**, 126–136.

Bowen, G.J., Revenaugh, J. (2003). Interpolating the isotopic composition of modern meteoric precipitation. *Water Resources Research* **39**(10), 1299.

Bowen, G.J. (2015). The Online Isotopes in Precipitation Calculator, version 2.2. http://www.waterisotopes.org.

Braitseva, O.A., Ponomareva, V.V., Sulerzhitsky, L.D., Melekestsev, I.V., Bailey, J. (1997). Holocene key-marker tephra layers in Kamchatka, Russia. *Quaternary Research* **47**, 125–139.

Cailleteau, C., Angeli, F., Devreux, F., Gin, S., Jestin, J., Jollivet, P., Spalla, O. (2008). Insight into silicate-glass corrosion mechanisms. *Nature Materials* **7**, 978–983.

Canavan, R.R., Carrapa, B., Clementz, M.T., Quade, J., DeCelles, P.G., Schenbohm, L.M. (2014). Early Cenozoic uplift of the Puna Plateau, Central Andes, based on stable isotope paleoaltimetry of hydrated volcanic glass. *Geology* **42**, 447–450.

Cassel, E.J., Graham, S.A., Chamberlain, C.P., Henry, C.D. (2012). Early Cenozoic topography, morphology, and tectonics of the northern Sierra Nevada and western Basin and Range. *Geosphere* **8**, 229–249.

Cassel, E.J., Breecker, D.O., Henry, C.D., Larson, T.E., Stockli, D.F. (2014). Profile of a paleo-orogen: High topography across the present-day Basin and Range from 40 to 23 Ma. *Geology* **42**(11), 1007–1010.

Castro, J.M., Bindeman, I.N., Tuffen, H., Schipper, C.I. (2014). Explosive origin of silicic lava: Textural and δD-H_2O evidence for pyroclastic degassing during rhyolite effusion. *Earth and Planetary Science Letters* **405**, 52–61.

Cerling, T.E., Brown, F.H., Bowman, J.R. (1985). Low-temperature alteration of volcanic glass: Hydration, Na, K, ^{18}O, and Ar mobility. *Chem. Geol.* **52**, 281–293.

Crovisier, J., Advocat, T., Dussossoy, J. (2003). Nature and role of natural alteration gels formed on the surface of ancient volcanic glasses (Natural analogs of waste containment glasses). *Journal of Nuclear Materials* **321**, 91–109.

DeGroat-Nelson, P.J., Cameron, B.I., Fink, J.H., Holloway, J.R. (2001). Hydrogen isotope analysis of rehydrated silicic lavas: Implications for eruption mechanisms. *Earth Planet. Sci. Lett.* **185**, 331–341.

Dettinger, M.P., Quade, J. (2015). Testing the analytical protocols and calibration of volcanic glass for the reconstruction of hydrogen isotopes in paleoprecipitation. In *Geodynamics of a Cordilleran Orogenic System: The Central Andes of Argentina and Northern Chile* (eds. P.G. DeCelles, M.N. Ducea, B. Carrapa, P.A. Kapp), Geological Society of America, vol. 212, pp. 261–276.

Dobson, P.F., Epstein, S., Stolper, E.M. (1989). Hydrogen isotope fractionation between coexisting vapor and silicate glasses and melts at low pressure. *Geochimica et Cosmochimica Acta* **53**, 2723–2730.

Eerkens, J.W., Vaughn, K.J., Carpenter, T.R., Conlee, C.A., Grados, M.L., Schreiber, K. (2008). Obsidian hydration dating on the south coast of Peru. *Journal of Archaeological Science* **35**, 2231–2239.

Fontijn, K., Ernst, G.G.J., Elburg, M.A., Williamson, D., Abdallah, E. Kwelwa, S., Mbede, E., Jacobs, P. (2010). Holocene explosive eruptions in the Rungwe Volcanic Province, Tanzania. *Journal of Volcanology and Geothermal Research* **196**, 91–110.

Fontijn, K., Lachowycz, S.M., Rawson, H., Pyle, D.M., Mather, T.A., Naranjo, J.A., Moreno-Roa, H. (2014). Late Quaternary tephrostratigraphy of southern Chile and Argentina. *Quaternary Science Reviews* **89**, 70–84.

Friedman, I., Smith, R.L., Long, W.D. (1966). Hydration of natural glass and formation of perlite. *Geological Society of America Bulletin* **77**, 323–328.

Friedman, I., Gleason, J., Sheppard, R.A., Gude, A.J. (1993a). Deuterium fractionation as water diffuses into silicic volcanic ash. *Geophysical Monograph* **78**, 321–323.

Friedman, I., Gleason, J., Warden, A. (1993b). Ancient climate from deuterium content of water in volcanic glass. *Geophysical Monograph* **78**, 309–319.

Giachetti, T., Gonnermann, H.M. (2013). Water in volcanic pyroclast: Rehydration or incomplete degassing?. *Earth and Planetary Science Letters* **369–370**, 317–332.

Giachetti, T., Gonnermann, H.M., Gardner, J.E., Shea, T., Gouldstone, A. (2015). Discriminating secondary from magmatic water in rhyolitic matrix-glass of volcanic pyroclasts using thermogravimetric analysis. *Geochimica et Cosmochimica Acta* **148**, 457–476.

Gin, S., Ryan, J.V., Schreiber, D.K., Neeway, J., Cabié, M. (2013). Contribution of atom-probe tomography to a better understanding of glass alteration mechanisms: Application to a nuclear glass specimen altered 25 years in a granitic environment. *Chemical Geology* **349–350**, 99–109.

Henderson, A.K., Nelson, D.M., Hu, F.S., Huang, Y., Shuman, B.N., Williams, J.W. (2010). Holocene precipitation seasonality captured by a dual hydrogen and oxygen isotope approach at Steel Lake, Minnesota. *Earth and Planetary Science Letters* **300**, 205–214.

Ihinger, P.D., Zhang, Y., Stolper, E.M. (1999). The speciation of dissolved water in rhyolitic melt. *Geochimica et Cosmochimica Acta* **63**, 3567–3578.

Jezek, P.A., Noble, D.C. (1978). Natural hydration and ion exchange of obsidian: An electron microprobe study. *American Mineralogist* **63**, 266–273.

Kyle, P.R., Ponomareva, V.V., Chluep, R.R. (2011). Geochemical characterization of marker tephra layers from major Holocene eruptions, Kamchatka Peninsula, Russia. *International Geology Review* **53**, 1059–1097.

Mazer, J.J., Stevenson, C.M., Ebert, W.L., Bates, J.K. (1991). The experimental hydration of obsidian as a function of relative humidity and temperature. *American Antiquity* **56**, 504–513.

Mulch, A., Sarna-Wojcicki, A.M., Perkins, M.E., Chamberlain, C.P. (2007). A Miocene to Pleistocene climate and elevation record of the Sierra Nevada (California). *Proceedings of the National Academy of Sciences* **105**(19), 6819–6824.

Newman, S., Stolper, E.M., Epstein, S. (1986). Measurement of water in rhyolitic glasses: Calibration of an infrared spectroscopic technique. *American Mineralogist* **71**, 1527–1541.

Newman, S., Epstein, S., Stolper, E. (1988). Water, carbon dioxide, and hydrogen isotopes in glasses from the ca. 1340 A.D. eruption of the Mono Craters, California: Constraints on degassing phenomena and initial volatile content. *Journal of Volcanology and Geothermal Research* **35**(1–2), 75–96.

Nolan, G.S., Bindeman, I.N. (2013). Experimental investigation of rates and mechanisms of isotope exchange (O, H) between volcanic ash and isotopically-labeled water. *Geochimica et Cosmochimica Acta* **111**, 5–27.

Parruzot, B., Jollivet, P., Rébiscoul, D., Gin, S. (2015). Long-term alteration of basaltic glass: Mechanisms and rates. *Geochimica et Cosmochimica Acta* **154**, 28–48.

Ponomareva, V., Kyle, P.R., Melekestsev, I.V., Rinkleff, P.G., Dirksen, O.V., Sulerzhitksy, L. D., Zaretskaia, N. E., Rourke, R. (2004). The 7600 (^{14}C) year BP Kurile Lake caldera-forming eruption, Kamchatka, Russia: stratigraphy and field relationships. *Journal of Volcanology and Geothermal Research* **136**, 199–222.

Ponomareva, V., Melekestev, I., Braitseva, O., Churikova, T., Pevzner, M., Sulerzhitsky, L. (2007). Late Pleistocene-Holocene volcanism on the Kamchatka Peninsula, Northwest Pacific Region. In *Volcanism and Subduction: The Kamchatka Region* (eds. J. Eichelberger, E. Gordeev, M. Kasahara, P. Izbekov, J. Lees), American Geophysical Union, Geophysical Monograph 172, 165–198.

Ponomareva, V., Portnyagin, M., Derkachev, A., Pendea, I.F., Bourgeois, J., Reimer, P.J., Garbe-Schönberg, D., Krasheninnikov, S., Nürnberg, D. (2013). Early Holocene M~6 explosive eruption from Plosky volcanic massif (Kamchatka) and its tephra as a link between terrestrial and marine paleoenvironmental records. *International Journal of Earth Sciences* **102**, 1673–1699.

Princen, H. (1979). Highly concentrated emulsions. I. Cylindrical systems. *Journal of Colloid and Interface Science* **71**, 55–66.

Proussevitch, A.A., Sahagian, D.L., Anderson, A.T. (1993). Dynamics of diffusive bubble growth in magmas: isothermal case. *Journal of Geophysical Research* **98**, 22283–22307.

Qi, H., Gröning, M., Coplen, T.B., Buck, B., Mroczkowski, S.J., Brand, W.A., Geilmann, H., Gehre, M. (2010). Novel silver-tubing method for quantitative introduction of water into high-temperature conversion systems for stable hydrogen and oxygen isotopic measurements. *Rapid Communications in Mass Spectrometry* **24**, 1821–1827.

Qi, H., Coplen, T.B., Olack, G.A., Vennemann, T.W. (2014). Caution on the use of NBS 30 biotite for hydrogen-isotope measurements with on-line high-temperature conversion systems. *Rapid Communications in Mass Spectrometry* **28**, 1987–1994.

Rébiscoul, D., Rieutord, F., Né, F., Frugier, P., Cubitt, R., Gin, S. (2007). Water penetration mechanisms in nuclear glasses by X-ray and neutron reflectometry. *Journal of Non-Crystalline Solids* **353**, 2221–2230.

Riciputi, L.R., Elam, J.M., Anovitz, L.M., Cole, D.R. (2002). Obsidian diffusion dating by Secondary Ion Mass Spectrometry: A test using results from Mound 65, Chalco, Mexico. *Journal of Archaeological Science* **29**(10), 1055–1075.

Ross, C.S., Smith, R.L. (1955). Water and other volatiles in volcanic glasses. *American Mineralogist* **40**, 1071–1089.

Rust, A.C., Cashman, K.V. (2011). Permeability controls on expansion and size distributions of pyroclasts. *J. Geophys. Res.* **116**, 1–17.

Sarna-Wojcicki, A.M., Davis, J.O. (1991). Quaternary tephrochronology. In *Quaternary nonglacial geology–conterminous U.S.* (eds. R. B. Morrison), Geological Society of America, Geology of North America K2, 93–116.

Shane, P., Ingraham, N. (2002). δD values of hydrated volcanic glass: A potential record of ancient meteoric water and climate in New Zealand. *New Zealand Journal of Geology & Geophysics* **45**(4), 453–459.

Silver, L.A., Ihinger, P.D., Stolper, E. (1990). The influence of bulk composition on the speciation of water in silicate glasses. *Contrib. Mineral. Petrol.* **104**, 142–162.

Steefel, C.I., Beckingham, L.E., Landrot, G. (2015). Micro-continuum approaches for modeling pore-scale geochemical processes. *Reviews in Mineralogy & Geochemistry* **80**, 217–246.

Stroncik, N.A., Schmincke, H. (2002). Palagonite – a review. *International Journal of Earth Sciences* **91**, 680–697.

Tuffen, H., Owen, J., Denton, J.S. (2010). Magma degassing during subglacial eruptions and its use to reconstruct palaeo-ice thicknesses. *Earth Sci. Rev.* **99**, 1–18.

Valle, N., Verney-Carron, A., Sterpenich, J., Libourel, G., Deloule, E., Jollivet, P. (2010). Elemental and isotopic (^{29}Si and ^{18}O) tracing of glass alteration mechanisms. *Geochimica et Cosmochimica Acta* **74**, 3412–3431.

Zhang, Y. (1999). H_2O in rhyolitic glasses and melts: Measurement, speciation, solubility, and diffusion. *Reviews in Geophysics* **37**, 493–516.

Zhang, Y., Behrens, H. (2000). H_2O diffusion in rhyolitic melts and glasses. *Chemical Geology* **169**, 243–262.

Chapter V

Anovitz, L.M., Elam, J.M., Riciputi, L.R., Cole, D.R. (2004). Isothermal time-series determination of the rate of diffusion of water in Pachuca obsidian. *Archaeometry* **46**, 301–326.

Banks, N.G., Hoblitt, R.P. (1981). Summary of temperature studies of 1980 deposits, *in* Lipman, P.W., and Mullineaux, D.R., eds, The 1980 eruptions of Mount St. Helens, Washington: U.S. Geological Survey Professional Paper 1250, p. 295–313.

Barnes, I. (1984). Volatiles of Mount St. Helens and their origins. *Journal of Volcanology and Geothermal Research* **22**, 133–146.

Bindeman, I.N., Kamenetsky, V., Palandri, J., Venneman, T. (2012). Hydrogen and oxygen isotope behavior during variable degrees of upper mantle melting: example from the basaltic glasses from Macquarie Island. *Chemical Geology* **310–311**, 126–136.

Blundy, J., Cashman, K.V., Berlo, K. (2008). Evolving magma storage conditions beneath Mount St. Helens inferred from chemical variations in melt inclusions from the 1980–1986 and current (2004–2006) eruptions, in Sherrod, D.R., Scott, W.E., and Stauffer, P.H., eds, A volcano rekindled: the renewed eruptions of Mount St. Helens, 2004–2006: U.S. Geological Survey Professional Paper 1750, p. 755–790.

Blundy, J., Cashman, K. (2005). Rapid decompression-driven crystallization recorded by melt inclusions from Mount St. Helens volcano. *Geology* **33**, 793–796.

Cashman, K.V., McConnell, S.M. (2005). Multiple levels of magma storage during the 1980 summer eruptions of Mount St. Helens, WA. *Bulletin of Volcanology* **68**, 57–75.

Cassel, E.J., Breecker, D.O., Henry, C.D., Larson, T.E., Stockli, D.F. (2014). Profile of a paleo-orogen: High topography across the present-day Basin and Range from 40 to 23 Ma *Geology* **42**, 1007–1010

Castro, J.M., Bindeman, I.N., Tuffen, H., Schipper, C.I. (2014). Explosive origin of silicic lava: Textural and δD-H_2O evidence for pyroclastic degassing during rhyolite effusion. *Earth and Planetary Science Letters* **405**, 52–61.

Dettinger M.P., Quade J. (2015). Testing the analytical protocols and calibration of volcanic glass for the reconstruction of hydrogen isotopes in paleoprecipitation, *in* DeCelles, P.G., Ducea, M.N., Carrapa, B., Kapp, P.A., eds., Geodynamics of a Cordilleran Orogenic System: The Central Andes of Argentina and Northern Chile: Geological Society of America 212, p. 261–276.

Eichelberger, J.C., Carrigan, C.R., Westrich, H.R., Price, R.H. (1986). Non-explosive silicic volcanism. *Nature* **323**, 598–602.

Friedman, I., Smith, R.L., Long, W.D. (1966). Hydration of natural glass and formation of perlite. *Geological Society of America Bulletin* **77**, 323–328.

Friedman I., Gleason J., Sheppard R.A., Gude A.J. (1993). Deuterium fractionation as water diffuses into silicic volcanic ash *Geophysical Monograph* **78**, 321–323.

Giachetti, T., Gonnermann, H.M. (2013). Water in volcanic pyroclast: Rehydration or incomplete degassing? *Earth and Planetary Science Letters* **369–370**, 317–332.

Giachetti, T., Gonnermann, H.M., Gardner, J.E., Shea, T., Gouldstone, A. (2015). Discriminating secondary from magmatic water in rhyolitic matrix-glass of volcanic pyroclasts using thermogravimetry analysis. *Geochimica et Cosmochimica Acta* **148**, 457–476.

Griggs, R.F. (1922) The Valley of Ten Thousand Smokes: National Geographic Society, Washington, D.C., p. 1–340.

Fierstein, J., Hildreth, W. (1992). The plinian eruptions of 1912 at Novarupta, Katmai National Park, Alaska. *Bulletin of Volcanology* **54**, 646–684.

Hoblitt, R.P., Reynolds, R.L., Larson, E.E. (1985). Suitability of nonwelded pyroclastic-flow deposits for studies of magnetic secular variation: A test based on deposits emplaced at Mount St. Helens, Washington, in 1980. *Geology* **13**, 242–245.

Hoblitt, R.P. Harmon, R.S. (1993). Bimodal density distribution of cryptodome dacite from the 1980 eruption of Mount St. Helens, Washington. *Bulletin of Volcanology* **55**, 421–437.

Holt, E.W., Taylor Jr., H.P. (1997). $^{18}O/^{16}O$ mapping and hydrogeology of a short-lived (~10 years) fumarolic (>500 °C) meteoric-hydrothermal event in the upper part of the 0.76 Ma Bishop Tuff outflow sheet, California. *Journal of Volcanology and Geothermal Research* **83**, 115–139.

Holt, E.W., Taylor Jr., H.P. (2001). $^{18}O/^{16}O$ studies of fossil fissure fumaroles from the Valley of Ten Thousand Smokes, Alaska. *Bulletin of Volcanology* **63**, 151–163.

Loewen, M.W., Bindeman, I.N. (2015). Oxygen isotope and trace element evidence for three-stage petrogenesis of the youngest episode (260–79 ka) of Yellowstone rhyolitic volcanism. *Contributions to Mineralogy and Petrology* **170**, 1–25.

Mastin, L.G., Christiansen, R.L., Thornber, C., Lowenstern, J., Beeson, M. (2004). What makes hydromagmatic eruptions violent? Some insights from the Keanakāko'i Ash, Kīlauea Volcano, Hawai'i. *Journal of Volcanology and Geothermal Research* **137**, 15–31.

Mulch, A., Sarna-Wojcicki, A.M., Perkins, M.E., Chamberlain, C.P. (2007). A Miocene to Pleistocene climate and elevation record of the Sierra Nevada (California). *Proceedings of the National Academy of Sciences* **105**, 6819–6824.

Newman, S., Epstein, S., Stolper, E. (1988). Water, carbon dioxide, and hydrogen isotopes in glasses from the ca. 1340 A.D. eruption of the Mono Craters, California: Constraints on degassing phenomena and initial volatile content: *Journal of Volcanology and Geothermal Research* **35**, 75–96.

Newman, S., Lowenstern, J.B. (2002). VolatileCalc: A silicate melt-H_2O-CO_2 solution model written in Visual Basic for EXCEL. *Computer & Geosciences* **28**, 587–604.

Nolan, G.S., Bindeman, I.N. (2013). Experimental investigation of rates and mechanisms of isotope exchange (O, H) between volcanic ash and isotopically-labeled water. *Geochimica et Cosmochimica Acta* **111**, 5–27.

Qi H., Gröning M., Coplen T. B., Buck B., Mroczkowski S. J., Brand W. A., Geilmann H., Gehre M. (2010). Novel silver-tubing method for quantitative introduction of water into high-temperature conversion systems for stable hydrogen and oxygen isotopic measurements. *Rapid Communications in Mass Spectrometry* **24**, 1821–1827.

Riciputi, L.R., Elam, J.M., Anovitz, L.M., Cole, D.R. (2002). Obsidian diffusion dating by Secondary Ion Mass Spectrometry: A test using results from Mound 65, Chalco, Mexico. *Journal of Archaeological Science* **29**, 1055–1075.

Scandone, R., Malone, S.D. (1983). Magma supply, magma discharge and readjustment of the feeding system of Mount St. Helens during 1980. *Journal of Volcanology and Geothermal Research* **23**, 239–262.

Seligman, A.N., Bindeman, I.N., Watkins, J.M., Ross, A.M. (2016). Water in volcanic glass: From volcanic degassing to secondary hydration. *Geochimica et Cosmochimica Acta*, **in review**.

Shane, P., Ingraham, N. (2002). δD values of hydrated volcanic glass: A potential record of ancient meteoric water and climate in New Zealand. *New Zealand Journal of Geology & Geophysics* **45**, 453–459.

Song, W., Lavallee, Y., Hess, K.U., Kueppers, U., Cimarelli, C., Dingwell, D.B. (2016). Volcanic ash melting under conditions relevant to ash turbine interactions. *Nature Communications* **7**, 1–10.

Taylor, B.E., Eichelerger, J.C., Westrich, H.R. (1983). Hydrogen isotopic evidence of rhyolitic magma degassing during shallow intrusion and eruption. *Nature* **306**, 541–545.

Underwood, S.J., Feeley, T.C., Clynne, M.A. (2013). Hydrogen isotope investigation of amphibole and glass in dacite magmas erupted in 1980–1986 and 2005 at Mount St. Helens, Washington. *Journal of Petrology* **54**, 1047–1070.

Watkins, J.M., Manga, M., De Paolo, D.J. (2012). Bubble geobarometry: A record of pressure changes, degassing, and regassing at Mono Craters, California. *Geology* **40**, 699–702.

Westrich, H.R., Eichelberger, J.C. (1994). Gas transport and bubble collapse in rhyolitic magma: An experimental approach. *Bulletin of Volcanology* **56**, 447–458.

Zhang, Y., Behrens, H. (2000). H_2O diffusion in rhyolitic melts and glasses. *Chemical Geology* **169**, 243–262.

Zheng, Y. (1991). Calculation of oxygen isotope fractionation in metal oxides. *Geochimica et Cosmochimica Acta* **55**, 2299–2307.

Zheng, Y. (1993). Calculation of oxygen isotope fractionation in hydroxyl-bearing silicates. *Earth and Planetary Science Letters* **120**, 247–263.

Chapter VI

Bao, H., Koch, P.L., Thiemens, M. (2000). Oxygen isotopic composition of ferric oxides from recent soil, hydrologic, and marine environments. *Geochimica et Cosmochimica Acta* **64**, 2221–2231.

Bao, H., Marchant, D.R. (2006) Quantifying sulfate components and their variations in soils of the McMurdo Dry Valleys, Antarctica. *Journal of Geophysical Research* **111**, 1–13.

Bechtel, A., Hoernes, S. (1990) Oxygen isotope fractionation between oxygen of different sites in illite minerals: A potential single-mineral thermometer. *Contributions to Mineralogy and Petrology* **104**, 463–470.

Bindeman, I.N., Eiler, J.M., Wing, B.A., Farquhar J. (2007). Rare sulfur and triple oxygen isotope geochemistry of volcanogenic sulfate aerosols. *Geochimica et Cosmochimica Acta* **71**, 2326–2342.

Bindeman I.N., Kamenetsky, V., Palandri J., Vennemann, T. (2012). Hydrogen and oxygen isotope behavior during variable degrees of upper mantle melting: example from the basaltic glasses from Macquarie Island. *Chemical Geology* **310–311**, 126–136.

Bindeman, I.N., Lundstrom, C.C., Bopp, C., Huang F. (2013). Stable isotope fractionation by thermal diffusion through partially molten wet and dry silicate rocks. *Earth and Planetary Science Letters* **365**, 51–62.

Blundy, J., Cashman, K. (2005). Rapid decompression-driven crystallization recorded by melt inclusions from Mount St. Helens volcano. *Geology* **33**, 793–796.

Brand, W. A., Tegtmeyer, A. R., Hilkert A. (1994). Compound-specific isotope analysis: Extending toward $^{15}N/^{14}N$ and $^{18}O/^{16}O$. *Organic Geochemistry* **21**, 585–594.

Cassel, E.J., Breecker, D.O., Henry, C.D., Larson, T.E., Stockli, D.F. (2014). Profile of a paleo-orogen: High topography across the present-day Basin and Range from 40 to 23 Ma. *Geology* **42**, 1007–1010.

Castro, J.M., Bindeman, I.N., Tuffen, H., Schipper C.I. (2014). Explosive origin of silicic lava: Textural and dD-H_2O evidence for pyroclastic degassing during rhyolite effusion. *Earth and Planetary Science Letters* **405**, 52–61.

Chamberlain, C., Poage, M. (2000). Reconstructing the paleotopography of mountain belts from the isotopic composition of authigenic minerals. *Geology* **28**, 115–118.

Clayton, R.N., Mayeda, T.M. (2009). Kinetic isotope effects in oxygen in the laboratory dehydration of magnesian minerals. *Journal of Physical Chemistry A* **113**, 2212–2217.

Colón, D.P., Bindeman, I.N., Ellis, B.S., Schmitt, A.K., Fisher, C.M. (2015). Hydrothermal alteration and melting of the crust during the Columbia River Basalt-Snake River Plain transition and the origin of low-$\delta^{18}O$ rhyolites of the central Snake River Plain. *Lithos* **224–225**, 310–323.

Dansgaard, W. (1964). Stable isotopes in precipitation. *Tellus* **16**, 436–468.

De Hoog, J.C.M., Taylor, B.E., Van Bergen, M.J. (2009). Hydrogen-isotope systematics in degassing basaltic magma and application to Indonesian arc basalts. *Chemical Geology* **266**, 256–266.

Drew, D.L., Bindeman, I.N., Watts, K.E., Schmitt, A.K., Fu, B., McCurry, M. (2013). Crustal-scale recycling in caldera complexes and rift zones along the Yellowstone hotspot track: O and Hf isotopic evidence in diverse zircons from voluminous rhyolites of the Picabo volcanic field, Idaho. Earth and Planetary Science Letters **381**, 63–77.

Druitt, T.H., Bacon, C.R. (1989). Petrology of the zoned calcalkaline magma chamber of Mount Mazama, Crater Lake, Oregon. *Contributions to Mineralogy and Petrology* **101**, 245–259.

Eiler, J.M. (2007) "Clumped-isotope" geochemistry – The study of naturally-occurring, multiply-substituted isotopologues. *Earth and Planetary Science Letters* **262**, 309–327.

Friedman, I., Smith, R.L., Long, W.D. (1966). Hydration of natural glass and formation of perlite. *Geological Society of America Bulletin* **77**, 323–328.

Friedman, I., O'Neil, J.R. (1977). Data of geochemistry: Compilation of stable isotope fractionation factors of geochemical interest. *US Government Printing Office* 440.

Friedman, I., Gleason, J., Sheppard, R.A., Gude, A.J. (1993a). Deuterium fractionation as water diffuses into silicic volcanic ash. *Geophysical Monograph* **78**, 321–323.

Friedman, I., Gleason, J., Warden, A. (1993b). Ancient climate from deuterium content of water in volcanic glass. *Geophysical Monograph* **78**, 309–319.

Giachetti, T., Gonnermann, H.M., Gardner, J.E., Shea, T., Gouldstone, A. (2015). Discriminating secondary from magmatic water in rhyolitic matrix-glass of volcanic pyroclasts using thermogravimetric analysis. *Geochimica et Cosmochimica Acta* **148**, 457–476.

Giggenbach, W.F. (1992). Isotopic shifts in waters from geothermal and volcanic systems along convergent plate boundaries and their origin. *Earth and Planetary Sciences Letters* **113**, 495–510.

Gilg, H.A., Girard, J.P., Sheppard, S.M.F. (2004) Conventional and less conventional techniques for hydrogen and oxygen isotope analysis of clays, associated minerals and pore waters in sediments and soils. *Handbook of Stable Isotope Analytical Techniques* **1**, 38–61.

Girard, J.P., Savin, S.M. (1996) Intracrystalline fractionation of oxygen isotopes between hydroxyl and non-hydroxyl sites in kaolinite measured by thermal dehydroxylation and partial fluorination. *Geochimica et Cosmochimica Acta* **60**, 469–487.

Halliday, A.N., Fallick, A.E., Dickin, A.P., Machenzie, A.B., Stephens, W.E., Hildreth, W. (1983). The isotopic and chemical evolution of Mount St. Helens. *Earth and Planetary Science Letters* **63**, 241–256.

Hamza, M.S., Epstein, S. (1979). Oxygen isotopic fractionation between oxygen of different sites in hydroxyl-bearing silicate minerals. *Geochimica et Cosmochimica Acta* **44**, 173–182.

Ihinger, P.D., Zhang, Y., Stolper, E.M. (1999). The speciation of dissolved water in rhyolitic melt. *Geochimica et Cosmochimica Acta* **63**, 3567–3578.

Kyser, T.K., O'Neill, J.R. (1984). Hydrogen isotope systematics of submarine basalts. *Geochimica et Cosmochimica Acta* **48**, 2123–2133.

Loewen, M.W., Bindeman, I.N. (2015). Oxygen isotope and trace element evidence for three-stage petrogenesis of the youngest episode (260–79 ka) of Yellowstone rhyolitic volcanism. *Contributions to Mineralogy and Petrology* **170**, 1–25.

Martin, E., Bindeman, I., Balan, E., Palandri, J., Seligman, A., Vollemant, B. (2016). Hydrogen isotope determination by TC/EA technique in application to volcanic glass as a window into secondary hydration. *Chemical Geology* in review.

Mulch, A. (2006). Hydrogen isotopes in Eocene river gravels and paleoelevation of the Sierra Nevada. *Science* **313**, 87–89.

Mulch, A., Sarna-Wojcicki, A.M., Perkins, M.E., Chamberlain, C.P. (2008). A Miocene to Pleistocene climate and elevation record of the Sierra Nevada (California). *Proceedings of the National Academy of Sciences of the United States of America* **105**, 6819–6824.

Newman S., Stolper E.M., Epstein S. (1986) Measurement of water in rhyolitic glasses: Calibration of an infrared spectroscopic technique. *American Mineralogist* 71, 1527–1541.

Newman, S., Epstein, S., Stolper, E. (1988). Water, carbon dioxide, and hydrogen isotopes in glasses from the ca. 1340 A.D. eruption of the Mono Craters, California: Constraints on degassing phenomena and initial volatile content. *Journal of Volcanology and Geothermal Research* **35**, 75–96.

Newman, S., Lowenstern, J.B. (2002). VolatileCalc: A silicate melt-H_2O-CO_2 solution model written in Visual Basic for EXCEL. *Computers & Geosciences* **28**, 587–604.

Nolan, G.S., Bindeman, I.N. (2013). Experimental investigation of rates and mechanisms of isotope exchange (O, H) between volcanic ash and isotopically-labeled water. *Geochimica et Cosmochimica Acta* **111**, 5–27.

Nye, C.J., Turner, D.L. (1990). Petrology, geochemistry, and age of the Spurr volcanic complex, eastern Aleutian arc. *Bulletin of Volcanology* **52**, 205–226.

Pineau, F., Semet, M.P., Grassinaeu, N., Okrugin, V.M., Javoy M. (1999). The genesis of the stable isotope (O, H) record in arc magmas: The Kamchatka's case. *Chemical Geology* **135**, 93–124.

Qi, H., Gröning, M., Coplen, T.B., Buck, B., Mroczkowski, S.J., Brand, W.A., Geilmann, H., Gehre, M. (2010). Novel silver-tubing method for quantitative introduction of water into high-temperature conversion systems for stable hydrogen and oxygen isotopic measurements. *Rapid Communications in Mass Spectrometry* **24**, 1821–1827.

Qi, H., Coplen, T.B., Olack, G.A., Vennemann, T.W. (2014). Caution on the use of NBS 30 biotite for hydrogen-isotope measurements with on-line high-temperature conversion systems. *Rapid Communications in Mass Spectrometry* **28**, 1987–1994.

Rose, W.I. Jr., Anderson, A.T. Jr., Woodruff, L.G., Bonis, S. B. (1978). The October 1974 basaltic tephra from Fuego Volcano: Description and history of the magma body. *Journal of Volcanology and Geothermal Research* **4**, 3–53.

Rose, W.I. Jr., Chuan, R.L., Cadle, R.D., Woods, D.C. (1980). Small particles in volcanic eruption clouds. *American Journal of Science* **280**, 671–696.

Rowley, D., Pierrehumbert, R., Currie, B. (2001). A new approach to stable isotope-based paleoaltimetry: implications for paleoaltimetry and paleohypsometry of the High Himalaya since the Late Miocene. *Earth and Planetary Science Letters* **188**, 253–268.

Savin, S.M. (1967) Oxygen and hydrogen isotope ratio in sedimentary rocks and minerals. [Ph.D. Thesis], California Institute of Technology.

Schütze, H. (1984) Intramolekulare Sauerstoffisotopengeothermemetrie an Hydrosilikaten. *Mitt. Zentralinst. Isot. Strahlenforsch. Leipzig* **84**, 357–363.

Seligman, A.N., Bindeman, I.N., Jicha, B., Ellis, B., Ponomareva, V., Leonov, V. (2014). Multi-cyclic and isotopically diverse silicic magma generation in an arc volcano: Gorely eruptive center, Kamchatka, Russia. *Journal of Petrology* **44**, 1561–1594.

Seligman, A.N., Bindeman, I.N., Watkins, J.M., Ross, A.M. (2016). Water in volcanic glass: From volcanic degassing to secondary hydration. Geochimica et Cosmochimica Acta in review.

Sharp, Z.D., Atudorei, V., Durakiewicz, T. (2001). A rapid method for determination of hydrogen and oxygen isotope ratios from water and hydrous minerals. *Chemical Geology* **178**, 197–210.

Shane, P., Ingraham, N. (2002). δD values of hydrated volcanic glass: A potential record of ancient meteoric water and climate in New Zealand. *New Zealand Journal of Geology & Geophysics* **45**, 453–459.

Shaw, A.M., Hauri, E.H., Fischer, T.P., Hilton, D.R., Kelley, K.A. (2008). Hydrogen isotopes in Mariana arc melt inclusions: Implications for subduction dehydration and the deep-Earth water cycle. *Earth and Planetary Science Letters* **275**, 138–145.

Sheppard, S.M.F., Gilg, H.A. (1996). Stable isotope geochemistry of clay minerals. *Clay Minerals* **31**, 1–24.

Silver, L.A., Ihinger, P.D., Stolper, E. (1990), The influence of bulk composition on the speciation of water in silicate glasses. *Contrib. Mineral. Petrol.* **104**, 142–162.

Snell, K.E., Koch, P.L., Druschke, P., Foreman, B.Z., Eiler, J.M. (2014). High elevation of the 'Nevaplano' during the Late Cretaceous. *Earth and Planetary Science Letters* **386**, 52–63.

Sveinbjörnsdóttir, A.E., Coleman, M.L., Yardley, B.W.D. (1986). Origin and history of hydrothermal fluids of the Reykjanes and Krafla geothermal fields, Iceland: A stable isotope study. *Contributions to Mineralogy and Petrology* **94**, 99–109.

Swanson, S.E., Harbin, M.L., Riehle, J.R. (1995). Use of volcanic glass from ash as a monitoring tool: An example from the 1992 eruptions of Crater Peak, Mount Spurr Volcano, Alaska. *US Geological Survey Bulletin* **2139**, 129–137.

Taylor, B.E. (1986). Magmatic volatiles: Isotopic variation of C, H, and S. In *Stable Isotopes in High Temperature Geological Processes* (eds. J.W., Valley, H.P., Taylor, J.R. O'Neil), Reviews in Mineralogy and Geochemistry **16**, 185–225.

Vennemann, T.W., Fricke, H.C., Blake, R.E., O'Neil, J.R., Colman, A. (2002) Oxygen isotope analysis of phosphates: a comparison of techniques of analysis of Ag_3PO_4. *Chemical Geology* **185**, 321–336.

Walowski, K.J., Wallace, P.J., Hauri, E.H., Wada, I., Clynne, M.A. (2015). Slab melting beneath the Cascade Arc driven by dehydration of altered oceanic peridotite. *Nature Geoscience* **8**, 404–409.

Watts, K.E., Bindeman, I.N., Schmitt, A.K. (2011). Large-volume rhyolite genesis in caldera complexes of the Snake River Plain: Insights from the Kilgore Tuff of the Heise Volcanic Field, Idaho, with comparison to Yellowstone and Bruneau-Jarbidge rhyolites. *Journal of Petrology* **52**, 857–895.

Zierenberg, R.A., Schiffman, P., Barfod, G.H., Lesher, C.E., Marks, N.E., Lowenstern, J. B., Mortensen, A.K., Pope, E.C., Bird, D.K., Reed, M.H., Fridleifsson, G.O., Elders, W.A. (2012). Composition and origin of rhyolite melt intersected by drilling in the Krafla geothermal field, Iceland. *Contributions to Mineralogy and Petrology* **165**, 327–347.

Zhao, Z.F., Zheng, Y.F. (2003). Calculation of oxygen isotope fractionation in magmatic rocks. *Chemical Geology* **193**, 59–80.

Zhang, Y., Jenkins, J., Zhengjiu, X. (1997) Kinetics of the reaction $H_2O + O = 2OH$ in rhyolitic glasses upon cooling: Geospeedometry and comparison with glass transition. *Geochimica et Cosmochimica Acta* **61**, 2167–2173.

Zheng, Y. (1991). Calculation of oxygen isotope fractionation in metal oxides. *Geochimica et Cosmochimica Acta* **55**, 2299–2307.

Zheng, Y. (1993). Calculation of oxygen isotope fractionation in hydroxyl-bearing silicates. *Earth and Planetary Science Letters* **120**, 247–263.